# Development of 3D Visualisation Algorithms For The Effective Interpretation of Tunnel & Transport Infrastructure Subsurface Radar Data

**Thomas Peter William McDonald**

School of Engineering
Newcastle University, UK

This thesis is submitted for the degree of
*Doctor of Philosophy*

September 2024

# Abstract

Ground Penetrating Radar (GPR) is a versatile technology for non-destructive inspection of subsurface structural anomalies, which ensures the safety and efficacy of ageing transport infrastructure. Effective subsurface inspection better informs targeted maintenance strategies, maximising long-term infrastructure resilience. However, multiple research gaps exist for traditional fixed-directional GPR. They extend to increasing the completeness of subsurface coverage (especially in fully-enclosed tunnel structures) and reducing reliance on unclear 2D visual output (based on hyperbolic signal artifacts); alongside addressing the lack of versatile, open-access data processing tools for 3D anomaly profiling.

This thesis advances emerging hybrid-rotational GPR technology, which utilise advanced 360-degree orientable antennas to maximise subsurface coverage. Work presented develops a unique 3D visualisation framework for this technology, focusing on the inspection of historic railway tunnels and retaining walls. The devised framework encompasses both data collection and conveyance strategies, returning practical 3D visual outputs for surveyors.

Investigatory work systematically analyses framework performance across multiple infrastructure analogues. A novel, highly versatile 3D visualisation workflow is developed for effective data conveyance, uniquely capable of profiling subsurface anomalies in (i) simulated, (ii) fixed-directional, and (iii) new hybrid-rotational GPR datasets.

This workflow innovatively utilises exclusively open-access tools and a three-phase pipeline for data extraction, regularisation, and 3D segmentation. Innovations for data collection focus on developing next-generation hybrid-rotational GPR equipment for laboratory and field testing.

Key advancements include successful anomaly detection at decimetre scales to within 30mm, and consistent mid-centre localisation within 3% deviation from ground truth geometry. Combined Processing Methodology further increases imaging resolution, enhancing response profile median frequency by 152%, sharpening amplitude peaks. Further high-impact research avenues are also identified, including automated anomaly characterisation, report generation, and dataset hybridisation.

Overall, this thesis highlights the significant potential of the 3D visualisation framework for increasing transport infrastructure resilience, and develops essential resources to catalyse future innovation.

*For Mum & Dad,*

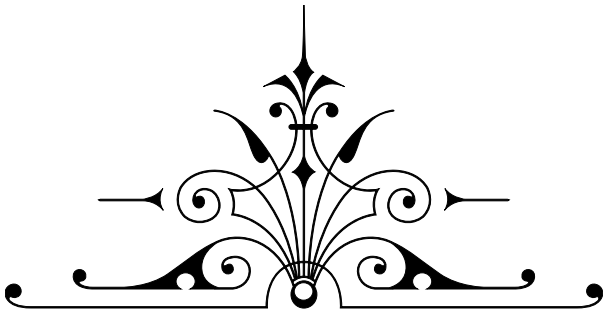

*T.A.G. you're it...*

# Acknowledgments

In a delightful parallel with the themes of the thesis, the complexity, significance, and challenges of undertaking a PhD research project become all the more extensive when one looks deeper. This section serves to acknowledge the individuals and groups who have provided support over the course of this research project.

For their expertise, wisdom, and unwavering support throughout this project, sincere thanks go to Professor Mark Robinson (Primary Supervisor) and Professor GuiYun Tian (Co-Supervisor). This gratitude is also extended to review panel members (Dr Richard Whalley and Dr Umair Ahmed) and examiners (Professor Jeffrey Neasham and Dr Han-Mei Chen), for their time, encouragement and constructive feedback. Further appreciation goes to Dr Craig Warren and Dr Alain Plattner for their collective insights into leading GPR approaches, simulation and data processing software gprMax and GPRPy, alongside their professional feedback on disseminated materials.

This project's industry partner Railview Ltd is also recognised, for technical consultation on the T-Vision system and access to specialist GPR equipment. Their confidence in the researcher's leadership — especially in coordinating with Barrow Hill Roundhouse, Innovate4Rail (University of Derby), and Euromobilita s.r.o — was instrumental in delivering successful field tests of this project's new hybrid-rotational GPR systems. Similarly, the Subsurface Inspection Radar development team and wider partners of the Horizon Europe Project CRISTAL (Grant 101069838) are also recognised for their guidance on fixed-directional GPR systems and providing the opportunity to support knowledge transfer to strengthen the resilience of European Inland Waterways infrastructure.

The financial support and practical resources which have enabled this project are now acknowledged. This work has been supported by UK EPSRC Grant EPT5179141 for Newcastle University (UK). Specialist tools, bespoke component fabrication and wide interdisciplinary engagement were made possible through the support of Newcastle University's Intelligent Sensing Laboratory, School of Engineering Workshop Teams (Electrical and Mechanical), Dry Lab Technicians and The Centre of Excellence for Mobility and Transport. Special mentions include: Stuart Baker, Professor Phil Blythe, Professor Said Boussakta, Carol Booth, Ian Clark, Dr Matthew Dyson, Matthew Herrington, Paul Killan, Connor Richardson, and Steve Robson.

Throughout this journey, this project has been made significantly more enjoyable and rewarding through the support and camaraderie of those who shared their knowledge and experiences. Their willingness to discuss ideas, offer advice and provide a listening ear has been invaluable. These colleagues have become close friends. Among them are: Jummah Abduwali, Emmanuel Ibrahim, Lawal Daura, Jacopo Franco, Jenny Olsen, Ben Sherlock and Changrong Yang.

Finally, heartfelt thanks are due to those closest to this researcher, including friends whose interest, encouragement, and unwavering support helped sustain perseverance throughout this journey. Gratitude especially goes to those loved unreservedly. Who have shared every part of this emotional roller coaster, could always see the wood for the trees and always – without hesitation or doubt – reminded this one that they are capable of greatness.

# Contents

# List of Figures

# List of Tables

# Nomenclature

| | |
|---|---|
| A/V/M/XR | Augmented/Virtual/Mixed/Extended Reality |
| ACT | Active Thermography |
| AI | Artificial Intelligence |
| ASCII | American Standard Code for Information Interchange |
| AFD/E | Automated Feature Detection/Evaluation |
| BAT | Windows Batch File |
| BIM | Building Information Modelling |
| CBA | Complete Bouguer Anomaly |
| CAD | Computer Aided Design |
| CCM | Category Connection Matrix |
| CNN | Convolutional Neural Network |
| CPM | Combined Processing Methodology |
| CRP | Close-Range Photogrammetry |
| DC | Direct Current |
| DIP | Dual In-Line Package |
| DL | Deep Learning |
| DSI | Dynamic Survey Interaction |
| DTT | Digital Twin Tunnels |
| EDCDIC | Extended Binary Coded Decimal Interchange Code |
| EM | Electromagnetic |
| E-CAL | Electronic Calibration |
| ERT | Electrical Resistivity Tomography |
| FWHM | Full Width at Half Maximum |
| GPIB | General Purpose Interface Bus |
| GPIO | General Purpose Input/Output |
| GPR | Ground Penetrating Radar |
| HDBSCAN | Hierarchical Density-Based Spatial Clustering of Applications with Noise |
| HDF5 | Hierarchical Data Format Version 5 |
| I/D/F/FT | Inverse/Discrete/Fast Fourier Transform |
| IP | Internet Protocol |
| IQR | Interquartile Range |
| IST | Infrasonic Testing |
| IRT | Infrared Thermography |
| KB/MM/TB | Kilobyte/Megabyte/Terabyte |
| LAN | Local Area Network |

| | |
|---|---|
| LiDAR | Light Detection and Ranging |
| M/SSP | Modified/Spatial Smoothing Process |
| MISE | Mean Integrated Square Error |
| MUSIC | Multiple Signal Classification |
| NDI | Non-Destructive Inspection |
| NEMA | National Electrical Manufacturers Association |
| PWM | Pulse Width Modulation |
| RAM | Random Access Memory |
| RADAR | Radio Detection and Ranging |
| RGB | Red, Green, Blue |
| RoI | Region of Interest |
| RMSD | Root Mean Square Deviation |
| RRV | Road-Rail Vehicle |
| RPM | Revolutions Per Minute |
| RT | Rail-Trolley |
| RTU | Robotic Traction Unit |
| RX | Receiver Antenna |
| S1P | Single Phase One Pole |
| SBC | Single Board Computer |
| SFCW | Step Frequency Continuous Wave |
| SH | Linux Shell Script |
| SEG-Y/SGY | Standard for the Exchange of Geophysical Data |
| SfM | Structure from Motion |
| SMA | Sub-Miniature Version A |
| SOLT | Short Open Load Through |
| TLS | Terrestrial Laser Scanning |
| TCMI | Tunnel Condition Monitoring Index |
| TEM | Transverse Electromagnetic Mode |
| TX | Transmitter Antenna |
| UAV | Unmanned Aerial Vehicle |
| USB | Universal Serial Bus |
| UART | Universal Asynchronous Receiver/Transmitter |
| UST | Ultrasonic Testing |
| VNA | Vector Network Analyser |

# Chapter 1. Introduction

Global transport networks are the physical backbone of modern society. Strengthening the resilience of critical infrastructure plays a crucial role in ensuring the safe and seamless movement of people, freight, and essential services.

As central elements of network design, targeted maintenance efforts that preserve the integrity of tunnels (and their associated structural elements) are of key importance. With age and increasing levels of traffic, structural degradation accelerates. This is very significant for the UK rail network, which relies extensively on older masonry structures that can be over 150 years old. Developing optimal repair strategies requires comprehensive knowledge of structural health, particularly concerning the onset and growth of concealed anomalies within the subsurface — structural aspects which cannot be physically occupied or directly touched. As invasive exploration inherently damages healthy structures, technology for Non-Destructive Inspection (NDI) has become the basis of modern subsurface surveys and is underpinning the digitalisation of transport infrastructure management.

Ground Penetrating Radar (GPR) stands out as a highly versatile NDI technology, capable of detecting subsurface anomalies, quantitative assessment of their location and depth and relaying qualitative insights into their shape, orientation, and form. Conventional systems for structural inspection range from compact handheld units to vehicle mounted arrays, but leading GPR systems routinely suffer from limitations on two key fronts. Firstly, returned visuals often lack interpretive clarity, especially for non-radar specialists (e.g. repair crews, infrastructure managers, etc.), which limits attainable survey insight. Secondly, with regard data collection, the restricted field of view also frequently limits the comprehensiveness of survey coverage, especially for fully enclosed tunnel structures. A solution is needed to tackle these limitations and improve the effectiveness of current GPR for NDI in the transport sector. In particular, a focus on surveys of older masonry tunnel and associated critical transport infrastructure presents a high impact innovation opportunity.

In reviewing leading work in the field, this thesis identifies emerging hybrid-rotational GPR as a promising candidate basis for the next generation of transport infrastructure subsurface survey technology. The systems utilise pioneering 360-degree orientable antennas to increase achievable field of view.

The hybrid modifier serves to highlight that the lateral and rotational motion of the antenna boresight vector can be controlled independently, or even disabled. This novel functionality uniquely allows a hybrid-rotational GPR system to capture:

1. **Planar Transects**: No antenna rotation and continuous lateral advance of the antenna. This emulates transects recovered from conventional data collection systems (i.e. fixed-directional GPR).
2. **Rotational Transects**: Sequential, periodic antenna rotation between incremented lateral advance of the antenna.
3. **Helical Transects**: Continuous antenna rotation during continuous lateral advance of the antenna.

Whilst the capabilities of prototype systems show promise for practical tunnel inspection, an effective workflow capable of clearly visualising the full range of subsurface data from these systems has yet to be developed. This refines the aforementioned innovation gap.

Two further complementary research gaps are also identified. First, the 3D visualisation of data produced from the rotational capabilities of these systems has yet to be formally investigated. Additionally, the GPR research community also lacks a standalone, non-proprietary toolkit for end-to-end 3D visualisation of GPR datasets. To ensure versatility, such a toolkit would need support input data from simulated, fixed-directional, and hybrid-rotational GPR sources. This is also necessary for underpinning the research methodology in development of the desired 3D visualisations.

To tackle the innovation and research gaps identified above, this thesis proceeds to develop a robust and versatile visualisation framework for effectively interpreting subsurface anomalies within simulated, fixed-directional, and hybrid-rotational GPR datasets. In particular, when applied in the context of surveying older masonry tunnel and associated critical transport infrastructure. Realising the framework centres on development of an innovative, modular data processing workflow based on entirely open-access tools, capable of returning clear 3D visualisations of subsurface structural anomalies; exhibiting accurate subsurface anomaly detection and localisation, and efficiently scaling for application to surveys of real tunnel and associated transport infrastructure. The development of the framework also encompasses the design and implementation of bespoke hybrid-rotational GPR systems for practical data collection in laboratory experiments and field tests, essential for validating the effectiveness of the proposed 3D visualisation workflow.

## 1.1 Contributions

1. Development and implementation of the first 3D visualisation workflow for the effective detection and localisation of subsurface structural anomalies in simulated, fixed-directional, and new hybrid-rotational GPR datasets. Based on modular ELT pipeline architecture and entirely open access tools, it provides a tractable, high efficiency data processing solution for GPR researchers and practitioners.

2. Design, fabrication and refinement of bespoke hybrid-rotational GPR data collection systems for practical laboratory experimentation and field testing.

3. Development of a robust, criteria-based rationale for evaluating visualisation frameworks in transport infrastructure inspection, with a focus on historic railway tunnels, and consolidation of key summaries of common assets and defects relevant to survey practitioners, notably absent from the encountered literature.

4. Design and numerical implantation of a dedicated algorithm for automated area scan functionality in gprMax, to return 3D datasets facilitating performance analysis of the proposed visualisation workflow on state-of-the-art simulations of fixed-directional GPR.

5. Investigation of laboratory benchmarking for the proposed 3D visualisation workflow, including comparative performance analysis in application to practical datasets of fixed-directional and hybrid-rotational GPR, recorded in a controlled environment.

6. Investigation of HDBSCAN clustering parameter optimisation to enhance the quality of 3D visualisation output from the proposed workflow, with a focus on minimum cluster size and the granularity tuning parameter.

7. Performance analysis of the 3D visualisation workflow when applied to hybrid-rotational GPR data obtained from a field survey of a large-scale tunnel subsurface analogue.

8. Investigation of the CPM algorithm for spatial resolution enhancement of hybrid-rotational GPR during the data extraction phase of the proposed 3D visualisation workflow, applied to data obtained from a field survey of a large-scale retaining wall analogue.

## 1.2 Publications

The following publications have been produced as a result of the research in this thesis:

1. T. McDonald, M. Robinson, and G. Tian, "Spatial resolution enhancement of rotational-radar subsurface datasets using combined processing method," Journal of Physics: Conference Series, vol. 2090, no. 1, p. 012001, 2021.
2. T. McDonald, M. Robinson, and G. Tian, "Developments in 3D visualisation of the rail tunnel subsurface for inspection and monitoring," Applied Sciences, vol. 12, no. 22, p. 11310, 2022.
3. T. McDonald, M. Robinson, and G. Tian, "T-Vision: A hybrid subsurface radar inspection system for intelligent asset management of railway tunnels," Transportation Research Procedia, vol. 72, pp. 3466-3473, 2023.
4. T. McDonald, et al., "3-D Visualization of New Hybrid-Rotational Ground-Penetrating Radar for Subsurface Inspection of Transport Infrastructure," IEEE Transactions on Geoscience and Remote Sensing, vol. 63, pp. 1–13, 2025.

## 1.3 Recognition

Research presented in this thesis has been recognised at three separate levels:

- **Internal**: Recognition within the academic institution where the research was conducted, namely Newcastle University (UK).
- **National**: Recognition form engagement with external bodies within the UK.
- **International**: Recognition from engagement with external bodies outside the UK.

Work conducted for this thesis has received the following noteworthy recognition:

- **Internal**: School of Engineering Poster Prize for Marine Technology and Mechanical Engineering, Post-Graduate Research Conference 2020/2021, Newcastle University (UK), Runner Up.
- **Internal**: School of Engineering Presentation Prize for Marine Technology and Mechanical Engineering, Post-Graduate Research Conference 2023/2024, Newcastle University (UK), Runner Up.
- **National**: Student and Apprentice Poster Award, Early Careers Forum 2022, Intelligent Transport Systems (UK), Runner Up.
- **International**: TRAVISIONS Young Researcher Competition (Rail Modality), Transport Research Areana 2022, EU Horizon 2020 Programme, First Place.
- **International**: TRAVISIONS Young Researcher Competition (Waterborne Modality), Transport Research Arena 2024, EU Horizon Europe Programme, Runner Up.

## 1.4 Wider Engagement

Work conducted in this thesis has led to several significant interactions with both the wider scientific research community and transportation industry, at both a national and international level. Noteworthy instances include:

- Presented a 30-minute technical presentation in person to industry representatives from Network Rail, COWI and Railview Ltd, alongside members of Innovate UK in June 2021 on the analysis of rotational transect datasets from an early trial of hybrid-rotational GPR technology.
- Presented a 15-minute scientific presentation virtually to academics from engineering and applied mathematics at the 10th International Conference on Mathematical Modelling in Physical Sciences (IC-MSQUARE) in September 2021, on research work into CPM spatial resolution enhancement of hybrid-rotational GPR data.
- Active coordinator for the UK-China-BRI Countries Education Partnership Initiative 2020-2024, as organiser of the 1st and 2nd International Workshops on Digital Twins in Railway Engineering and Rail-Related Research, in KMUTNB (Bangkok, Thailand, 2022) and SWJTU/UESTC (Chengdu, China, 2023). Responsibilities included serving as the UK-based secretary, session chair and as guest presenter across both events.
- Presented a 1-hour talk virtually as an invited guest speaker at the ECTRI Seminar Series on Freight and Logistics in December 2022, on collective research work to date into the 3D visualisation of hybrid-rotational GPR data, with a focus on the impact-potential such innovations presented for networks in regard to increased infrastructure resilience and more effective targeted maintenance.
- Secured the position of Research Assistant in the Centre of Excellence for Mobility and Transport at Newcastle University (UK) in July 2024, serving as the lead electrical engineer for research and development of a novel subsurface inspection radar system for European Inland Waterways lock wall structural health assessment as part of the Horizon Europe project 'Climate Resilient and Environmentally Sustainable Transport Infrastructure, with a Focus on Inland Waterways' (CRISTAL).

## 1.5 Thesis Outline

Chapter 2 provides the key background for this thesis. It begins with an overview of Ground Penetrating Radar (GPR) operating principles, survey concepts and interpretation. The motivation for this research area is outlined, centred on the challenge of detecting and localising subsurface structural anomalies in aging UK railway infrastructure, specifically tunnels and retaining walls.

A comprehensive review of state-of-the-art subsurface surveying technologies applicable to such historic masonry infrastructure is presented, uniquely addressing both data acquisition *and* information conveyance. Heuristic analysis of leading literature utilises a Category Connection Matrix to formulate a robust criteria underpinning *effective* subsurface inspection techniques and visualisation frameworks.

The process highlights the potential of emerging hybrid-rotational GPR technology to meet the full criteria. Its unique 360-degree orientable antenna configuration notably affords swift, high-penetration, full-circumferential tunnel coverage. A feasibility study is undertaken to explore the scope of the technology, which demonstrated its efficacy for hidden shaft detection. Findings further indicate promising potential for it to return high-fidelity 3D subsurface visualisations, subject to improved positioning accuracy and downscaling for laboratory-based tests. Collectively, this motivates focus on the development of pioneering 3D visualisation algorithms for hybrid-rotational GPR technology, directly informing the research questions, aims, and objectives of the thesis.

Chapter 3 details the research methodology, in which the development of an effective 3D visualisation workflow is prioritised — essential for future optimisation of helical scan parameters. The devised workflow is based on a modular ELT pipeline, divided into three phases: (i) Data Extraction, Alignment, and Pre-Processing; (ii) Grid Regularisation and Post-Processing; and (iii) Cluster-Based 3D Segmentation and Rendering. The unique design natively supports not only simulated and fixed-directional input data, but also new hybrid-rotational GPR, granting significant versatility, with the addition of a multi-layer model for high-accuracy 3D data alignment in each case. Innovative joint Isovalue and HDBSCAN clustering is also integrated for improved anomaly segmentation.

The devised workflow is evaluated progressively, starting with simulated datasets in Chapter 4, followed by laboratory and eventually field tests in Chapters 5 and 6, respectively, each utilising physical GPR systems and structural analogues. Fundamentally, the investigatory process transitions from idealised scenarios with absolute ground-truth knowledge towards increasingly more realistic, practical datasets.

Throughout, the principal focus of each chapter is analysing the workflow's accuracy of subsurface anomaly detection and localisation, with computational efficiency for practical implementation also considered.

In Chapter 4, the workflow is tested on a fixed-directional GPR survey generated using leading simulation software gprMax. Not natively supporting area scan functionality, a bespoke automation algorithm is developed based on shell scripts to facilitate dataset generation. Results demonstrate accurate detection and localisation of known targets to within decimetre length scales, with 3D visual output recovered in under 5 seconds across 20 independent runs. Chapter 5 expands analysis through use of practical GPR datasets, collected under controlled laboratory conditions with a commercial fixed-directional GPR system. The accuracy of 3D visual output is qualitatively compared to established ground-truth geometry, with segmentation accuracy evaluated quantitatively through inspection of cluster mid-centre coordinates. The runtime impact of integrating higher efficiency checkpointing functionality during data extraction is also examined.

In Chapter 6, a bespoke miniaturised hybrid-rotational GPR system is developed for the final stage of laboratory benchmarking. The system profiles the same ground-truth geometry used in the previous chapter, thereby validating the experimental data collection setup and establishing a baseline for workflow performance with hybrid-rotational GPR data. A key area of investigation is the influence of HDBSCAN cluster segmentation, specifically examining how variations in minimal cluster size and the granularity tuning parameter affect the accuracy of returned 3D spatial profiles. Observed performance recovers optimised parameter configurations and justifies subsequent progression to field testing.

Chapter 7 details two separate field tests, designed to assess workflow performance on data from more realistic, practical survey environments. The first test utilises pre-placed hollow targets in a backfilled railway inspection pit to serve as a defective tunnel subsurface analogue, while the second test employs a concealed target behind a masonry retaining wall analogue. In both cases, the laboratory hybrid-rotational GPR system is adapted from a linear rail to a pushcart configuration for onsite data collection.

In the first test, consistency between footprints and mid-centres of 3D subsurface visuals returned by the workflow provides confidence in its ability to accurately profile targets in field conditions. Evidence of cluster fragmentation notably draws parallels with ringdown artifacts inherently associated with hollow structural geometries.

Looking towards future refinement of the devised workflow, the second test explores the potential of the CPM algorithm for enhancing hybrid-rotational GPR trace data. In analysis of a rotational transect, observed agreement between CPM temporal response profiles and anticipated peak locations — for wall interfaces and an obscured metallic reflector — demonstrates accurate numerical implementation. Comparisons with temporal profiles recovered from the IFFT and MUSIC algorithms subsequently evidence the CPM algorithm's superior trace resolution capabilities, compared to either of the respective standalone methods.

Finally, Chapter 8 consolidates key findings from across the thesis. Concluding remarks are presented, followed by a brief summary of prospects for short term and long-term future work.

# Chapter 2. Background, Motivation and State-of-the-Art

This chapter presents an in-depth examination of the fundamental background information that underpins the research presented in this thesis.

## 2.1 Introduction

An outline of the literature review approach is first detailed in Section 2.2 — which includes a high-level breakdown of both primary and secondary sources — before elaborating on relevant operational theory, terminology, and practical practices related to Ground Penetrating Radar (GPR) surveys in Section 2.3.

Motivation underpinning the project storyline follows in Section 2.4. The context of research is refined, establishing a focus on the subsurface inspection of historic masonry transport infrastructure, specifically for tunnels and their constituent structural elements. A unique consolidated summary of key assets and defects commonly encountered in these surveys is subsequently presented, addressing a significant knowledge gap identified across literature encountered. In Section 2.5, an in-depth literature review examines both established and experimental technologies for non-destructive subsurface inspection of tunnel and transport infrastructure. By identifying the critical limitations of each technology and the leading research trends, this review establishes a robust set of criteria for defining an *effective* subsurface inspection technology for transport infrastructure, as discussed in Section 2.6.

The work presented in the above sections was summarised and disseminated in [24].

Pioneering hybrid-rotational GPR technology emerges as a notable and promising advancement in this field, exhibiting potential to become the first practical technology to fully meet the established criteria among approaches identified in this review. In Section 2.7, deconstruction of a feasibility trial of this technology, specifically regarding hidden shaft detection within an in-service UK railway tunnel, subsequently shapes the research questions, aims, and objectives for research conducted in this thesis, formally outlined in Section 2.8.

The work presented in the above sections was summarised and disseminated in [22].

## 2.2 Review Strategy

This review consults journal references, practical studies and commercial systems linked to subsurface visualisation frameworks[1] for large-scale transport infrastructure, which serve to inform targeted maintenance of enclosure and otherwise inaccessible structural aspects.

The full study is published as a standalone review in [24]; here, a brief overview of its motivation and methodology is provided.

No prior reviews encountered during literature analysis jointly examined both data collection and conveyance methods in detail. Only two relevant works, [25] and [26], were identified, both primarily focused on data collection. Notably, [25] was the only dedicated review, heavily relied upon by [26] — significantly limiting its standalone merit. As [25] was over five years old, an updated assessment was needed to capture recent innovations. Additionally, the lack of attention to advancements in data conveyance highlighted a further knowledge gap to address.

In response, this review employed the 360-degree search method [27], drawing from over 300 independent sources. A total of 255 primary resources (i.e. journal articles, conference proceedings, etc) across IEEE Xplore, Springer and MDPI were formally analysed, along with 60 secondary resources (i.e. technical reports, corporate media, etc.). Conservatively, data collection underpinned 76% of encountered works, data conveyance represented 55% and 33% provided contextualisation.

Given the inherent interdependence between advancements in data conveyance and data collection schema, sources frequently contributed to discussions of both. As a conservative estimate, the total distribution of considered literature was approximately 67% across data collection and 55% across data conveyance, with 33% providing contextualisation. Maximal crossover was approximately 69%.

Academic publications were obtained using the 360-degree search method [27], applied to journal articles and conference proceedings primarily sourced through the following databases: IEEE Xplore, Springer, MDPI and Google Scholar. Materials associated with commercial systems were primarily sourced from the relevant corporate organisations websites, system manuals and associated technical specifications. Keywords recurringly searched included, but were not limited to: Subsurface, Non-Destructive Inspection, Structural Health Monitoring, Transport Infrastructure, Tunnels, Computer Vision, Human Computer Interaction and Visualisation. The full systematic breakdown of the key sources consulted in this review is available as part of the supplementary materials provided in [24].

[1] In this work, a *visualisation framework* encapsulates both data collection *and* conveyance — the latter, notably extending to the communication of subtext and inferred insights from recovered data.

## 2.3 Background – Ground Penetrating Radar (GPR)

Ground Penetrating Radar[2] (GPR) is a Non-Destructive Inspection (NDI) technology. Unlike surface-level inspection techniques, which detail the condition of the outermost layer of a structure, GPR is a subsurface inspection method, capable of revealing concealed features within the structure, obscured by the surface.

Surveys conducted using GPR typically divide the inspection of a large structure into smaller, more manageable sections. Based on prior knowledge of subsurface condition (i.e. ground-truth geometry), certain areas within a section may be of greater interest to surveyors and are here designated as a specific Region of Interest (RoI), which can be either two-dimensional (2D) areas or three-dimensional (3D) volumes depending on the nature of the survey.

### *2.3.1 Theoretical Foundations*

From a high-level abstract perspective, a GPR system requires a signal generator, which produces an excitation signal[3] that is directed into the subsurface by a transmission antenna (Tx). A complementary receiver antenna (Rx) then detects the reflected signals which backscatter from material interfaces associated with subsurface geometry.

The properties of the returned signals provide insight into the characteristics of this geometry, which can be both quantitative (e.g. depth) and qualitative (e.g. shape) making GPR a highly versatile and informative inspection tool when used by an experienced operator.

Some subtleties of this explanation are highlighted at this point.

First, as illustrated in Figure 2.1, it is possible to combine both types of antenna into a monostatic configuration, which use a single antenna that continuously alternates between transmitting and receiving during a scan. In contrast, bistatic configurations use a pair of separate transmit and receive antennas, which can be further multiplexed to produce larger multistatic arrays. Subject to survey context, the simpler and more compact design of monostatic setups can be more desirable than more cumbersome, complexly interfaced bistatic and multistatic arrays.

[2]Radio Detection and Ranging (RADAR).
[3]In the electromagnetic (EM) spectrum, typically achieved using microwaves between 10MHz-4GHz.

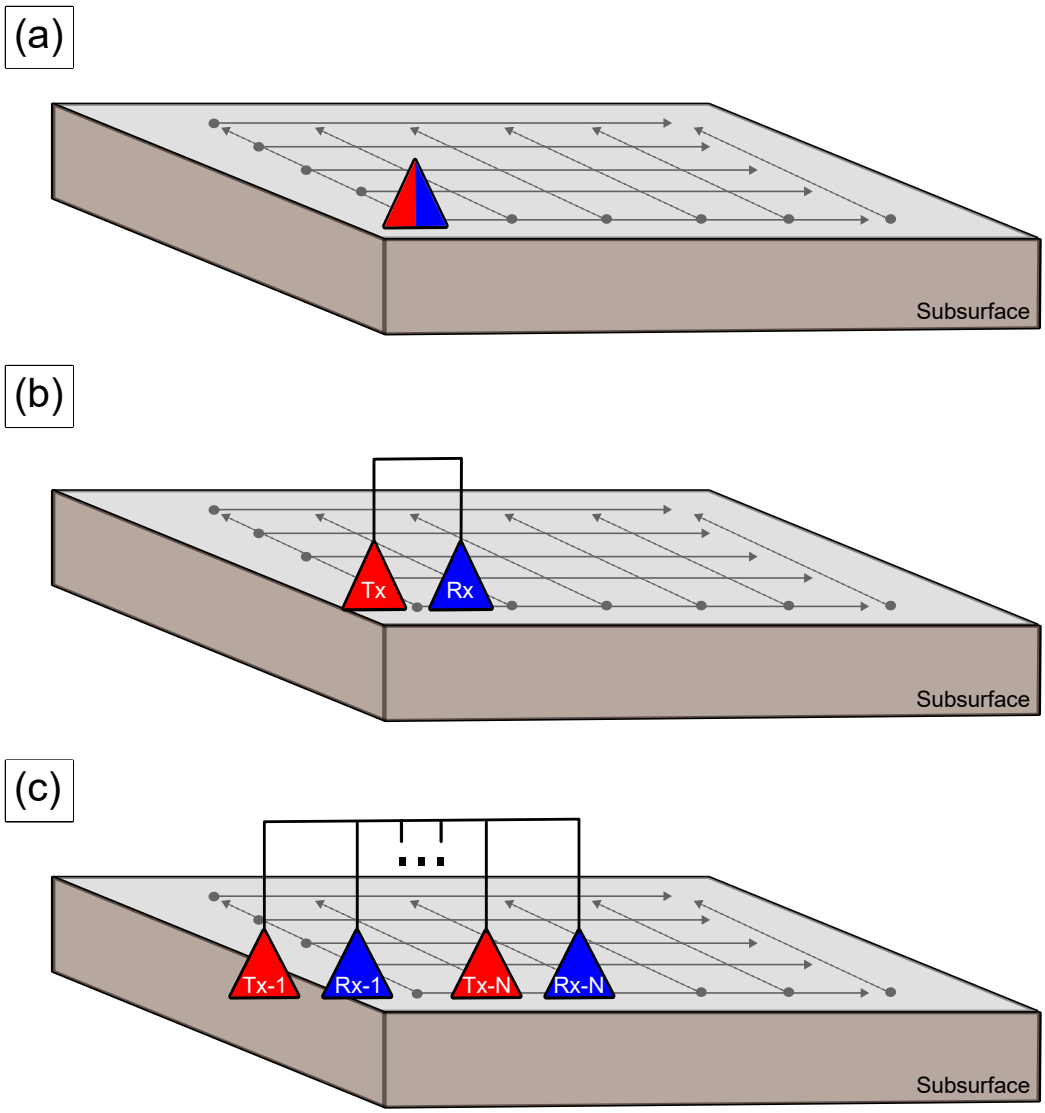


Figure 2.1: Common GPR antenna configurations include: (a) monostatic; (b) bistatic and (c) multistatic antenna arrays.

The choice of antenna centre frequency optimises the balance between spatial resolution and penetration depth, with higher frequencies enhancing resolution and lower frequencies increasing depth capability. Antennas can be ground-coupled, operating very close to the outermost interface of the RoI (i.e. the contact surface) for high-efficiency energy transfer and improved data quality, or air-launched, which are beneficial for maintaining separation (i.e. significant antenna lift off) from the ground to prevent fouling, particularly in vehicle-mounted systems.

Second, an antenna's direction in this context is often associated with a line extending outward from the midpoint of the surface of the antenna (i.e. its aperture[4]) into the subsurface. This is termed the antenna boresight vector, and its orientation relative to the antenna aperture will be considered strictly fixed, orthogonal[5] to its midpoint.

In addition, when signal wavefronts reflect off material interfaces, as shown in Figure 2.2, a portion of the incident energy is also transmitted through the boundary, while some is absorbed. The inherent roughness of real-world boundary interfaces also results in scattering, which causes outgoing ray paths to diverge in multiple directions.

At the interface between two media, such reflections and refractions abide Snell's Law. The angle of reflection is equal the angle of incidence, while the angle of refraction is given by:

$$n_1 \sin(\theta_1) = n_2 \sin(\theta_2), \tag{2.1}$$

where $\theta_1$ is the angle between the incident ray and the normal to the interface, and $\theta_2$ is the angle between the refracted ray and the normal. The terms $n_1$ and $n_2$ denote the refractive index associated with each respective media, and in GPR are typically considered in terms of associated relative electrical permittivity, $\epsilon_r$, related by

$$n = \sqrt{\epsilon_r}. \tag{2.2}$$

[4]This can also refer to an opening through which EM-waves pass, depending on the specific type of antenna. Ultimately, this term denotes the particular shape and form of an antennas physical profile, which significantly influences its performance.

[5]Geometric alignment that meets at right angles when a formal coordinate system is defined.

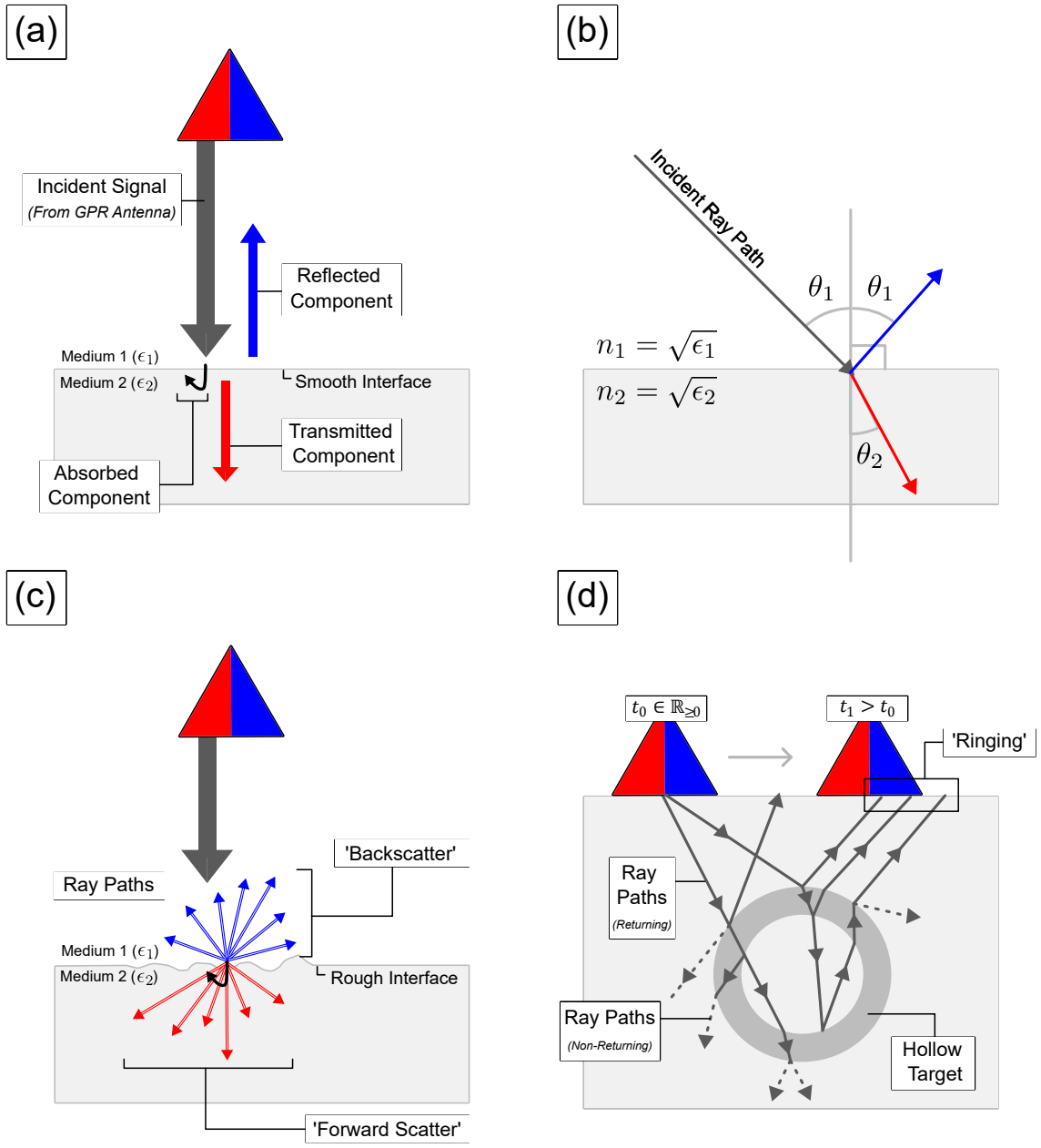


Figure 2.2: Interaction between incident GPR signals and material boundary interfaces. In an ideal scenario, a proportion of the incident signal is transmitted, a fraction is absorbed, and the remainder is reflected directly back to the antenna (a) with ray paths abiding Snell's Law (b). Practically, scattering occurs in both directions (c) owing to inherent boundary roughness, alongside ringing phenomena (d) — most notable in hollow targets, which have multiple independent interfaces.

When encountering hollow geometries, this process occurs repeatedly across internal and external interfaces in rapid succession, this phenomena can produce a series of successive backscatter events, akin to the resonation of a struck bell. This effect, known as 'ringing' or 'ringdown', gradually diminishes as energy is both absorbed and dispersed by scattering, resulting in the measured signal response displaying a consistent sequence of strong, progressively decaying amplitude peaks separated by regular time intervals. These hallmarks also manifest in higher-dimensional GPR datasets described in later sections.

The relative proportion of transmission and reflection at material interfaces is principally dictated by the ratio of relative electrical permittivity of each material media. The reflection coefficient is defined,

$$R = \left( \frac{\epsilon_{r_2} - \epsilon_{r_1}}{\epsilon_{r_2} + \epsilon_{r_1}} \right)^2 \tag{2.3}$$

where $R \in [0, 1] \subset \mathbb{R}$ and $\epsilon_{r_2}, \epsilon_{r_1}$ denote the relative electrical permittivity of each respective medium. By symmetry, the transmission coefficient is defined,

$$T = 1 - R. \tag{2.4}$$

Metals in particular have extremely high relative electrical permittivity, such that $\epsilon_r \to \infty$ is commonly assumed. Therefore, effectively all incoming excitation energy is reflected, aside a small fraction which is directly absorbed by the material in all situations.

It should be further noted that not every backscattered signal eventually reaches the receiver antenna, subject to its point of contact with the geometry. Backscatter from interfaces of geometry parallel to the boresight vector result in significantly fewer signals which eventually intersect the receiver antenna, those which do not typically continue onward into the subsurface before attenuating to the level of background noise.

Moreover, when the subsurface medium has a significantly heterogeneous composition, signals can be further scattered due to the potentially significant but highly localised variation in relative electrical permittivity throughout the media. Energy losses on interaction with such 'clutter' can serve to rapidly attenuate signals in highly heterogeneous media.

Geometric spreading also contributes to the attenuation of GPR signals. This phenomenon occurs due to the natural expansion of the excitation wavefront as it propagates, which causes the energy to spread over an increasingly larger area. As a result, the energy density decreases, leading to a weaker signal.

Observed signal attenuation can be used to inform the maximum penetrative depth achieved during a GPR scan. Namely, maximal penetration is known to have been reached when no further significant backscattered signals (above the residual background noise) are detected by the receiver antenna.

### *2.3.2 Resolution and Propagation Factors*

The performance of a GPR system is dependent on multiple factors, including the interplay between frequency-dependant signal propagation effects, antenna characteristics and associated resolution limits [5]. Typical systems are ultrawideband[6] (UWB), operating across frequency intervals between 10MHz to 2.6GHz [28]. Frequency selection is an application-specific trade-off between desired levels of penetrative depth and imaging resolution, underpinned by the frequency-wavelength relation,

$$v = f\lambda \implies \lambda = \frac{c}{f\sqrt{\epsilon_r}}, \tag{2.5}$$

where $f$ is the considered frequency value; $\epsilon_r$ is the releative electrical permittivity of the media; $\lambda$ is the associated wavelength and $v \approx c$ is the GPR signal propagation velocity, often assumed to be reasonably approximately by the speed of light in a vacuum $c$. Higher frequencies correspond to shorter wavelengths, which are more sensitive to signal variation across finer length scales, improving attainable levels of imaging resolution. However, they are susceptible to rapid attenuation, especially in lossy media (e.g. water-saturated soil), resulting in reduced penetration depth. Conversely, the longer wavelengths of lower frequencies can penetrate deeper, but limit the resolution of smaller, smaller closely spaced targets.

Antenna design must also be considered, and is similarly motivated by survey context. For example, as shown in Figure 2.3a, the flared aperture and high directivity of a horn antenna facilitates a smooth transition from the transmission line to free space, which focuses radiated energy into a narrow beam, minimising loss. This design enables deep signal penetration and effective operation over large lift-off distances up to the order of metres [29, 30]. For shallower surveys, antennas with moderate directivity and compact designs, such as dipoles (Figure 2.3b) or bowties (Figure 2.3c), are often preferred. Similarly, the Vivaldi antenna (Figure 2.3d), with its logarithmic tapered slot design, offers a wide aperture, high directivity, and broad frequency coverage, making it ideal for high-resolution imaging in shallow-depth applications.

[6]Typically characterised by an operating bandwidth spanning at least 500MHz, or 20% either side of the centre frequency.

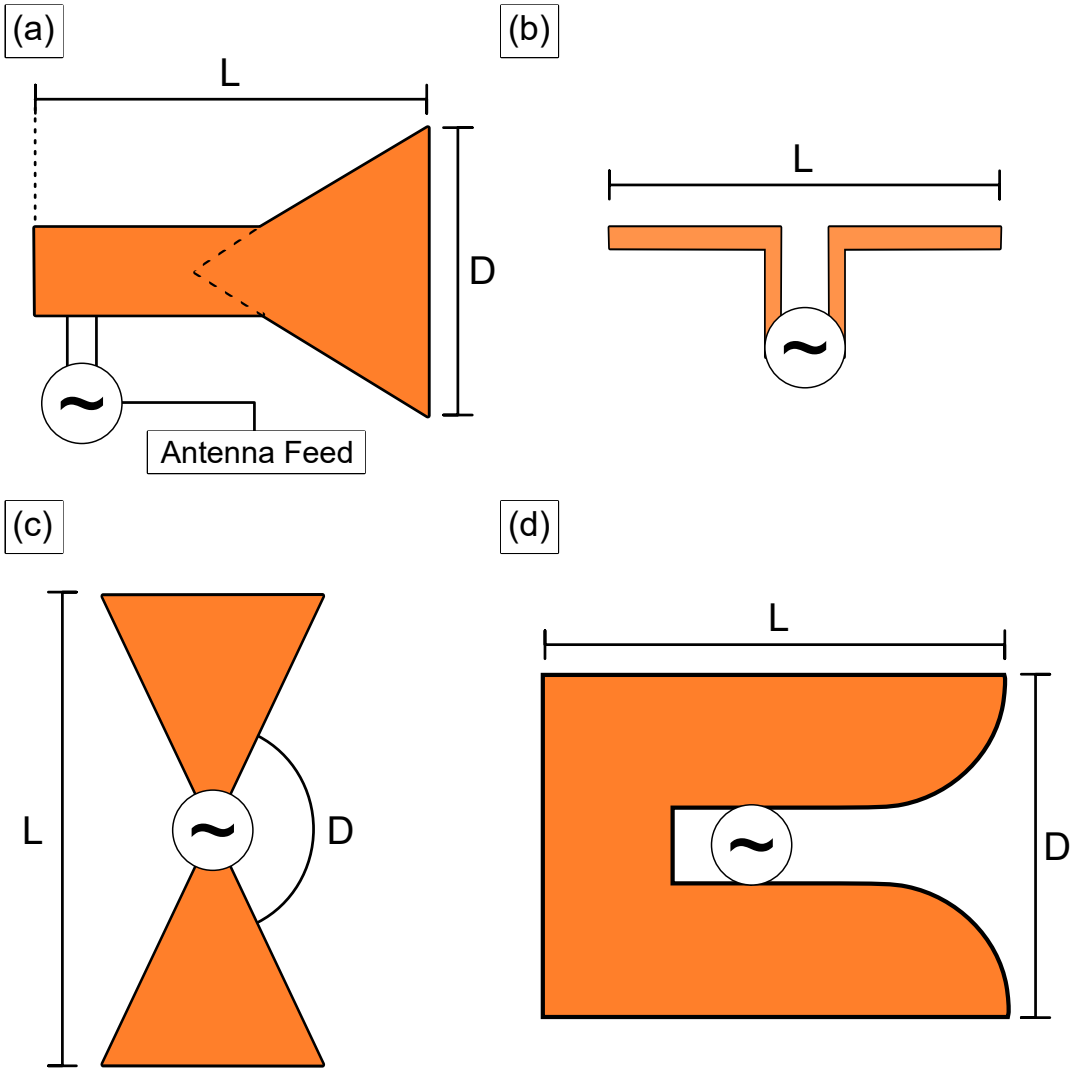


Figure 2.3: Cross sections of horn (a), dipole (b), bowtie (c) and Vivaldi (d) antennas [1]. Annotations show typical feed location, aperture size ($D$) and largest characteristic dimension ($L$) of each antenna.

Attainable levels of resolution are a recurrent theme. In a typically GPR survey, as illustrated in Figure 2.4a, range resolution is the minimal length-scale over which two separate targets can be distinguished in the vertical plane. In an idealised survey environment, assuming a homogeneous background media, range resolution is inversely proportional to measurement bandwidth, $B$, and can be expressed as,

$$\Delta y = \frac{c}{2B\sqrt{\epsilon_r}}. \tag{2.6}$$

In reality, $\epsilon_r$ is often depth dependant, typically increasing as the signal propagates into the ground, which becomes more saturated as it approaches the water table.

Cross range resolution in the horizontal plane is also inherently proportional to signal propagation depth, $R$, and is given by,

$$\Delta x = \left(\frac{\lambda_c}{D}\right) R = \left(\frac{c}{f_c D\sqrt{\epsilon_r}}\right) R \tag{2.7}$$

where $D$ is the largest characteristic dimension of the antenna (typically its aperture), $f_c$ is the centre frequency of the measurement (the midpoint of the bandwidth), and $\lambda_c$ is the corresponding wavelength. This resolution is fundamentally limited by diffraction, which becomes most significant when the transmitted signal crosses the antenna aperture. The diffraction effect imposes a limit on how narrowly the beam can be focused and the resulting level of imaging resolution that can be directly attained.

The nature of GPR survey conducted also influences expected signal propagation characteristics. In ground-coupled systems exhibiting limited lift-off significantly less than the length scale of a single wavelength, interactions associated with the antenna's near-field region are of principal interest. In this region, wavefronts are complex and non-uniform, often resulting in variable coupling effects and less predictable propagation paths. Resulting propagation complexity is further compounded by subsequent interactions with the close proximity rough contact surface boundary and inhomogeneous media residing beneath. In contrast, air-launched systems typically operate at lift-off separations of multiple wavelengths, residing in the far-field region of the antenna. Here signal propagation is characterised by stable, planar wavefronts with well-defined, regular beam patterns [3]. In general, for an arbitrary antenna — as illustrated in Figure 2.4b — this critical separation threshold is given by,

$$R_{ff} \geq \frac{2D^2}{\lambda}. \tag{2.8}$$

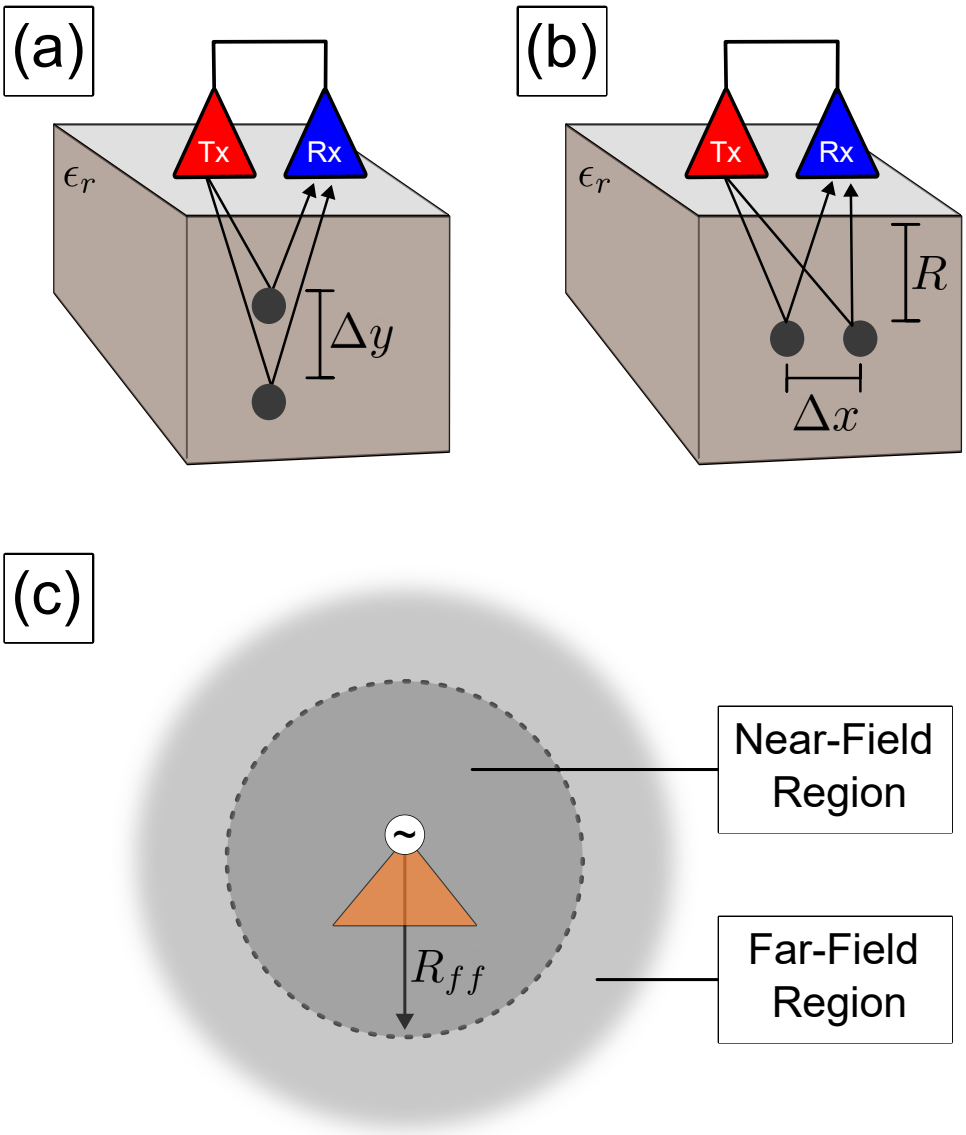


Figure 2.4: Illustration of GPR range resolution (a); cross-range resolution (b) [2] and field regions (c) [3]. The orange triangle represents an arbitrary measurement antenna.

In both regimes, accurate interpretation of captured data is reliant on extensive post-processing techniques (e.g. gain compensation, dewow[7] , migration[8] , etc.) especially in the more complex near-field scenario as signals are susceptible to significant distortion. However, the greater stability of far-field wavefronts typically has a lower impact on the quality of recorded measurements, when the appropriate beamwidth and directivity are selected to ensure the antenna beam covers the region of survey interest.

Finally, a distinction should be made between an antenna's physical and synthetic beam shapes. The physical beam shape describes the natural distribution of energy radiated by the antenna, primarily governed by its design, operating bandwidth, and the propagation characteristics of the signal. In GPR systems, this typically results in moderate directivity, with the energy extending in 3D as a broad conical beam profile into the survey region. Through constructive, phase-centric summation of judiciously selected measurement signals acquired across different antenna positions (or times), Synthetic Aperture Radar (SAR) can effectively emulate the capabilities of a much narrower, more highly directional antenna [31,32]. Beam focusing techniques can significantly enhance system resolution by reducing the main lobe width and suppressing sidelobes, improving target discrimination at shorter length scales and overall interpretability of the resulting images. However, SAR techniques may not always be practically implementable, as they require precise knowledge of signal phase components, precise control of antenna positioning, sufficient data density, and further assumptions about medium homogeneity — factors that may be difficult to achieve in complex or logistically constrained field environments.

### *2.3.3 Practical Implementation and Interpretation*

The measurement process for a GPR system generally follows one of two approaches.

Impulse GPR systems transmit short-duration pulses into the subsurface and record the intensity and time delay of the backscatter over a defined interval, capturing data directly in the time domain. The simplicity these systems results in more time-efficient equipment configuration, while the higher sampling rates allow measurement equipment to be mounted to fast moving vehicles (e.g. cars, trains, etc.) and still return sufficiently dense datasets to draw meaningful conclusions about the subsurface.

Systems most commonly encountered in the literature were developed by MALA Guideline Geo, GSSI, Sensors and Software, Leica Geosystems and Radar Systems Inc. [33–37].

[7] Suppression of low frequency noise ('wow') components attributed to instrument drift and resonation.
[8] Attempts to compensate for the true spatial position of anomaly profiles and collapse their hyperbolic signal artifacts into points.

Alternatively, Step Frequency Continuous Wave (SFCW) systems use a discretised linear frequency sweep to analyse the backscatter in the frequency domain. Although this method is more complex, often requiring a Vector Network Analyser (VNA) or similar advanced controller, it can deliver improved signal-to-noise ratios compared to Impulse GPR systems. While less frequently encountered in the literature, and more commonly specialised for concrete inspection, advanced commercial solutions most frequently utilised included the Leica C-Thru Concrete Scanner [38] and the Proceq GP8000 [7].

Block diagrams of basic Impulse and SFCW GPR systems are presented in Figure 2.5.

Both methods are commonly employed in practical surveys using kinematic data acquisition, where the antenna is moved across the RoI contact surface in a straight-line trajectory to generate a 2D cross-section of the subsurface, known as a transect[9]. These transects consist of sequentially recorded individual traces, each representing a standalone GPR measurement (from an effectively stationary antenna). Each trace is comprised of multiple sample points, which encode the temporal response profiles of observed backscatter[10], for which the amplitude is often denoted $A(t)$. During visual analysis, the absolute magnitude $|A(t)|$ is frequently considered, as this represents the real observable profile, since amplitude measurements can be complex-valued depending on the GPR system used (e.g. for VNA-based measurements).

In 1D traces, temporal response profiles plot these quantities against the delay time between the transmission of the excitation signal and the detection of the backscatter. This delay represents the two-way travel time of the signal as it propagates from the transmission antenna into the subsurface and returns to the receiver antenna. Fundamentally, this delay is proportional to the one-way propagation distance, which facilitates the conversion from a time axis to a depth axis. Consequently, spatial and temporal displacement are often used interchangeably in discussions of GPR surveying.

Strong backscatter events linked to significant elements of subsurface geometry appear as prominent amplitude peaks[11]. During GPR surveys, such events are indicative of the presence of subsurface anomalies (e.g. hidden structural assets, defects, features, etc.).

[9] Multiple alternative examples of common terminology are adopted throughout the literature. Traces also go by 'A-scans' and transects by 'B-scans', 'Line Scans' and 'Radargrams'.

[10] Measurements made directly in the frequency domain are converted to the temporal domain via an appropriate mathematical transform during data processing.

[11] If the geometry is anticipated, it is typically referred to as a 'target'. Else, it is commonly termed an 'anomaly'.

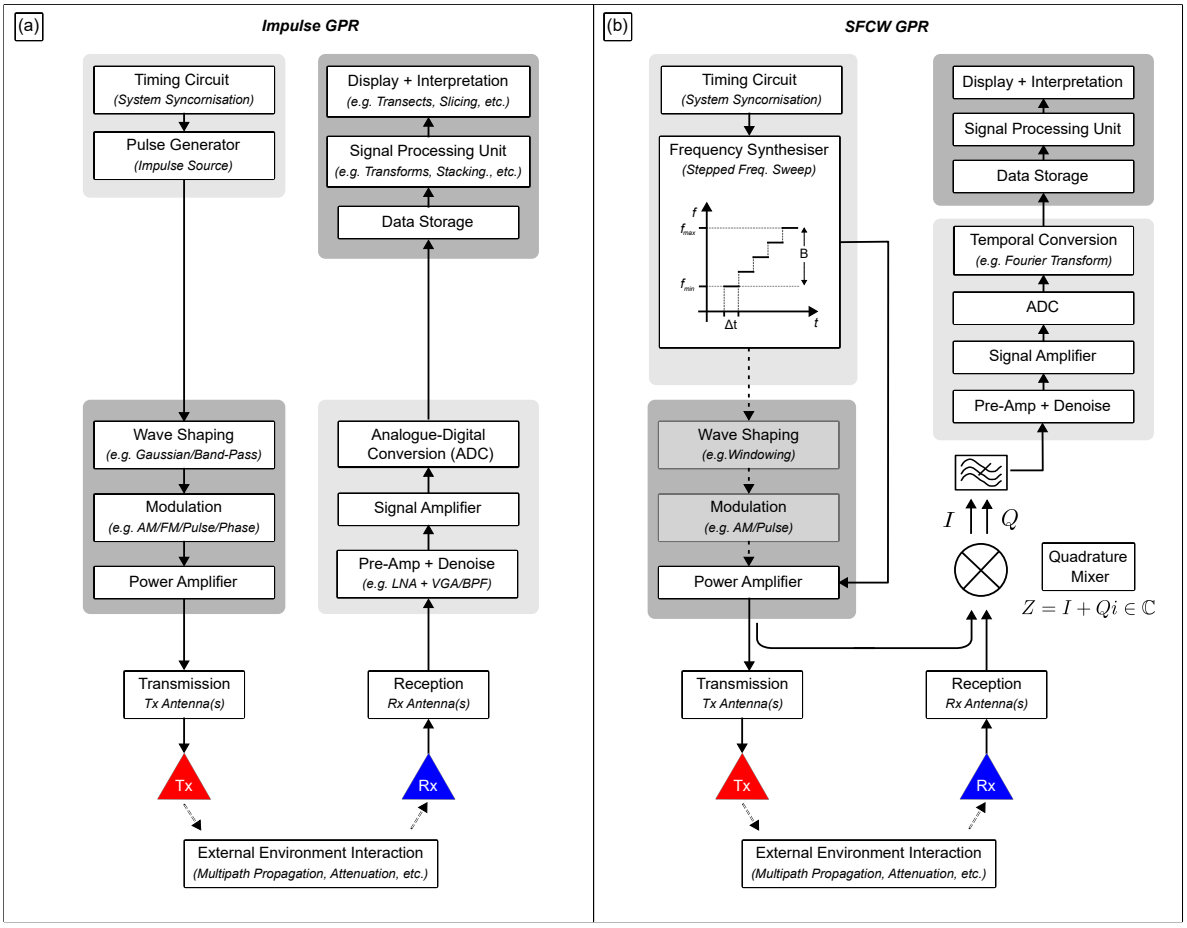


Figure 2.5: Block diagram of basic Impulse (a) and SFCW (b) GPR systems, based on schematics presented in [4] and [5].

In higher-dimensional datasets, the kinematic acquisition process, combined with the inherent conical emission profile of the GPR antenna, can cause subsurface geometry to be detected slightly before and after the antenna passes directly over it. This results in subsurface geometry appearing as hyperbolic artifacts. Consequently, advanced and often highly involved data processing operations are crucial for recovering more accurate spatial profiles of subsurface geometry, such as migration techniques, along with data cleaning and enhancement to maximise the quality of the visual survey output.

This topic is explored in greater detail in Chapter 3. For now, a visual summary outlining the fundamentals of GPR data acquisition and interpretation, alongside annotated photographs of two typical Impulse and SFCW GPR systems, is presented in Figure 2.6.

### *2.3.4 Higher-Dimensional Datasets*

To form higher-dimensional datasets, 1D traces are combined to form 2D transects, which can in turn be combined to form 3D datasets [39], as illustrated in Figure 2.7. When the recovery of 3D datasets is the express intent of GPR surveys, it is common practice to record transects in a regular 2D rectilinear grid of straight-line transects extending across the full lateral span of the RoI as viewed from above, known as an area scan[12]. For further practical details and examples see [40,41].

It is important to remark that this type of grid is considered best practice when subsurface geometry is unknown, because it is a systematic data collection process. Critically, it provides consistent transect separation along each axis and across the entire area, thereby reducing the risk of overlooking important anomalies, which are rarely aligned parallel with a single axis[13]. This separation is frequently chosen to ensure that between 3-5 GPR measurements (traces or transects, subject to context) are recorded across the shortest critical length scale in the survey scenario. This is often associated with the smallest target to be accurately resolved in a given RoI. Practically, the exact separation adopted is a subjective decision, influenced by factors such as available time for data capture, as a smaller separation requires more transects to recorded and, consequently, extends the total duration of the survey. Moreover, this rationale does not guarantee that any target can be resolved with sufficiently close separation measurements for the same GPR equipment setup, as horizontal resolution is also dictated by antenna centre frequency and the associated signal propagation velocity in the RoI background media.

[12]This term can be misleading, whilst the trajectories map out a gird spanning a 2D area on the contact surface, the individual trace measurements extend into the subsurface, returning a 3D dataset for the RoI volume.

[13]This can be the case for utility pipe inspections, in which transects along the lateral axis that is perpendicular to the expected long side of the utility are frequently prioritised.

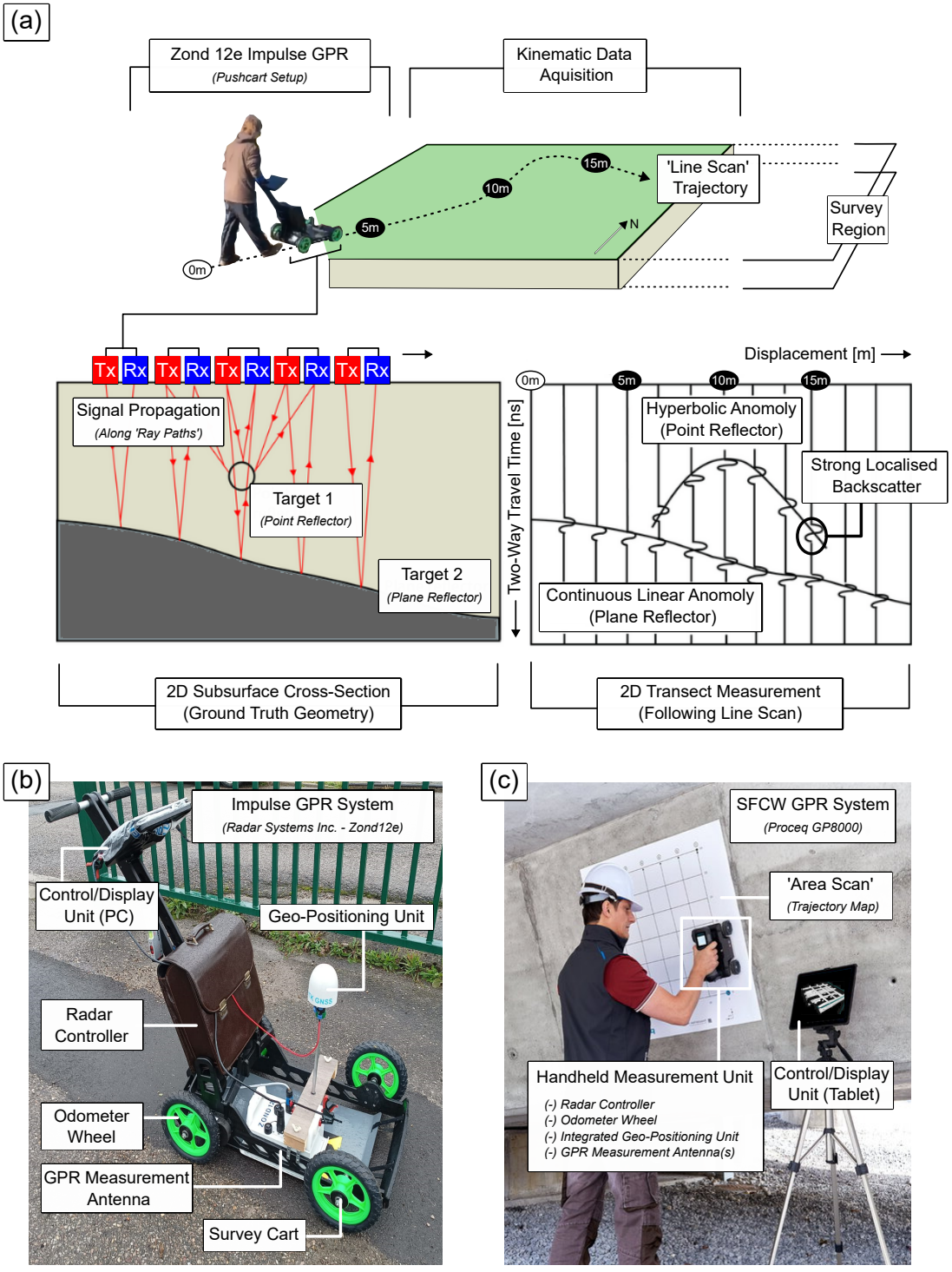


Figure 2.6: GPR system fundamentals. Antenna setups are moved along individual scanning trajectories whilst transmitting an excitation signal into the survey region (a) — adapted from [6]. Measurements of incident signal backscatter in both Impulse (b) and SFCW (c) systems [7] highlight localised regions of strong reflection events, with anomalies typically indicated by hyperbole or continuous linear profiles.

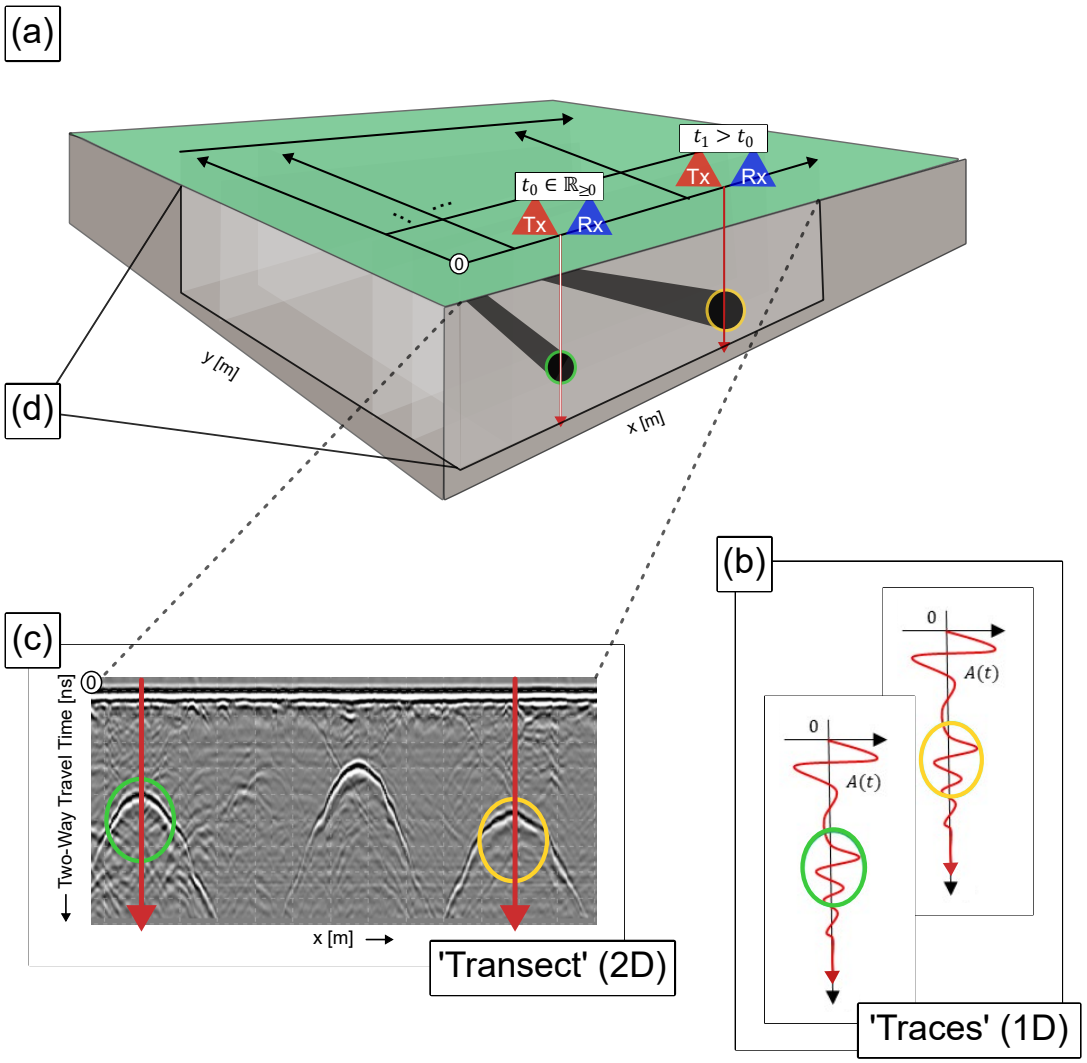


Figure 2.7: A typical GPR survey (a) records effectively instantaneous 1D measurements (traces) of backscatter at each point along a scan trajectory (b), which can be combined along the trajectory path (c) to produce 2D cross sections (transects). The union of multiple cross sections across separate intersecting scans forms 3D datasets (d).

### 2.3.5 *Further Reading*

For additional information on the above topics, the extensive technical summary of GPR fundamentals presented in [4] offers a comprehensive breakdown of key equations, operational theory, and practical survey conventions, as well as multiple case studies. Technical considerations regarding antenna design and consolidated tables of the relative electrical permittivity of various subsurface media are also summarised in [42]. For further technical details on VNA system fundamentals [43,44] provide digestible breakdowns. Lastly, an in-depth exploration of the recovery of temporal response profiles from frequency-domain data is provided in Appendix C.

## 2.4 Motivation – Tunnel and Transport Infrastructure Subsurface Inspection

This section outlines the contextual basis for the research presented in this thesis.

Section 2.4.1 establishes the crucial role of subsurface inspection in assessing structural health and informing targeted maintenance strategies. It further acknowledges the increased vulnerability of aging masonry transport infrastructure to accelerated degradation, emphasising the need to prioritise the maintenance of historic railway tunnels within the transport sector to ensure long-term network resilience. This highlights the lack of a consolidated summary of common assets and defects in the assessment of these structures within the literature reviewed for this research project, especially those most frequently considered in subsurface inspection surveys. To address these knowledge gaps, consolidated summaries are presented in Section 2.4.2 and Section 2.4.3, respectively.

### 2.4.1 *Historic Railway Tunnels and Associated Infrastructure*

Strengthening the resilience of critical infrastructure presents a demanding yet essential challenge for global transport networks. The principal modalities of road, air, waterways, and rail commonly share physical infrastructure. These networks rely on large scale engineering structures such as bridges, embankments, and tunnels to provide links between otherwise inaccessible locations, each providing vital connections for people, goods, and services. Therefore, ensuring their long-term safety and efficacy is of paramount importance, and has motivated global resilience initiatives, such as the European Reference Network for Critical Infrastructure Protection [45].

The pursuit of resilient transport infrastructure has been met by a range of challenges. Examples include the rising frequency of extreme weather events [46,47], alongside modal shift towards more sustainable modes of transport associated with decarbonisation efforts and urbanisation [48]. Additionally, there is also the need to consider associated infrastructure resilience in the virtual setting, as digitalisation continues to drive developments [49,50].

The physical maintenance of large-scale engineering structures is a core component of infrastructure management. One of the key challenges in enhancing infrastructure resilience is the transition from reactive maintenance to more targeted, preventative strategies. To develop effective strategies, it is essential to have a thorough understanding of structural health. This knowledge allows for the early identification and repair of subsurface anomalies before they worsen, which can otherwise threaten structural integrity, complicate repairs, and result in prolonged closures and costly disruptions to the transport network.

Subsurface structural anomalies present a serious risk to transport infrastructure, as they can develop and grow within the structure, often going undetected by surveyors without specialised inspection technology. If left unaddressed, the growth of such anomalies can lead to breaches that may not fully reveal the extent of structural damage. Additionally, they can precipitate more severe problems that endanger services, complicate repair efforts, and, in the most critical cases, jeopardise lives. This risk is especially significant for fully enclosed subterranean infrastructure, like tunnels, where weakened structural integrity can result in partial or complete collapses. Recent incidents, including the partial collapse of the Yangshan Tunnel [51] and a similar failure in the tunnel between Kautenback and Wilwerwiltz [52] (shown in Figure 2.8), illustrate the grave consequences of such structural failures.

Concerningly, the rate of structural degradation increases significantly with the age of the infrastructure. This is a major concern in UK railway tunnels, which represent some of the oldest large-scale transport infrastructure in the world, with many masonry tunnel structures now over 150 years old [53], but still form the backbone of the national transport network. Although older tunnel infrastructure exists in the UK's inland waterway networks, with tunnels dating from the 18th century [54], tunnels on the UK's rail network are used with substantially higher frequency, which is only expected to increase further by 2050, with a forecast 30-50% increase in rail-traffic demand forecast [55]. A further consequence of increased throughput is the associated exacerbation this causes structures, which only further accelerates degradation.

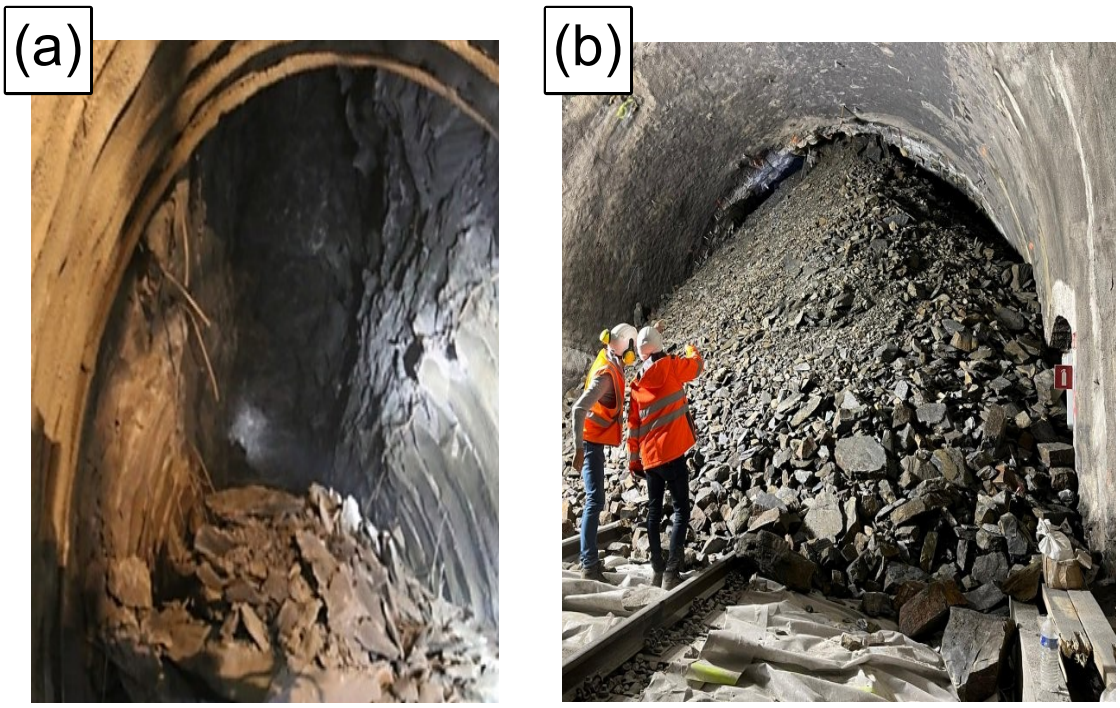


Figure 2.8: Partial section collapse of the Yangshan Tunnel (a) and the tunnel between Kautenback and Wilwerwiltz (b) highlights the severity of failure to detect growing subsurface structural defects.

The subsurface[14] inspection of historic masonry railway tunnels forms the core focus of this thesis. Attention further extends to the subsurface inspection of associated structural elements, including the trackbed, sidewalls, haunches and crown, as illustrated in Figure 2.9. Notably, these key structural components share many similarities with other earthworks, such as abutments, embankments and retaining walls.

In light of this, the research presented in this thesis seeks to improve the resilience of historic tunnels and associated transport infrastructure by advancing the capabilities of current state-of-the-art approaches for subsurface inspection, to better inform targeted maintenance strategies.

### *2.4.2 Common Assets*

This review identified several pertinent works that provided summaries of historic practices and modern assessment methods related to historic masonry railway tunnels in the UK. The two most comprehensive works encountered were a dedicated summary of historic construction methods presented in [56] and a detailed review of multiple rehabilitation schemes explored in [57]. However, the review highlighted the notable absence of a clear, consolidated summary of key structural assets and defects, particularly those most relevant to subsurface surveys. This presented two knowledge gaps that this review sought to address.

In this context, it was decided that the high-level definition of an asset would denote any useful or valuable structural element associated with rail network operation, encompassing employees, track, signalling, buildings, utilities, and civils (structures, earthworks) [58]. An unprotected structurally significant entity of this type is designated a critical asset.

Critical assets pertinent to subsurface surveys include, but are not limited to:

- **Open Ventilation Shafts**(see Figure 2.10a): Hollow columns extending from tunnel crown to the surface above. They facilitate air circulation and were originally used to remove material during construction [59].
- **Maintenance Shafts** (see Figure 2.10b): To enable the simultaneous excavation of multiple tunnel faces, numerous shafts were often sunk along proposed tunnel routes [60]. These shafts were typically infilled or repurposed as ventilation shafts, with aesthetic capping frequently concealing their presence (see Section 2.7.1). However, being unreinforced, many of these shafts have since deformed or partially collapsed.

[14]Here, a tunnel's '**subsurface**' denotes any obstructed and otherwise physically inaccessible region of the structure, primarily located beneath the floor and extending beyond the interior lining, which collectively define its '**surface**'.

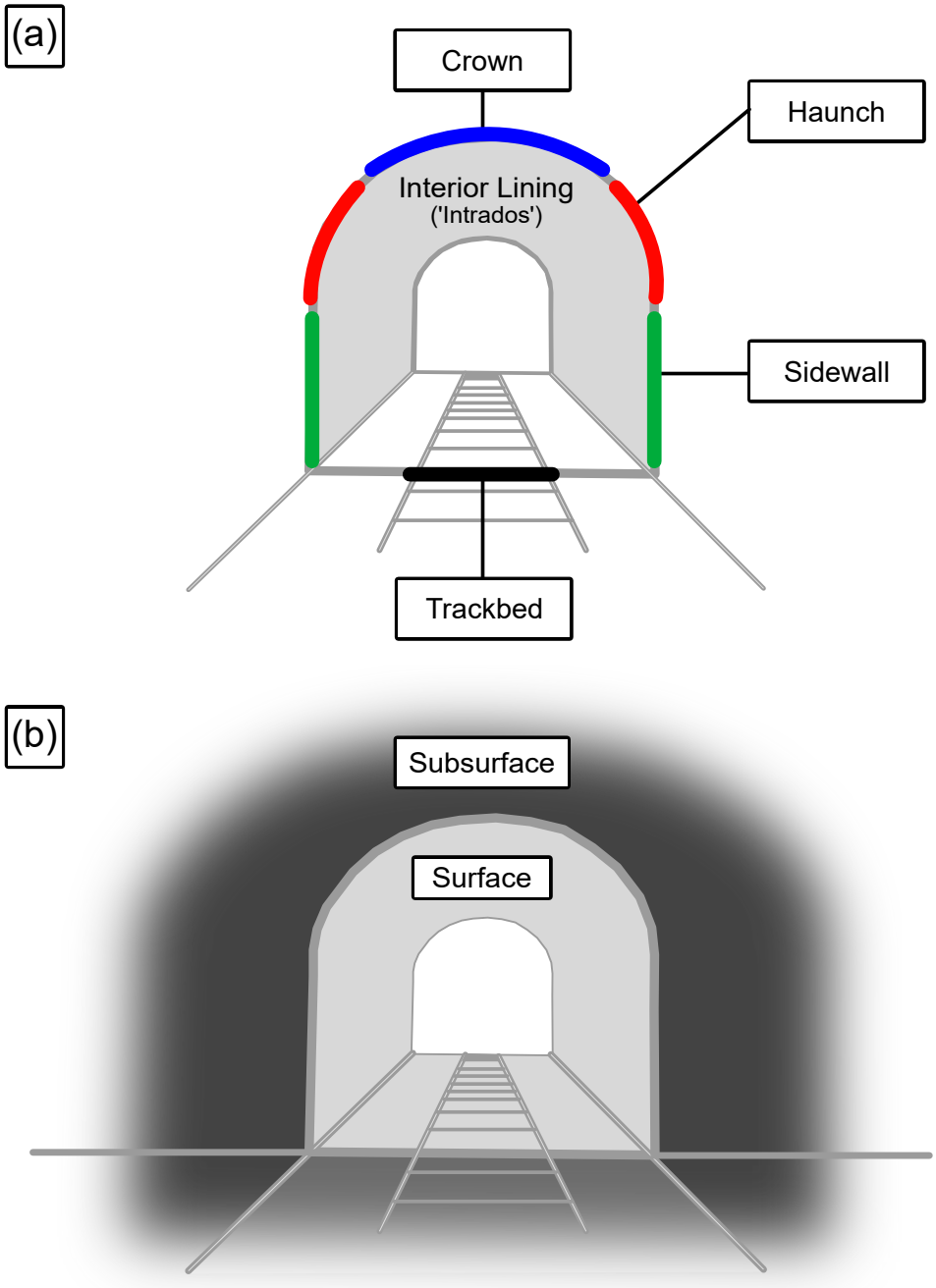


Figure 2.9: Key structural components of railway tunnels: The crown (a) sits at the top, supported by haunches that rest on sidewalls extending down to the trackbed. The subsurface region (b) extends beyond the surface boundary, which itself encompasses the floor and interior lining.

- **Portals** (see Figure 2.10c): Reinforced surfaces around tunnel entrances counteract outward deformation caused by shear stresses from the ongoing movement of the surrounding landmass [61]. As these surfaces are exposed to the elements, their rigidity can deteriorate, increasing the risk of collapse if cracks and displacement are not identified and addressed promptly. Reinforcement measures include the use of buttresses, ground anchors, and steel mesh coverage secured with soil nails [62].

- **Refuges** (see Figure 2.10d): Small recesses within the tunnel lining to protect railway workers from passing locomotives.

- **Overhead Line Equipment** (see Figure 2.10e): Also referred to as 'traction wires' or the 'catenary', these high-voltage electrical pickup lines supply power to electric locomotives through onboard pantograph connectors. During electrification projects, systems can be integrated into older tunnels. These systems include tensioned metallic cables mounted to the tunnel crown and the Rigid Overhead Conductor Rail System (ROCS) [63], which is particularly effective in tunnels with low clearance. However, the installation process can weaken the tunnel structure due to necessary drilling, and the strong EM-fields generated by the power feed can interfere with data acquisition systems and obstruct visibility during inspections of the haunch or crown.

- **Culverts**: Passageways designed to allow accumulated ingress and watercourses, including underground rivers [64], to pass beneath railway tracks. Older masonry culverts, in particular, can become weakened due to solution and hydraulic action, leading to partial collapses that deform the trackbed above and cause water backlog, potentially resulting in tunnel flooding.

- **Other Buried Utilities**: These can include both metallic and plastic drainage pipes [65], electrical wiring and telecom cables.

- **Trackside Objects**: This can include signage, signals, electrical junction boxes and CCTV units.

### *2.4.3 Common Defects*

In the context of subsurface inspection, a defect constitutes any undesirable imperfections within a structure, indicative of degradation and increased failure likelihood under strain, thereby exhibiting potential to undermine structural integrity. Addressing defects in an enclosed tunnel environment is therefore of critical importance, both from a safety and resilience perspective.

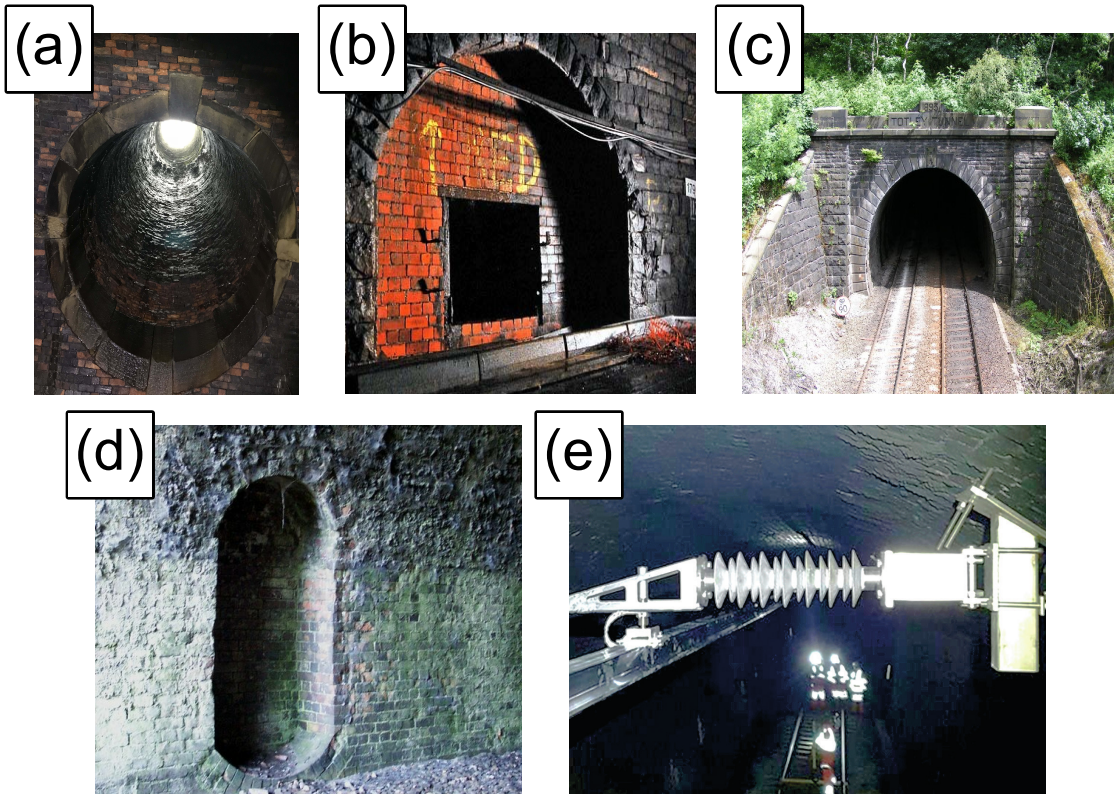


Figure 2.10: Several common assets in historic masonry railway tunnels, relevant to sub-surface surveys, include: (a) open shafts; (b) maintenance shafts, here partially concealed; (c) portals; (d) refuges and (e) overhead line equipment.

Below several key hallmarks associated with common defects in masonry railway tunnels are summarised. These include, but are not limited to:

- **Cross-Sectional Deformations** (see Figure 2.11a): Shifting tunnel landmasses can result in substantial tensile and compressive forces acting on a tunnel, which vary significantly over time. This can lead to sidewall bulging and buckling, distortion of the haunch, bowing of the tunnel floor and lateral displacement of the crown.
- **Cracks and Fracturing** (see Figure 2.11b): Localised shear forces and vibrations from rolling stock can cause masonry to crack and shift. Damage can vary from hairline fractures with minimal displacement to large, open fractures with significant dislocation.
- **Water Ingress** (see Figure 2.11c): Rain can infiltrate tunnels through shafts, while groundwater can propagate through dissolved subsurface joints and fissures [66]. As water percolates between masonry and flows down the sidewalls, it can begin to leach mortar. This lubrication of masonry joints leads to structural movement and deformation of the lining. Due to the length of the joints, significant quantities of ingress can accumulate, potentially scouring supports and flooding tunnels if drainage or saturated catchpits are inadequate. Ingress often carries dissolved ochre, which forms crystallised limonite deposits [67] that can block drainage channels. Outflow down the sidewalls creates noticeable white streaks emanating from the breach, serving as indicators of the ingress source.
- **Open Joints and Perished Mortar** (see Figure 2.11d): This is characterised by the deterioration and eventual loss of mortar between brickwork. Given that brick tunnels can be over 150 years old, the mortar naturally deteriorates due to reactions with moisture in the bricks, air, and subsurface conditions [59, 63, 68]. The process is accelerated by wash from nearby ingress, vibrations from rolling stock, and air-pressure waves from passing locomotives.
- **Loose and Missing Brickwork** (see Figure 2.11e): Early onset of spalling and failed patching repairs can lead to loosened or missing brickwork, often evidenced by rubble on the trackbed. While individual gaps may not significantly compromise structural rigidity, they can allow for the development of larger defects if not addressed promptly. Additionally, if such gaps occur in the tunnel haunch or crown, falling rubble can damage rolling stock or pose serious risks to ground crews working below.
- **Spalling** (see Figure 2.11f): Deteriorating masonry in the tunnel lining near the haunch or crown can often eventually be dislodged by gravity, exposing the underlying layer of brickwork. Over time, this process can create non-uniform recessed quadrants. Bricks in the newly exposed layers, lacking the tarnishing from soot and locomotive exhaust fumes, exhibit a more vibrant colouration as a second distinctive feature.

- **Ring Separation and Debonding** (see Figure 2.11g): Tunnel linings can consist of multiple concentric layers of brickwork rings. Based on encountered sources, historic tunnel linings were found to be typically comprised from 3 to 15 layers of brickwork [68–70]. Ingress, deterioration of mortar, and poor-quality workmanship can cause neighbouring rings to separate within the wall. Gravity can then subsequently dislodge the innermost layers which drop downward, leading to debonding from the layers behind and forming slit voids (subsurface hairline fractures). Over time, these voids can enlarge. This can cause visible cracking of the mortar, viewable from the tunnel interior, thereby making detection possible. However, separations deeper than a single ring are invisible to an in-tunnel observer. As the process progresses, large sections of rings can debond and fall away in small or large slabs. Such events can deform rails or damage the trackbed, presenting a derailment risk. Depending on its size, debonding can significantly weaken surrounding masonry.

- **Trackbed Faults**: Layers of ballast beneath railway tracks help evenly distribute the weight of rail traffic, ensuring that rails remain level on uneven ground and thus prevent derailments. However, displacement caused by ballast fouling [10, 71, 72] and frost heave [73–75] can damage the rails and disrupt weight distribution, increasing the risk of in-tunnel derailments and potentially leading to significant network disruptions.

- **Drainage Faults**: Tunnels can be equipped with integrated pipework and catchment pits to safely manage excess water and silt. Flooding may occur if these pipes become blocked, rupture due to freezing and expansion, or are overwhelmed by severe weather events [76]. Even improvement works can fail; for instance, in Balcombe Tunnel in 2011, a total of eighteen bolts supporting a water catchment tray became decoupled due to resin failure [77]. This caused the tunnel clearance to decrease from 0.87m to just 0.30m, creating a hazardous obstruction for rail traffic.

## 2.5 State-of-the-Art – Subsurface Inspection of Transport Infrastructure

This section presents a detailed breakdown of current state-of-the-art visualisation frameworks pertaining to subsurface inspection of transport infrastructure. In accordance with the previously outlined review strategy and the established context for project research, examination focuses on more recent developments in academic research, alongside both established and cutting-edge industry solutions more directly relevant to current survey practitioners. Furthermore, emphasis is placed on examining leading developments in both data collection and conveyance schema underpinning the relevant technologies identified.

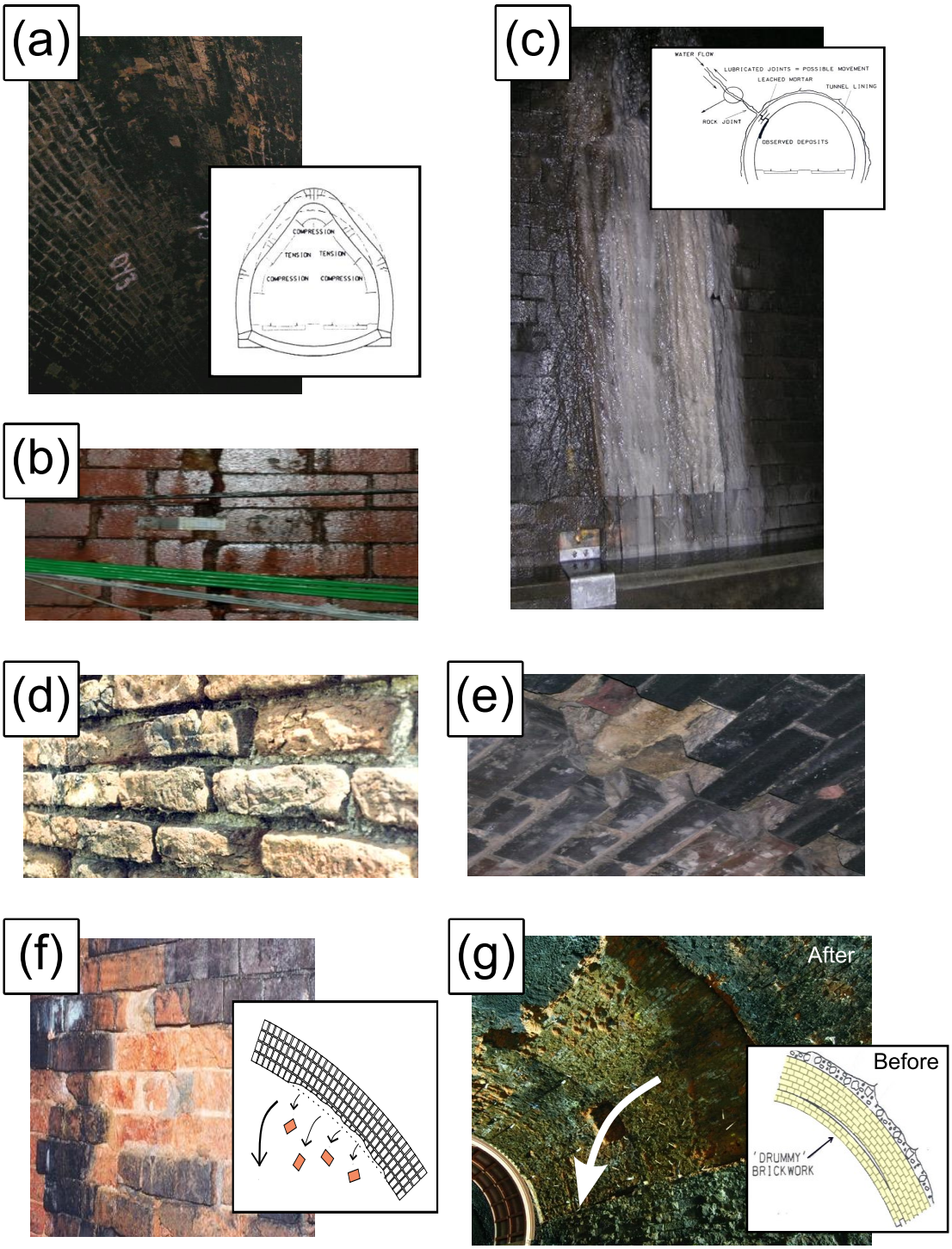


Figure 2.11: Several common defects in historic masonry railway tunnels, relevant to subsurface surveys, include: (a) haunch deformation; (b) cracks; (c) water ingress; (d) perished mortar; (e) missing/loose brickwork; (f) spalling; (g) ring separation and deboned wall sections.

Progression through the approaches identified follows a pattern of increasing abstraction, starting with advancements closely linked to established general survey practices, before moving towards innovations in more specialised, experimental methods. This extends to the consideration of conceptual strategies entering early prototype stages of development, alongside high-level infrastructure management techniques associated with virtual survey environments and digital twins.

Visual inspection techniques are first explored in Section 2.5.1, followed by acoustic methods in Section 2.5.2. Next, advancements in laser, thermal, and gravimetric surveying are sequentially discussed in Section 2.5.3 through to Section 2.5.5. Key developments pertaining to GPR are detailed in Section 2.5.6, marking the transition towards examination of more specialised experimental methods, including unmanned aerial survey vehicles in Section 2.5.7 and adaptive inspection robots in Section 2.5.8. Recent developments in virtualised BIM models of large-scale transport infrastructure are discussed in Section 2.5.9, followed by a brief summary of other relevant methods in Section 2.5.10.

### *2.5.1 Visual Inspection and Photogrammetry*

Visual assessment is the longest-established NDI method for railway tunnel inspections and is still widely adopted today, particularly across the UK and Chinese rail networks [78, 79]. Here methods were subdivided methods into two classes: (i) Traditional and (ii) Modernised.

Traditional evaluation is exclusively based on engineers' learnt association between visual indicators (e.g. workmanship inconsistencies, material fatigue hallmarks) and fault likelihood. Problematically, engineers infrequently share similar extents of practical experience, resulting in high subjectivity. Crosschecks and multi-pass surveys can partially reduce accuracy and consistency variations but take significantly longer to implement at increased resource cost, closure times and risk to workers. Handwritten notetaking ambiguity, incompleteness, and inherent susceptibility to human error also present issues for later analysis. They are commonly subject to misinterpretation, causing unnecessary delays and disruption. However, being affordable and reasonably accurate (if performed by more experienced engineers), coupled with human-aptitude at informed predications from non-structural information (e.g. history of construction practices); traditional methods can time-efficiently localise visibly degraded quadrants requiring repair.

The latest methods principally utilise Close-Range Photogrammetry (CRP) to provide reference-able imagery, but this is restricted to surface-level profiling of cracks, ingress, spall and larger delamination events. Systems commonly employ RGB optical cameras mounted on moving platforms for stability and time-efficiency. These include Pushcarts/Rail-Trollies (RT), Road-Rail Vehicles (RRV) and Robotic Traction Units (RTU). Merging resultant overlapping orthophotos via mosaicing [80] [81] was found to be common practice amongst leading research publications, in which tunnels were 'unwrapped' to facilitate analysis in 2D. It was also observed that the most recent studies took this a step further, employing 3D CRP topography model reconstruction via 'Structure from Motion' (SfM) algorithms [82–85].

A noteworthy recent innovation included 'Digital Imaging for Condition Asset Monitoring System' (DIFCAM) [86]; an RRV-mounted optical array deigned to reduce crew sizes and inspection durations. Although 2014 marked DIFCAM's last major study [87], scope of its successor project DIFCAM Evolution [88] had potential to significantly build upon this work, including the integration of subsurface imaging and automated defect recognition techniques.

Of comparable interest, [89] presented a 'Moving Tunnel Profile Measurement' system (MTPM-1) which deployed a novel rotating camera for CRP, which tracked a translating laser target to achieve swift 3D capture of a 100 m tunnel in 3 minutes. Use of an alternative, more lightweight camera was raised as a key refinement for future iterations of the system, necessary to attain smoother rotation and reduce the prevalence of lens-distortion.

Overall, these approaches exhibited considerable surface-level inspection prospects. However, it was further noted that both traditional and photogrammetry-based methods inherently struggle to directly profile the *subsurface* condition of tunnel and associated transport infrastructure, since these regions are inherently masked by opaque boundaries (e.g. tunnel walls), except where defect growth had already undermined the integrity of the boundary and exposed the subsurface.

Proposed revisions of MTPM-1 system were considered to exhibit the greatest potential for indirect analysis of subsurface condition, capable of highlighting subtle distortion of tunnel sidewalls indicative of cavity formation and changes to force distributions associated with shifting subsurface landmass. It was also noted that the system could also further benefit from integration with a suitable RTU, to provide automatous locomotion as described in [90]. This could enable the first practical 24/7 remote deployment of such an inspection system, which would be especially beneficial for tunnels in remote or hard-to-access mountainous regions, commonly subject to more intense environmental conditions and thereby increased risk of accelerated degradation.

Lastly, the fusion of surface-level inspection photogrammetry methods with a counterpart inspection method better-optimised for direct inspection of the tunnel *subsurface* presents a further notable innovation opportunity, which could return significancy more comprehensive structural survey datasets to better. A key challenge to overcome would be the georeferencing and offset of combined technology measurement data in tunnel environments, which are inherently prone to drop-out of satellite-positioning methods. However, complementary integration of 'dead-reckoning' approaches utilising on vehicle odometers or SLAM[15] methods coupled with an Inertial Measurement Unit (IMU), present two practical solutions to address this.

### *2.5.2 Acoustic Inspection*

Subsurface structural anomalies inherently modify the characteristics of propagating soundwaves. Acoustic methods pulse predefined waveforms into subsurface and analyse resultant distortion and delay to identify audible indicators associated with anomaly presence. Acoustic methods were subdivided into Ultrasonic Testing (UST) and Infrasonic Testing (IST). In UST, reductions in travelling pulse velocity correspond to elastic deformation of defected regions [92,93]. By contrast, in IST defects are indicated by high resonant frequency components in returning pulses [94].

This review identified two research groups directly applying UST for tunnel subsurface inspection. In [95], UST was found to be highly time-inefficient, taking between 9 and 25 minutes to profile just one metre of the tunnel sidewall. Additionally, a preliminary GPR scan was required to locate suspected features and guide which areas of the sidewall should be prioritised for inspection. Similarly, despite robotic automation, UST scans performed by the tunnel profiler ROBOSPECT achieved comparably inefficient durations (of the order of hours) to scan just 6m of sidewall [96]. Furthermore, both systems were primarily optimised for detecting surface-level cracks and spalling [97,98], limiting their effectiveness in identifying deeper subsurface structural anomalies beyond the initial layer of the subsurface, associated with the contact surface. Based on these observations, UST systems were deemed to have limited practical benefit for comprehensive profiling of the full subsurface in large-scale transport infrastructure, particularly tunnels, where time-efficient surveys are essential to minimise closure durations and reduce disruption to the network.

IST presented a more practical alternative. Traditionally, hammer-strike tests were conducted by skilled human operators who relied solely on detecting audible defect indicators 'by ear'.

[15]SLAM (Simultaneous Localisation and Mapping) estimates camera position in real-time by tracking surface features and integrating external sensors like IMUs and LiDAR (see Section 2.5.3). Unlike SfM methods, which reconstruct scenes in-post from global feature correspondences, SLAM continuously updates a local map with loop closure for drift correction, enabling real-time operation [91].

However, these experienced individuals are now few in number, nearing retirement, and are not being replaced. Faster robotic schemes detailed in the encountered literature were found to be more preferential in modern surveying, boasting improved access to less accessible elevated structural aspects, achieved by mounting hammers to robotic arms [99–102], on Variable Guide Frames [103] and Unmanned Aerial Vehicles (UAVs) [104, 105]. Notably, this review identified a unique non-contact infrasonic UAV system [106], capable of inducing hammer-strike-like flexural vibrations in concrete infrastructure from distances of up to 5m. Its potential application as a basis for the design and implementation of remote subsurface inspections of transport infrastructure, conducted by offsite crews, presented a particularly intriguing research opportunity.

Detrimentally, a significant drawback of these systems was their reliance on human interpretation of audio spectra, which do not physically resemble the subsurface features they represent. This recurring limitation inherently restricted the insights that non-specialist users, such as infrastructure managers, could derive from IST without substantial investment in costly training and tedious cross-checking with additional contextual metadata (e.g. maps of striking locations).

### *2.5.3 Terrestrial Laser Scanning*

Terrestrial Laser Scanning (TLS), based on LiDAR (Light Detection and Ranging) technology, uses directed lasers to scan and capture the visible aspects of transport infrastructure. This process can generate dense 3D point clouds (see Figure 2.12a) at rates of up to one million data points per second [18, 107–109]. A typical TLS system emits visible light impulses that reflect off contact surfaces. The variations in the intensity of these reflected impulses are used to determine the relative distance between the scanning unit and the surfaces being measured. However, datapoints lack classification labels and do not penetrate the subsurface. This makes segmentation of tunnel features challenging [110], but does permit indirect insight into subsurface condition. For example, distortions to tunnel sidewalls can indicate abnormal strains associated with shifting landmass [111].

The integration of TLS technology with complementary penetrating NDI methods represents a promising area of ongoing research. This review highlights that developing a standardised, efficient, and reliable method for aligning multiple point cloud datasets — thereby creating a unified digital environment — presents a critical milestone. Achieving this milestone would be essential before such integrated approaches can become mainstream in the practical deployment of subsurface inspection for transport infrastructure.

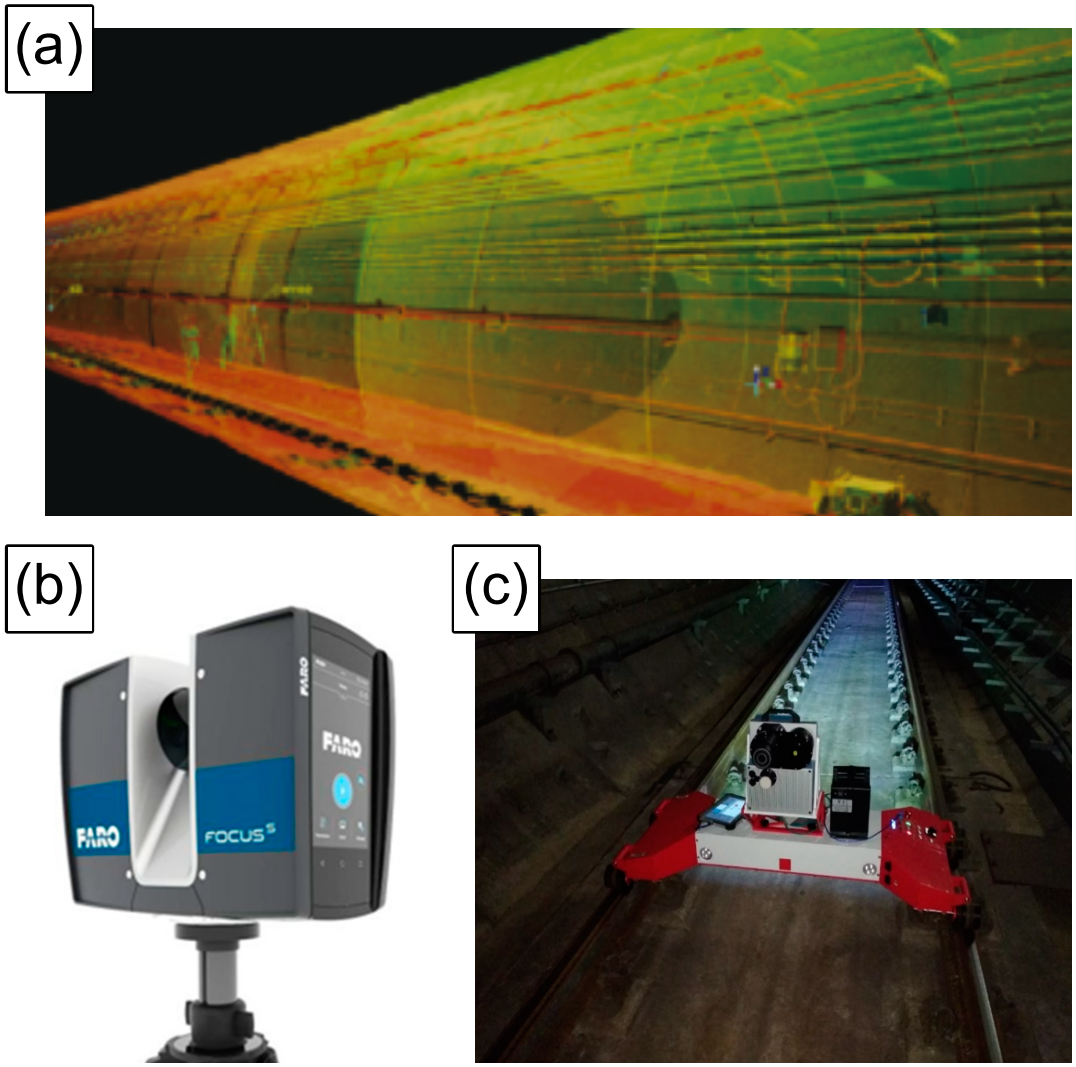


Figure 2.12: TLS for tunnel surface inspection: (a) a 3D point cloud returned from a TLS metro tunnel survey [8]; (b) a FARO FOCUS 350 scanning module, a versatile standalone TLS system commonly deployed in infrastructure surveys across the transport sector, including in tunnels; (c) the TMMS rail-trolley, an advanced automated tunnel inspection prototype based on a Z+F9012 TLS module, here capturing a 3D point cloud of a metro tunnel in the Zhengzhou metro network.

Returning to standalone laser methods for, TLS studies and commercial contractors most frequently use FARO FOCUS scanning modules [112–115] (see Figure 2.12b) or the Z+F Profiler 9012 [8,116,117] to integrate TLS with RGB optical photography in application to railway tunnel inspection. This integration importantly enhanced levels of intuitive navigation around the survey environment for end-users examining the resulting point clouds. Noteworthy innovations among this work included an automated deformation detection assembly [26], which utilised a novel Circular Laser Scanning System (CLSS), which highlighted the practicality of adopting circular sensing arrays that complemented the natural curvature of fully and partially enclosed transport infrastructure, such as tunnels, underpasses, culverts and some retaining walls.

Notable innovation was also showcased in the Tunnel Monitoring and Measurement System (TMMS) developed by [8]. The prototype visualisation framework utilised a Z+F Profiler 9012 mounted on a bespoke rail trolley as shown in Figure 2.12c, to pass RGB LiDAR tunnel point clouds and a 'roaming video' feed of contact surface condition to an engineer's tablet PC. The developed hardware bore strong similarities with a similar mobile TLS apparatus used in [115], which was based on a FARO X330 scanner. Validation trials in China's Zhengzhou Metro network demonstrated practical deployment capability but also relayed that the framework's primary functions of ingress and cross-sectional deformation detection suffered significant accuracy and stability reduction when applied to non-circular tunnel profiles (e.g. horseshoe, elliptical, etc.). Thus, for the purposes of this review, the TMMS system made clear the importance of an adaptable visualisation framework for transport infrastructure inspection. Such adaptability could be considered crucial for managing the diverse types and variations of survey environments encountered during practical surveys, especially in the context of older infrastructure such as UK railway tunnels, which exhibit multiple 'standard' cross-section variants.

### *2.5.4 Thermography*

Subsurface structural anomalies can also modify thermal emission patterns of infrastructure contact surfaces if in sufficiently close proximity, causing abnormal variations. Visualising temperature distribution profiles (Thermometry) facilitates localisation of suspected near-surface anomalies (Thermography) [118, 119], but recovery of specific attributes commonly defers to higher quality UST or localised GPR imaging.

Active Thermography (ACT) heats surfaces using halogen lamps [120], air guns [121] or inductive-heating elements [122] to induce exaggerated thermal responses. Testing in [123] and remarks from [124] affirm that heating element operation for full coverage surveys of large-scale transport infrastructure, such as tunnels, would incur impractical cost and could debond masonry in older structures. This explains why such methods were rarely encountered during this review.

The use of infrared camera arrays for passive Infrared Thermography (IRT) was found to be more common practice, owing to its more time-efficient and less costly implementation. Systems encountered were capable of identify both air and water filled voids, with individual scans displayable as 2D panoramic imagery [118] or more cutting-edge 3D mesh overlays on digital structural models rendered using the TOSCA-FI platform [9] (see Figure 2.13) or Augmented Reality (AR) as in [125].

Despite recent work, it was noted that IRT systems still suffered from persistent limitations [119] which had potential to undermine the technology' direct application to practical subsurface inspection of large-scale transport infrastructure.

Such limitations included, but were not limited to:

- High sensitivity to ambient temperature conditions, such as those associated with daily and seasonal variation. This could significantly diminish subsurface structural anomaly contrast against the background media, limiting clarity in returned visuals.
- In tunnels, thermal insulation and heat-resistant coatings use for temperate regulation and fire resilience can also skew temperature profiles, with high thermal dissipation capable of restricting subsurface penetration to less than 30mm [126].
- Masking and exaggeration of thermal profiles could result from variations in subsurface moisture content, associated with increased permeation following rainfall or snow.
- Enclosed, curved contact surface geometries can severely restrict available viewing angles, reducing visual output to 2D, even when overlaid on 3D meshes, as seen in [9]. This limitation makes it particularly challenging to infer the depth and spatial profiles of anomalies, even for more experienced practitioners.

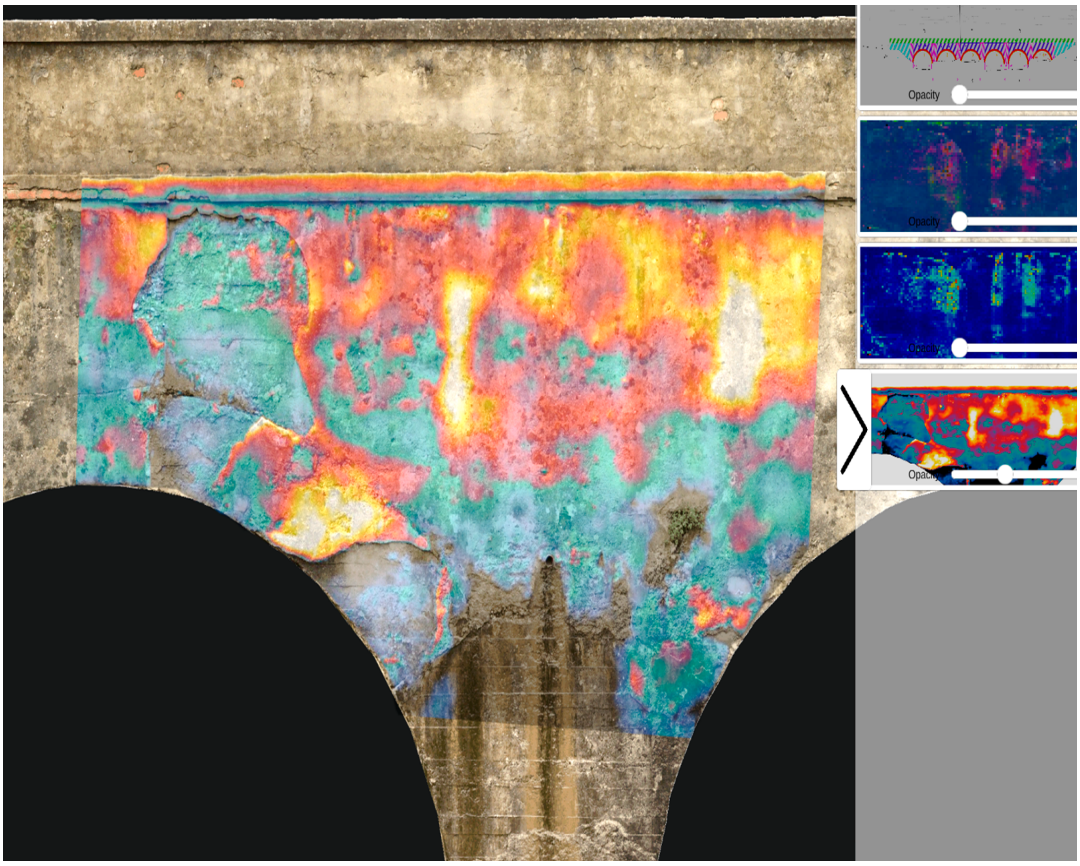


Figure 2.13: The TOSCA-FI Software Platform is a promising new development for thermographic surveying, here intuitively conveying subsurface structure health using 2D heatmap overlays on a 3D digital bridge model [9].

### 2.5.5 Gravimetric Surveying

Gravity Surveys (GS) use portable gravimeters [127], placed at regularly spaced sampling locations, to measure subtle variations in gravity surrounding large-scale transport infrastructure, including tunnels [128]. Anomalies appear as profile distortions in the returned Complete Bouguer Anomaly (CBA) curves, which relay subsurface material composition [129] and can indirectly provide insights into structural health. Regional trends in subsurface density, as shown by CBA curves, can vary across scales comparable to the characteristic footprint of the infrastructure, providing extensive inspection coverage. Similarly, localised negative field displacements can signal the presence of irregular low-density regions, which are strong indicators of voids and deformation zones [130–132].

However, few common defects exhibit significantly large density variations (compared to their surrounding landmass) that would markedly affect a CBA curve. While CBA curves provide insight into the general nature of the subsurface, they do not offer a comprehensive or clear visualisation of subsurface features themselves. Additionally, localising large features within a fully enclosed structure is further complicated by the inherent symmetries of their often-cylindrical profiles. This complexity makes modelling the corresponding gravity field a multi-solution problem, introducing significant uncertainty and greatly increasing computational efforts [133].

### 2.5.6 Ground Penetrating Radar

As detailed in Section 2.3, GPR signals directed into the subsurface, penetrate and partially backscatter off the interfaces between different material media, including those associated with structural anomalies [25]. Systems encountered in the literature were most commonly consecutively emitted wideband waveforms to directly measure backscatter in the time domain or performed linear swept measurements to directly record responses in the frequency domain [134–138].

For the purposes of this review, GPR systems associated with the subsurface inspection of transport infrastructure were grouped under three categories:

- **Pushcart/Trolley-Mounted** [10, 71, 72] (see Figure 2.14a): Systems commonly featured interchangeable air-launched antenna of differing frequencies to optimise achieved levels of penetrative depth of measurement with the resolution of visual output [95]. The configurations encountered were typically non-motorised, with scans following unidirectional paths (usually focused solely on the trackbed) and provided no protection for operatives from environmental conditions during data collection.

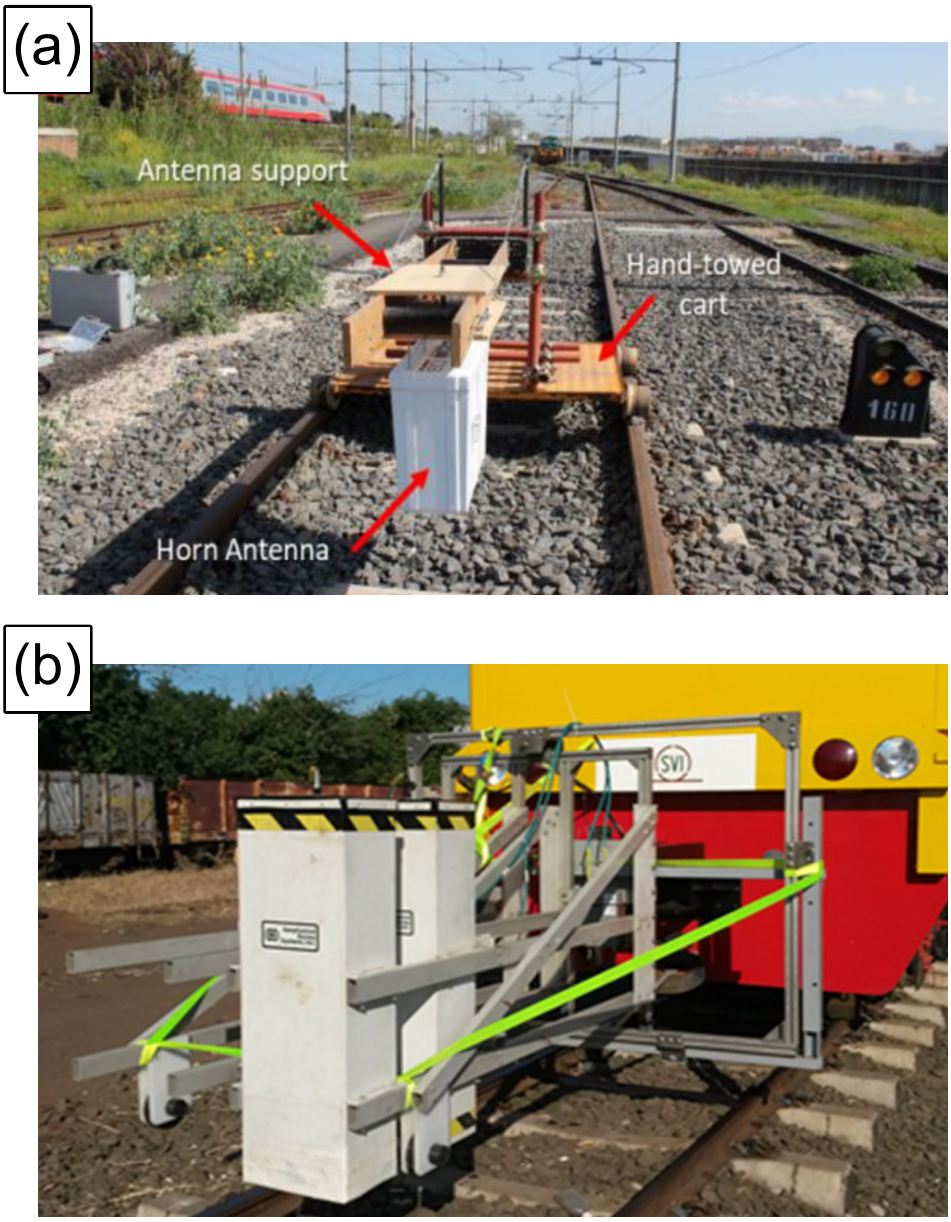


Figure 2.14: A selection of GPR systems for inspection of the track subsurface, principally for detecting ballast fouling. Systems shown include a manually advanced railway inspection pushcart (a) with an interchangeable GPR antenna module to more readily facilitate frequency adjustment for varying the penetrative depth of surveys [10], alongside a similar train-mounted fixed-directional air-coupled GPR configuration (b).

- **Handheld** [7, 139–141]: Compact manually guided ground-coupled scanners are capable of achieving real-time scanning, typical of vertical walls. However such systems could also be reasonably deployed on horizontal level surfaces or even the curved contact surfaces of a tunnel's sidewalls and crown. Systems frequently encountered limited penetrative depth, rarely exceeding 0.5m, and exhibited slow coverage speeds, often less than $1m^2$ per hour. Additionally, these systems required extension boom arms and access gantries to profile structural features at higher elevations, which significantly limited their practicality for conducting comprehensive subsurface surveys of tunnels.
- **Vehicle-Mounted** [19, 142–145] (see Figure 2.14b): Multidirectional fixed antenna units attached to vehicles such as locomotives, rolling stock or RRVs for the inspection of railway infrastructure. Although capable of data collection at speeds ranging upwards of 50kmph, the typically fixed-direction of the antenna frequency restricted the maximal field-of-view of these system, particularly in fully enclosed subterranean structures such as tunnels where the subsurface fully surrounds the data collection system.

The majority of GPR systems and research encountered in this review relied on traditional 2D transects to convey visual output from surveys, which, while capable of encoding multiple feature characteristics (e.g. depth, extent, orientation, heterogeneity, etc.) [134–137], required extensive and complex digital filtering to return useful insight into the condition of the subsurface [146–150]. Although suitable filtering was observed to significantly reduce false artifacts such as ringdown from railway tracks or manhole covers and airwaves from overhead structures like catenary lines or bridges, the selection of suitable filtering was a highly subjective process, and certain hallmarks frequently persisted [151–153].

Consequently, the interpretation of GPR transects has gained a reputation for being notoriously challenging and unintuitive, motivating its outsourcing to private consultancy firms and other third parties.

A key approach adopted by both GPR researchers and practitioners to enhance the clarity of returned visuals is spatially aligning 2D transect profiles in 3D space, thereby simulating a 3D image of the subsurface.

The two most common methods of spatial alignment encountered were orthogonal intersection [39, 154] (see Figure 2.15a) and parallel stacking [11, 155] (see Figure 2.15b).

The latter method was noted as the most frequently used in commercially available GPR processing software packages [12–14, 156, 157]. Such datasets can advantageously leverage time/depth slicing [158–160] (see Figure 2.16), in situ transparency filtering [161], and false colouration [162] techniques to enhance the clarity of subsurface structural anomalies within the data.

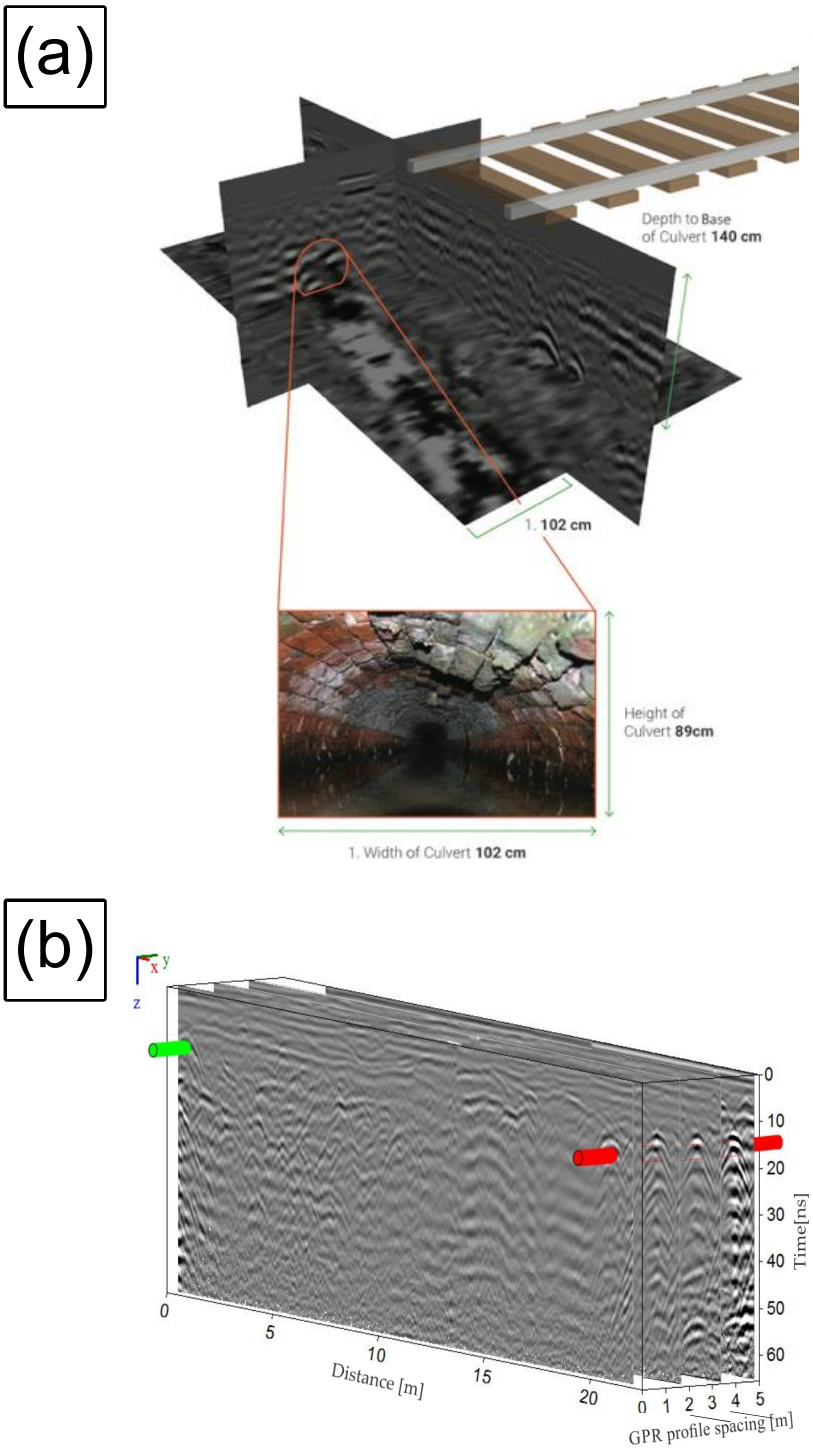


Figure 2.15: Principal methodology for combining 2D transects into visuals resembling 3D scenes. Orthogonal Intersection (a) sees transects meet at right angles, which focuses attention on the central region. Alternatively, Parallel Stacking (b) aligns transects as sequential slices of a cuboidal volume, which aids identification of reoccurring and elongated geometry, such as subsurface utilities [11].

The 3D visualisation and volumetric reconstruction of subsurface geometry represents the forefront of development and innovation in GPR data processing [155, 163–171] (see Figure 2.16c). The literature reviewed highlighted significant potential for further developments in this field, for which it was noted current trends are gravitating towards the creation of practically feasible, fully immersive GPR-based subsurface inspection surveys, that could be conducted in fully digitised virtual environments [7, 172–176].

It is, however, important to recognise that for such future developments to be practically deployed as commercial visualisation frameworks, especially in the context of tunnel subsurface inspection, several challenges must be addressed. Namely, the restricted field-of-view and associated limited subsurface coverage of systems based on fixed-directional antennas. A potential solution identified in this review was the use of a circular antenna configuration or rotational scanning motion that complements the curvature of enclosed infrastructure, in particular fully enclosed tunnel structures. A feasible rationale, given resultant datasets would draw parallels with the superposition of concentric cylindrical transects developed by the TULIPS system [20], a 'look-ahead' GPR system retrofitted onto a tunnel boring machine for subsurface monitoring during tunnel excavation.

As a result, expanding the coverage of GPR surveys was highlighted as a crucial focus for future research and development efforts, aimed at enabling more comprehensive subsurface surveys of transport infrastructure, particularly within fully enclosed tunnel structures.

### *2.5.7 Unmanned Aerial Vehicles (UAVs)*

UAVs have become increasingly popular for tunnel inspection owing to their low-cost designs, programmability, and exceptional manoeuvrability, which has motivated in excess of $4 billion global investment in UAV technology development for infrastructure inspection [177]. However, the practical performance of current UAVs remains limited by poor onboard charge retention [178], stabilisation challenges from near-wall turbulence and common dependency on GPS. Also, when deployed in subterranean infrastructure such as tunnels, Global Positioning Systems (GPS) typically struggle to operate reliably [179, 180].

An emerging trend in the research encountered was the application of collision-avoidance protocols [181, 182] and smart pathfinding [183–186] to develop autonomous UAVs [187–190] for inspecting large-scale infrastructure, particularly in the transport sector. However, it was also evident that backup pilots remain an essential addition to assume control in the event of system malfunctions, which adds additional survey costs and increases the hazard posed to operators, requiring them to physically enter potentially hazardous infrastructure [190].

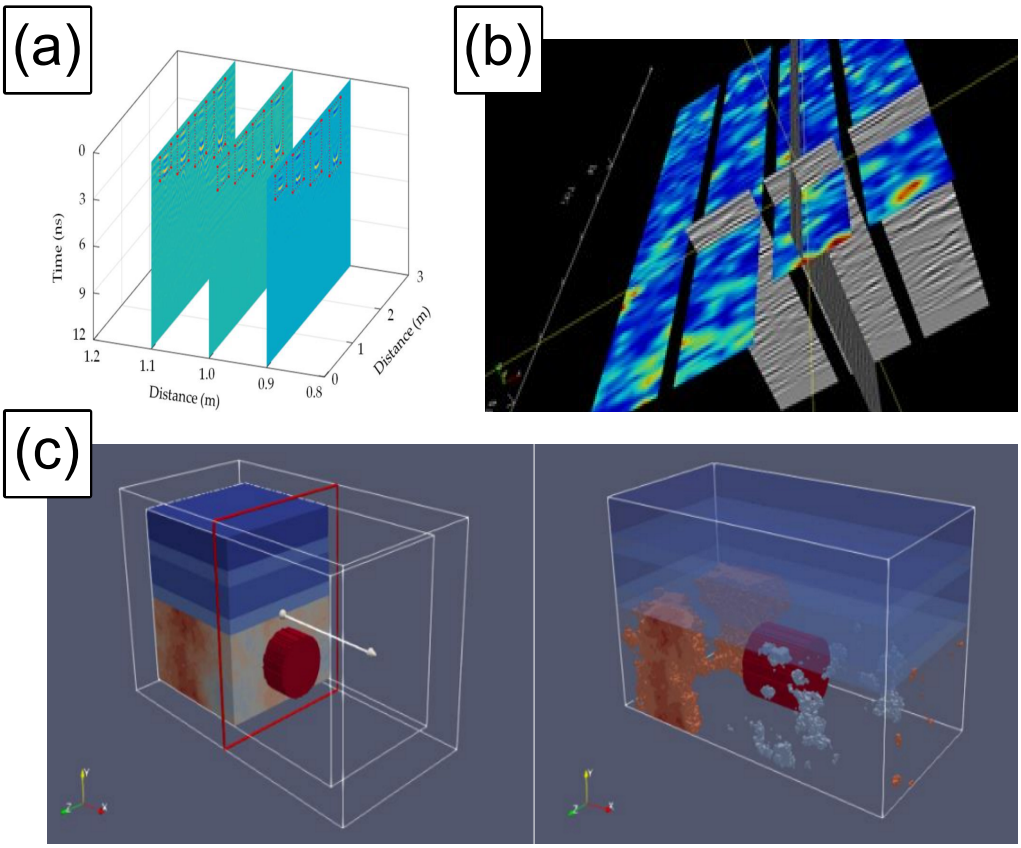


Figure 2.16: Mechanisms for improved contextualisation of GPR survey output in 3D. Time-slicing performed (a) horizontally [12] or (b) vertically [13] can improve perception of 3D spatial profiles, in particular the relative depth of independent profiles. Volumetric reconstruction (c) can further increase the fidelity of subsurface geometry, providing more intuitive survey feedback, subject to more highly involved data processing [14].

It was further noted that no commercially available autonomous UAV encountered in this review had been developed specifically for the subsurface inspection of railway tunnels, despite similar systems existing for visual inspection of the interiors of hydroelectric penstocks in [191].

A key advantage of UAV systems is their ability to swiftly deliver NDI sensors to structural aspects that are otherwise inaccessible, which systems based on articulated boom arms cannot reach. For instance, the UAV-SWIRL system is capable of stable hovering inside vertical ventilation shafts [178, 192]. This and similar systems encountered were based on optical photometry and TLS [193–195], which permitted only implicit subsurface measurements.

Some further noteworthy innovation concerning UAV development included the development of UAV-mounted GPR prototypes [196–198], of which this review identified a commercial system capable of 10m penetration as demonstrated in [199], although it was unclear if this claimed penetration incorporated the altitude of the UAV itself. In addition, the development of new hybrid locomotion UAV also presented a significant emerging trend in encountered research, which extended to:

- **Fixed Anchor-Point Docking** [200–203]: These systems sustained surface contact for IST and UST sensors but required highly involved pre-installation of anchors in the contact surface of the infrastructure undergoing inspection.
- **Pivoting RTUs** [151] (see Figure 2.17a): Integrated caterpillar tracks facilitated uninterrupted adhesion to the contact surface and continuous (albeit unidirectional) surface coverage for scan trajectories. However, the increased weight and associated power drain of these systems reduced uptime, with could limit survey completeness in more time-sensitive inspections.
- **Negative Pressure Wall-Climbers** [204, 205]: As the name suggests, these systems utilise negative pressure to remain in contact with flat vertical surfaces. They are faster than track-based RTUs but require much larger, very flat contact surfaces, which presents a challenge for application to curved contact surfaces in enclosed infrastructure such as tunnels, risking the UAV slipping and losing control.
- **Fully Actuated Configurations** [206, 207]:This review identified these systems as the most promising all-round solution for subsurface inspection surveys of transport infrastructure, offering unrestricted multidirectional movement, even on non-flat contact surfaces. The primary challenge for future development is the current systems' tendency to destabilise when contacting or launching from the inspection surface, due to near-surface turbulence.

### *2.5.8 Adaptive Robots*

This review defines an adaptive inspection robot capable of informing a subsurface survey of large-scale transport infrastructure (principally tunnels) to be devices capable of automatic geometry, operation or locomotion mechanism modification that combats demanding environmental conditions. It should be noted that the systems encountered in this review were primarily early-stage proof-of-concept prototypes, designed to demonstrate the feasibility of a conceptual inspection strategy. In several, though not all, cases, further iterative refinement was deemed necessary before these systems could be practically deployed for the subsurface inspection of in-service transport infrastructure.

Nonetheless, this review considered each system detailed below to hold significant potential future benefits for survey practitioners. Foremost, adaption permits infiltration of inaccessible survey areas (e.g. drainage pipe interiors, capped shafts), increasing survey coverage. Moreover, units can swiftly traverse complex terrain (e.g. steps, tracks, damaged surfaces, angled walls) without human interaction, inviting remote inspection innovation potential.

Reconfigurable UAVs discussed in [16] and [208] demonstrated the novel capability to fold (see Figure 2.17b) and be passed through boreholes, before unfolding (see Figure 2.17c) to survey otherwise inaccessible but expansive void-like environments, such as cave systems. The potential was noted for such a system to be used in preliminary surveys of hidden shafts in older masonry railway tunnels. This could, in principle, be achieved by creating small-diameter drill holes in suspected capping facades, provided their approximate locations had been identified using one of the aforementioned NDI survey technologies. However, with more moving parts, more robust system design would be required to mitigate the risk of damage during transit through boreholes or operation in the inaccessible spaces, which could result in systems becoming trapped behind walls and incurring additional repair, replacement, or recovery costs. The self-disassembly functionality explored in [209] offered a potentially more straightforward approach to such recovery efforts.

Burrowing inspection devices [210] were also encountered during the review process, capable of creating subsurface channels. A promising innovation opportunity was identified for developing a multi-stage system that could subsequently deploy snake robots [211, 212] equipped with endoscopes or fibre-optic sensing elements. Such a system would enable direct imaging of subsurface conditions, as well as the detection of ground movement as in [213], or moisture content as in [214].

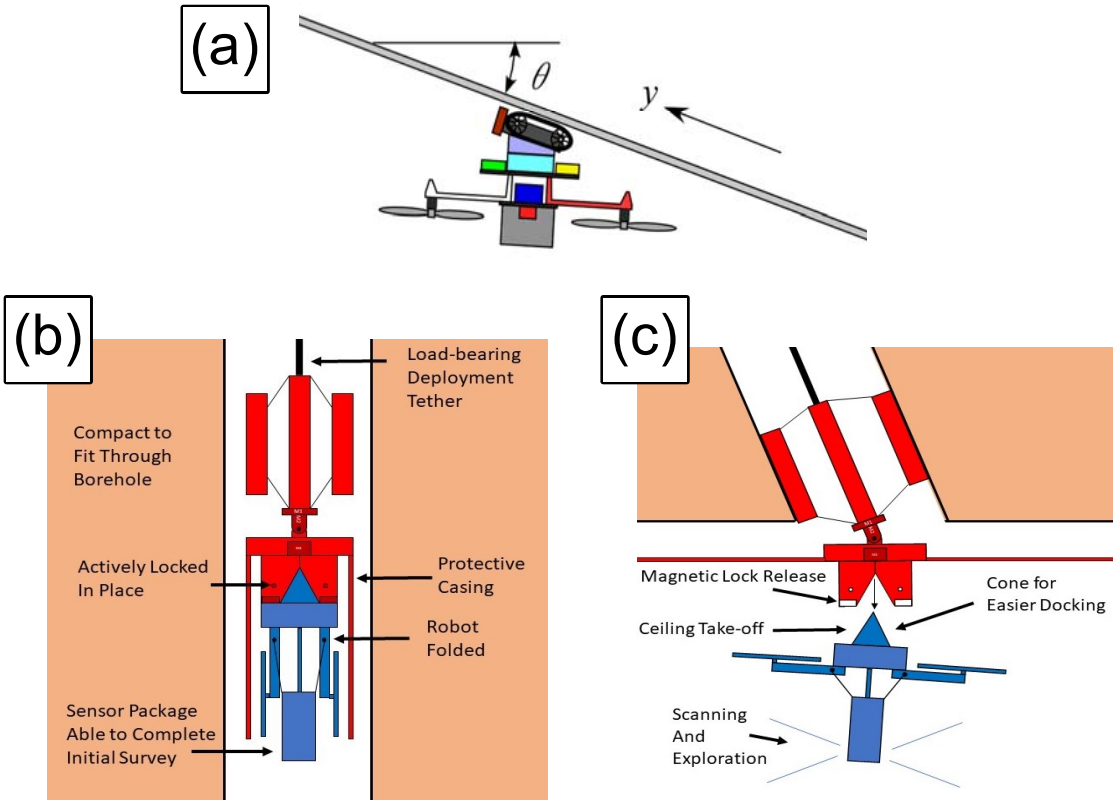


Figure 2.17: Recent noteworthy innovations include a (a) hybrid-locomotion, pivoting traction crawler UAVs [15] and the adaptive UAV PROMETHEUS (b,c) [16].

However, it was noted that burrowing is inherently a destructive procedure and could exacerbate damage to already defective regions of the subsurface. The alternative use of modular configurations [215, 216], compact step-climbers [165, 217, 218], or deformable soft robots [219–221] equipped with NDI sensors was identified as a secondary development avenue. These adaptive robots exhibited potential to navigate small, pre-existing subsurface channels (e.g. pipes, vents, data cables), thereby alleviating dependency on destructive burrowing in situations where existing access would be available within the surveyed infrastructure. In addition, the use of soft robots also offered the unique capability to contort, allowing them to bypass obstructions and provide multidirectional inspection. However, extensive development remains necessary to form a coherent self-arrangement of modular robots [222–226] capable of implementing established NDI practices.

### *2.5.9 Building Information Management (BIM) Integration*

BIM represents a new paradigm for large-scale infrastructure lifecycle information management [227, 228]. The majority of current survey outputs facilitated one-way information exchanges between the physical survey environment and reconstructed digital models of specific infrastructure. By contrast, BIM models underpinning the next generation of more 'idealised' Digital Twin Tunnels (DTT) would be capable of automatically facilitating two-way information exchange from any point in time during its perpetual update cycle. In such two-way exchange, state changes in physical tunnel would prompt reactive changes in the digital tunnel informing future maintenance, leading to further state changes in the physical tunnel et cetera [229].

This review encountered multiple recent experimental BIM studies linked to rail tunnel inspection [17, 230–233], which typically deployed laser methods to profile and categorise trackside assets (see Figure 2.18). However, only [234] directly addressed the subsurface inspection of rail tunnel infrastructure, developing a prototype BIM assisted by Artificial Intelligence (AI) for ingress detection (base on the Amber Inspection Cloud online service management platform). It was noted that although developed BIM systems encountered provided a clear breakdown of structural health condition based on a specific survey, none were observed to exhibit sufficient levels of automation (i.e. two-way information exchange) to be considered a practically deployable next-generation DTT. By inference, progress towards practical two-way information exchange would benefit from increases to currently achievable levels of visualisation fidelity and reductions to associated computational overheads. Two viable strategies for achieving this would include increasing the size of available survey data repositories and further optimisation of network architectures [235].

However, challenges remain. Existing BIM architectures were noted to frequently lack specialisation to account for unique challenges associated specifically with the inspection of tunnels and other full or partially enclosed infrastructure, such as complex terrain deformations and changeable subsurface geological conditions [233, 236]. A further reoccurring theme was the incompleteness of feeder datasets from data collection methods described in the previous sections — which further limited BIM efficacy in this context — despite recent improvements to automated structural asset and defect characterisation methods, including multi-label dataset recovery methods [237–240].

### *2.5.10 Other Technologies*

Aforementioned NDI methods were most commonly deployed in routine surveys based on encountered literature, which motivated their distinction from (i) more antiquated methods (e.g. invasive, inefficient, overly localised), (ii) less established experimental practices and (iii) schemes for real-time subsurface monitoring. Methods grouped in (i) included: Borehole/Drill Core Sampling [241,242], Electrical Resistivity Tomography (ERT) [243–246], Endoscopic Probing [67,247] and Schmidt Hammer Strength Testing [118, 248]. In group (ii): Radiography/Muon Tomography [249, 250] and multiple further early-stage prototype robotic subsurface inspection systems [80, 217, 251–254]. Lastly, methods belonging to group (iii) included Time Domain Reflectometry schemes [255, 256], in addition to other embedded sensor systems [257].

## 2.6 Motivation – Effective Subsurface Inspection

In this section, the primary challenges associated with state-of-the-art approaches for subsurface inspection of large-scale transport infrastructure, as identified in the preceding review, are consolidated and discussed, alongside current research and development trends in this field. Particular emphasis is placed on how these challenges impact the targeted maintenance of historic railway tunnels and their associated structural elements. Critique of heuristic comparisons in Section 2.6.1 highlights the need for a more robust set of criteria to assess the effectiveness of visualisation frameworks, particularly those based on the technologies and techniques reviewed. Following this, works showing promising alignment with the effectiveness criteria were examined, considering both data conveyance in Section 2.6.2 and data collection in Section 2.6.3, in line with the review's remit.

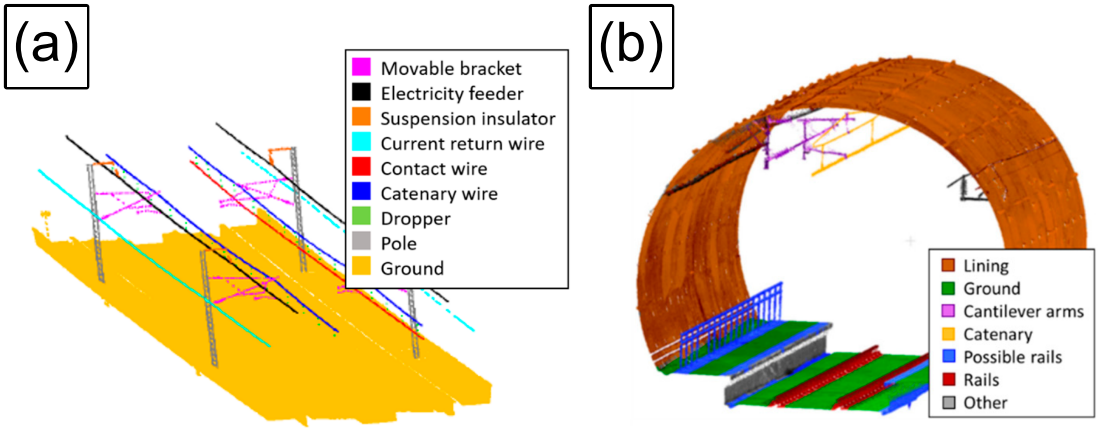


Figure 2.18: BIM for rail infrastructure inspection. 'As-is' BIMs [17] frequently adopt TLS point cloud segmentation (via RANSAC and Supported Vector Machine methods) to label trackside assets both (a) outside and (b) within the tunnel environment [18].

### *2.6.1 Criteria For Effective Subsurface Inspection*

After reviewing state-of-the-art subsurface inspection methods, attention turned towards identifying key research and development opportunities to formulate the research questions, aims, and objectives for this thesis. To narrow focus to a specific technology, it was essential to identify recent developments showcasing the 'more effective' visualisation framework(s) and most significant innovation potential for practical subsurface inspection in the context of this research.

To achieve this, a criteria-based evaluation strategy was developed. As illustrated in Figure 2.19, this approach offered a more robust and objective foundation for assessment, avoiding reliance on direct heuristic comparisons[16] of individual methods' advantages and disadvantages. Notably, the formalisation of such a criteria marked a novel development in the field, as no comparable approach had been identified across the review.

At this stage, it was essential to define, based on the review and general intuition, what constituted effectiveness from a high-level perspective in this context. The review highlighted that significant disparities were an intrinsic factor to consider when examining operating principles, deployment methodologies, and the presentation of survey findings related to subsurface inspection surveys, both for railway tunnels and across broader transport infrastructure. These differences were also further compounded by the complex and context-dependent criteria for assessing suitability and performance. Two specific examples identified included: (i) the nature/variety of detectable subsurface anomalies and (ii) the timescale over which a survey could be conducted, extending from the initial planning stages through to the practical implementation of targeted maintenance strategies they served to inform. The basis for the proposed effectiveness criteria would therefore be two-fold.

First, it was crucial to recognise that each technology discussed in Section 2.5 was found to have at least one critical limitation (see Table 2.1). An effective visualisation framework would, therefore, be one that did not suffer from these identified limitations. Innovations addressing these shortcomings would also likely have the most substantial impact on advancing the state-of-the-art in this field.

Second, consolidating a Category Connection Matrix (CCM) from the encountered literature (see Table 2.2) — inspired by the hybrid workflow matrix presented in [258] — provided a clear breakdown of emerging research trends.

[16]The 'heuristic comparison' approach problematically often resulted in circular arguments, due to implicit variation in the grounds for comparison being considered and contextual variation between their relative significance.

| **Approach** | **Critical Limitation(s)** |
|---|---|
| A, B | Lack necessary penetrative capability to directly inspect the subsurface. |
| C,D,E | 2D projections of 3D structural profiles can limit the faithfulness/fidelity of visual output. |
| | Inefficient implementation. |
| | Skew from ambient temperature variation. |
| | Limited survey coverage and restricted field-of-view. |
| | Output visuals lack interpretative clarity. |
| F | Struggles to resolve localised subsurface structural anomalies. |
| G,H,I | Systems share the limits of their constituent sensors. |
| | Onsite supervision still required. |
| | Majority of systems are still concepts or early-prototypes. |
| | Architecture frequently lacks sufficient optimisation to dynamically react to practical survey data in transport infrastructure management applications. |

Table 2.1: Key challenges facing different approaches for subsurface inspection of transport infrastructure. Approaches include Visual Inspection (A); Laser Methods (B); Acoustic Inspection (C); Thermographic Methods (D); GPR (E); Gravimetric Surveying (F); UAVs (G); Adaptive Robots (H) and BIM Integration (I).

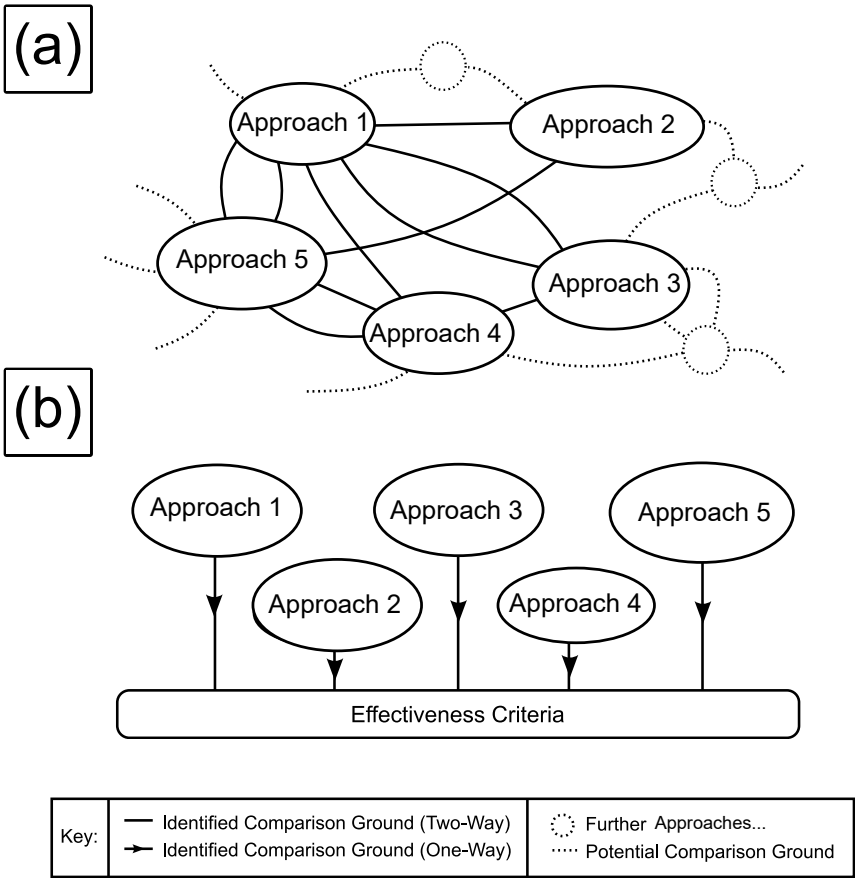


Figure 2.19: An effectiveness criteria simplifying a comparison network. Heuristic comparisons (a) are irregular and multi-directional networks, whereas the integration of a criteria (b) collapses the network to be regularised and unidirectional.

Hollow dot icons (○) denote an identified but relatively unexplored research avenue, indicating a prime knowledge or innovation gap. Half-filled dot icons (⊖) indicate that works connected to the given research avenue were encountered but were mostly indirectly related to the subsurface inspection of tunnel and transport infrastructure, marking opportunity for new research via novel idea synthesis either amalgamated from or inspired by current state-of-the-art technology and more recent literature. Solid dot icons (●), on the other hand, denote that work directly relevant to a given research avenue was encountered which strongly aligned with the aforementioned context, signifying that relevant practical research is proposed, presently underway or considered surplus to requirement.

This matrix highlighted the main future research avenues in the field and indicated where current research efforts were most concentrated. It was also reasonable to assume that in principle, that the motivation behind relevant work encountered was collectively aligned develop the most effective visualisation framework possible. Therefore, it was decided that each identified research category should align with at least one criterion in the formulated effectiveness criteria.

| **CCM** | **Identified Research Avenues** | | | | | | | |
|---|---|---|---|---|---|---|---|---|
| Approaches | A | B | C | D | E | F | G | H |
| Visual Inspection | ● | ⊖ | ⊖ | ⊖ | ⊖ | ⊖ | ⊖ | ● |
| Acoustic Inspection | ○ | ○ | ○ | ● | ⊖ | ○ | ○ | ○ |
| Laser Methods | ⊖ | ⊖ | ⊖ | ● | ○ | ⊖ | ⊖ | ⊖ |
| Thermographic Methods | ○ | ○ | ⊖ | ● | ⊖ | ○ | ○ | ○ |
| Gravimetric Surveying | ○ | ○ | ⊖ | ○ | ○ | ○ | ○ | ○ |
| GPR | ○ | ⊖ | ⊖ | ○ | ⊖ | ⊖ | ○ | ⊖ |
| UAVs and Adaptive Robots | ● | ⊖ | ○ | ● | ○ | ○ | ○ | ○ |
| BIM Integration | ○ | ○ | ○ | ○ | ⊖ | ○ | ⊖ | ⊖ |

Table 2.2: CCM summarising key research trends identified across the encountered literature. Research avenues identified included: Autonomous Tunnel Surveys (A); Alternatives to Fixed-Direction Sensor Arrays (B); Surface-Subsurface Tunnel Survey Fusion (C); Automated Tunnel Feature Detection (D); Tunnel Subsurface Feature Severity Ranking (E); Volumetric Tunnel Feature Reconstruction (F); BIM and Digital Twin Tunnel Development (G); XR Technology Integration (H).

Based on this rationale, the following criteria for an effective visualisation framework for the subsurface inspection of tunnel, and associated transport infrastructure, was formulated.

Data Collection:

1. **Survey Completeness**: Comprehensive subsurface coverage should be achieved to facilitate detection of anomaly presence in any critical structural aspects. Current approaches notably lack sufficient penetrative capability or suffer from restricted field of view due high localisation of scans or fixed-directional sensing elements.

Data Conveyance:

2. **Accessibility/Tractability/Interpretive Clarity**: An end-user of a developed visualisation framework, who is not a specialist in the specific technology (e.g. an infrastructure manager), should independently be able to understand both how returned output was produced (at least at an abstract level) and make informed decisions based on that output[17].

3. **Faithfulness/Fidelity**: High fidelity[18] visual output should be recovered from deployment of a visualisation framework , in which inconsistency between physical subsurface geometry and returned visual output should be minimal[19].

4. **Interactivity**: Returned survey output should react intuitively to end-user engagement to make the navigation and analysis of survey findings more efficient, economic and versatile[20].

Both Aspects:

5. **Duration**: Subsurface surveys should be completed in a time-efficient manner to minimise infrastructure closure durations and associated network disruption. Data collection should balance speed of data capture with recovered data quality, while data conveyance should balance time required for data processing with the precision of analysis performed.

[17]Consider standard 2D transects from GPR surveys representative of the antithesis to this notion, as they contain considerable but mostly incomprehensible information.

[18]In this work, 'fidelity' can be regarded as how faithfully data returned from a visualisation framework compares to the true physical form of the structural anomaly that was inspected.

[19]A specific example of poor faithfulness would be how overhead structures can confusingly appear as below-ground anomalies in GPR data [152, 259].

[20]Again, consider GPR data, in which the ability to progressively reveal individual transects in 3D aligned datasets can provide easier navigation and more visually intuitive interpretation than an isolated transect or the full dataset presented as a solid, inert mass of datapoints.

Based on the ongoing research outlined in the CCM, and considering the two-fold basis adopted prior, no single framework identified in this review yet satisfies all the established criteria. Furthermore, while the development of a fully effective framework remains a long-term goal, informed predictions can still be made at this stage.

At this point, the review has highlighted that, in this research context, GPR currently offers the greatest versatility for subsurface inspection. As a result, it is reasonable to expect that the earliest impactful research will likely focus on overcoming its key challenges, principally increases to its field-of-view and the interpretive clarity of its output visuals. In the longer term, further advances may come from integrating GPR with more sophisticated data conveyance methods, established already or currently at an early stage of development. Scope identified would include partnership with interpolative techniques as presented in [165] and [170], alongside AI-assisted 3D spatial profile recovery methods, such as DepthNet [168].

### *2.6.2 Towards Criteria Fulfilment – Data Conveyance*

The body of work encountered during this review, most closely aligned with the outlined effectiveness criteria, is now examined, starting with innovations in data conveyance schema. These works can be grouped into two key areas: automated subsurface anomaly detection and evaluation, along with the dynamic interaction between end-users and the returned survey output. The groups are explored in sequence to provide a clear summary of relevant advancements in each area.

Automated Subsurface Anomaly Detection and Evaluation:

If an end-user cannot clearly interpret subsurface survey data, the inspection provides little useful insight into structural health or targeted maintenance. Identifying degradation indicators is crucial for detecting subsurface structural anomalies. Moreover, evaluating associated characteristics such as position, extent, and extremal depths can further guide the urgency of repairs to affected areas.

Manually searching through raw survey data and visual output can be highly impractical, particularly for large-scale infrastructure such as tunnels. The range of potential subsurface anomalies that can arise throughout a tunnel's lifespan is also extensive (see Section 2.4). As a result, manual analysis is often critically limited by the relatively slow speed of human cognition, as well as errors in judgement caused by subjective interpretation.

Unintuitive visualisations of survey data can compound these issues, perhaps explaining why research focused on Automated Feature Detection/Evaluation (AFD/E) accounted for over a third of the research trends identified in the CCM. This includes the use of Convolutional Neural Networks (CNNs) [260,261] and Deep Learning (DL) [49,215,216] detectors, as well as ranking schemes to assess the severity of anomalies and the urgency of maintenance intervention [262,263].

The range and complexity of structural anomalies that current AFD can accurately identify were of principal interest. Focusing on studies specifically related to subsurface inspection, the DL image grid workflow presented in [39] demonstrated notable capability for asynchronous discrimination of up to four distinct anomaly types in GPR datasets: manholes, cavities, utility pipes, and the background media. Among the works reviewed, this was the most versatile detection capability identified.

Further studies were identified that successfully achieved simultaneous detection of realistically complex defect configurations [264,265]. These studies, which similarly utilised GPR transect data, were able to discriminate up to a maximum of two anomaly types in 2D [141]. However, with the sole exception of [39], it was observed that the anomalies in test environments were associated exclusively with either assets or defects, but not both. Based on these findings, GPR-based research — which appears to be at the forefront of developments in AFD — and the full potential of DL-based anomaly detectors, have yet to be thoroughly explored. Thus, any study capable of classifying more than four anomalies of mixed types (i.e., structural assets and defects), variety (e.g., shafts, voids, pipes), or complexity would represent a significant advance in AFD within the context of this research.

Defect severity ranking within AFE was found to be a less extensively researched area. Studies focusing on dictionary-based schemes were less frequently encountered compared to research into more sophisticated, contextual evaluation methods such as fuzzy logic devices [266, 267] and probabilistic analysis [100, 268]. This suggested that more advanced evaluation methods were being explored for assessing the urgency[21] of anomalies within survey datasets, although it appeared that methods presented in these works had not yet been directly applied to historic masonry railway tunnels. This indicates that developing a robust contextual severity ranking scheme tailored specifically for historic masonry railway tunnels presents a valuable opportunity for future research.

Overall, AFD/E is clearly moving from proof-of-concept simulations to practical deployment tests. In the context of subsurface inspection for tunnels and related transport infrastructure, schemes will need to more accurately and efficiently differentiate between anomalies related to structural assets and more hazardous defects.

[21] Consider a cluster of small anomalies in close proximity. Depending on survey context, this observation might pose a greater risk to a structurally sound element than a single larger anomaly in isolation.

The consolidated summaries of common assets and defects presented in this chapter also offer a valuable entry point for new researchers. They provide a clearer understanding of common (but less well-documented) critical elements in older masonry railway tunnels, and can thereby better-support future research into the application of advanced AFD/E techniques associated with this field.

Extended Reality for Dynamic Survey Interaction:

Dynamic Survey Interaction (DSI) is defined here as any information conveyance technique that intuitively responds to end-user triggers (e.g. gestures, camera proximity, movement speed, metadata, field-of-view) [269–271]. This approach enhances both the clarity of information within survey data and the ergonomics of use. DSI attributes fundamentally simplify the complexity of interaction, improving data usage efficiency and accessibility for non-specialists, which has made them prevalent in Extended Reality (XR) interfaces concerning structural survey data.

For clarity, XR will be subdivided into Augmented/Mixed Reality (AR/MR) and Virtual Reality (VR). It is important to note the distinction between AR and MR: AR is essentially a passive overlay of information, while MR is interactive, allowing the physical environment to influence the digital environment and vice versa. In both cases, survey data is conveyed through a head-mounted display. In AR/MR, this display superimposes assistive digital information over the user's view, whereas in VR, it provides full immersion in a digitally rendered environment [271,272]. As an emerging and exploratory medium, both academics and industry are now investigating practical applications of XR for DSI, including its use for infrastructure inspections relevant to this research project.

This review encountered several noteworthy developments in AR/MR visualisation. For instance, [171] proposed a rendering pipeline that employs back-projection of air-coupled 3D multistatic GPR data combined with Jerman Enhancement Filtering, but it notably lacked a practical end-user interface. In contrast, [273] presented a prototype AR visualisation method for pavement subsurface inspection, built using Unity3D and based on 'Reality-Capture' modelling for iOS. However, the performance of all subsurface AR inspection tools reviewed appears to be untested in the context of in-service railway tunnels.

In the near future, it is reasonable to assume that large volumes of subsurface data required for practical surveys would eventually necessitate a shift from the use of local storage on individual tablets to wireless data relay from offsite locations, likely in remote data hubs. However, studies directly applying underground wireless communication networks in older railway tunnels were notably absent from the works reviewed, highlighting a promising opportunity for future innovation.

In contrast, several synchronisation schemes for real-time VR-BIM data exchange (e.g. BVRS [274]) have been developed and tested in real tunnel construction projects, such as the Shenzhen-Zhongshan Immersed Tunnel [275]. For operating tunnels, the literature mainly focuses on disaster situation training [276, 277], with studies applying this technology directly to practical inspection being relatively scarce.

Among the VR visualisation frameworks encountered, only one was specifically tailored for the structural inspection of in-service railway tunnels (detailed across [263, 278]). The Enhanced Photorealistic Immersive (EPI) Survey Platform, developed in UE4 using SfM techniques, processes CRP data to feed a novel interactive dashboard that offers an extensive range of DSI attributes. Innovative attributes demonstrated included: (i) defect highlighting filter toggles; (ii) a mini-map of in-model user location and (iii) proximity-triggered defect information modules detailing TCMI (Tunnel Condition Monitoring Index) grading. The TCMI ranges from 0 to 100, where 100 denotes a defect free aspect of the tunnel [86, 279]. However, the platform's reliance on visual CRP data does not explicitly profile subsurface structural conditions, which at this stage limits the direct application of this work for subsurface inspection.

Applying recent innovations in XR for DSI to the subsurface inspection of tunnels and related transport infrastructure presents a promising direction for future research. These advancements could significantly improve the clarity and accessibility of survey data, benefiting not only survey and maintenance practitioners but also a broader range of roles in tunnel management, including asset engineers, environmental managers, and operations risk advisors [280–282].

A key milestone for deploying AR/MR systems in this context will be the development of a dedicated wireless subterranean communication network capable of supporting real-time information exchange between onsite surveyors and remote rail network data hubs. The use of emerging IoT/WSN Wireless Mesh communication nodes [282–284] presents a feasible solution and represents a notable research opportunity.

For VR systems, the visualisation framework presented in [263] exemplifies the current state of the art in DSI for tunnel infrastructure. In both cases, advancing developments according to the proposed criteria in the previous section presents opportunity for innovation with the most significant impact potential. In particular, enhancing the comprehensiveness of subsurface coverage during data collection would provide a foundation for creating more detailed environmental models to support the development of future XR survey environments.

### *2.6.3 Towards Criteria Fulfilment – Data Collection*

Sources encountered during this review that are most closely aligned with the outlined effectiveness criteria for data collection schema are now summarised. Building on the recommendations from the previous section regarding frameworks that provide more comprehensive subsurface coverage, this review highlights emerging hybrid-rotational GPR technology [21,22] as a significant recent advancement. This approach has the potential to underpin a future visualisation framework and could be among the first to practically meet the full effectiveness criteria proposed earlier, representing a major innovation opportunity.

The key innovations which underpin hybrid-rotational GPR are its novel 360-degree orientable sensing antenna and its unique capability to automate both lateral and rotational movements[22]. It can also independently isolate either (or both) mechanisms during data collection, which is responsible for the 'hybrid' functionality of this technology.

This novel functionality uniquely allows a hybrid-rotational GPR system to capture:

1. **Planar Transects**: No antenna rotation, but continuous lateral advance.
2. **Rotational Transects**: Generated by sequential, periodic antenna rotation between incremented lateral advance of the antenna.
3. **Helical Transects**: Continuous antenna rotation *and* concurrent lateral advance.

A significant aspect of this technology is its unique capability to capture helical transects in 3D space, previously unachievable without dual automation of both lateral and rotational antenna movements. This opens a new research avenue focused on optimising helical scan parameters, which would be crucial for maximising the potential of this technology, most significantly in tunnel infrastructure surveys. In this scenario, where the cylindrical geometry is prominent, helical transects provide a natural and efficient approach for profiling both the structure and its subsurface.

To meet the effectiveness criteria, it is essential that the data collected in such surveys is dense enough to produce high-fidelity output while ensuring the process is efficient enough to minimise inspection time and reduce tunnel closure durations. Optimisation would likely need to factor in the lateral speed of the data collection system, the antenna's rotation rate, and the sampling frequency of the measurement equipment.

[22]Note that when rotation is considered in terms of relative displacement from a given reference point, the term azimuth will be adopted.

Additionally, with appropriate biasing, it may be possible to recover optimised parameter sets that prioritise either higher fidelity output or more efficient data collection, potentially enabling different operational modes for the helical scanning system.

A further key advantage of hybrid-rotational GPR technology is its versatility compared to conventional fixed-directional GPR systems[23].

By leveraging the parallel stacking of planar and rotational transects during data processing, there is potential to utilise multiple avenues for creating 3D survey datasets using this technology. Specifically, the use of helical transects could generate unique, effectively in-situ 3D datasets.

It was also noted that commercial tools for subsurface inspection of railway infrastructure (see Section 2.5) typically rely on downward-oriented antennas focused on inspecting the trackbed for ballast fouling. Leading systems in this category include the Zetica Advanced Rail Radar (ZARR) [143, 285] and the IDS SafeRail System (SRS) [144]. Hybrid-rotational GPR systems have the ability to emulate this functionality by recording planar transects with the antenna orientated directly downward. Across multiple passes with the antenna set to at different azimuth, the technology also exhibits the potential to readily emulate planar transects for inspection of inaccessible aspects of enclosed infrastructure, including a tunnel's sidewalls, haunch and crown as achieved by state-of-the-art multi-antenna fixed-directional GPR arrays fixed to railway rolling stock [19].

Several alternative works based on rotating sensors were also encountered during this review. However, these systems often lacked automation [19, 286, 287] or were unable to capture full 360-degree circumferential profiles [288]. One example is the TULIPS system developed in [20], which features a GPR array mounted on the cutting face of a tunnel boring machine to monitor subsurface conditions during tunnel construction. Unlike hybrid-rotational GPR, this system operated in a 'look-ahead' role, probing the subsurface ahead of the cutting face rather than surveying the sidewalls. Although, because it was based on a tunnel boring machine, its use was limited to the construction phase of a tunnel's lifecycle, restricting its applicability for practical surveying. These limitations have restricted the scope for innovation in each system compared to developments in hybrid-rotational GPR, setting it apart as a leading innovation in the field.

[23]The term 'fixed-directional' serves to emphasise that the relative orientation between the antenna(s) and the main body of the physical data collection system does not change throughout data collection.

A visual comparison between such 'look-ahead' rotational GPR, the fixed-directional GPR system presented in [19] and the hybrid-rotational GPR presented across [21] and [22] is provided in Figure 2.20. Notably, both fixed and hybrid systems utilise highly directive TEM feedhorn antenna designs ($O(10)dB$) [289] to minimise energy losses through air-launched operation. By contrast, the 'look ahead' system adopts the comparatively broader directivity ($O(1)dB$) bow-tie antenna design to reduce the antenna footprint, simplifying system integration onto the TBM cutting head.

## 2.7 Feasibility Study – Prototype Hybrid-Rotational GPR

In this section, the analysis of a recent feasibility study uncovers research gaps related to the latest hybrid-rotational GPR technology, providing a foundation for the research presented in the subsequent chapters of the thesis. After outlining the motivation behind the feasibility study in Section 2.7.1, the evolution of hybrid-rotational GPR system design is summarised in Section 2.7.2. This is followed by an overview of the experimental setup in Section 2.7.3 prior to discussion of findings in Section 2.7.4 and consolidation of scope for future development in Section 2.7.5.

The candidate actively contributed to work presented in Section 2.7 and was primarily responsible for visualisation, analysis and interpretation of collected data from Section 2.7.4 onward. Railview Ltd. coordinated the design of the T-Vision system and decisions on experimental setup, as detailed in Section 2.7.2 and Section 2.7.3, respectively.

### *2.7.1 Motivation*

This feasibility study sought to examine the practical capabilities of a newly developed hybrid-rotational GPR prototype system for the subsurface inspection of railway tunnels, specifically in older masonry structures commonly found on the UK rail network.

Previously used as construction shafts, hidden shafts are subsurface structural anomalies that were a byproduct of Victorian engineering practices. After completing a tunnel, a thin layer of brickwork, known as capping, was added to these shafts if they were not being used as ventilation shafts. This was done to enhance the aesthetic appeal of the tunnel lining, with the touchable surface also formally termed the intrados[24].

[24]This can also be regarded as the contact surface from the perspective of a GPR survey.

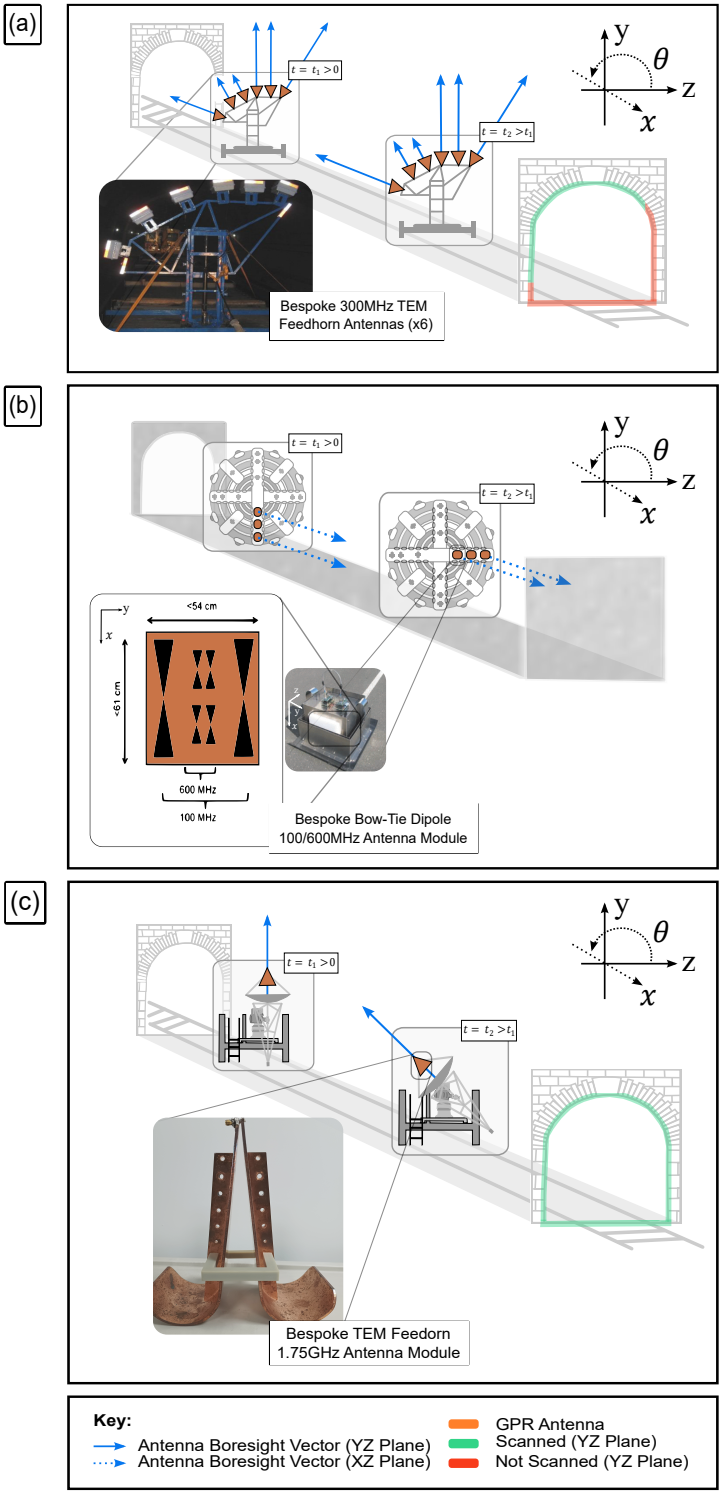


Figure 2.20: Visual comparison between: (a) fixed-directional GPR for tunnel subsurface inspection presented in [19]; (b) look-ahead GPR mounted on a tunnel boring machine as developed in [20] and (c) new hybrid-rotational GPR presented across [21] and [22].

Critically, such actions were often left undocumented in construction records [59, 290], resulting in numerous hidden shafts existing in UK rail network's tunnels. These shafts, ranging upwards of 3m in diameter, may extend partially or fully to ground level above the tunnel. While many have been identified through structural failures or surveys using detailed inspection methods (then termed blind shafts), many still remain undocumented (i.e. hidden shafts).

The Office of Road and Rail had consistently emphasised the risk of unaddressed degradation of undocumented hidden shafts within these structures, as noted in multiple reviews of rail network infrastructure management [291, 292]. The primary risk posed to services and tunnel crews is the partial or complete collapse of the capping masonry, which could potentially bring down surrounding masonry in the upper tunnel lining (the crown). In the worst-case scenario, this could lead to a section collapse. More commonly, dislodged masonry could obstruct the tunnel, resulting in significant network disruption due to the need for repairs and cleanup. The mechanisms behind capping failure vary but are often attributed to water ingress and shifting landmasses, which can damage and dislodge masonry in the walls of the shafts.

This debris accumulates on the capping, and as the process remains hidden from view, the capping eventually gives way under the weight. Therefore, accurately detecting hidden shafts is crucial to enable timely intervention through targeted maintenance, preventing critical failures of this nature from occurring.

From both an industrial and academic perspective, it was also noted that the GPR hallmarks of hidden/blind shafts had not before been formally profiled nor analysed amongst the relevant literature, owing to the impracticalities of conducting extensive GPR surveys of the crown of these tunnels prior to the development of T-Vision[25]. The capture and analysis of these profiles therefore presented a significant knowledge gap for this study to address.

### *2.7.2 System Design*

The T-Vision system design is visually deconstructed in Figure 2.21.

GPR measurements were recorded directly in the frequency domain using a Hewlett-Packard HP8753D VNA, which performed a linear frequency sweep across a $B = 2.5$GHz bandwidth with centre frequency $f_c = 1.75$GHz.

[25]While feasible in principle using elevated platforms and handheld GPR systems, the extended closures required and the significant effort involved in advancing platforms through tunnels, combined with the prioritisation of repair efforts, was a key reason why similar investigatory work has not been previously attempted in the literature encountered. In addition, aforementioned studies using rolling stock mounted sensors were almost exclusively not based in the UK, further limiting available technology for such work.

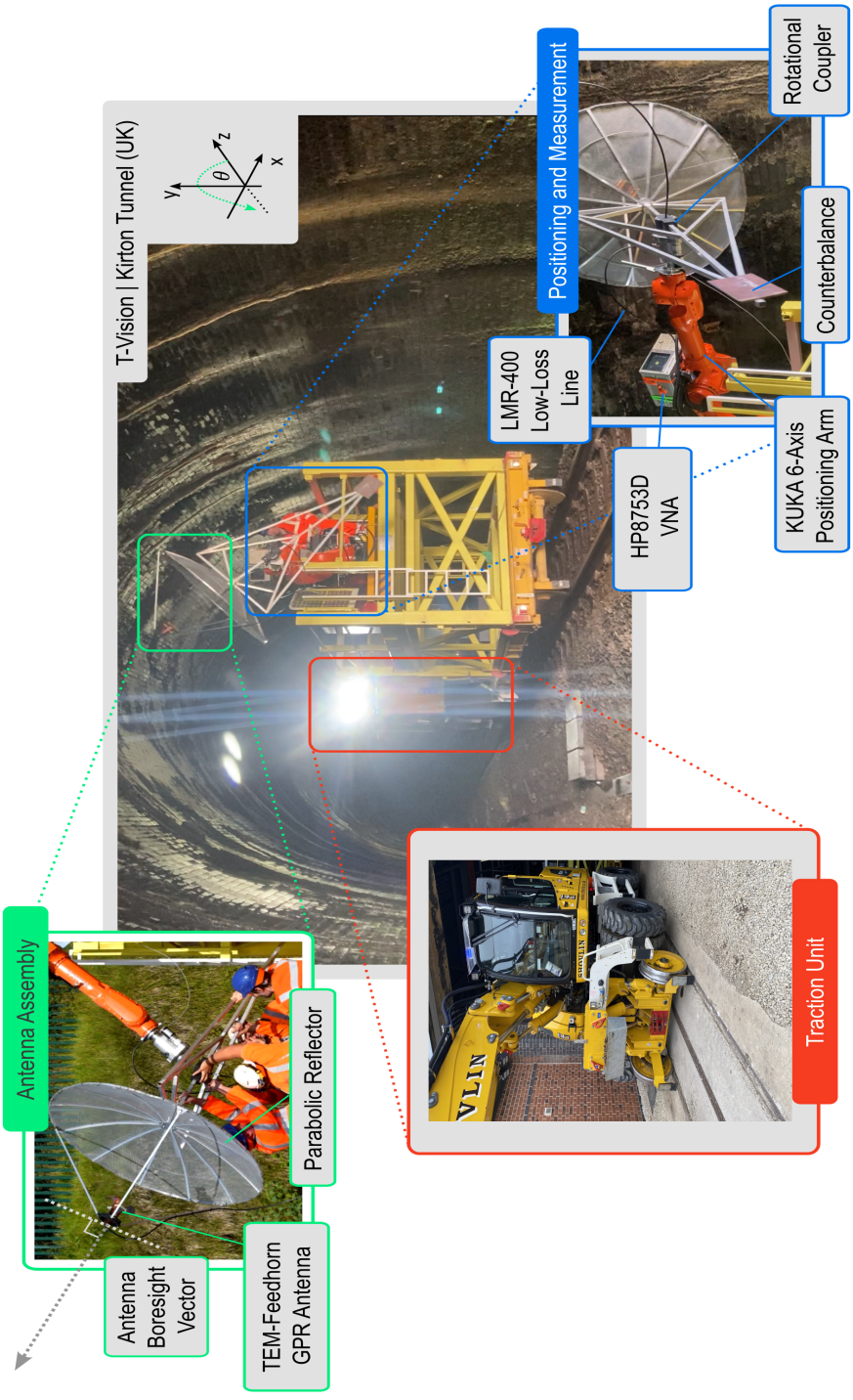


Figure 2.21: T-Vision system design was comprised of a rotating measurement antenna (green), combined positioning and measurement systems (blue), and a road-rail excavator to serve as a traction unit for the assembly (red).

This signal was transmitted through a bespoke TEM (Transverse Electromagnetic Mode) feed-horn antenna, focused by a 1.5m diameter parabolic reflector to reduce beam dispersion.

The system was designed to maximise energy transfer to the contact surface, to increase attainable penetrative depth beyond an air-launching distance of 2m. This separation was critical to ensure safe clearance between the rotating antenna and contact surface (i.e. tunnel intrados). The associated theoretical range resolution was within

$$\Delta y = \frac{c}{2B} \approx 60\ [mm], \tag{2.9}$$

with a cross-range resolution of,

$$\Delta x = \left(\frac{\lambda_c}{D}\right) R = \left(\frac{c}{f_c D}\right) R \approx 0.114R\ [m], \tag{2.10}$$

inherently proportional to propagation distance $R > 0$, where the wavelength $\lambda_c = c/f_c$ and the parabolic reflector provided an effective aperture size of $D = 1.5m$.

These levels of resolution were considered more than sufficient to accurately profile the hallmarks of expected 3m diameter shafts, and had potential to detect individual brickwork layer interfaces within the tunnel lining itself.

To offset the mass of the reflector, a counterbalance was positioned approximately 1.5m from the central rotational coupler. This custom coupler prevented the VNA measurement cable from twisting around the antenna during data collection and served to suppress cable-flex artifacts from manifesting in measurement data (see Chapter 6). The assembly could be rotated a full 360-degree within 10 seconds, achieved using a 24V DC motor directly connected to the rotational coupler via a shaft drive. A low loss pair of 3m and 2m measurement cables connected the VNA to the antenna through the coupler.

Positioning the rotating antenna configuration was accomplished using a 6-axis articulated KUKA KR 50 R2100 robotic arm. This setup enabled the centre of rotation to be approximately aligned with the tunnel's cross-sectional centre, helping to maintain a consistent lift-off from the contact surface.

Additionally, the robotic arm enabled the antenna to extend beyond the track gauge, allowing measurements of twin-track tunnels even if the tracks had been removed. The full unit, mounted on a T8 rail trailer along with a portable generator for power, was moved laterally by a road-rail excavator to ensure steady and repeatable traversal along the tunnel's full length.

### *2.7.3 Experimental Setup and Methods*

The T-Vision system was deployed in Kirton Tunnel (UK), a former twin-track structure build in 1848 measuring 1.22 km in length [293]. It was selected for its combination of well-separated open ventilation shafts and multiple blind shafts with intact masonry capping. The location and extent of each shaft, along with the surrounding landmass layers (i.e. strata), are shown in Figure 2.22. Descriptive details of expected shaft characteristics and the general structural condition of the tunnel lining were provided by the infrastructure managers in the form of survey reports from previous structural inspections [23].

Prior to data collection, the system was calibrated by directing the antenna skyward outside the tunnel and recording a standalone trace measurement free of obstructions. This captured signal backscatter within the measurement cables and antenna, which were later suppressed by subtracting this reference from each trace during the main data collection. Further technical details on GPR background calibration are provided in Chapter 6.

The VNA was configured to record 201 samples per trace and perform Inverse Fast Fourier Transform (IFFT) between consecutive measurements to recover the corresponding time-domain response profiles. These results were exported to a Panasonic Toughbook laptop via a National Instruments GPIB-USB connector. The laptop also automatically triggered the VNA measurements, found to provide a more reliable and time-efficient method compared to manual triggering via the VNA's physical controls during development.

A total of four independent scanning passes were conducted, with T-Vision traversing the full length of the tunnel at a steady speed of approximately 2.8kmph, the minimum operating speed of the traction unit. All tests maintained a clearance of 2.5-3.0m between the antenna and the tunnel's contact surface, with variations due to the tunnel's cross-sectional profile.

The process was divided into two tests.

In the first test, the antenna was locked in a vertical orientation throughout the traversal, capturing a fixed-directional transect of the tunnel crown. This test aimed to directly inspect the shafts, assess the system's hidden shaft detection capabilities (i.e. via detection of the known blind shafts), and compare GPR hallmarks of blind shafts with those of open shafts. In a subsequent test, the antenna was continuously rotated at a preset rate of 6rpm during traversal, creating a helical transect of the tunnel.

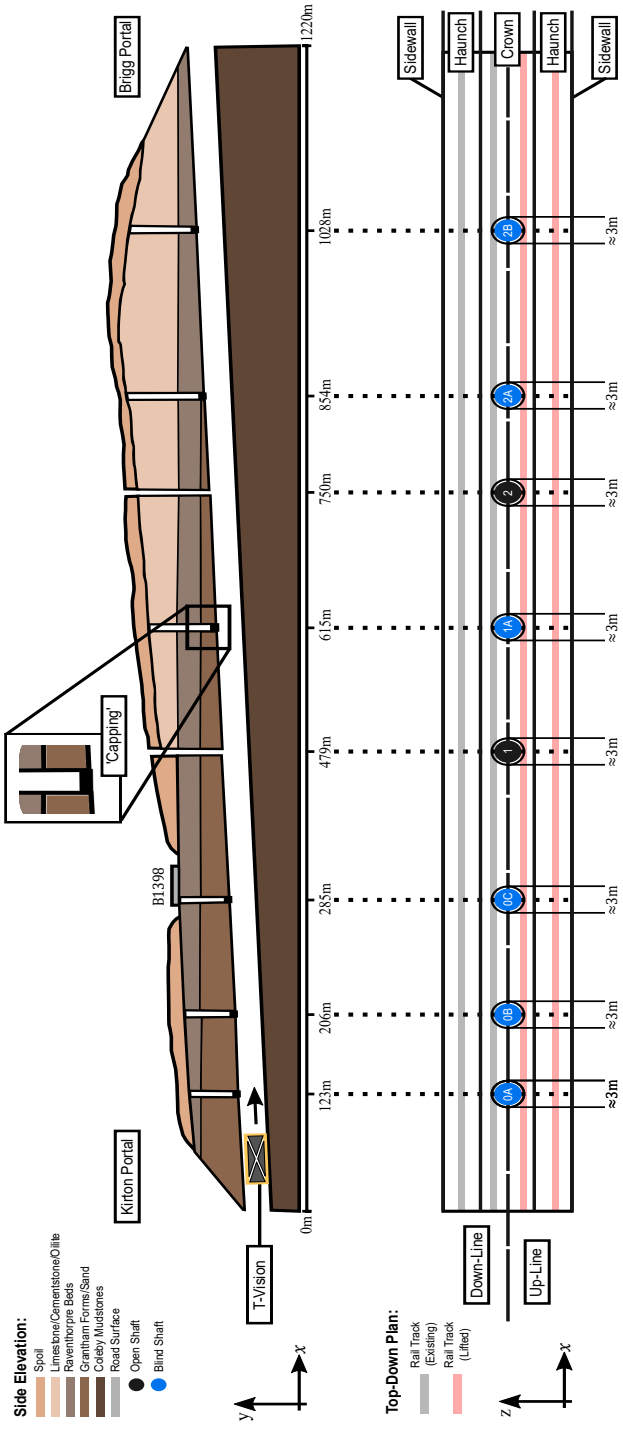


Figure 2.22: Locations and extent of shafts throughout Kirton Tunnel (UK), which were informed through examination of structural survey records [23].

This test aimed to explore the additional survey insights provided by this scanning mode, when performed with minimal data processing. It was designed to assess whether key layers of the tunnel lining, such as concentric masonry brickwork and the excavation layer[26], could be accurately identified. Both tests also provided an indication of the system's maximal attainable subsurface penetration depth.

Two scan passes were recorded for the first test: once with the antenna vertically oriented and centred over the existing 'up-line' tracks, and then repeated with the antenna instead over the formerly adjacent 'down-line' tracks — which were removed in 1983. Consistent signal artifacts at the same approximate locations across both transects would provide stronger evidence that a physical subsurface anomaly (ideally a shaft) had been detected, rather than a false artifact associated with more random ambient noise or subsurface heterogeneity, especially at greater depths near the excavation layer. In the second test, a single helical transect was recorded with the centre of rotation aligned to the approximate centre of the tunnel's cross-sectional profile.

### *2.7.4 Results and Discussion*

The fixed-directional transects of the tunnel crown from the first test are shown in Figure 2.23.

Open shafts 1 and 2 were clearly identifiable, marked by high-contrast (almost solid white) vertical bands appearing in both the up-line and down-line transects. These features exhibited high lateral localisation, spanning approximately 2-4m. This observation aligned with the physical characteristics of an open ventilation shaft, which has an empty region largely free of material interfaces that generate backscatter, unlike the surrounding subsurface regions. The latter returned traces with variable intensity backscatter, as expected when penetrating the brickwork layers of the intrados.

The onset of signal noise dominance was observed across the full lateral extent of the transects once the two-way travel time of the temporal response profiles exceeded 75-80 ns. This suggests that a maximum penetrative depth of over 2.5m (behind the intrados) had been achieved, sufficient to reach the excavation layer.

[26]The deepest interface behind the tunnel lining is where the man-made structure meets the surrounding landmass, typically consisting of a mixture of rock, stone, and sand.

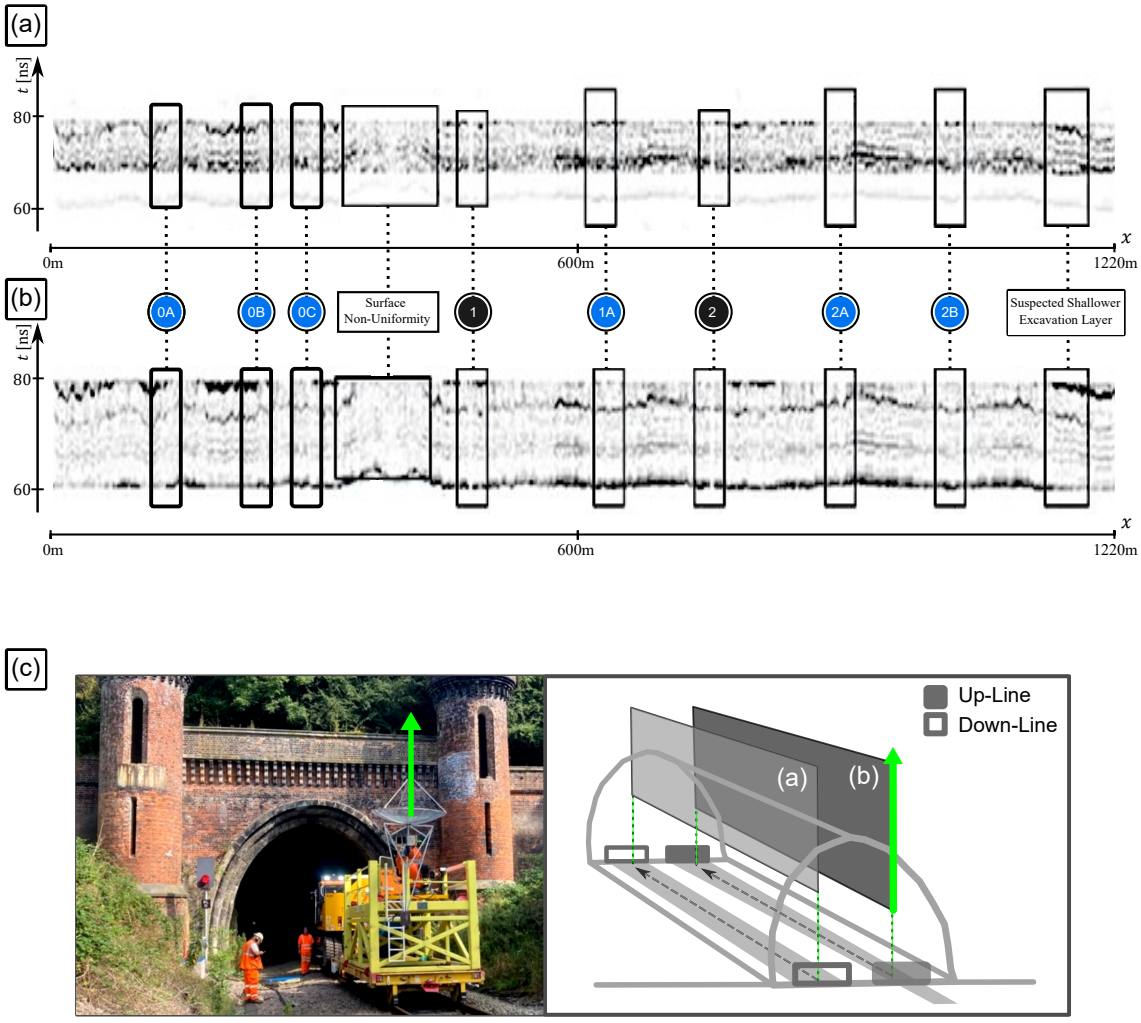


Figure 2.23: Fixed-directional transects of the crown subsurface for down-line (a) and up-line (b) scanning passes of Kirton Tunnel (c). The antenna boresight vector orientation is shown by the green arrow. Darkened hyperbolae denote subsurface structural anomalies. The contact surface is at the bottom of each transect, extending upwards into the crown's subsurface region. Critically, subsurface anomalies are observed at each shafts' location.

Critically, blind shafts 1A, 2A, and 2B were clearly distinguishable, as were similar artifacts near 125m, 208m, and 285m, corresponding to the locations of blind shafts 0A, 0B, and 0C, respectively. These features were characterised by highly localised banding that appeared consistently across both transects near the expected shaft locations based on survey records. Unlike the open shafts, these were not solid white but were overlaid with noise resembling background signal heterogeneity. This overlay was consistent with the anticipated partial infilling of the shafts, caused by displaced masonry and material washed in by water ingress over time, which was expected to have accumulated on top of the capping. The noise also exhibited vertical discontinuities in the transects, ranging between 2-4m wide (consistent with the expected diameter of a shaft), indicative of the boundary between the void-like shaft region and the surrounding masonry. Additionally, these features were observed at a noticeably greater depth than the open shafts (not immediately from the contact surface), aligning with the nature of the blind shafts' capping.

Further noteworthy observations emerged during the survey and from reviewing past structural reports. A surface-level non-uniformity in the tunnel intrados was identified between blind shaft 0C and open shaft 1. This non-uniformity was evident in the recorded transects, where a clear delay in the first significant backscatter event indicated deformation of the contact surface, consistent with the expected irregularity. Additionally, a strong backscatter event with a wide lateral profile and thin depth profile was detected just before the system exited the tunnel. This anomaly, characterised by its elongated shape, significant depth, and proximity to the end of the tunnel, was suspected to correspond to a shallower region of the excavation layer.

Collectively, these findings demonstrated that the T-Vision system successfully detected hallmarks associated with all shafts present in Kirton Tunnel, aligning with their expected physical dimensions and structural characteristics. The system achieved subsurface penetration exceeding 3m from an air-launched clearance of over 2m from the tunnel contact surface. This evidence showed that hybrid-rotational GPR technology had practical capability for subsurface inspections of historic railway tunnel infrastructure and, importantly, this included for detecting and accurately profiling hidden shafts. From a scientific perspective, this work also provided clear examples of GPR hallmarks for both open and hidden/blind shafts in these structures, addressing the identified knowledge gap.

The helical transect captured during the second test is shown in Figure 2.24, with individual traces aligned in 3D to correspond with the approximate location of the antenna's boresight vector for each measurement. As in the first test, the full tunnel was efficiently scanned, with the process completed in under 30 minutes.

Temporal response profiles began from 0ns. However, time was required for the signals to propagate through the measurement cables and antenna body to reach the aperture before entering the external measurement environment. Therefore, traces were truncated during alignment, with $t \approx 33ns$ aligned to the centre of rotation. This corresponded to the approximate interval prior to emission from the antenna aperture. Further details on this and similar estimations conducted throughout the thesis can be found in Chapter 3.

The observed distribution of backscatter intensities was consistent with the expected radial displacement of each key tunnel lining layer based on consultation of the previous survey reports. These layers included the intrados at $r \approx 3.0m$, concentric brickwork layers between $3.0m \leq r \leq 5.0m$, and the excavation layer for $r > 5.0m$. The region occupied by the tunnel interior was also clearly discernible for $r < 3m$, with its low backscatter intensity consistent with free space, akin to the open shafts observed in the previous test.

The findings from this test demonstrated that key layers of the tunnel lining could be accurately identified in helical transects with minimal additional data processing. Furthermore, the maximal radial displacement of $r > 5.0m$ corresponded to an approximate subsurface penetration (behind the intrados) of over 2m, consistent with the maximal penetrative depth achieved in the previous test.

Finally, the work conducted across these tests highlighted several areas for the future refinement of hybrid-rotational GPR to improve data collection and data conveyance. These areas included:

- Further enhancing the clarity of survey data, representing encoded subsurface geometry more intuitively than sole reliance on fixed-directional 2D transects and 3D alignment of traces comprising helical (and by extension, rotational) transects.
- Increasing knowledge of specific spatial profiles linked to subsurface structural anomalies, when assessing the quality of returned data. While sufficient for hidden/blind shaft detection confirmation in this study, survey reports from prior inspections notably lacked the sufficient levels of detail required to serve as comprehensive ground-truth data, especially if surveying for smaller-scale anomalies (e.g. individual ring separation events).
- Reducing variability in the speed of the RRV and rotating antenna to increase practically achievable levels of precision in antenna placement during data collection.
- Explicitly separating data collection and data processing operations to increase the frequency of trace measurement capture, thereby returning a denser 3D dataset and further increasing achievable levels of subsurface survey coverage.

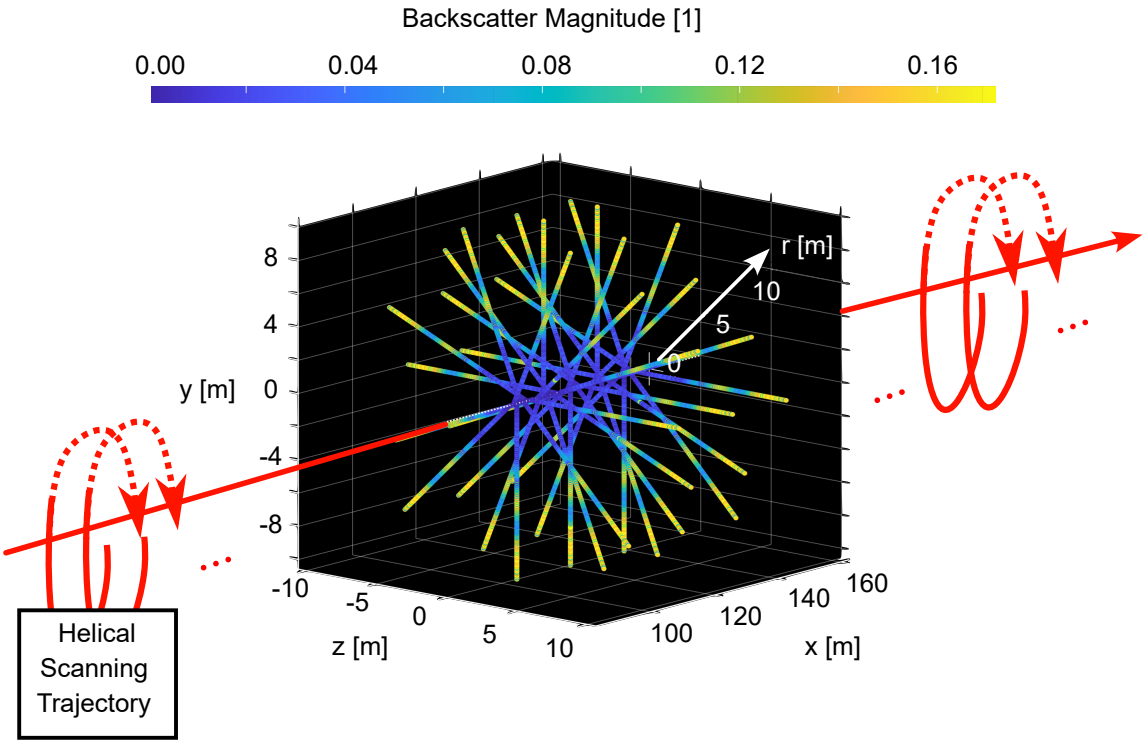


Figure 2.24: Helical transect of Kirton Tunnel. Successive traces are aligned with the antenna boresight vector in 3D space. Instances of localised high intensity backscatter are shown in yellow. The observed intensity distribution closely aligned with the expected depths of key subsurface layers within the tunnel lining.

### *2.7.5 Research and Development Opportunities*

Based on findings from the feasibility study, this provided insight into multiple relevant research and development opportunities. These encompassed, but were not limited to:

- Development of a pioneering end-to-end data processing workflow, capable returning 3D visualisations of the spatial profiles of subsurface structural anomalies and handling the multiple input data types generated by a hybrid-rotational GPR system, performing data processing operations strictly after data collection has been performed, in line with the previously defined effectiveness criteria.
- Comparative assessment of attainable system performance against more established (ideally directly observable) ground-truth geometry in controlled laboratory conditions, for which miniaturisation of the data collection equipment would likely be necessary.
- Integration of higher accuracy lateral and azimuthal positioning mechanisms, to provided more precise control over the exact antenna position of the antenna at any instant during data collection.
- An investigation to optimise scan parameters to return higher quality 3D output from survey datasets based on helical transects.

At this point the subtle nuances between a 'workflow', 'pipeline' and 'algorithm' should be explicitly clarified, as this terminology will be used throughout the thesis.

The term 'workflow' will refer to the complete sequence of interconnected processes that collectively constitute a full 3D visualisation 'pipeline' — which encompasses the natural progression of relevant operations from raw data input to the generation, rendering, and analysis of output meshes. Here, an individual 'algorithm' will denote a defined set of computational steps designed to perform a specific operation within a specific phase of the workflow.

While a workflow inherently follows a systematic sequence of operations (exhibiting an algorithmic structure) and the union of its processes can contextually be viewed as a singular construct, it need not itself be comprised *only* of a 'singular' algorithm. It represents a higher-level organisational construct that coordinates multiple algorithms and consists of multiple processing phases, that together, ultimately achieves the objectives of the pipeline.

## 2.8 Research Questions, Aims and Objectives

To address research gaps and development opportunities identified in this chapter, the following questions were posed:

1. Can 3D visualisations be developed for hybrid-rotational GPR datasets?
2. Can a visualisation framework be created to effectively capture and convey this data?
3. How can subsurface structural anomalies be identified and returned as 3D objects?

To explore these research questions, two main project aims were established:

1. To develop algorithms to perform 3D visualisation of subsurface radar data, including hybrid-rotational GPR datasets.
2. To analyse the performance efficacy of developed algorithms, when applied to datasets pertaining to tunnel and associated transport infrastructure.

Based on these aims, five corresponding objectives were formulated:

1. To gain familiarity with advanced GPR technology and collect a pool of datasets to facilitate the development of key algorithms for the cleaning, enrichment, and visualisation of subsurface radar data.
2. To develop an understanding of conventional and state-of-the-art data visualisation approaches, synthesising techniques and applying suitable augmentations where necessary to ensure functionality on hybrid-rotational GPR data.
3. To develop a versatile, tractable data processing work workflow capable of efficiently returning clear, high-fidelity 3D spatial profiles of subsurface structural anomalies.
4. To examine achievable levels of subsurface structural anomaly detection and localisation accuracy in returned 3D visualisations.
5. To appraise the effectiveness of the developed visualisation workflow by comparing output with established ground-truth geometry, for analogues of tunnel and associated transport infrastructure.

# Chapter 3. Methodology

This chapter explores the research methodology for this thesis. An overview of research practice adopted is followed by relevant theory underpinning the innovative 3D visualisation workflow developed across the project.

The work presented hereon, has been summarised and disseminated in [294].

## 3.1 Introduction

In response to research gaps identified in the previous chapter, work that follows centres on development the first standalone data processing workflow, capable of returning clear visualisations of the 3D spatial profiles of subsurface structural anomalies captured using hybrid-rotational GPR. For clarity, underlying research methodology has been divided into strategic and operational components, respectively.

## 3.2 Strategic Methodology – Research Practice

This section outlines the strategic methodology underlying high-level research practices. Section 3.2.1 details the sequence of investigations, followed by Section 3.2.2, which highlights research priorities. Safety, ethics, and data management strategies are covered in Section 3.2.3. Next, Section 3.2.4 discusses key factors influencing subsurface structural anomaly analogue selection. Finally, Section 3.2.5 discusses the evaluation of workflow performance.

### *3.2.1 Investigation Structure*

A visual summary of the investigatory work in this project is provided in Figure 3.1. After an initial literature review to identify key research gaps, sequential practical investigations followed, which applied the proposed 3D visualisation workflow to GPR data from increasingly realistic survey environments. At each stage, workflow performance was analysed. Findings informed both the progression of tests, and any refinements required.

Investigations were divided into laboratory benchmarking and subsequent field testing. Laboratory benchmarking readily enabled strict environmental control and precise knowledge of ground-truth geometry. This included exact target placement, shape, and form, through numerical simulations and small-scale practical setups.

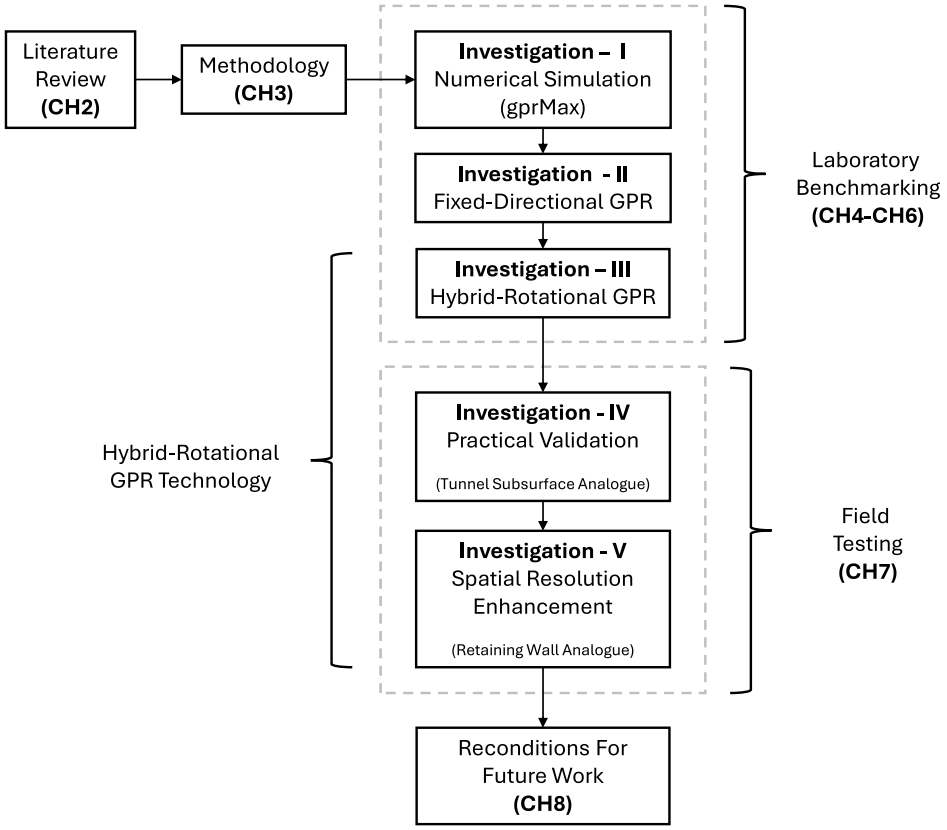


Figure 3.1: Visual summary of investigatory work structure across literature analysis, laboratory benchmarking and field testing.

Unlike in-service infrastructure, targets representing structural anomalies could be fully removed, allowing thorough background calibration and noise reduction, and readily repositioned to generate new test setups if required.

In the first laboratory benchmarking test, numerically simulated GPR datasets were used to validate the new workflow's performance in an idealised survey environment. With absolute knowledge of subsurface geometry for reference, this approach offered the most direct, easily modifiable, and precisely repeatable starting point for investigatory efforts. Critically, it also ensured findings were solely attributed to the proposed theoretical framework, as opposed to hardware or human errors during measurements.

Subsequent practical tests replicated the simulation setup in an anechoic chamber, incorporating real-world factors such as background heterogeneity and discontinuous domain boundaries while minimising ambient EM interference. The second test used a leading fixed-directional GPR system, followed by a third employing a bespoke compact hybrid-rotational GPR system. Critically, the inclusion of an intermediary fixed-directional test helped isolate the effects of transitioning to physical measurements and using a custom apparatus. This allowed their respective influence on observed workflow performance to be independently analysed. It also served to validate the efficacy of the experimental hardware setup.

Progression to field testing served to examine the effectives of the developed workflow in more realistic, larger-scale, practical survey environments. The use of structural analogues, resembling in-service infrastructure, was essential to provide accurate knowledge of ground-truth geometry and direct control over target placement. These tests also served to explore potential future refinements of the developed workflow, to enhance the quality of returned visualisations.

### *3.2.2 Prioritisations*

For tests focus on hybrid-rotational GPR, investigation design prioritised the use of practical datasets — gathered through physical measurements — over developing a dedicated numerical simulation. Both approaches offered significant novel research opportunities, however practical measurements provided the more direct solution, which allowed greater focus to be directed towards returning 3D visualisations, therein more strongly aligning with the project aims. This decision also allowed project resources to be allocated more effectively, streamlining the development process.

It should be noted that an approach for numerical simulation was formulated, and presented a practically feasible solution[1]. However, realising this would have required complex numerical implementation, alongside extensive EM field modelling and validation — whether from first principles or by adapting non-rotational models like COMSOL RF-Module [295], GPRSIM [296], or gprMax [297]. Moreover, accounting for specific physical antenna geometry and optimisation for realistic environment scaling, would have quickly extended beyond the scope of the project. Ultimately, the devised simulation-based approach remained a viable and relevant avenue for investigation at a later date, without diminishing its scientific novelty or potential impact on the broader GPR research community.

At a more fundamental level, the generation of 3D visualisations from hybrid-rotational GPR survey data was prioritised over the optimisation of helical scan parameters. Both research areas had been highlighted in the previous chapter's discussion of the proposed effectiveness criteria. Critically, formal assessment of the impact from helical scanning parameter adjustment on data quality would significantly benefit from the ability to inspect changes survey output in 3D. Ergo, developing an effective 3D visualisation workflow for hybrid-rotational GPR was considered a pre-requisite, and thereby motivated its selection as the basis for this research project.

In addition, parallel-stacked rotational transects were selected as the basis for data collection. Benefits were twofold. First, this approach granted improved control over sampling density — improving on levels achieved during the feasibility study. Moreover, such versatile datasets could also be used in future research efforts into helical scan optimisation, noting that through judicious selection of sample points, data from multiple helical scanning trajectories (of different parameter configurations) for the same ground-truth geometry could be directly extracted.

### *3.2.3 Safety, Ethics and Data Management*

To ensure safe research conduct, a comprehensive risk assessment was compiled at the outset of the project, and updated throughout its duration. Primary mechanical and electrical hazards involved entanglement in moving equipment and static discharge. Risk was mitigated by mechanically isolating power to moving components when automated systems were idle, preventing unintended movement. Dedicated grounding cables safely dissipated static buildup, while fixing tape and cable ties secured trailing antenna cables to minimise trip hazards. Radiation exposure was reduced by using shielded antennas and, where possible, conducting tests in an anechoic chamber.

[1]Instead of rotating an antenna in a stationary environment, this would have involved emulating rotary and helical scan trajectories by 'rotating the world' about a stationary GPR antenna using gprMax, subject to the addition of lateral translation.

A data management plan was also developed and maintained throughout the project, which addressed data sizing, storage, archiving, and sharing. Numerical simulations generated approximately 100 `.hdf5` output files per test (160MB), increasing to 240 `.sgy` files (250MB) and 4,200 `.s1p` files (85MB) for fixed-directional and hybrid-rotational tests, respectively. To prevent data loss and facilitate sharing, all data was synchronised to Microsoft OneDrive for Business, with secondary backups stored on an external 1TB HDD. When handling sensitive technical data, such as tunnel survey records, file owners were consulted to determine appropriate storage and safeguarding measures.

No significant ethical concerns were identified in this project.

### *3.2.4 A Suitable Subsurface Anomaly Analogue*

In consolidating the defect summary presented in the literature review, issues linked to subsurface void formation (e.g. ring separations, hidden shafts, etc.) were recurrently flagged as a critical concern in surveys of masonry-based transport infrastructure across encountered literature, and in discussions with infrastructure managers and structural engineers.

Although not assigned a formal metric (e.g. TCMI score) nor internationally standardised, a common theme identified was that 'significant' anomalies — warranting priority intervention — were typically characterised by spatial footprints spanning decimetre length scales, often exceeding 100mm, in at least one dimension. This was corroborated by first hand viewing of spall and delamination sites in Kirton Tunnel, which arising due to concealed void growth, conveyed their sizable extent prior to critical structural failure. Additionally, when viewed from the perspective of investigation design, a 100mm target length scale also closely aligned with the average dimension of a standard brick (127.5mm [298]), commonly used in the construction and repair of historic UK masonry infrastructure[2]. While the ability to visualise anomalies at ever-finer length scales would always be desirable, collectively, these observations motivated adoption of a 100mm upper-limit on target size as the basis for all investigatory work conducted across this project.

Additional considerations extended to target composition and form. Uniform, solid targets with low geometric complexity were preferred to facilitate direct visual comparisons between returned and established 3D spatial profiles when analysing workflow performance. Targets also needed sufficient dielectric contrast with the background to minimise ambiguity during assessment of visualisation fidelity. These requirements motivated the selection of solid steel spherical targets for laboratory benchmarking, akin to investigations conducted across [299–303].

[2]Specified in Standard BS EN 771-1:2011 for clay masonry units in load-bearing structures [285].

For field tests, larger scale targets exhibiting higher geometrical complexity were required. Hollow targets were selected to increase alignment with structural anomalies associated with voids, however a rigid boundary interface was required to maintain target geometry under the pressure of surrounding backfill. Plastic utility pipes provided a solution, themselves commonly featuring on GPR surveys as subsurface assets across the transport sector, notably used for drainage and utility pass-throughs in both railway tunnels and embankments.

Note, a visual overview of both types of analogue considered is presented in Figure 3.2.

### *3.2.5 Practical Assessment of Effective Workflow Performance*

Planned investigations required a strategic analysis of the proposed workflow, with a formal definition of effective performance based on a subset of criteria from Chapter 2 to ensure a focused assessment of relevant metrics. Key considerations included interpretative clarity, visualisation fidelity and processing duration, given the feasibility study had already sufficiently demonstrated the extensive coverage capability of hybrid-rotational GPR. Similarly, improvements in interactivity were deemed a long-term goal beyond this study's scope. As the first work formally addressing recovery of 3D visualisations from hybrid-rotational GPR data, focus would be on the geometrical accuracy of spatial profiles, more so than the ergonomics of information display (e.g., cluster coloration, opacity, and labelling), which could be refined in the future. Based on this, criteria for high clarity and fidelity were conflated. The finalised subset of workflow performance assessment criteria follows:

1. **Target Detection and Localisation Accuracy**: Demonstrated jointly through agreement between returned 3D spatial profiles and targets within established ground-truth geometry, in alignment with conflated criteria for high levels of fidelity and clarity.
2. **Computational Efficiency**: Demonstrated by consist, short duration elapsed runtimes. This draws parallels with the desirable shorter durations associated with survey report generation, expediting the implementation of targeted maintenance strategies.

It was essential that performance analysis returned both qualitative and quantitative findings. The analysis of 3D spatial profiles required additional specifications, to robustly formalise grounds for accurate anomaly detection and localisation. Absolute detection accuracy would constitute an ideal one-to-one correspondence between returned segmented clusters (i.e. spatial profiles) and individual targets.

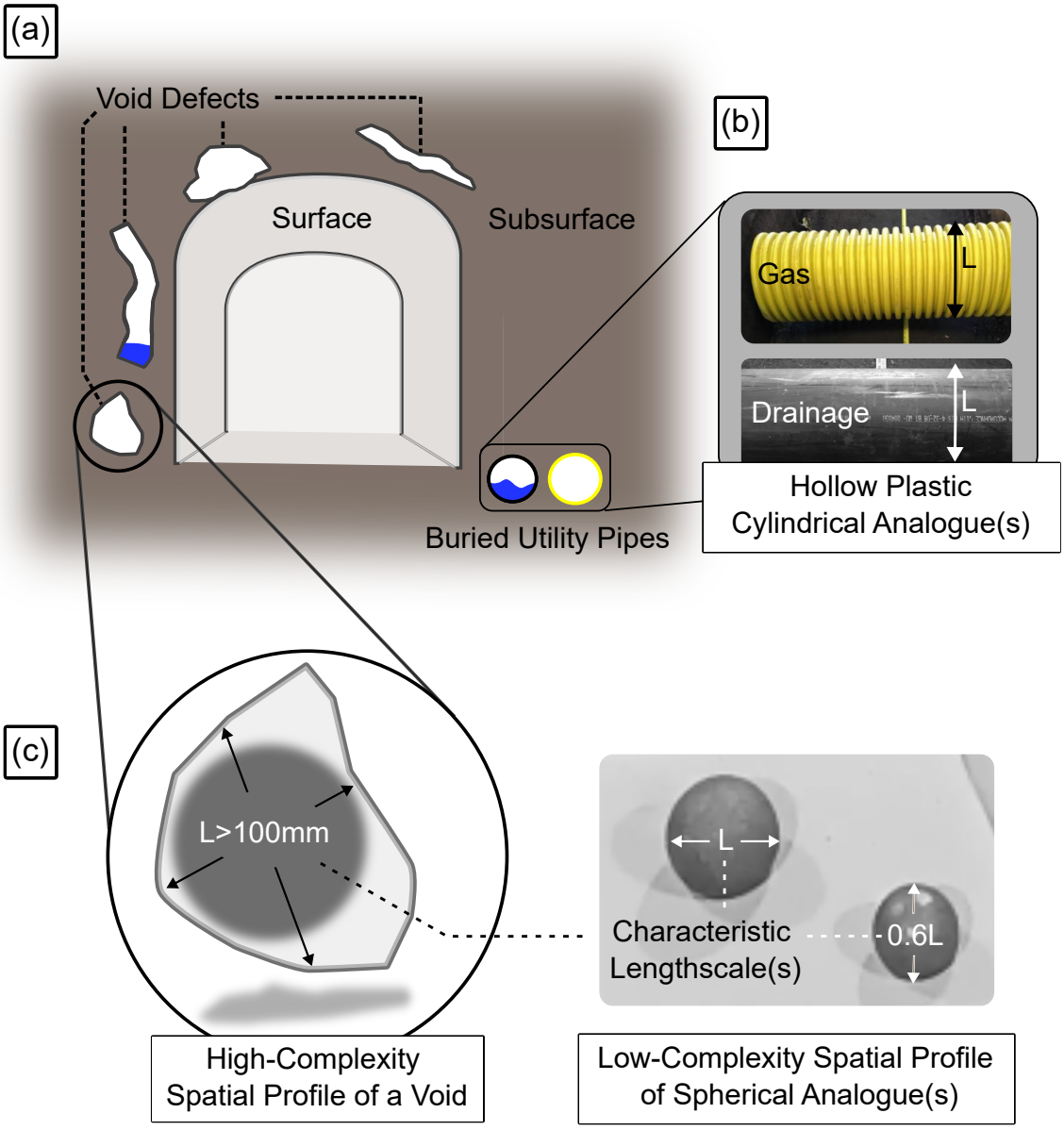


Figure 3.2: Visual overview of subsurface structural anomaly analogues for naturally occurring void defects (a). Considerations include hollow plastic utility pipes (b) and solid metallic spheres (c) exhibiting comparable characteristic length scales.

Qualitatively, accurate localisation would consider observed visual agreement between the 3D spatial footprint of clusters with corresponding ground-truth geometry.

Quantitatively, the 'position' of a 3D profile would be defined by its mid-centre, here defined as the arithmetic mean of a profile's centre of mass (i.e. centroid) and the central coordinate of its associated bounding box.

Assessments would also be based on datasets resembling cylindrical sectors, formed by parallel stacking rotational transects spanning less than a full rotation. Through a rotational symmetry argument — assuming isotropy of the enclosed environment — findings could be generalised to an arbitrary subsurface region within the considered structure. Since the feasibility study had already demonstrated 360-degree subsurface coverage capability, this approach improved data collection efficiency, allowing greater focus on processing and performance analysis.

## 3.3 Proposed 3D Visualisation Workflow

This section presents the operational methodology, covering the theoretical foundation of the innovative 3D visualisation workflow this thesis develops for hybrid-rotational GPR. It fundamentally serves as the basis for performance evaluation in all subsequent chapters.

The workflow is based on a modular architecture, as outlined in Section 3.3.1. The following sections break down its three main phases: Section 3.3.2 covers input data extraction, 3D spatial alignment, and pre-processing for data quality enhancement; Section 3.3.3 addresses grid regularisation and post-processing, while Section 3.3.4 details segmentation and rendering.

The full numerical implementation can be found in Appendix A.

### *3.3.1 High Level Overview*

As an emerging technology, the development of a 3D visualisation workflow for hybrid-rotational GPR represents a novel endeavour. The complete proposed architecture is shown in Figure 3.3. The design of this workflow draws inspiration from the architecture of GPRPy [304], which represents a key state-of-the-art open-source software for GPR data processing, based on the literature reviewed in the previous chapter.

Akin to GPRPy, the workflow developed in this research is built on a Python foundation to enhance accessibility for emerging researchers. It also incorporates a modular top-level architecture, based on vectorised arithmetic, enabling efficient switching and augmentation of distinct process chains for each data capture technology.

This design improves scalability, particularly for handling large datasets from full-scale transport infrastructure surveys. However, it should be noted that the GPRPy workflow is primarily geared towards the visualisation and enhancement of 2D transects, with a focus on datasets from widely-used GPR systems such as MALA (`.rad/.rd7`) [305], GSSI (`.dtz`) [306], and Sensors & Software (`.dt1`) [307].

In contrast, the newly developed workflow for hybrid-rotational GPR, presented in this section, focuses on the direct recovery of 3D spatial profiles and is tailored to support input data formats from gprMax simulations (`.out/.hdf5`) [297], Zond 12e Advanced GPR system Prism2 exports (`.sgy`) [308], and VNA-based hybrid-rotational GPR systems (`.s1p`) [309].

Further novel attributes of the developed 3D visualisation workflow include:

1. Dedicated subroutines for automating 3D spatial alignment of sample points, to alleviate highly involved manual placement (see Section 3.3.2).
2. An ETL pipeline[3] sub-architecture that consolidates grid regularisation, post-processing, segmentation, and rendering into a unified process chain, to increase tractability for future developers and reduce computational overhead for improved efficiency (see Section 3.3.3).
3. Synergistic integration of both isovalue and proximal-based clustering to increase 3D segmentation accuracy of subsurface anomalies (see Section 3.2.4).

### *3.3.2 Phase A – Data Extraction, Alignment and Pre-Processing*

As detailed in Figure 3.3 block (A), each GPR technology has a characteristic input file-type and associated data structuring convention, necessitating three independent process chains to efficiently handle data extraction.

Hierarchical Data Format Version 5 (`.hdf5`) files generated by gprMax store real-valued 3D Cartesian coordinates $\underline{x} \in \mathbb{R}^3$ and temporal amplitudes $A[t] \in \mathbb{R}$ for each sample point. Multiple trace files are natively merged into a single transect file by gprMax. This workflow also adopts `.hdf5` files for storage and retrieval of checkpointing data post-import and prior to rendering, to optimise trade-off between the human readability of ASCII text data and the compact size and rapid computation capability of binary file counterparts.

[3]ELT meaning 'Extract → Transform → Load' task sequence, or equivalently a 'converge-diverge' or 'hourglass' workflow, shaped (><).

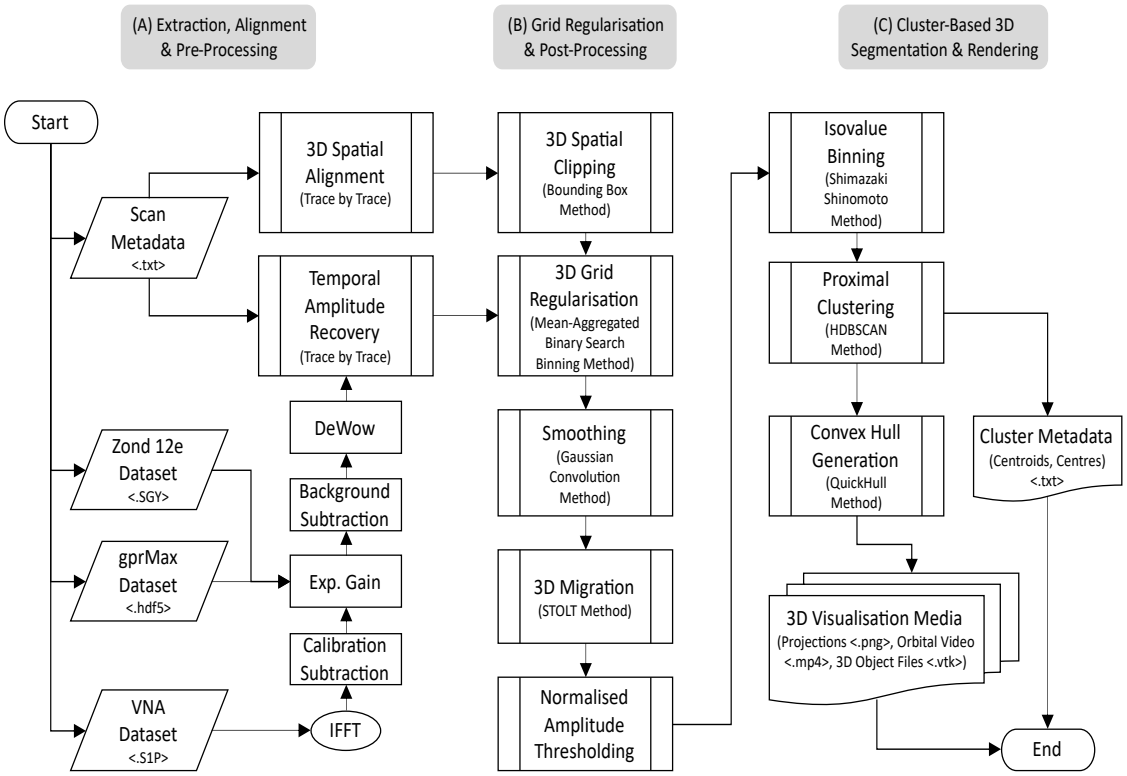


Figure 3.3: The developed end-to-end data processing workflow, based on a modular ELT-pipeline architecture. It is capable of efficiently recovering 3D visualisations of suspected subsurface structural anomalies from simulated, fixed-directional, and new hybrid-rotational GPR datasets.

Where the `h5py` module facilitates direct import of gprMax datasets, bespoke subroutines are required for spatial-temporal data extraction from fully binary `.sgy` transect data files generated by data capture software Prism2 — responsible for controlling the selected fixed-directional GPR system (see Chapter 5).

Further bespoke subroutines were required to recover spatial-temporal amplitude data from `.s1p` Touchstone files generated by the hybrid-rotational GPR systems' VNA unit, which directly records the complex amplitude response of backscatter in the frequency domain.

Using convolution theorem, temporal conversion first applies a Kaiser Bessel windowing filter $w$, which grants precise control of antenna lobe levels through a tuning parameter (here empirically defined $\alpha = 3$) to suppress spectral leakage artefacts from subsequent IFFT, which recovers the complex-valued temporal response. It is formulated:

$$w[n] = \frac{I_0\left(\pi\alpha\sqrt{1-\left(\frac{2n}{N}-1\right)^2}\right)}{I_0(\pi\alpha)}, \quad 0 \leq n < N, \tag{3.1}$$

where $n$ indexes one of $N$ sample points within a given amplitude trace $A[f] \in \mathbb{C}$, $I_0$ denotes the $0^{th}$ order modified Bessel function of the first kind and filter application in the frequency domain is performed by the matrix product $A_w[f] = wA[f]$. Finally, calibration subtraction is performed to suppress artefacts associated with backscatter events within the VNA measurement cable prior to signal emission from the antenna. Such events result from inherent cable flex as the antenna repositions between trace measurement. An ideal calibration response results from a full scanning pass with no targets of interest present (i.e. an empty RoI volume). Whilst possible in the laboratory, in practice unalterable RoI geometry necessitates a single, partial transect of a skyward directed antenna. Duplication by symmetry across the full scanning pass emulates the desired targetless RoI response.

Metadata files populated by the system operator also accompany each repository of input data, principally detailing: (i) parameters defining the scanning trajectory; (ii) RoI span $\underline{\mathrm{L}} = (L_x, L_y, L_z)$, and (iii) approximate relative electrical permittivity $\epsilon_r$ of the background media. For gprMax simulations and fixed-directional GPR, industry-standard 'area scan' trajectories are adopted, wherein the antenna tracks along a regular 3D rectilinear grid of orthogonally intersecting transects during a scanning pass. The rectilinear grid is defined by the number of rows and columns, alongside their associated spatial separations. Similarly for hybrid-rotational GPR, scanning trajectories follow a regular 3D curvilinear grid, shown in Figure 3.4.

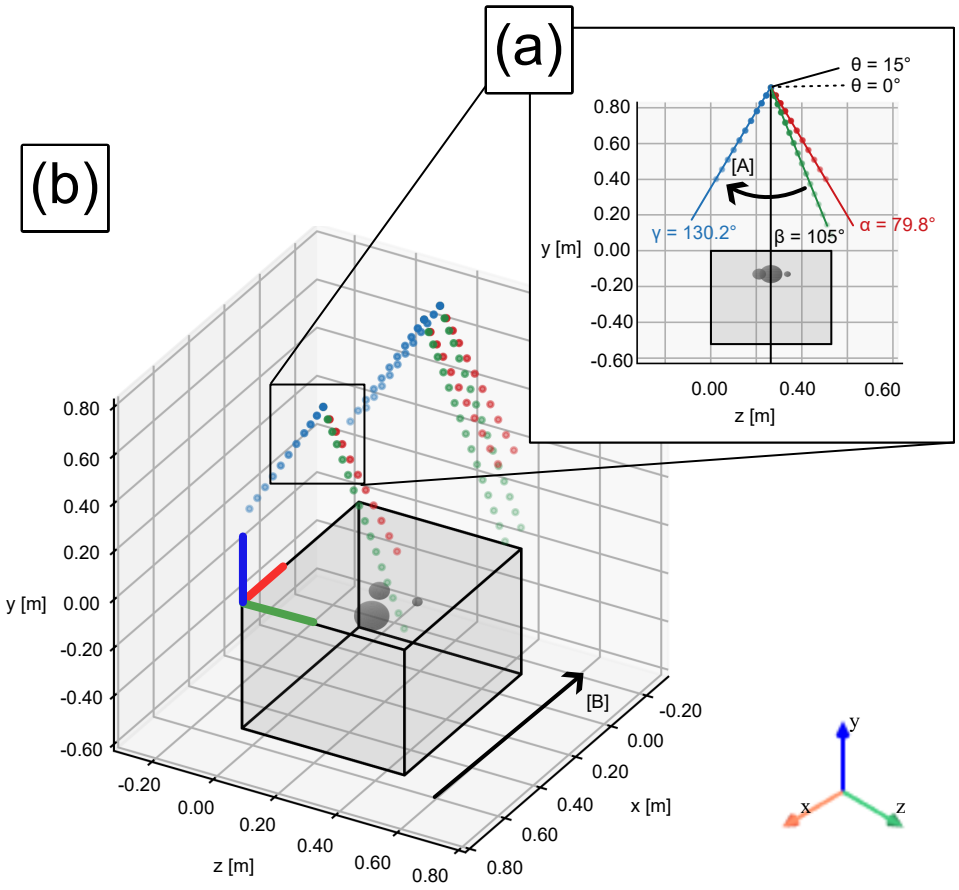


Figure 3.4: Aligning hybrid-rotational GPR data in 2D (a) and 3D (b). Individual sample points (dots) denote instantaneous amplitude measurements, which radially advance along straight lines mapped to the antenna boresight vector (decreasing opacity), forming traces. Successive trace orientations increment azimuthally along [A] between extremal limits $\alpha$ (red) and $\gamma$ (blue), generating rotational transects, which first intersect the RoI at $\theta = \beta$ (green). Successive transect planes increment laterally along [B].

Initial and final displacements of the antenna from the respective lateral and azimuthal datums ($x = 0$ and $\theta = 15°$) define the grid, alongside respective spatial incrementation along each axis. Additional required metadata includes: VNA cable length $L_0 = 5m$; antenna body length $L_1 = 0.222m$; and downward orientation lift-off from the RoI contact surface, $L_2(\theta = \beta) = 0.69m$, necessary to define the multilayered model for estimating radial displacement of the air-launched system.

Performing 3D spatial alignment of sample points is equivalent to defining displacement of a sample point along the antenna boresight vector, which extends radially outward from the midpoint of the antenna aperture. For area scan trajectories, this reduces to locating the midpoint of the bistatic antenna and monotonically increasing the vertical coordinate ($y$) of successive samples along a trace. Note that antenna lift off from the contact surface is negligible, therefore the conversion from a sample's two-way sample travel time $t$ to vertical depth follows the single layer model,

$$y[t] = \frac{vt}{2} = \frac{c(n\Delta t)}{2\sqrt{\epsilon_r}} \in \mathbb{R}_{\geq 0}, \quad 0 \leq n < N \tag{3.2}$$

subject to localised heterogeneity of the RoI media. Here, $c$ denotes speed of light in a vacuum, $v$ is the estimated GPR wavefront propagation velocity and $\Delta t$ is the discrete time step between successive sample measurements.

Defining the radial displacement of hybrid-rotational scan trajectories is more involved. A multilayer model is required to accommodate variable signal propagation speeds between the (i) VNA and antenna base; (ii) antenna base and aperture; (iii) aperture and RoI contact surface and (iv) within the RoI. The formulation for sample point displacement $l \geq 0$ from the VNA is given by,

$$l[t, \theta] = \frac{c}{2} \begin{cases} t\left(\sqrt{\epsilon_{r_0}}\right)^{-1} & \text{, if } 0 \leq t \leq t_0 \\ l[t_0] + (t - t_0)\left(\sqrt{\epsilon_{r_1}}\right)^{-1} & \text{, if } t_0 < t \leq t_1 \\ l[t_1] + (t - t_1)\left(\sqrt{\epsilon_{r_2}}\right)^{-1} & \text{, if } t_1 < t \leq t_2[\theta] \\ l[t_2] + (t - t_2)\left(\sqrt{\epsilon_{r_3}}\right)^{-1} & \text{, if } t \geq t_2[\theta] \end{cases} \tag{3.3}$$

where $\epsilon_{r_i}$ for $i \in [0, 1, 2, 3]$ denotes the relative electrical permittivity of regions (i)-(iv) respectively, $t_0 \in \mathbb{R}_{\geq 0}$ and $t_1 \in \mathbb{R}_{\geq 0}$ are the expected arrival times at the antenna base and aperture respectively and $t_2[\theta]$ is the expected arrival time at the contact surface, noting contact surface lift off is dependent on the azimuth of the antenna boresight vector.

Contact surface lift off can be defined as,

$$L_2(\theta[n]) = \frac{L_1 + L_2(\beta)}{\cos(\beta - \theta[n])}, \quad 0° < \alpha \leq \theta \leq \gamma < 180°, \tag{3.4}$$

where $\alpha$ and $\gamma$ are the initial and final azimuths spanned in a single rotational transect — see Figure 3.4a.

A further coordinate transform is required to map $l$ to radial displacement $r$ from the centre of antenna rotation, approximately located at the antenna base. Namely:

$$r[t] = \begin{cases} NaN & \text{, if } l[t] < l[t_0] \\ l[t] - l[t_0] & \text{, if } l[t] \geq l[t_0] \end{cases} \tag{3.5}$$

where `NaN` denotes a 'non-value' associated with sample points with ill-defined radial displacement (i.e. within the VNA connector cable). Concatenation with associated azimuthal and lateral displacements yields sample point 3D transverse cylindrical polar coordinates $\underline{\tilde{x}} = (r, \theta, \tilde{x})$, which are converted to required Cartesian coordinates $\underline{\mathrm{x}} = (x, y, z)$ by,

$$\begin{aligned} x &= \tilde{x} \\ y &= -r\cos(\theta) \\ z &= r\sin(\theta) \end{aligned} \tag{3.6}$$

To further map trajectories to global coordinates (defined at the datum marker of the RoI, see Figure 3.4), sum $\underline{\mathrm{x}}$ with the initial position coordinates $\underline{\mathrm{x}}_0 = (x_0, y_0, z_0) \in \mathbb{R}^3$ of the antenna, noting in this study $x_0 = 0.325m$, $y_0 = L_1 + L_2(\beta) = 1.21m$ and $z_0 = L_z/2 = 0.265m$.

Pre-Processing enhances and de-noises temporal amplitude responses to maximise clarity of subsurface anomalies. First, a time variable gain filter is applied to compensate for attenuation of the propagating wavefront. The developed module facilitates power gain ($G[t] \propto t^a$ where $a \in \mathbb{R}$) and exponential gain ($G[t] \propto e^{at}$). This study uses exponential gain, setting $a = 1$ to align with expected exponential decay typical of EM signal propagation. Background subtraction follows, which subtracts the mean average global trace response (across the *full* 3D domain) from each individual trace. This suppresses horizontal artefacts (e.g. airwaves) and systematic background targets (e.g. RoI volume housing) from the final visualisations.

Lastly, dewow is applied. Here, the mean average response of each *individual* trace is subtracted from itself, serving as an effective low-cut filter, which suppress low frequency noise components potentially associated with antenna resonation, minor power supply fluctuations or mechanical vibrations from the automated positioning systems (where utilised).

### 3.3.3 Phase B – Grid Regularisation and Post-Processing

As detailed in Figure 3.3 block (B), grid regularisation and post-processing operations are performed prior to volume clustering. GPR signal emissions are intrinsically conic profiles extending out from the antenna boresight vector, which scatter on interaction with the subsurface [4]. The conic form results in a moving GPR antenna detecting backscatter from a target slightly prior, during and slightly after the boresight vector directly intersects a target. This results in distorted geometric profiles, which at a base level converts an idealised point target into a hyperbolic hemisphere in 3D aligned measurement data. Recovering more faithful 3D spatial profiles necessitates the application of 3D migration, here based on the Stolt method for maximal tractability and scalability at this stage of visualisation development.

As a penetrative technology, the GPR signal naturally extends beyond the confines of the RoI, particularly at the extremal azimuthal limits of the hybrid-rotational GPR transects. To maximise computational efficiency, sample points residing outside the end-user RoI are purged by defining an RoI bounding box and clipping the sample point array (using Python's masked index slicing). This inherently truncates traces, transforming the data into an irregular grid[4]. Stolt migration implicitly assumes sample points reside on a regular rectilinear grid, warranting grid regularisation. 3D interpolation is a natural solution, but even without up sampling, computational runtime of a small $0.25m^3$ volume on a commercial grade PC proved impractical on such high-density datasets. High sample point density renders interpolation unnecessary; a more resource-efficient approach is 3D grid regularisation by mean aggregated binary search binning, exploiting vectorised operations and the `digitize()` module. To avoid unnecessary up sampling, symmetry of scanning trajectories is exploited to define the bin count, which is set to the number of unique sample points per axis.

Edge artefacts and over fitting can potentially arise from aggregated binning, and high frequency noise associated with subsurface heterogeneity can remain prevalent even post-binning, motivating subsequent application of a Gaussian Smoothing filter. Since the RoI geometry represents a finite sample of an assumed 'infinite' measurement domain (i.e. the full transport infrastructure subsurface) periodic boundary conditions are selected for implementation of the smoothing kernel.

Stolt migration follows, implemented using a bespoke Python module adapted from the CREWES Matlab Toolbox [310]. First, IFFT transforms the 3D spatial-temporal response field to the frequency domain, governed by signal wave number ($\underline{k}$) and angular frequency ($\omega$).

[4] In gprMax datasets, further irregularity stems from numerical truncation of trace position coordinates (which must be divisible by Yee Cell resolution).

It is reasonable to assume frequency-associated phase shifts can and will occur in any direction within an arbitrary RoI. This motivates selection of the isotropic 3D spatially dependent operator,

$$m = e^{-i\omega}, \quad \text{with } \omega = ||\underline{\mathrm{k}}||. \tag{3.7}$$

Wave number grids are generated using Python's `meshgrid()` functionality for computational efficiency, and operator is applied by convolution theorem and returned to the spatial-temporal domain by Fast Fourier Transform (FFT).

Post-processing operations follow migration. First, as migration must accommodate potential complex input amplitudes (from VNA datasets), resultant FFT yields complex amplitude responses irrespective of utilised technology. For simulated and fixed-directional datasets, this is attributable to truncation error during the discretised IFFT and FFT operations, which introduces negligible but non-zero imaginary components to FFT output. The absolute magnitude is taken to recover observable the 3D response profile.

Normalisation follows to standardise amplitude response profiles ahead of isovalue recovery, mapping magnitudes $A \rightarrow \tilde{A}[\underline{\mathrm{x}}] \in [0, 1]$ whilst preserving the distribution. Finally, thresholding is applied to eject sample points not associated with suspected anomalies. The lower limit $A = 0.5$ is heuristically selected, representing a natural partition between 'weak' backscatter events ($0leqA < 0.5$) and 'strong' backscatter events ($0.5 \leq A \leq 1$). Noting that direct arrival wavefronts, resonating reflections off the RoI contact surface and residual internal backscatter events within the VNA cable not fully suppressed by calibration subtraction could still be present in response field, an upper threshold is also introduced to prevent such backscatter events dominating the domain. The default value $A = 0.8$ is also heuristically selected, providing adequate separation from $A = 1$ for iterative refinement, if required.

### *3.3.4 Phase C – Cluster-Based 3D Segmentation and Rendering*

As detailed in Figure 3.3 block (C), the recovery and rendering of 3D spatial profiles of suspected subsurface anomalies is the final stage of the proposed visualisation workflow.

This problem can be subdivided into: (i) segmentation of suspected anomalies into sample point subsets; (ii) recovery of 3D convex hulls from segmented sample point subsets.

Recalling that a subsurface structural anomaly exhibits 'significant' discrepancy from GPR signal responses in the immediate vicinity, 'significant' anomalies inherently backscatter larger proportions of incoming GPR wavefronts, due to:

- Close proximity to the surface, representing a considerable breaching risk, which is therefore a high inspection priory for surveyors.
- Considerable volume, thereby at risk of undermining the integrity of healthy structural elements in the immediate vicinity.
- Highly reflective material composition (e.g. metallic targets, such as utilities and other non-natural elements) often added by humans during infrastructure construction and of surveyor interest for health monitoring.
- One or more of the above.

As such, segmentation seeks strong backscatter events. This is achieved in part by the aforementioned amplitude thresholding. Moreover, amplitude variation due to penetrative depth variation has been suppressed via gain filtering and anomaly spatial profiles. It is therefore reasonable to assume sample points belonging to the same anomaly exhibit comparable backscatter amplitudes at this stage of the workflow, motivating segmentation by amplitude isovalue. Furthermore, sample points belonging to the same anomaly must also be in 'close' relative proximity, motivating segmentation by proximal clustering. As a result, the proposed workflow implements an integrated approach, utilising both Isovalue Binning and Hierarchical Density-Based Spatial Clustering of Applications with Noise (HDBSCAN) [311].

Isovalue binning partitions thresholded sample point amplitudes into $M$ mutually exclusive bins. The developed module facilitates computation of $M$ through computation of optimal bin width $K$, either by explicit definition, the Freedman-Diaconis Rule [312] or the Shimazaki Shinomoto method [313]. The approaches are considered for their tractability, numerical efficiency and robustness to outliers and skew respectively, apt for anticipated heterogeneity and erratic spatial profiles of more realistic anomalies in GPR surveys.

The Freedman-Diaconis Rule estimates bin width proportional to the Interquartile Range (IQR) of the threshold amplitude data $A_{IQ}$, given by:

$$K = \frac{2A_{IQ}}{\sqrt[3]{N_S}} = \frac{2(A_{0.75} - A_{0.25})}{\sqrt[3]{N_S}}, \tag{3.8}$$

where $N_S$ here denotes the total number of sample points the amplitude thresholded dataset, with $A_{0.75}$ and $A_{0.25}$ shorthands for the upper and lower quartiles, respectively.

This technique is designed to be robust against outliers and skew, however, can potentially lead to under/over smoothing of the isovalues if data is highly spread or multimodal. As thresholding forcibly limits data spread, robustness against multimodality is more pertinent in this work, as more than one anomaly can easily be present in an arbitrary RoI. A more suitable computation is the Shimazaki Shinomoto method, which instead minimises the Mean Integrated Square Error (MISE) of the thresholded amplitude data improving performance on multimodal datasets. The computation defines the range $R = \max(A) - \min(A)$, candidate bin count values $m \in [0, M] \in \mathbb{Z}_{\geq 0}$ and associated candidate bin width $k = R/m$, alongside the MISE cost function,

$$C[h] = \frac{2\bar{k}_m - \sigma^2_{k_m}}{h^2} \tag{3.9}$$

which computes MISE for each candidate bin count, returning $m$ for minimal MISE output.

Here,

$$\begin{aligned} \bar{k_m} &= (1/m) \sum_{i=0}^{m-1} k_i \\ \sigma^2_{k_m} &= (1/m) \sum_{i=0}^{m-1} (k_i - \bar{k})^2 \end{aligned} \tag{3.10}$$

are the mean average number of sample points per bin and associated variance, respectively.

Proximal clustering of isovalue bin contents follows, based on the HDBSCAN method — now an integrated component of the `sklearn` module for Python. HDBSCAN is an extension of the DBSCAN (Density-Based Spatial Clustering of Applications with Noise) method to handle clusters of variable sample point densities. The $D$ dimensional HDBSCAN algorithm is detailed in [311]. Breakdowns provided in [314] and [315] provide further details considered beyond the scope of this work, alongside intuitive illustrations of key concepts including mutual reachability, spanning tree formation and dendrograms which underpin the stability metric. Here a brief overview is provided for $D = 3$. First, the mutual reachability graph of all points in the sample domain is computed, defined between two arbitrary sample points $\underline{\mathrm{x}}_i$ and $\underline{\mathrm{x}}_j$ to be:

$$D_m[\underline{\mathrm{x}}_i, \underline{\mathrm{x}}_j] = \max\left[core_k[\underline{\mathrm{x}}_i], core_k[\underline{\mathrm{x}}_j], d(\underline{\mathrm{x}}_i, \underline{\mathrm{x}}_j)\right], \tag{3.11}$$

where $d(\underline{\mathrm{x}}_i, \underline{\mathrm{x}}_j)$ is the Euclidean distance between the considered points and $core_k(\underline{\mathrm{x}})$ denotes the $k^{th}$ nearest neighbour of sample point $\underline{\mathrm{x}}$, recovered from a pre-computed Minimum Spanning Tree (MST) by the KD-tree or Ball-tree methods (subject to context).

The minimum number of samples points per cluster ($\hat{N}_\Omega$) is an explicitly defined parameter which sets $core_k(\underline{x}) \to \infty$ to highlight a feasible cluster as underpopulated. Recursive removal of the longest MST edge forms a dendrogram (i.e. hierarchy) of feasible clusters. Key clusters exhibit the longest 'lifetimes' between first and last occurrence in the dendrogram[5]. The stability metric of a cluster $\Omega$ is defined,

$$Stability(\Omega) = \sum_{\underline{x} \in \Omega} \left( \frac{\lambda_{birth}(\Omega) - \lambda_{death}(\Omega)}{\alpha} \right) \tag{3.12}$$

where $\lambda_{birth}$ and $\lambda_{death}$ denote the respective levels in the dendrogram at which cluster $\Omega$ appears and disappears respectively, and $\underline{x} \in \Omega$ are the sample points within the cluster of interest. Here $\alpha$ is a cluster granularity tuning parameter, when $\alpha > 1$ larger clusters become more stable, granularity reduces, and macroscopic structures are better highlighted. Reducing $\alpha < 1$ destabilises larger clusters, granularity increases, and microscopic structures are better highlighted. As output, underpopulated clusters are flagged as noise and a hierarchy of feasible clusters is returned prioritised by the stability score. The centroid coordinate (i.e. mass centre) of a feasible cluster $\Omega_c \in \mathbb{R}^3$ containing $N_\Omega$ sample points is in turn given by,

$$\Omega_c = \frac{1}{N_\Omega} \left( \sum_{i=0}^{N_\Omega - 1} x_i, \sum_{i=0}^{N_\Omega - 1} y_i, \sum_{i=0}^{N_\Omega - 1} z_i \right). \tag{3.13}$$

Having identified feasible clusters for each binned amplitude isovalue, the final 3D visualisation is generated using the `pyvista` module [316]. Renders of point subsets as interactive 3D objects requires generation of convex hull meshes for each feasible cluster. This is achieved using `ConvexHull()` from the `SciPy` module [317], based on the QuickHull Method (now packaged as the Qhull library) [318]. For the purposes of this study, regard the high-level 3D interpretation to be analogous to shrinking a balloon over the point set, which stabilises at the minimum bounding volume defined by the points on the outermost boundary of the subset. From recovered meshes for simulated, fixed-directional and hybrid-rotational GPR datasets, the developed visualisation workflow can export:

- Orbital animations (`.mp4` and `.gif`);
- 2D planar/isometric projections (`.svg`, `.pdf`, `.png`);
- Interactive 3D object files (`.vtk`,`.ply`,`.obj`,`.stl`).

[5] A cluster is 'born' when branches of the dendrogram join together, and 'dies' when it merges with another cluster or subsequently subdivides.

## 3.4 Summary

This chapter provided a detailed breakdown of the strategic and operational methodology underpinning research presented in this thesis.

The rationale for the sequential structuring of investigations — split across laboratory benchmarking and later field tests — was to provide insight into the performance efficacy of the proposed 3D visualisation workflow when applied to progressively more authentic GPR survey data for subsurface inspection of transport infrastructure. This was achieved through the sequential application of the workflow to datasets obtained from simulated, practical fixed-directional, and ultimately practical hybrid-rotational GPR systems during laboratory benchmarking, followed by its application to hybrid-rotational GPR datasets recorded from large-scale structural analogues in later field testing.

Exploration of the strategic methodology rationale highlighted three key priorities considered during the planning stages of the research. First, the focus was placed on the 3D visualisation of hybrid-rotational GPR data rather than optimising helical transect scan parameters.

This prioritisation was based on the understanding that effective optimisation required insight from changes observed in returned visualisations, which made development of an effective data processing workflow capable of returning such 3D output a pre-requisite.

Second, practical investigations using hybrid-rotational GPR were prioritised over simulation-based approaches. This was the more pragmatic approach, given the complexities involved in simulating EM-propagation for a rotating antenna. Additionally, this approach facilitated the development of refined physical data collection equipment, which could serve as a foundation for the next generation of hybrid-rotational GPR technology. Where developments concerning such simulations offered more limited practical applications for researchers and practitioners, an emphasis on practical investigatory work provided immediate relevance, critically with more direct applicability to deployment of hybrid-rotational GPR technology in practical surveys of transport infrastructure.

Another key consideration was the emphasis on specific criteria identified in the previous chapter for analysing the performance of the developed workflow. Efficient data processing and collection, along with the generation of high-fidelity 3D outputs, were recognised as the most pertinent criteria to underpin performance analysis in subsequent investigations.

The strategic methodology further justified the use of solid metallic spheres as analogues for subsurface structural anomalies in the ground-truth geometry for performance analysis of the proposed 3D visualisation workflow. This choice was motivated by established practices in similar leading studies and the practical challenges associated with accurately incorporating hollow voids into physical subsurface volumes while maintaining precise knowledge of ground-truth geometry.

A refined focus on targets characterised by decimetre length scales was justified through consultations with structural engineers and by considering the characteristic length scales of the bricks used in the masonry of historic tunnels and transport infrastructure in the UK.

The operational methodology provided a detailed deconstruction of the theoretical framework underlying the proposed 3D visualisation. It innovatively utilised a modular architecture to enhance versatility in processing input datasets from simulated, fixed-directional, and hybrid-rotational GPR systems. Additionally, the framework was built on matrix-based operations to ensure high computational efficiency.

In the primary phase, after extracting initial data using windowed IFFT (when applicable), a custom multi-layer model ensured accurate spatial alignment of sample points in 3D. This was followed by applying exponential time-varying gain, background subtraction, and dewow operations to address signal attenuation and reduce noise, thereby enhancing the clarity of the temporal response profiles. In the secondary phase, the mean-aggregated binary search binning method was employed for efficient grid regularisation. This facilitated subsequent Gaussian smoothing, 3D Stolt migration, and amplitude thresholding, which further refined the encoded target profiles.

The final phase involved a novel approach for segmentation and rendering, combining isovalue binning (based on the Shimazaki-Shinomoto method) with proximal HDBSCAN clustering and the QuickHull method. This combination facilitated the direct recovery of high-fidelity convex hulls to convey the 3D spatial profiles of suspected subsurface structural anomalies.

# Chapter 4. Benchmarking I – GPR Numerical Simulation

In this chapter, the efficacy of the proposed 3D visualisation workflow is validated on an idealised, numerically simulated GPR dataset. To achieve this, a bespoke algorithm is developed for gprMax area scan functionality.

## 4.1 Introduction

The first stage of laboratory benchmarking was to numerically implement the proposed workflow and establish whether it returned 3D spatial profiles aligned with pre-established subsurface geometry. As a validation test, both the achievable levels of visualisation fidelity and the workflow's computational performance were examined. Accurate detection and localisation of known targets would demonstrate high fidelity, while consistent short-duration data processing runtimes would indicate computational efficiency.

## 4.2 Motivation

Numerically simulated GPR data formed the basis of the investigation. It was used to ensure absolute knowledge of subsurface composition, alongside target placements and dimensions, providing a reliable baseline for assessing spatial profile accuracy. This approach also minimised environmental variability and human error (e.g. scan trajectory deviations), ensuring result reproducibility and delivering an 'idealised' survey scenario.

State-of-the-art software gprMax [297]was utilised due to its widespread adoption across encountered literature [319–321] and its open-source design.

Unlike proprietary alternatives (such as GPRSIM [296]) gprMax permitted the addition of modifications to implement area scan functionality, despite lacking native support.

However, being optimised for modelling standalone transects in a 3D volume, developing such an area scan algorithm for gprMax would require automation, as manually updating scan trajectories between successive simulations was found to be highly impractical and frequently introduced human errors (e.g. mistakenly overwriting files).

## 4.3 Aims and Objectives

The primary aim of this investigation was to validate that the proposed visualisation workflow returned 3D spatial profiles consistent with the established ground-truth geometry of an idealised gprMax area scan simulation, and within a reasonable timescale. Development of an effective algorithm to simulate area scans was an essential prerequisite.

Objectives for this investigation were:

1. To augment native transect simulations in gprMax to facilitate area scan functionality.
2. To generate a numerically simulated area scan dataset for a subsurface volume devoid of target geometry, for use in background calibration.
3. To generate a similar numerically simulated area scan dataset for a subsurface volume containing established target geometry.
4. To numerically implement the proposed 3D visualisation workflow in Python, and return 3D spatial profiles of anomalies within the subsurface volume(s).
5. To quantitatively analyse target detection and mid-centre localisation accuracy, alongside data processing runtime, to gauge the effectiveness of workflow performance.

## 4.4 Experimental Setup and Methods

This section details the setup and numerical implementation of fixed-directional GPR simulation in gprMax. Selected ground-truth geometry is detailed in Section 4.4.1, followed by a breakdown of computational hardware and specification in Section 4.4.2. Selected simulation parameters are summarised and discussed in Section 4.4.3 before the design and numerical implantation of a dedicated algorithm for automated area scan functionality in gprMax is detailed in Section 4.4.4.

### *4.4.1 Setup – Ground Truth Geometry*

Three spherical solid metal spheres emulated subsurface structural anomalies for detection and localisation within the simulated subsurface RoI volume. The inclusion of multiple targets served to test that the developed 3D visualisation workflow was capable of localising multiple anomalies occupying the same RoI volume, and accurately segmenting their independent physical spatial profiles.

The choice to use exactly three targets at this early stage of workflow development — prior to field testing — was multifaceted. Three targets allowed the workflow to segment multiple distinct targets whilst maintaining manageable levels of signal backscatter and interference from these strong reflectors. This helped to mitigate the risk of oversaturating the measurement domain, which could have inadvertently skewed conclusions about the performance of the proposed workflow. By choosing more than two targets, this also afforded greater variation in the characteristic length scales of targets, which offered greater insight into the workflow's resolution limits.

The spheres $S_{1-3}$ had diameters of 100mm, 60mm and 30mm, respectively. The largest sphere represented a structural anomaly with the same characteristic length scale associated with the assumed threshold for maintenance intervention, as outlined in the previous chapter. This selection was informed by the physical availability of spherical targets, which beneficially closely aligned with initially desired diameters of 100mm, 50mm, and 25mm. By recursively halving the characteristic length scale of each successive target, this would allow the limits of the workflow's resolution to be examined in a more systematic manner.

The relative placement of each sphere within the simulation domain is detailed in Figure 4.1. To reduce the risk of interference artifacts associated with the boundaries of the simulation domain, target placement was selected to ensure that the extremal interface of each sphere was a minimum separation of at least one and a half times the diameter of the largest sphere in the simulation (i.e. 150mm) from the region marketing the absorbing boundary. Symmetric placement about the centre of the RoI volume's lateral footprint was also ensured. By placing each target in a separate quadrant of the XZ plane, this more readily facilitated 'at-a-glance' association between known target geometry and returned visualisations during subsequent analysis.

In terms of vertical placement, all target mid-centres were at the same depth, 0.13m below the contact surface. This was within the RoI associated with the principal layers of masonry within a typical tunnel (see Chapter 2) which maintained contextual relevance with the visualisation of structural anomalies within masonry infrastructure. This choice of depth also provided a practically reproducible geometry setup for subsequent physical laboratory benchmarking in later chapters, as deeper target placement would have required highly impractical excessive quantities of backfill to be removed from a counterpart physical RoI volume.

The subsurface RoI volume was a homogeneous cuboid with relative electrical permittivity $\epsilon_r = 5$, which emulated the dry clay that characterises historic masonry infrastructure (see Section 5.4.1). The RoI volume laterally spanned 0.42m by 0.42m and extended vertically over 0.4m. This represented the largest volume for which the requisite area scans (see Section 4.4.3) could be practically simulated. Attempts to increase the maximal size of the RoI volume by partitioning simulations into smaller quadrants were undertaken, but proved highly involved, which motivated the direct simulation of a single RoI volume.

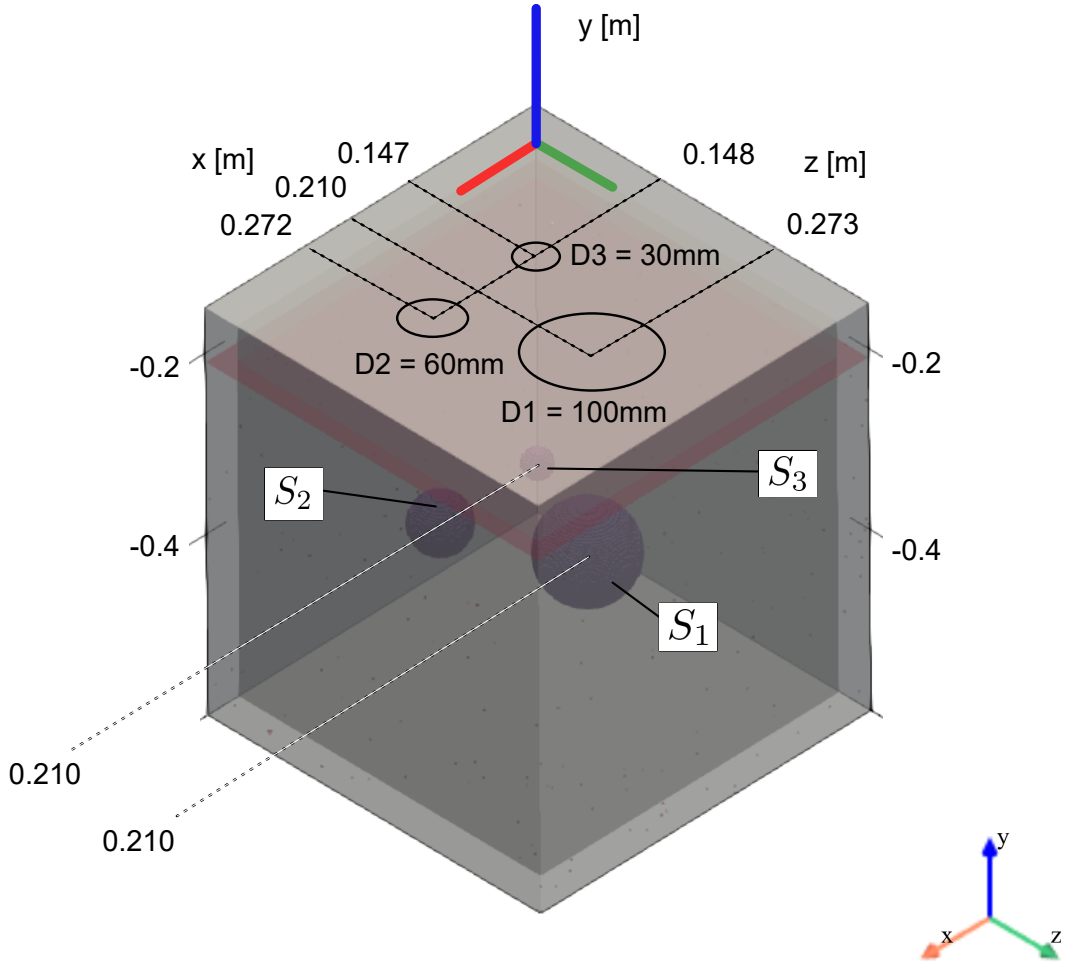


Figure 4.1: Paraview 3D render of ground-truth geometry for area scan simulation in gprMax. The contact surface (red plane) is directly above the subsurface RoI volume (dark grey region) surrounded on all sides by the absorbing boundary (light grey regions) of the global simulation domain.

Collective ground-truth geometry was generated using the native `Sphere()`and `Box()`input commands for gprMax respectively, during generation of the `.in` configuration files for each individual transect simulation.

In accordance with the national convention adopted by gprMax, the global coordinate system aligned the x-axis to the longest side of the RoI volume, which extended outward for $x > 0$. The y-axis was associated with target depth, extending downward into the subsurface for $y < 0$. The z-axis was defined orthogonal to both, extending outward from the origin for $z > 0$. The global origin was defined at the upper vertex of the subsurface RoI volume — see Figure 4.1.

### *4.4.2 Setup – Computational Hardware and Specifications*

All numerical simulations and executions of the proposed 3D visualisation workflow were conducted on a Dell Precision 3600 desktop PC, equipped with Windows 11 Pro, Python 3.10.3, and a Gen-13 Intel Core i7-13700 (2100MHz) 16-core CPU with 24 logical processors, 32GB of RAM, and a 1TB solid-state drive. The Windows Subsystem for Linux was also enabled, which provided a virtual Linux environment that facilitated the automation of gprMax simulations via the execution of `.sh` batch files.

Simulations were performed using gprMax v3.1.6, for which content stored in output data files was directly inspected using freeware HDFViewer v3.1.1 when required. Programming for area scan functionality in gprMax and development of the 3D visualisation workflow was exclusively performed in Microsoft Visual Studio Code v1.92.2. The recovery of 3D geometry renders associated with simulation ground-truth geometry were recovered using freeware Paraview v5.11.1, supported by custom parameter extraction macros supplied with gprMax.

The consumer-grade equipment specified above underpinned all experimental procedures and analysis presented in this thesis. Additional specialist hardware and trials of alternative programming environments are explicitly detailed where relevant.

### *4.4.3 Setup – Simulation Parameters*

Parameter settings adopted in gprMax for numerical simulation of the fixed-directional GPR area scan are summarised in Table 4.1.

The global simulation domain extended 0.42m laterally along both the x-axis and z-axis, with a vertical depth of 0.45m along the y-axis. This configuration encompassed the previously defined subsurface RoI volume and also included a recommended 10 cell buffer on all sides.

| Parameter | Description | Value | Units |
|---|---|---|---|
| - | Antenna type. | Hertzian Dipole | - |
| - | Associated radiation pattern. | Toroidal (3D). | - |
| $F_w$ | Transmission antenna waveform type. | Ricker | - |
| $F_p$ | Transmission antenna waveform polarity. | $z$ | - |
| $F_c$ | Transmission antenna centre frequency. | 1.75 | GHz |
| $N_s$ | Number of samples per trace. | 1300 | 1 |
| $N_A$ | Number of traces per transect. | 51 | 1 |
| $N_{B_0}$ | Number of area scan grid rows (in $z$). | 51 | 1 |
| $N_{B_1}$ | Number of area scan grid columns (in $x$). | 51 | 1 |
| $\Delta B_0$ | Area scan gird row separation. | 6.098 | mm |
| $\Delta B_1$ | Area scan grid column separation. | 6.098 | mm |
| $T$ | GPR trace duration. | 5 | ns |
| $L$ | Lift-off distance from contact surface. | 2 | mm |
| $\Gamma$ | Transmitter/receiver antenna separation. | 40 | mm |
| $(dx, dy, dz)$ | Simulation spatial resolution. | 2 | mm |

Table 4.1: Numerical simulation parameters.

The buffer provided sufficient clearance from the absorbing boundaries to minimise the likelihood of artificial boundary-related artifacts manifesting in the returned data. It was also necessary to incorporate a region of free space above the contact surface sufficiently deep to accommodate the antenna elements. Therefore, an additional 10 cells of free space were incorporated to match the recommended clearance for the absorbing boundary.

Scan parameters were based on the configuration recommended in [322], which informed the selection of: (i) a hertzian dipole antenna (plus its associated element separation); (ii) approximately 50 traces per transect across an RoI spanning 0.25m; (iii) waveform type and polarity.

The dipole configuration consisted of a single transmitter-receiver pair, each represented by a single simulation cell and positioned directly above the RoI contact surface. It exhibited a toroidal radiation pattern, characterised by an azimuthally symmetric double-lobe in the E-plane (aligned with the XY plane in gprMax), with nulls parallel to the contact surface. Following a $\sin^2(\theta)$ dependence, the broad radiation pattern exhibited a maximum directivity of approximately 1.76dBi.

A trace duration of 5ns was selected to provided sufficient two-way travel time for these signals to propagate through the full RoI volume during individual trace simulations, which required traces to be comprised of 1300 individual sample points.

The Ricker waveform was characterised by significant frequency components up to approximately $f = 4\text{GHz}$, with associated wavelengths of,

$$\lambda = \frac{c}{f\sqrt{\epsilon_r}} \approx 34\text{mm}, \tag{4.1}$$

where $c$ denoted the speed of light and relative electrical permittivity of the subsurface RoI was $\epsilon_r = 5$ as described prior. Following standard practice, an acceptable maximal simulation cell size of approximately $\lambda/10$ motivated selection of a simulation cell size of 3-4mm. This was further reduced for a simulation spatial resolution of 2mm, which significantly increased the resolution of the smallest spherical target from 10 cells to 15 cells.

Combined with the buffer requirements outlined above, this resulted in an RoI volume — fully contained within the global simulation domain — that resembled a cube, with side lengths of approximately 0.25m.

The design of the area scan grid maximised the achievable coverage of the RoI volume and minimised the characteristic length scales of resolvable targets therein, whist ensuring simulations were computed within a feasible timescale. The square lateral profile of the RoI volume also motivated an area scan with equal and consistently separated transects across both lateral axes, akin to conventional area scans performed using handheld GPR scanners [7]. Furthermore, in accordance with established GPR practices (see Chapter 2), it was necessary for a minimum of 3-5 transects to intersect the target across both lateral axes. Given that the smallest sphere had a diameter of 30mm, this motivated selection of 6mm separation between successive transects in the grid.

In accordance with the above conditions, a square area scan grid comprised of 51 rows and 51 columns of transects was selected to fully cover the lateral footprint of the RoI volume, with 50 traces per transect. In practice, this became 51 traces per transect, as simulated traces abided zero-indexing convention. The additional trace ensured a trace was recorded at the initial location of the antenna for each transect in the area scan grid.

### *4.4.4 Method – Automating Area Scans in gprMax*

To efficiently generate area scan datasets using gprMax in a reasonable timeframe, it was necessary to automate the configuration and execution of each constituent transect simulation involved, as illustrated in Figure 4.2.

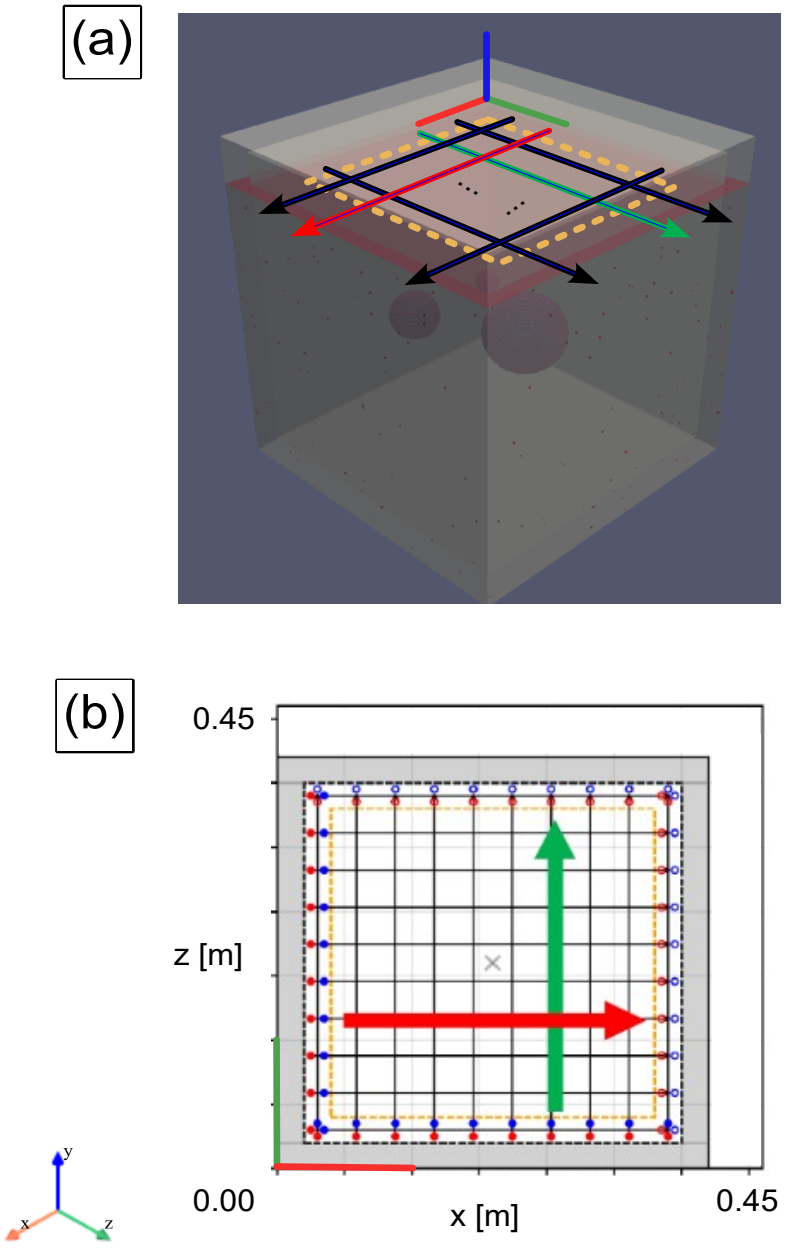


Figure 4.2: A simulated area scan in gprMax (a) is a 2D grid of straight line transect trajectories (b). The yellow boundary denotes the lateral footprint of the RoI volume. The absorbing boundary is shown in grey. Red and blue dots denote the GPR antenna's transmitter and receiver elements. Solid and hollow dots mark the start and end of an individual transect, respectively.

Transect simulations were configured independently via individual `.in` files, containing a sequence of gprMax input file commands in ASCII text, associated with metadata (e.g. the simulation handle, user-defined description etc.); ground-truth geometry (e.g. target placement, domain dimensions, material properties etc.) and scan parameters (e.g. antenna centre frequency, movement incrementation, etc.). For an example, see Figure 4.3.

s002_b000_a.in

```
#title: anechoic chamber geometry (down-scaled) 3x pec spheres
#domain: 4.20210000e-01 4.50120000e-01 4.19900000e-01
#dx_dy_dz: 2.00000000e-03 2.00000000e-03 2.00000000e-03
#time_window: 5.0e-09
#waveform: ricker 1 1.5e+09 my_ricker
#material: 4 0 1 0 drySand_Homo
#box: 0.00000000e+00 0.00000000e+00 0.00000000e+00 4.20210000e-01
3.90120000e-01 4.19900000e-01 drySand_Homo n
#sphere: 2.72657500e-01 2.10060000e-01 2.09950000e-01 5.00000000e-02 pec n
#sphere: 1.47552500e-01 2.10060000e-01 2.72425000e-01 3.00000000e-02 pec n
#sphere: 1.47552500e-01 2.10060000e-01 1.47475000e-01 1.50000000e-02 pec n
#hertzian_dipole: z 3.75000000e-02 3.90120000e-01 5.75000000e-02 my_ricker
#rx: 7.75000000e-02 3.90120000e-01 5.75000000e-02
#src_steps: 6.10420000e-03 0.00000000e+00 0.00000000e+00
#rx_steps: 6.10420000e-03 0.00000000e+00 0.00000000e+00
```

Figure 4.3: A `.in` configuration file from a gprMax transect simulation.

Windows Batch Files (`.bat`) showed promise as a solution for predefining each execution command and running simulations sequentially. Importantly, the sequential executions were triggered in a blocking manner, which mitigated the risk of computational resource exhaustion that could stall area scan simulations and potentially corrupt the generated datasets.

Following initial tests, the decision was made to switch to using Linux Shell Scripts (/textttt.sh files). This change improved the reliability of activating the gprMax conda environment necessary to start the first simulation and allowed gprMax simulation commands to be executed directly, without the additional complexity of batch scripting syntax required in `.bat` files.

Automation of configuration file generation was accomplished with the development of a dedicated Python-based automation script (see Appendix A). This script consolidated user-defined input parameters for both area scan design and the essential gprMax simulation setup. From this, the automation script populated syntax templates for each configuration file command required to simulate a transect and generated a complementary `.sh` script to sequentially trigger each respective simulation. This procedure is visually summarised in Figure 4.4.

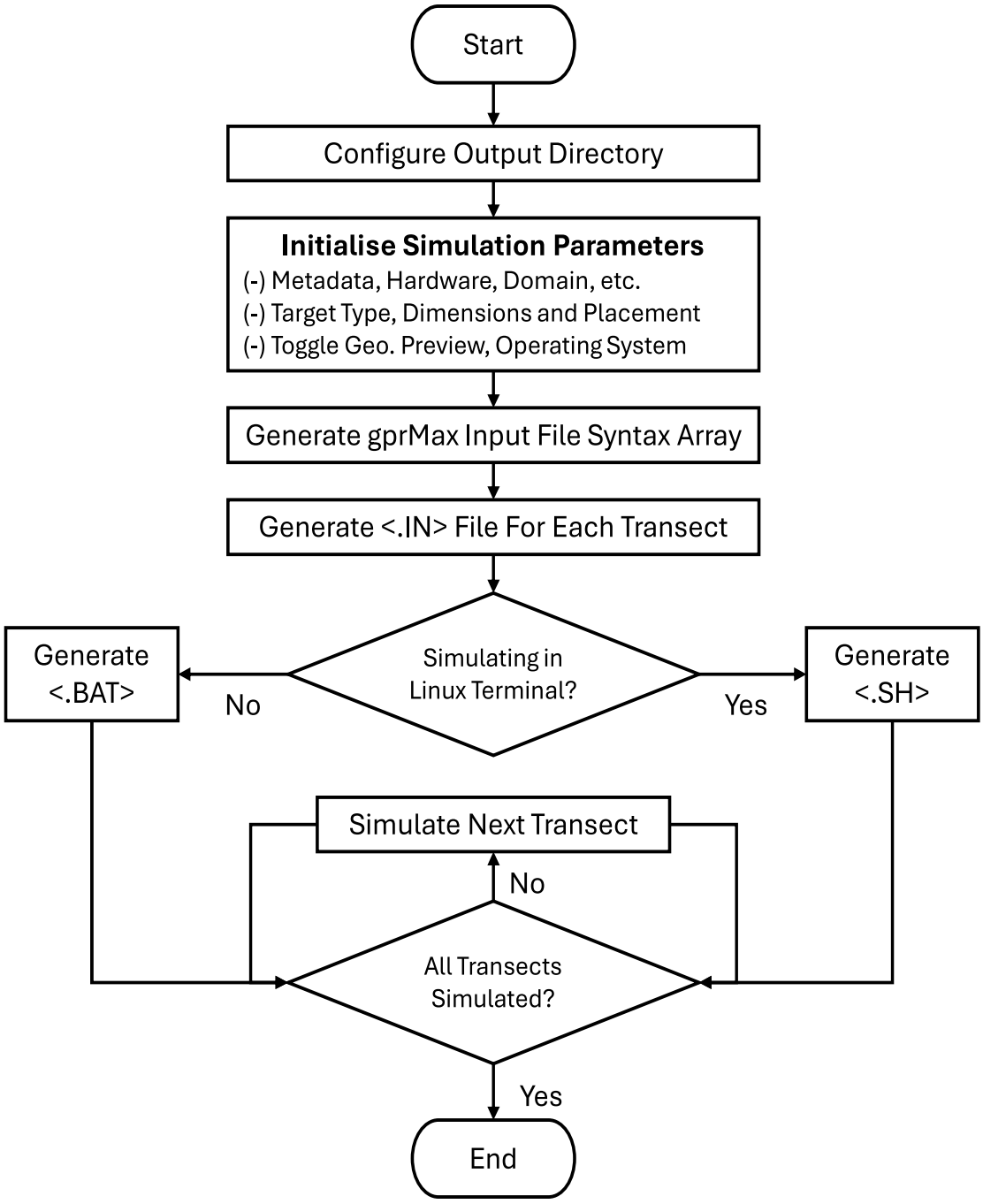


Figure 4.4: Flowchart for bespoke gprMax area scan automation functionality.

During the development of the automation script, several additional challenges were addressed. As compound trajectories formed form multiple straight line transects, the added complexity of area scan design motivated the integration of a more intuitive trajectory preview functionality. This enhancement on the native gprMax setup procedure aided in refining the simulation setup and provided swift, visual confirmation of the accuracy of programmed configuration parameters. In contrast, the native setup procedure relied solely on programming syntax, for which visual confirmation of programmed antenna trajectories were only available after the complete execution of a full transect simulation.

The automation script also needed to provide a tractable record of the initial area scan configuration parameters to provide a direct and accessible reference, thereby more effectively supporting later analysis of returned 3D visualisations. This was achieved by exporting: (i) a timestamped log file of all operations performed during execution of the automation script; (ii) independent ASCII text files containing both a legend and parameter summarises concerning geometry, materials and scan settings; (iii) raster and vectorised exports of the area scan trajectory preview, alongside (iv) a duplicated copy of the automation script itself. This metadata provided a comprehensive record for each area scan conducted.

Finally, the automation script included a local coordinate transform that allowed geometry placement to be defined relative to the centre of the subsurface RoI volume. This method was deemed more intuitive than the native gprMax approach, which defined target geometry relative to the global simulation origin, beyond the absorbing boundary region. The reduction in manual computations required to define the coordinates for each target enhanced the efficiency of simulation design and revisions conducted in this chapter.

## 4.5 Results and Discussion

This section presents the results of the performance analysis for the proposed 3D visualisation workflow, applied to an idealised, numerically simulated fixed-directional GPR dataset generated using the newly developed area scan functionality in gprMax, as detailed prior.

In accordance with Objective (1), area scan functionality for gprMax was successfully implemented through the development of a dedicated automation script. This script was capable of generating both `.in` files to configure individual transects and `.sh` files to enable direct sequential execution of each simulation. Practical implementation of these tools further facilitated generation of simulated area scan datasets for background calibration and a main scanning pass containing previously defined target geometry, addressing Objective (2) and Objective (3).

In accordance with Objective (4), the theoretical workflow deconstructed in the previous chapter was numerically implemented in Python as a standalone program based on entirely open-access tools. It was capable of end-to-end data processing as desired, returning fully rendered 3D visualisations of raw input data files, sourced from gprMax simulations, alongside practically recorded fixed-directional and hybrid-rotational GPR datasets.

In line with Objective (5), Section 4.5.1 details analysis of the detection and localisation accuracy of the returned 3D spatial profiles, relative to the established ground-truth geometry. This is followed in Section 4.5.2 by the analysis of end-to-end data processing runtime, to provide insight into achieved levels of computational efficiency.

### *4.5.1 Subsurface anomaly Detection and Localisation*

The spatial profiles recovered from application of the proposed 3D visualisation workflow are presented in Figure 4.5. Two sizable, highly localised clusters were clearly identifiable.

The footprints of these clusters closely aligned with the known positions of the 100mm and 60mm diameter spheres respectively, indicating that the proposed workflow had accurately detected both targets. Spatial cluster mid-centres also exhibited a high degree of localisation accuracy, exhibiting agreement at decimetre length scales to within an average 9.5% tolerance across all three spatial dimensions, reducing to within 4.2% tolerance when exclusively considering lateral agreement.

It is noteworthy that both profiles exhibited a distinct elongation directed toward the known location of the 30mm sphere, most notably in the cluster associated with the 60mm sphere. This suggests that while the workflow did not explicitly localise the 30mm sphere as a standalone cluster, it had detected its presence and significantly influenced the localisation of the other clusters.

A plausible explanation for this observation was that the workflow did detect the smaller target, but its reduced size and deeper leading interface resulted in a weaker backscatter signature compared to the larger 60mm and 100mm spheres. It was therefore likely that the segmentation process associated this weaker signature with background noise, but that the interaction of its backscatter profile with those of the larger spheres was sufficient to cause the elongations observed in both spatial profiles.

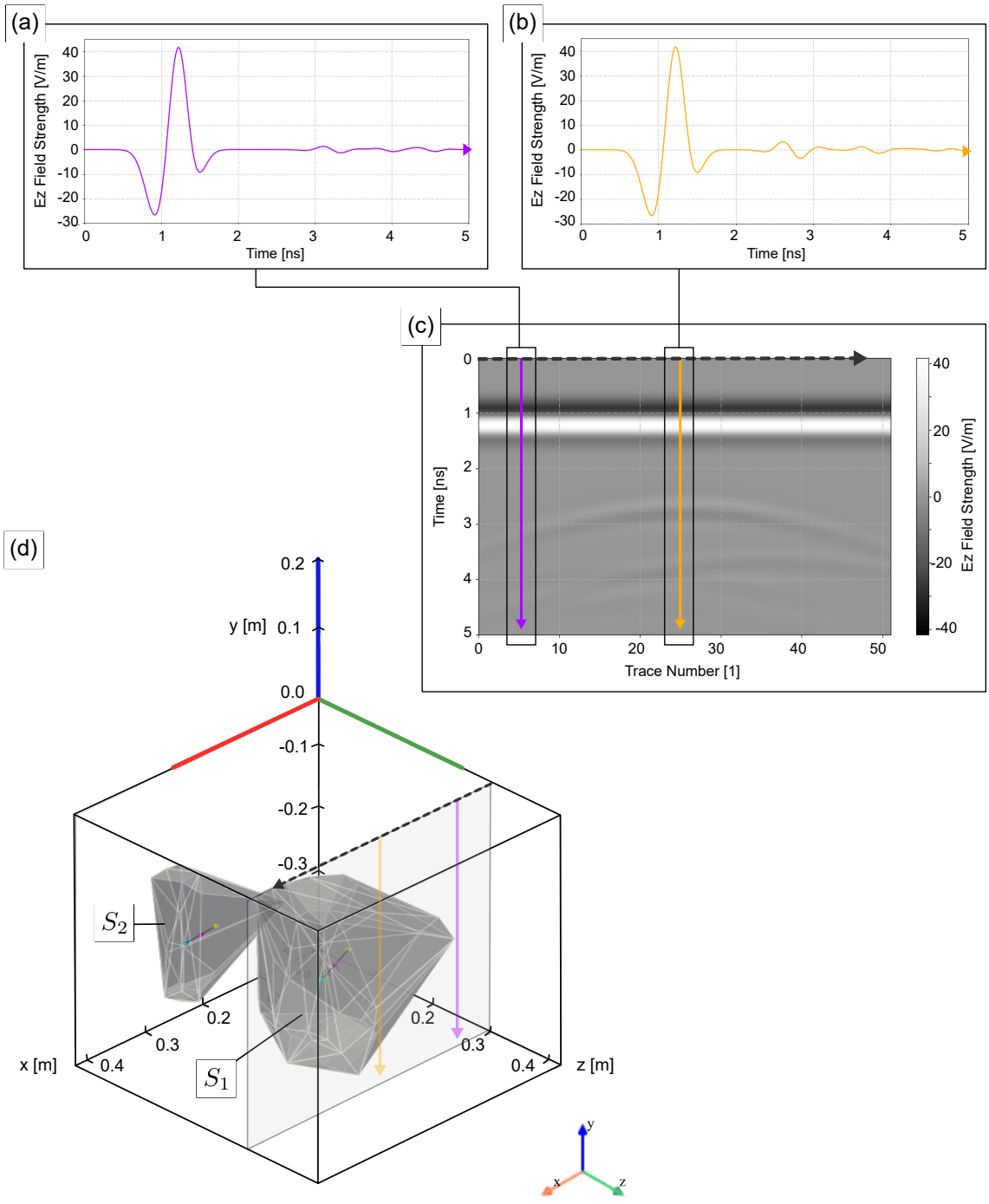


Figure 4.5: Returned 1D trace (a, b), 2D transect (c) and 3D (d) spatial profiles, from application of the proposed 3D visualisation workflow to a gprMax area scan output dataset, on an RoI volume containing three spherical metallic targets. Cluster mid-centres (●) are recovered by averaging cluster centroid (●) and bounding box (●) coordinates. The black dashed arrow represents the the scan trajectory path of transect (c).

A further observation was that the returned clusters exhibited larger footprints than their associated targets in all directions, most notably vertically above the known location of the targets.

As perfect electrical conductors, backscatter from the metallic target interface was expected to experience minimal attenuation, expanding outward uniformly, particularly from the upper surfaces of the spheres nearest to the antenna. This isotropy was also evident in the expanded footprints of the segmented clusters relative to the target geometry, alongside the vertical skew above the targets leading interfaces. The implication was that the phenomenon had been driven by the spherical shape and metallic composition of the targets. Beneficially, this also served to amplify the presence of both structural anomalies, reducing the risk of oversight in a real survey.

### *4.5.2 Elapsed Workflow Runtime*

The computational efficiency of the proposed workflow was analysed based on the average elapsed computational runtime between the initialisation call and successful export of a rendered 3D visualisation. Execution of the workflow was considered complete when all output files had been saved to the working directory. Exported files included a single raster (.png) and two vectorised formats (`.svg`, `.pdf`). Elapsed runtime was recovered using the Python `time` module.

As shown in Figure 4.6, the average elapsed runtime was an impressive 5 seconds, with a variation of only 1 second across all executions. Importantly, it should be recalled that all computations were exclusively conducted on the previously detailed consumer-grade PC, therefore these observations highlight that the proposed workflow achieved significantly high levels of computational efficiency, a result that was directly attributed to its streamlined ELT-pipeline architecture and foundation on matrix operations rather than slower element-wise computations.

Looking closer, the extremal range of elapsed runtimes recorded spanned 0.95 seconds between 4.50 seconds and 5.45 seconds, and the IQR spanned 0.53 seconds between a lower quartile of 4.72 seconds and upper quartile of 5.25 seconds. Comparable separations of approximately 0.25 seconds of the IQR either side of the mean were also observed, indicative of highly stable runtime performance in conjunction with highly efficient data processing across all executions tested. This inference was further supported by observations of negligible skewness in the runtime data, indicated by the comparable relative separation (approximately 0.20 seconds) between each of the upper and lower quartiles with their respective adjacent extrema.

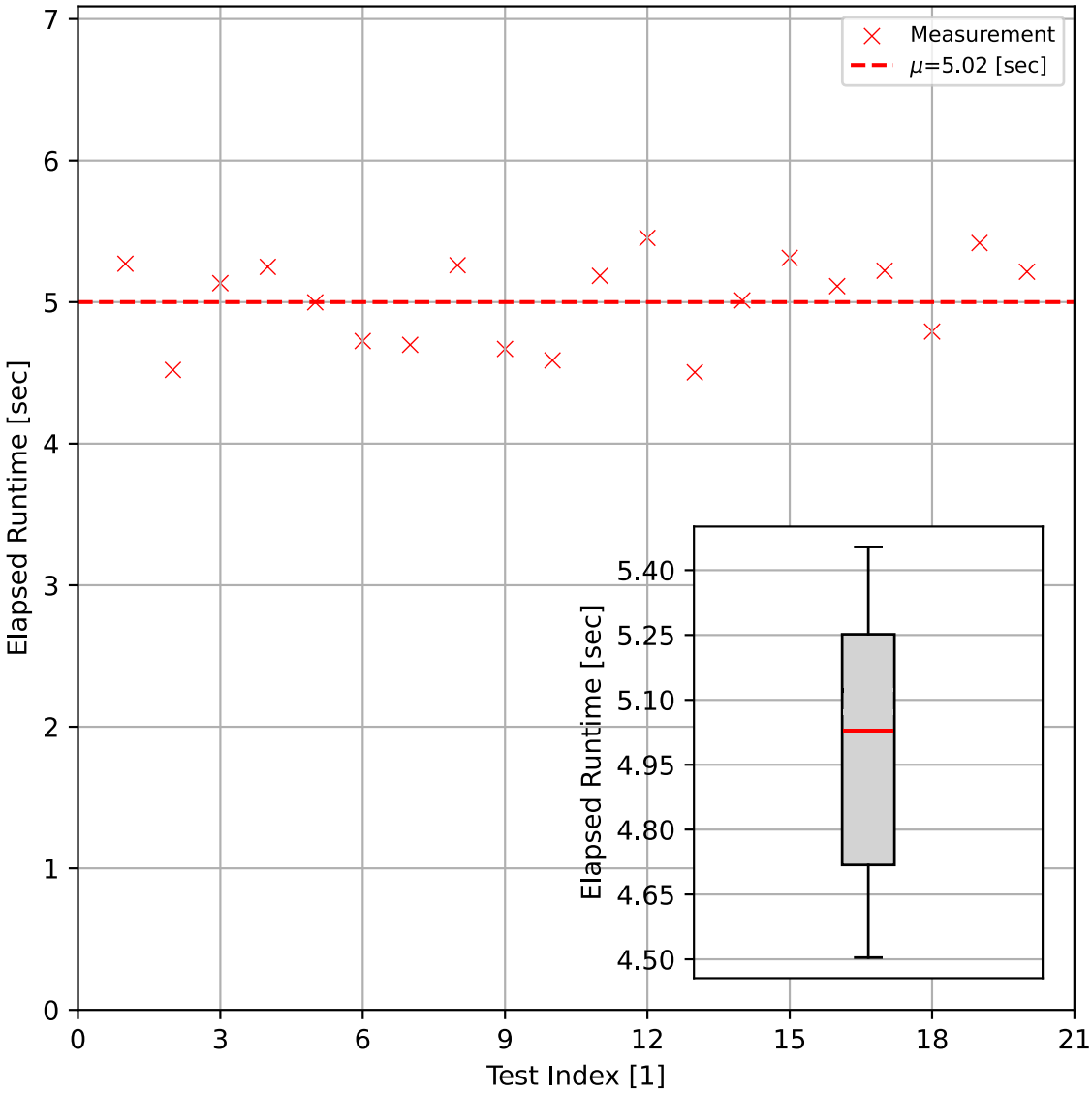


Figure 4.6: Breakdown of elapsed 3D visualisation workflow runtime duration between program initialisation and final render, averaged over 20 independent executions (a) with associated box and whisper plot insert relaying extremal range, mean and IQR.

## 4.6 Summary

This chapter examined the efficacy of the proposed 3D visualisation workflow, based on application to idealised simulated fixed-directional GPR area scan dataset, generated using an augmented version of leading software gprMax. Collectively, the findings demonstrated the workflow's high computational efficiency, along with its ability to accurately detect and localise subsurface structural anomalies, justifying subsequent progression to the next stage of laboratory benchmarking.

To facilitate practical numerical simulation of area scan measurements in gprMax, this work developed a dedicated automation strategy based on Shell Script batch files and configuration syntax templates, which successfully sequentially initialised and executed simulations of the area scans' constituent transects, circumventing reliance on human intervention to update configuration files and trigger each individual simulation.

Subsequent quantitative and qualitative performance analysis of return 3D visualisations evidenced accurate detection and localisation of known targets, with mid-centre localisation accuracy at decimetre length scales observed to within a 4.2% tolerance. Furthermore, analysis of elapsed data processing runtimes demonstrated high levels of stability and efficiency of the workflow's computational operations, with full end-to-end processing from initialisation to returned 3D spatial profile renders consistently achieved within 5 seconds.

# Chapter 5. Benchmarking II – Fixed-Directional GPR

In this chapter, the performance of the developed 3D visualisation workflow is analysed using a practical fixed-directional GPR dataset, recorded in controlled laboratory conditions using established targets and commercial measurement equipment. Findings are compared against results from the previous chapter.

## 5.1 Introduction

The second stage of laboratory benchmarking moved from analysing workflow performance on idealised simulated GPR data to more realistic practical data, introducing influences from factors such as authentic subsurface heterogeneity and non-absorbing boundaries. Grounds for appraisal remained consistent with those outlined in the previous chapter.

## 5.2 Motivation

To meaningfully assess workflow performance on practical data recovered from experimental hybrid-rotational GPR apparatus in later chapters, it was first necessary to validate its effectiveness using practical data from an established, commercial-grade GPR system. Since no such systems yet existed for hybrid-rotational GPR, a fixed-directional setup was naturally employed.

Comparisons with findings from the previous chapter were also of interest. Firstly, whether similar or exaggerated spatial profile deformation, potentially indicating detection of the smallest target, would manifest in larger resolved targets. Additionally, whether introducing a checkpointing approach during data extraction would improve workflow efficiency.

To enable valid comparison with numerical simulations, the physical RoI volume created contained identical targets with consistent separations. Its scale was maximised within the lab to emulate an infinite subsurface domain, to ensure boundary interference effects did not dominate returned measurements. The setup was placed in an anechoic chamber to combat random EM-interference, and a background scan with all targets removed allowed for background subtraction, supressing non-random interference sources (e.g. the RoI housing).

## 5.3 Aims and Objectives

The primary aim of this investigation was to validate workflow performance efficacy (as in the previous chapter), now on a practical fixed-directional GPR dataset gathered in controlled laboratory conditions. The secondary aims were to cross-check observations with findings from the numerical simulations, and examine the influence of input data checkpointing on the level of computational efficiency achieved.

Objectives for this investigation were:

1. To capture a fixed-directional GPR background calibration pass of a subsurface volume devoid of target geometry, in a practical survey under controlled conditions.
2. To capture a similar fixed-directional GPR scanning pass of the same subsurface volume containing established target geometry.
3. To augment the workflow's data extraction subroutine an incorporate checkpointing.
4. To use the developed workflow to generate 3D visualisations of subsurface anomalies.
5. To quantitatively analyse the impact of checkpointing on observed runtime efficiency.
6. To quantitatively analyse the fidelity of returned 3D spatial profiles.
7. To quantitatively and qualitatively compare returned 3D spatial profiles with those from the earlier numerical simulation investigation.

## 5.4 Experimental Setup and Methods

This section details the practical setup of the laboratory and commercial fixed-directional GPR measurement equipment for data collection, including the ground-truth geometry adopted for practical experimentation (Section 5.4.1); hardware selection (Section 5.4.2) and parameters adopted for area scanning (Section 5.4.3). Methods associated with practical data collection and data recovery are presented in Section 5.4.4 and Section 5.4.5, respectively. This is followed by a breakdown concerning the numerical implementation of input data checkpointing functionality in Section 5.4.6.

### 5.4.1 Setup – Ground Truth Geometry

To maximise the size of the subsurface whilst ensuring the robustness of its housing and the load bearing limit of the laboratory floor, an RoI volume with a 0.66m by 0.53m lateral footprint and depth of 0.52m was selected. To introduce a controlled degree of subsurface heterogeneity without excessive variation, the RoI volume was backfilled with kiln dried sand with grain sizes of 0.5mm to within a tolerance of 0.25mm. A reasonable estimate for the relative electrical permittivity of dried sand was $\epsilon_r = 5$ [42], providing a more readily displaceable granular analogue for solid masonry bricks, for which constituent clay exhibited comparable relative electrical permittivity $\epsilon_r \in [2, 6]$. The use of dry sand was critical to minimise subsurface water content, as excess moisture had potential to rapidly attenuate the radar signal, obscure target geometry, and thereby significantly limit the levels of achievable subsurface penetration afforded by the fixed-directional GPR equipment.

Creation of the RoI volume required the design and fabrication of a custom housing to withstand the outward pressure from the 325kg of sand necessary to backfill the $0.18m^3$ subsurface volume. The housing was manufactured in from 8mm thick plywood for rigidity, assembled using an electric impact screwdriver and encircled by a heavy-duty ratchet strap to provide maximal structural integrity. The setup was assembled inside the laboratory's anechoic chamber to minimise interference from external EM-noise sources through this test and subsequent laboratory benchmarking work.

Detachable plywood outriggers were also created to support the antenna when scanning transects at the extremal limits of the RoI lateral footprint. A 3mm acrylic panel was also placed on top of the upper interface of the sand backfill, such that its upper surface sat flush with the that of the outriggers. As a homogeneous, low-loss medium, the inclusion of the acrylic panel would have a negligible impact on the quality of the GPR measurements recorded. Its inclusion was necessary to provide reliable traction on the RoI volume contact surface for the antenna base place and odometer wheel.

Moreover, this further prevented the antenna from colliding with the sides of the RoI volume housing as it moved onto the outriggers at the start and end of each transect in the area scan. As an additional benefit, the acrylic panel also reduced the risk of disturbed sand entering the sensitive electrical equipment in close proximity during data collection, which could have potentially damaged the critical internal systems.

The global coordinate system was configured to match that used in the previous chapter. The origin was positioned at the upper vertex of the RoI volume, specifically at the vertex nearest the door of the anechoic chamber, as this was most practical for physical measurement references due to the available space and single point of entry.

The orientation of the lateral and vertical axes is indicated by the RGB orientation marker in all figures presented throughout this chapter related to equipment setup and returned 3D visualisations. This orientation, in line with earlier work, aligned the x-axis to the longest side of the RoI volume, and designated the y-axis as the vertical axis, adhering to the notational convention used by gprMax.

For this and subsequent laboratory benchmarking, the contact surface was defined as the uppermost surface of the acrylic panel placed on top of the sand backfill. In turn, to simplify practical measurements of target depth, the global origin was vertically aligned with this surface.

The same three solid metal spherical targets used in the previous chapter were employed throughout the laboratory benchmarking, as detailed prior. These included a 100mm diameter sphere ($S_1$), a 60mm diameter sphere ($S_2$), and a 30mm diameter sphere ($S_3$). The relative placement of these targets remained consistent across all laboratory benchmarking work. A detailed layout is provided in Figure 5.1.

The physical setup of the RoI volume presented several practical challenges, which required ingenuity to overcome. The main challenge encountered was accurately and reliably controlling the exact placement of the metallic spheres within the RoI volume. This was attributed to the granular composition of the sand backfill, which could be easily displaced.

Creating a level surface at a fixed depth was a significant practical challenge to overcome. The mass of the spheres was substantial enough to cause them to sink by up to a full diameter if the sand was not adequately packed in their immediate vicinity. The solution devised overcame this challenge by partially submerging multiple 250mm wide, 3mm thick acrylic panels on all four sides of the target. This created a closed boundary which prevented the sand from displacing when the sphere was added. By backfilling around the exterior of the panels, it was then possible to remove the panels without disturbing the freshly placed targets (see Figure 5.1c).

An additional challenge for accurate positioning arose when providing a reference level for the contact surface while the RoI volume was partially emptied during target placement. The initial solution, also depicted in Figure 5.1c, successfully overcame this issue using a tape measure to span the RoI volume, which allowed for more accurate measurements of target depth and lateral displacement from the global datum, taken against the tangible interfaces of the targets using an acrylic displacement gauge. This method was later enhanced with the addition of a more rigid spirit level to span the RoI volume, which provided a more consistent vertical reference level during target placement.

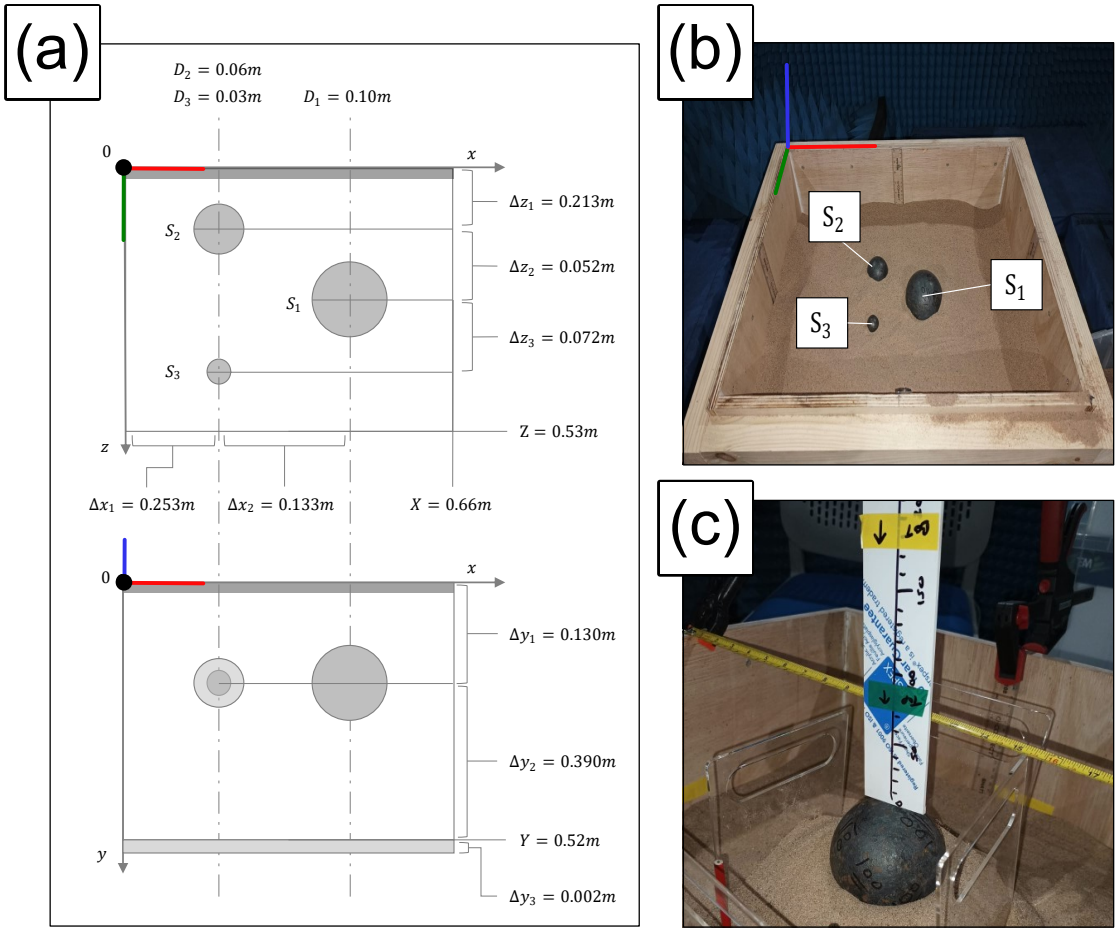


Figure 5.1: Ground truth geometry (a) of physical RoI volume, which contained three solid steel spherical targets (b). Removable acrylic panels held back sand around the targets during placement (c) to ensure vertical target positioning accuracy.

### 5.4.2 Setup – Measurement Equipment

Physical measurement equipment utilised for this work is presented in Figure 5.2.

The fixed-directional GPR data collection system was based on a Zond 12e Advanced GPR controller, physically interfaced via an RJ45 Ethernet Local Area Network (LAN) cable to a consumer grade laptop running Prism2 [308], proprietary software designed specifically to operate this controller. It was responsible for GPR measurement control, data capture and relaying real-time previews of recorded transects. The laptop used was a Lenovo IdeaPad Flex 5, with following specifications: Windows 11 Pro operating system, 8 GB of RAM, and an 8-core AMD Ryzen 7 4700U processor.

The GPR controller was interfaced via a single 3m Amphenol connector cable to a shielded Zond 12e 1GHz bistatic GPR antenna, weighting 2.1kg with a footprint of 250mm by 100mm. This centre frequency was considered the most practical compromise, dictated by available hardware (a 0.5GHz and 1GHz antenna, respectively). Use of a 1.75GHz antenna[1] had been desired to better facilitate direct comparison between numerical simulation, fixed-directional and hybrid-rotational GPR tests across Chapter 4 through Chapter 6.

A manually triggered laser pointer was connected to the front-centre of the antenna, angled such that the laser dot tracked 10mm in front of the antenna base plate lip (i.e. its leading edge) when activated by the operator. This was added to provide a clear reference marker when aligning the midpoint of the antenna to the desired trajectory line when the position of the antenna was reset between successive transect measurements.

To the rear of the antenna a 200mm diameter odometer wheel was connected via a short 0.3m Amphenol cable to an interface port on the 1GHz antenna. The wheel was mechanically connected via a pivot mount to a fixture plate, locked out using cable ties to help ensure the antenna did not deviate from its straight-line trajectories as the antenna position was manually advanced during data collection.

This was complemented by a lightweight 2m guide bar made from rigid angled corrugated cardboard, along which the antenna's side was pressed during data collection to minimise trajectory deviation. The odometer wheel was based on a 200 pulse per revolution rotary encoder, which resolved the lateral displacement of the antenna from its initial position at the beginning of each transect to within 3.14mm. This data was recorded and saved alongside measured backscatter amplitude data in binary `SEG-Y` files by Prism2 during data collection.

[1] A 1.75GHz centre frequency was chosen to align with the GPR parameters adopted in the feasibility study (see Chapter 2). Notably, the opportunity had arisen to utilise the same antenna originally developed for T-Vision as the basis of the planned laboratory apparatus for hybrid-rotational GPR benchmarking (see Chapter 6).

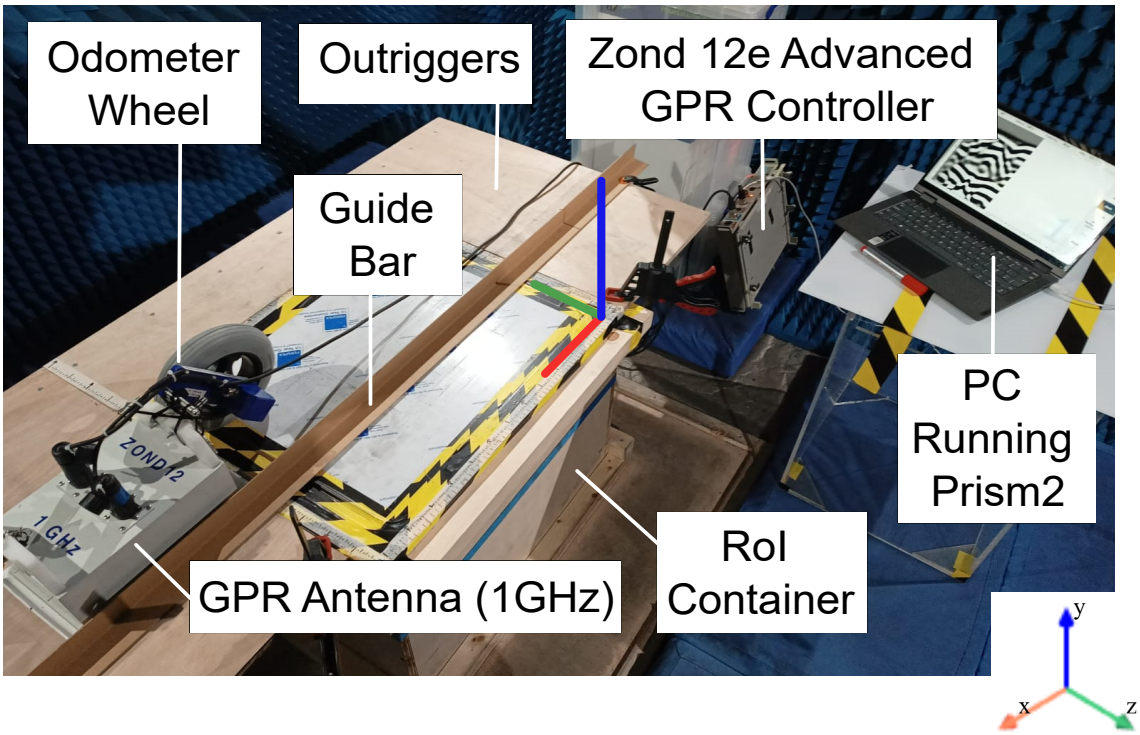


Figure 5.2: Physical fixed-directional GPR measurement equipment used in laboratory data collection included a Zond 12e Advanced GPR controller, 1GHz bistatic antenna and manual positioning feedback via an odometer wheel.

To provide necessary traction for smooth movement of the antenna and odometer wheel across the sample, a 3mm acrylic panel was placed across the contact surface of the sand backfill. This addition prevented the antenna and wheel fouling on the edges of the RoI volume housing, which in preliminary tests prevented the antenna from moving across trajectory lines in full without being lifted off and placed back down, often resulting in misalignment between the current location of the antenna and its recorded lateral displacement, which could create significant discontinuities in the recorded transects.

It should further be noted that the fixed-directional GPR system recorded backscatter amplitude directly in the time domain. Initial tests were performed using the leading commercial handheld GPR system supporting direct measurement in the frequency-domain (a Proceq GP8000) [7]. However, the system was reliant on automated trace measurement triggering, which would only record trace measurements when its integrated, small, plastic odometer wheels were turning. In practice, the wheels could not grip the sand backfill, and would repeatedly foul on the RoI volume boundary, even with the addition of the acrylic panel. Subsequent trials with the aforementioned Zond 12e system performed much more reliably, and exhibited comparable data collection efficiency, recording full transects across the RoI volume within 5-10 seconds. Ultimately, the specific GPR measurement principle behind the fixed-directional GPR system would not undermine the validity of any subsequent performance analysis. Given its practical advantages over the Proceq GP8000 in the preliminary tests, this motivated selection of the Zond 12e system as the basis for this work.

### *5.4.3 Setup – Scan Parameter Selection*

For a summary of parameter settings adopted for fixed-directional GPR data collection in the laboratory, refer to Table 5.1.

To optimise data collection efficiency, minimising the total scan duration for the entire area was crucial. Therefore, the temporal response measurement interval for each trace was set to 9 ns — defining the trace duration and maximal attainable. The interval corresponded to a maximum one-way signal propagation distance of approximately 0.55 m, which was sufficient to cover slightly beyond the 0.52 m depth of the RoI volume. This choice ensured measurements did not significantly extend beyond the RoI. Practical selection of the measurement interval was achieved by setting the controller to record 1024 samples per trace, noting that the 7ps sampling interval of the GPR controller was a fixed hardware constraint.

| Parameter | Description | Value | Units |
|---|---|---|---|
| $N_s$ | Number of samples per trace. | 1024 | 1 |
| $N_A$ | Average number of traces per transect. | 458 | 1 |
| $N_{B_0}$ | Number of area scan grid rows (in $z$). | 107 | 1 |
| $N_{B_1}$ | Number of area scan grid columns (in $x$). | 133 | 1 |
| $\Delta B_0$ | Area scan grid row separation. | 5 | mm |
| $\Delta B_1$ | Area scan grid column separation. | 5 | mm |
| $T$ | GPR trace duration. | 9 | ns |
| $F_c$ | Transmission antenna centre frequency. | 1 | GHz |
| $F_w$ | Transmission antenna waveform type. | Continuous | - |
| $F_p$ | Transmission antenna waveform polarity. | $z$ | - |
| $L_1$ | Antenna body length. | 0.250 | m |
| $L_2$ | Lift-off distance from contact surface. | 3 | mm |
| $\Gamma$ | Odometer/antenna midpoint offset. | 0.225 | m |
| $O_D$ | Odometer wheel diameter. | 0.200 | m |
| $O_p$ | Odometer wheel pulses per revolution. | 200 | 1 |

Table 5.1: Fixed-directional GPR laboratory data collection parameters.

Following established best practices for GPR area scan measurements (see Chapter 2), the span of transects comprising the area scan grid was carefully selected to ensure that the antenna's midpoint tracked across the full lateral extent of the RoI volume, maximising subsurface coverage. Transects in both rows and columns were spaced 5mm apart, a choice that maximised the likelihood of detecting the smallest target ($S_3$) by ensuring it was intersected by at least 3-5 consecutive transects along each axis. This spacing also minimised the total number of transects needed, which improved data collection efficiency across the entire area scan.

These requirements collectively guided the selection of the number of transects forming the rows and columns of the area scan grid, as well as their respective spacing. The number of traces per transect varied inherently, primarily due to the rectangular lateral profile of the RoI volume and minor variations in transect length caused by the manual positioning of the antenna during data collection. It should be noted that the workflow included a dedicated subroutine for 3D spatial clipping (see Chapter 3), which was designed to account for this expected variability by truncating 3D-aligned transects to fit within the approximate boundaries of the RoI volume.

The dimensions and other hardware-defined parameters of the physical measurement equipment further determined the antenna body length, contact surface lift-off, and the signal characteristics of the transmission antenna. Similarly, the diameter and pulse count per revolution of the odometer wheel were also fixed.

### 5.4.4 *Method – Practical Data Collection Procedure*

Data collection was conducted in two stages. In the first stage, before the target geometry was introduced, the antenna was positioned with its midpoint aligned to the centre of the RoI volume at the contact surface (i.e. the plane $y = 0$). After the GPR controller completed an automatic measurement calibration, an area scan was performed, capturing temporal response profiles related to background elements of the survey environment (e.g. RoI volume backfill and housing).

In the second stage, the target geometry was added, and a second area scan was conducted, generating the dataset for the main scanning pass. To reduce signal artifacts caused by the environment and measurement hardware configuration, temporal response profiles from matching antenna positions in the background scan were subtracted from those in the main scan during the 3D visualisation workflow's data extraction process. This served as the background calibration.

Both area scans followed identical antenna trajectories, as shown in Figure 5.3. During each scan, the antenna's location was defined to align laterally with its midpoint in the XZ plane and vertically with the contact surface, where the upper interface of the RoI volume met the lower interface of the antenna housing.

Trace measurements were aligned with the boresight vector, extending vertically downward from this alignment point. Grid markers etched on the RoI volume housing provided reference points for the centreline of each transect in the area scan grid.

For each transect, the antenna was initially positioned so that its front laser dot aligned with the corresponding grid marker. The guide bar was then aligned with the side of the antenna housing and clamped at both ends to prevent movement.

Data collection in Prism2 was initiated with a single keystroke on the laptop, during which the antenna was manually advanced laterally across the RoI volume, keeping the side of its housing flush with the guide bar to minimise deviation. A second keystroke ended data collection and saved the transect as a `SEG-Y` file when the odometer wheel's contact point at the rear of the antenna housing aligned with the marker on the opposite side of the RoI volume. This ensured that the antenna midpoint covered the full lateral extent of the RoI volume.

This process was repeated for each transect in the area scan grid. Transects representing the columns of the grid were recorded after all row transects had been completed. Throughout, rows and columns were incrementally advanced in the direction of increasing lateral displacement from the global datum along each respective axis.

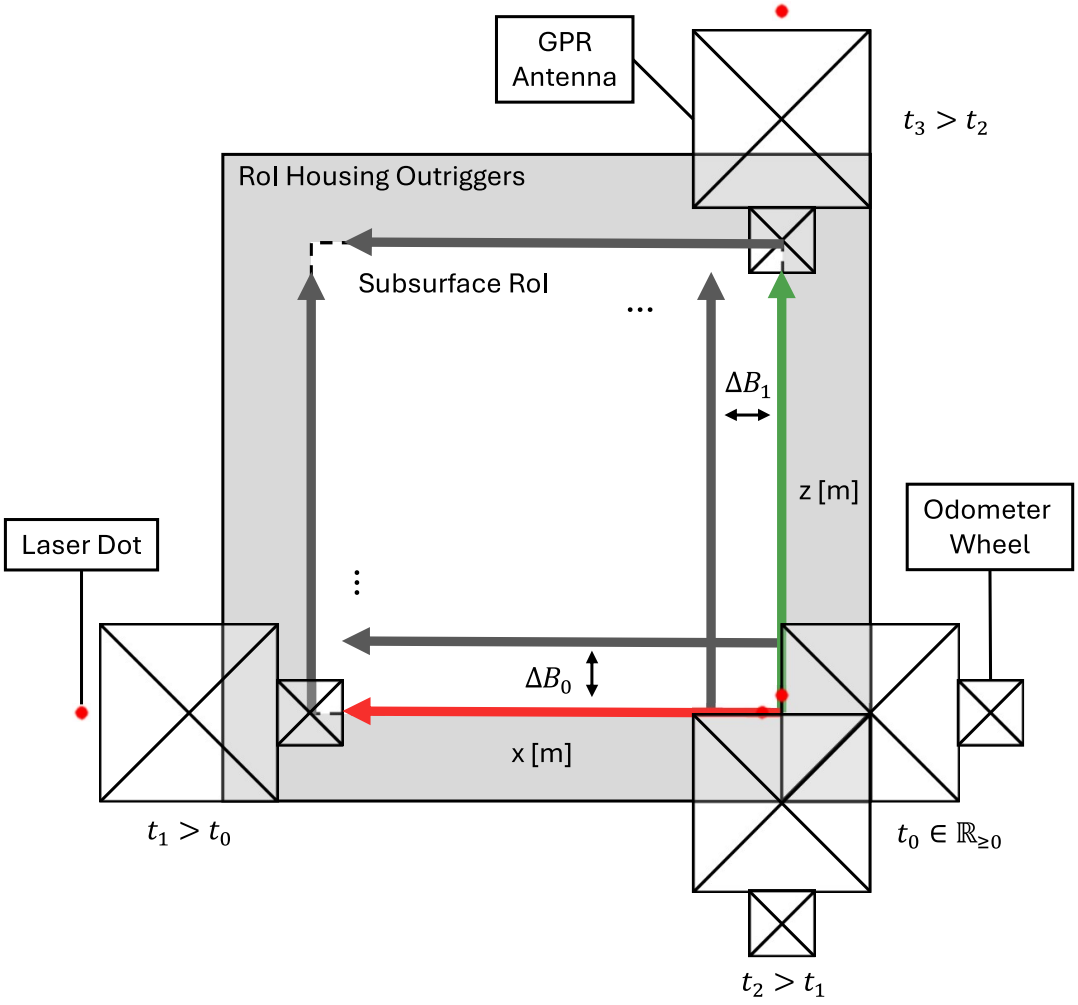


Figure 5.3: Diagram of area scan grid trajectories manually tracked with the antenna during fixed-directional GPR data collection.

### 5.4.5 *Method – SEG-Y Data Recovery*

The 3D visualisation workflow required extracting trace amplitude data and the antenna's lateral displacement from individual transect files. Prism2 generated `SEG-Y` [323] files[2] , each containing a standard $b_H = 3600$ byte `EBCDIC` global header block[3] with an additional $b_P = 692$ byte descriptive preamble. Trace measurements were divided into a $b_h = 240$ byte local header and a $b_t = 256$ byte amplitude data block — illustrated in Figure 5.4.

The added non-standard SEG-Y preamble led to failures in established readers (`SEGYIO` [324], `SEGPY` [325], `SGY2TXT` [326]), therefore a custom Python script was developed for importing the `SEG-Y` files into the workflow (Appendix A). It followed the byte indexing formula,

$$b_{start} = b_H + i(b_h + 2b_t), \tag{5.1}$$

where $b_{start} \in mathbbZ_{>0}$ denotes the index of the first byte of the first sample for an arbitrary trace with index $i \in [0, 1, \ldots, N_A]$. Offsets for global header and local header blocks are $b_H = 3600$ and $b_h = 240$ bytes, respectively.

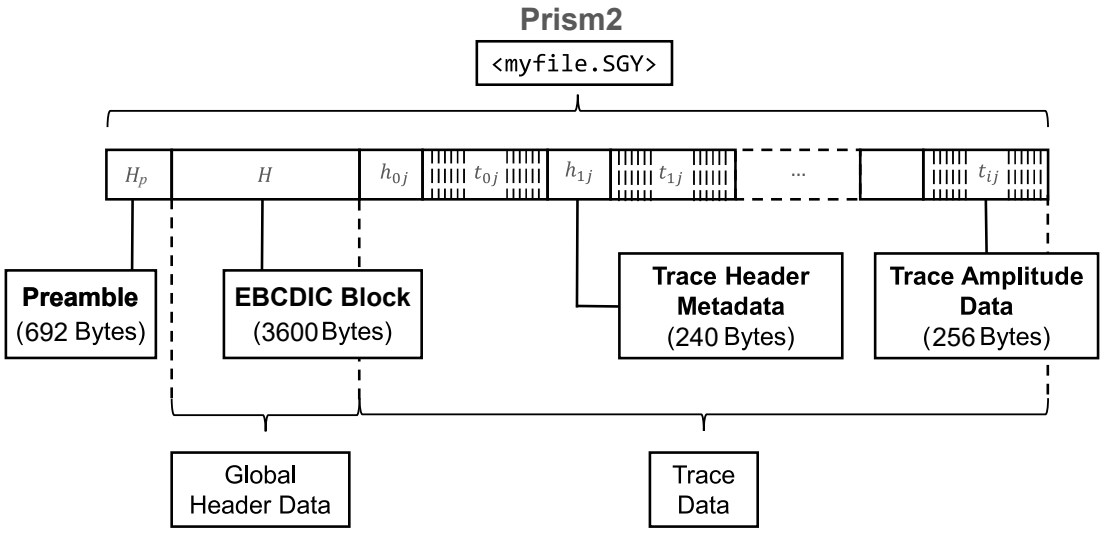


Figure 5.4: Diagram of `SEG-Y` file data structure. Here, $0 \leq i < N_A$ denotes trace index and $0 \leq j < N_S$ denote sample index, where $N_S$ is the total number of samples per trace.

[2] `SEG-Y` — 'International Geophysical Data Format for the Society of Exploration of Geophysicists'.
[3] `EDCDIC` — 'Extended Binary Coded Decimal Interchange Code'.

### *5.4.6 Method – Input Data Checkpointing*

It was noted that the computational overhead associated with the extensive number of read-write operations in handling GPR input data files significantly affected the computational efficiency of the proposed data processing workflow. These operations were observed to account for up to 15% of the total end-to-end data processing runtime for analysis conducted in the previous chapter. This analysis involved processing over 5,000 individual trace measurement files, representing a relatively small RoI volume compared to the subsurface of a typical tunnel or retaining wall. A solution to reduce computational demand associated with read-write operations was required to improve the scalability of the proposed workflow.

During data extraction, the original workflow first opened each target input file, read its contents, and then closed the file, as illustrated in Figure 5.5a. This process was repeated for each individual file, with a buffer of the order of milliseconds between successive operations.

Proposed input data checkpointing functionality utilised a hierarchical intermediary file to store consolidated input data from across all individual GPR input data files, as illustrated in Figure 5.5b. A `.hdf5` file was chosen for this role to combine the low computational overhead of binary files with the structured organisation and readability of ASCII text files.

This augmentation served to reduce the number of unique read-write operations required during the data extraction process whilst maintaining the accessibility of raw input data. As a result, it had significant potential to reduce the proportion of computational runtime associated with data extraction and could further lead to a substantial reduction in the overall runtime of the workflow.

## 5.5 Results and Discussion

This section presents results from performance analysis of the proposed 3D visualisation workflow applied to a fixed-directional GPR dataset recorded in controlled laboratory conditions (as detailed prior).

In Section 5.5.1 of the detection and localisation accuracy achieved by returned 3D spatial profiles is analysed with respect to established ground-truth geometry. This is followed in Section 5.5.2 by a comparison between visualisation outputs recovered using numerical simulated data (see Chapter 4) and those recovered practically using fixed-directional GPR. Finally, computational efficiency subject to the implementation of input data checkpointing is examined in Section 5.5.3.

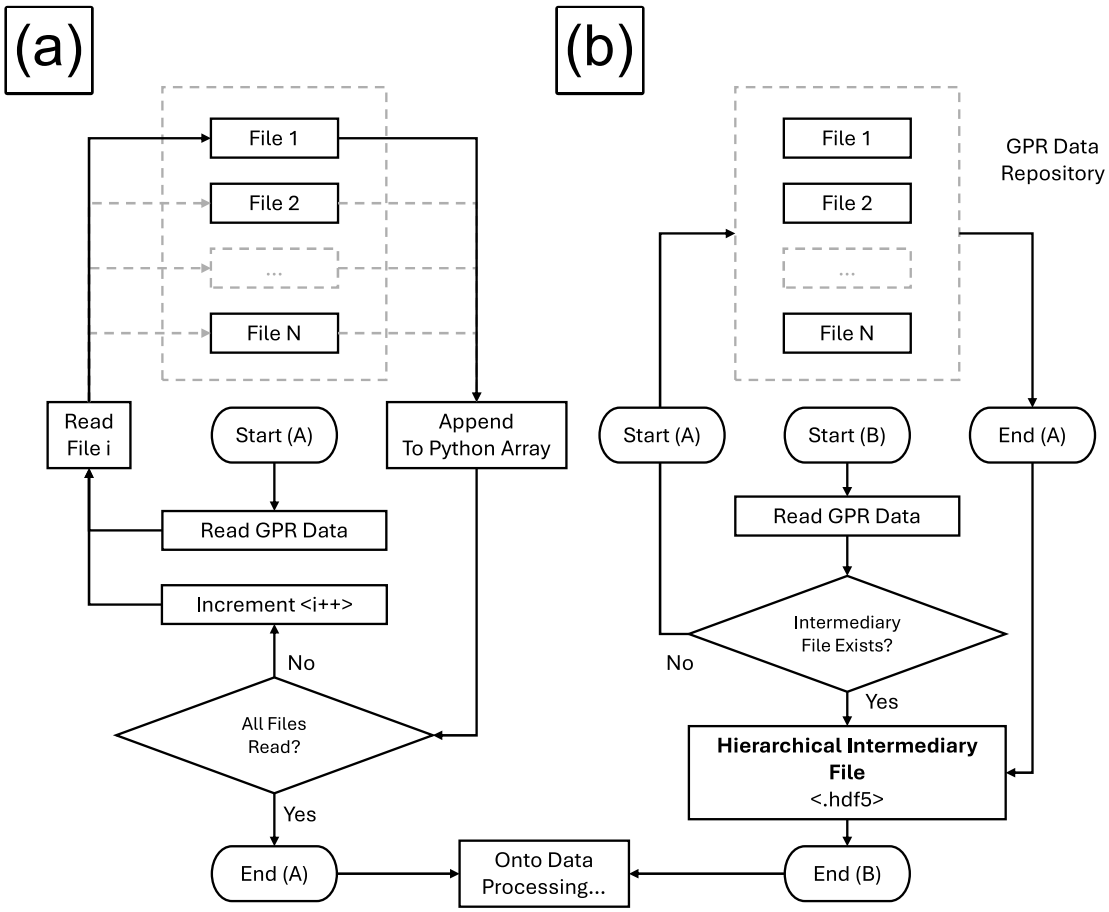


Figure 5.5: Data extraction without (a) and with (b) input data checkpointing.

In accordance with Objectives (1) and (2), a commercial fixed-directional GPR system was used to capture measurement and background calibration datasets in controlled conditions for a tangible RoI volume, consistent with ground-truth geometry used in the previous chapter.

Input data checkpointing functionality was also numerically implemented in accordance with Objective (3), leveraging a `.hdf5`intermediate file to consolidate individual trace measurements from across the full area scan. Application of the original and augmented workflow returned 3D visualisations to underpin performance analysis — in line with Objective (4) — with respect to computational runtime, subsurface anomaly detection and localisation accuracy and comparison to findings from earlier application to simulated GPR data — aligning with Objectives (5)-(7) respectively.

### *5.5.1 Subsurface Anomaly Detection and Localisation*

The 3D spatial profiles recovered from application of the workflow are presented in Figure 5.6. From comparison with the known ground-truth geometry, the sizable cluster resolved for $x > 0.33$m was consistent with the expected location of the larger 100mm diameter sphere $S_1$. Likewise, the cluster resolved for $x < 0.33$m and $z < 0.27$m was consistent with the expected location of the smaller 60mm diameter sphere $S_2$.

Analysis of cluster mid-centres further corroborated findings from the previous chapter, again exhibiting suitable localisation accuracy to within decimetre length scales for each respective target. Most notably, exceptional localisation accuracy was observed for both lateral and vertical cluster mid-centre coordinates, to within a 0.5% and 1% tolerance respectively across the resolved targets.

### *5.5.2 Comparison to Simulated GPR*

Having analysed the quality of returned spatial profiles recovered from the practical fixed-directional GPR dataset in isolation, the next logical step was to compare these profiles with those recovered from the simulation conducted in the previous chapter (see Figure 4.5).

Prior to comparison, it was essential to assess the theoretical resolution limits associated with each measurement configuration. Based on the selected centre frequencies, corresponding bandwidths, and the characteristic length scales of each antenna, both the practical and simulated setups were expected to achieve comparable range resolution to within $O(10mm)$, which would be sufficient to resolve the targets.

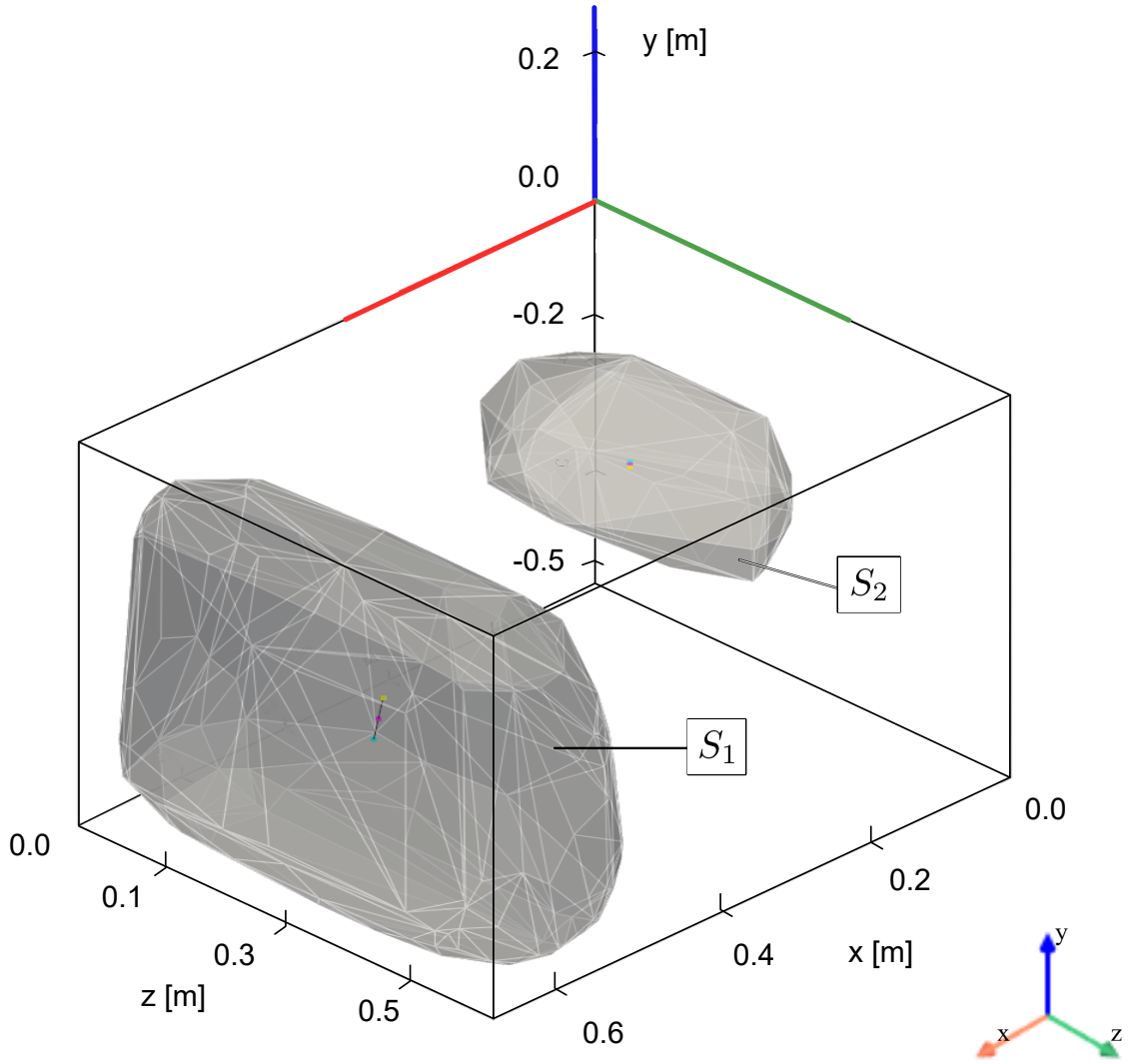


Figure 5.6: Returned spatial profiles from application of the proposed 3D visualisation workflow to practical GPR input data, generated via area scans using a commercial fixed-directional GPR system, on an RoI volume containing three spherical metallic targets.

Preliminary estimates of cross-range resolution — which was of greater relevance in this context due to the consistent target depth — suggested a similar resolution scale, with the practical setup theoretically capable of delivering up to twice the resolution of the simulated configuration However, it was conceivable that, despite the separation from the targets, the physical boundary of the RoI volume (a constraint unique to the practical setup) could influence, and potentially limit, the achievable cross-range resolution. On this basis, the resolution characteristics were deemed sufficiently comparable to justify a direct comparative analysis of the visual outputs produced by both configurations, for which key observations are discussed below.

Both sets of visualisations very clearly resolved the 100mm diameter sphere $S_1$ and the smaller 60mm diameter sphere $S_2$. The convex hulls returned from visualisation of the fixed-directional GPR dataset exhibited a higher degree of regularity in the size and relative difference in orientation between its constituent faces than those from the simulated dataset, yielding a smoother boundary interface profile more faithful to that of the spherical targets. It was suspected that the improved fidelity was linked to the higher density of unique sample points recorded across the RoI volume by the fixed-directional GPR system compared to the numerical simulation. During the grid regularisation stage of the workflow, the higher density of sample points would inherently yield a smoother scalar field and subsequently smoother cluster boundaries post-segmentation, as observed.

A further noteworthy observation was significantly increased exaggeration of the cluster associated with $S_2$ in the direction of $S_3$, to the point where the cluster footprint had intersected the footprint associated with $S_3$ — compared to the more subtle extension of the cluster observed in the previous chapter. This observation provided stronger evidence than results from the previous chapter, to suggest that the workflow had indeed detected the presence of the 30mm sphere, but that localisation at this smaller length scale was approaching the limit of the achievable spatial resolution, causing the profile to coalesce with the cluster associated with $S_2$ during segmentation. This motivated a more formal, quantitative assessment into achieved levels of spatial resolution in subsequent laboratory benchmarking (see Chapter 6), and further interest in spatial resolution enhancement techniques that could be integrated into a future refinement of the workflow (see Chapter 7).

Lastly, it was noted that the spatial profile of $S_1$ in the fixed-directional GPR results exhibited significantly greater vertical and lateral exaggeration than its counterpart in the simulation results. Moreover, lateral exaggeration observed in $x$ was notably less than that observed in $z$. Critically, from a practical survey standpoint (see Section 7.3.1), the exaggeration of anomaly profiles was actually beneficial, as this phenomenon better emphasised the presence of structural anomaly reducing the risk of oversight in larger scale datasets. From a scientific standpoint, explanations for a mechanism behind this phenomenon were of interest.

The discontinuous boundaries of the physical RoI volume were suspected to have contributed to observations, which unlike the absorbing boundaries implemented in gprMax, reflected backscatter from the spherical targets back towards them. Given the lateral and vertical symmetry of both the targets and boundary, secondary backscatter from the boundary interface would be reasonably uniform[4] and naturally propagate across a significant portion of the $y$ and $z$ axes respectively, before eventually attenuating to the level of background noise. As observed, a significant associated increase in the footprint of returned segmented clusters follow (across both axes) would result.

To explain the reduced lateral exaggeration of the cluster in $x$ compared to $z$, it was noted that lateral exaggeration in $x$ extended fully up to the RoI boundary with $x > 0$ but did not extend beyond the midpoint of the RoI volume in the other direction. The expected interference between wavefronts from backscatter associated with $S_1$ and combined backscatter from $S_2$ and $S_3$ provided a feasible explanation for this. Given the relative placement of the targets in the XZ and XY planes respectively, it was reasonable that more ray paths associated with backscatter wavefronts would intersect in the vicinity of the midpoint than would occur directly below either individual target — principally $S_1$.

### *5.5.3 Elapsed Workflow Runtime*

As in the previous chapter, elapsed runtime was recorded across 20 independent executions of the full data processing workflow. A subsequent 20 independent executions were performed with newly integrated input data checkpointing functionality enabled.

Results are presented in Figure 5.7.

Observed runtimes of the original workflow ranged between 96.4 seconds to 117.3 seconds, averaging at 107.8 seconds across all 20 executions. A significant 12% reduction in average runtime was observed with input data checkpointing functionality enabled, with elapsed runtime averaging 88.2 seconds. This was accompanied by a noticeable reduction in the average proportion of data processing runtime concerning data extraction, which decreased significantly from a maximum of 15% to just 4.5%.

A further significant reduction of more than 60% was also observed for the associated IQR between respective measurement sets, implying that input data checkpointing had considerably increased the stability of the data processing workflow.

[4]Subject to minor variations associated with the inherent heterogeneity of a physical backfill (when considered at the microscale).

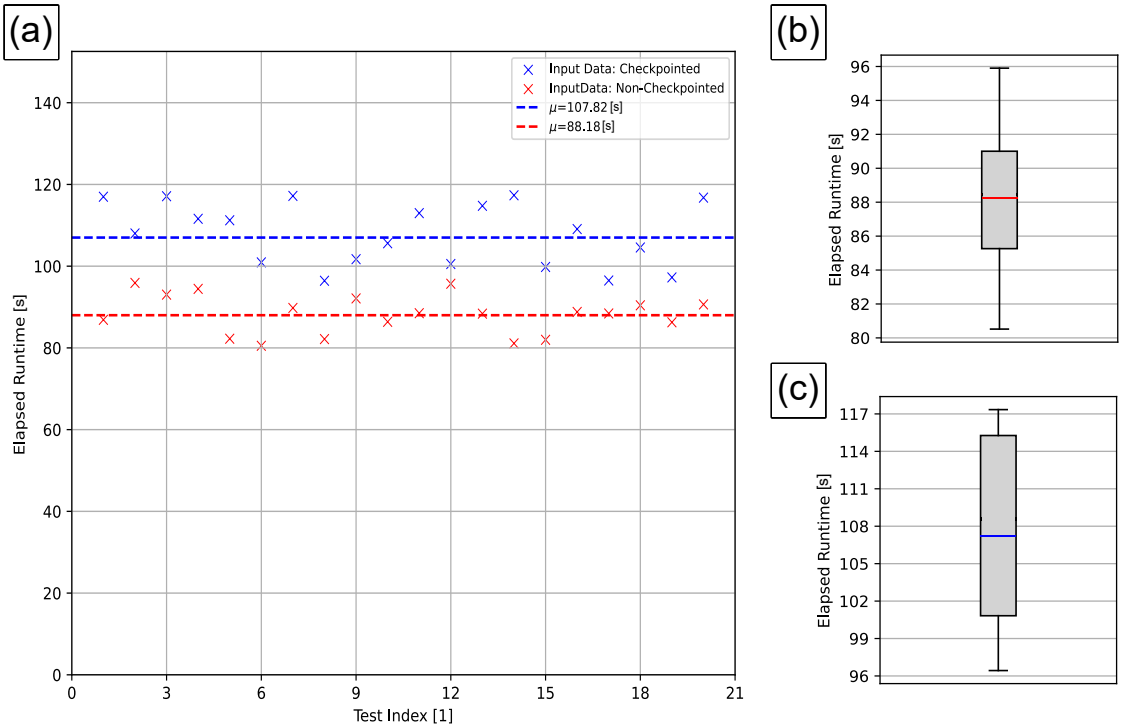


Figure 5.7: Breakdown of elapsed 3D visualisation workflow runtime averaged over 20 independent executions (a) with associated box and whisper plots (b,c) relaying extremal range, mean and IQR. Blue and red markers indicate measurements when the workflow imported checkpointed data, and non-checkpointed data, respectively.

These findings were consistent with the principle behind the augmented data extraction procedure implemented, since the act of checkpointing fundamentally reduced the unique number of read-write operations involved during data extraction. In this case, operations for opening, reading, and closing two sets of 8,290 individual `.s1p` files were reduced to accessing single `.hdf5` file containing the consolidated dataset. Furthermore, as in the previous chapter, the observed average runtime remained within the order of seconds to minutes, even with a more than tenfold increase in RoI volume. This reliable performance further demonstrated the high processing efficiency of the workflow and motivated the utilisation of data checkpointing functionality for work performed in all subsequent chapters.

## 5.6 Summary

This chapter presented performance analysis of the proposed 3D visualisation workflow, based on data captured of a physical RoI volume with known ground-truth geometry. Measurements were recorded under controlled laboratory conditions using a commercial fixed-directional GPR data collection system. By incorporating practical measurements in this second stage of laboratory benchmarking, factors such as the heterogeneity of the background media and the discontinuous nature of the physical RoI boundary contributed to the recovery of a more authentic dataset. This approach facilitated assessment of the workflow's effectiveness in a more realistic survey environment, whilst maintaining well-established ground truth geometry.

Through the design and fabrication of a bespoke physical RoI volume, it was possible to capture a practical area scan of the subsurface using a Zond 12e Advanced GPR data collection system, 1GHz antenna and odometer wheel to record lateral displacement along each constituent transect.

A key outcome was the successful deconstruction of the `SEG-Y`measurement data format, coupled with the practical implementation of a bespoke Python subroutine to extract the raw transect data, which encoded both antenna position and backscatter amplitude.

Subsequent quantitative and qualitative analyses of the returned 3D visualisations revealed exceptional lateral and vertical localisation accuracy when compared to the known target geometry. Notably, mid-centre coordinate agreement was within fractional tolerances of 0.5% and 1% respectively. Furthermore, a viable mechanism for the observed exaggeration of the footprint for the larger 100mm diameter sphere along the y and z axes was identified, attributed to interactions between backscattered wavefronts and the discontinuous RoI boundaries.

Beneficially, this phenomenon increased the visibility of subsurface anomalies in the returned 3D visualisations compared to those based on simulated GPR data. The greater prevalence of smaller scale structural anomalies within, thereby improved detection performance, especially for future consideration of larger scale survey volumes (see Chapter 7).

In conjunction, to improve the computational efficiency of the proposed workflow, a higher efficiency strategy was devised for the collective data extraction process of the proposed workflow. This input data checkpointing functionality consolidated raw measurement data — across each individual input file generated by the data collection system utilised — into a standalone `.hdf5` intermediary file.

In principle, the process had potential to significantly reduce the number of unique read-write operations required during data processing, therein reducing associated latency, and increasing overall computational efficiency. This was evidenced by a significant 12% observed reduction in overall elapsed data processing runtime across 20 independent executions of the augmented workflow. High processing efficiency was also demonstrated through the return of full renders of 3D spatial profiles in an average of 94.8 seconds.

Overall, the results in this chapter corroborate the workflow's effective performance and support the initial conclusions drawn from simulated input data during the first stage of laboratory benchmarking.

# Chapter 6. Benchmarking III – Hybrid-Rotational GPR

In this chapter, the performance of the developed 3D visualisation workflow is analysed using a practical hybrid-rotational GPR dataset, recorded in a controlled environment. Unique miniaturised measurement equipment is developed to enable data collection in the laboratory. The investigation further examines the impact of segmentation parameter selection on the quality of returned spatial profiles.

## 6.1 Introduction

The final stage of laboratory benchmarking shifted from analysing workflow performance with fixed-directional GPR data, to data from a hybrid-rotational GPR system. Evidence of effective performance, consistent with findings from previous chapters, would justify progression to field testing. As prior, grounds for appraisal remained consistent with previous benchmarking tests.

## 6.2 Motivation

A miniaturised hybrid-rotational GPR setup was required for this investigation, as the larger system utilised for the feasibility study was impractical for operation in a lab environment. Developing a bespoke system design also provided an opportunity to enhance boresight positioning accuracy (see Section 2.7.5) through strategic hardware and programming choices, alongside optimise scan frequency selection and validate measurement accuracy. Being bespoke, it was also essential to demonstrate that all subsystems operated effectively when interfaced together, and returned output consistent with findings from earlier benchmarking.

In these later stages of laboratory benchmarking, preparations for field testing were also being considered, for which a clearer understanding of how segmentation parameters influence 3D spatial profiles was of interest to guide baseline reference value selection. With isovalue selection largely predetermined by the Shimazaki Shinomoto method, focus was directed toward HDBSCAN's proximal-segmentation parameters minimum cluster size and the granularity tuning parameter, which provided the most natural candidates for immediate study.

## 6.3 System Design

This section details development of the proposed hybrid-rotational GPR setup for data collection in the laboratory. A high-level overview of system architecture is provided in Section 6.3.1. Mechatronic design is explored in Section 6.3.2, discussing both mechanical and electrical subsystems. Finally, a summary of measurement, automation and control strategies is outlined in Section 6.3.3.

### *6.3.1 System Architecture*

In developing the first hybrid-rotational GPR system for laboratory data collection, efforts built on refinements from the feasibility study. The design followed best practices, prioritising the use of readily available components and multifunctional hardware to increase design efficiency and minimise resource duplication. Additional practical considerations extended to: (i) minimising extraneous EM-interference; (ii) ensuring precise replicability of scan passes and deliver more reproducible results, alongside (iii) creating a versatile design basis, to provide a system suitable for both laboratory investigations and planned field testing.

To address (i), similar to the approach followed in [327], the system was designed to operate within a 3M-Compliant Anechoic Test Chamber[1], manufactured by Global EMC [328]. Its design was based on an 3D polar plotter, which used two independently programmable stepper motors to enable precise antenna boresight positioning along the lateral ($x$) and azimuthal ($\theta$) axes, respectively. Automating motor control addressed (ii), while adoption of a system architecture comprised from standalone-operable modules satisfied requirement (iii). A visual summary of the modules is provided in Figure 6.1a.

### *6.3.2 Mechatronics*

The finalised system design, illustrated in Figure 6.1b, required the concurrent development and integration of multiple subsystems, interfacing both mechanical and electrical elements. For efficiency, and to maintain alignment with system prototype developed for the feasibility study, permission was secured to use the T-Vision system's custom TEM-feedhorn antenna as the basis for the new design. Scaled diagrams of antenna geometry are presented in Figure 6.2.

[1]Rated immunity from EM-radiation sources between 80-6000MHz (compliant to standard IEC/EM61000-4-3); rated emissions containment for EM-radiation sources between 30-6000MHz (compliant to standard CISPR 16-1-4).

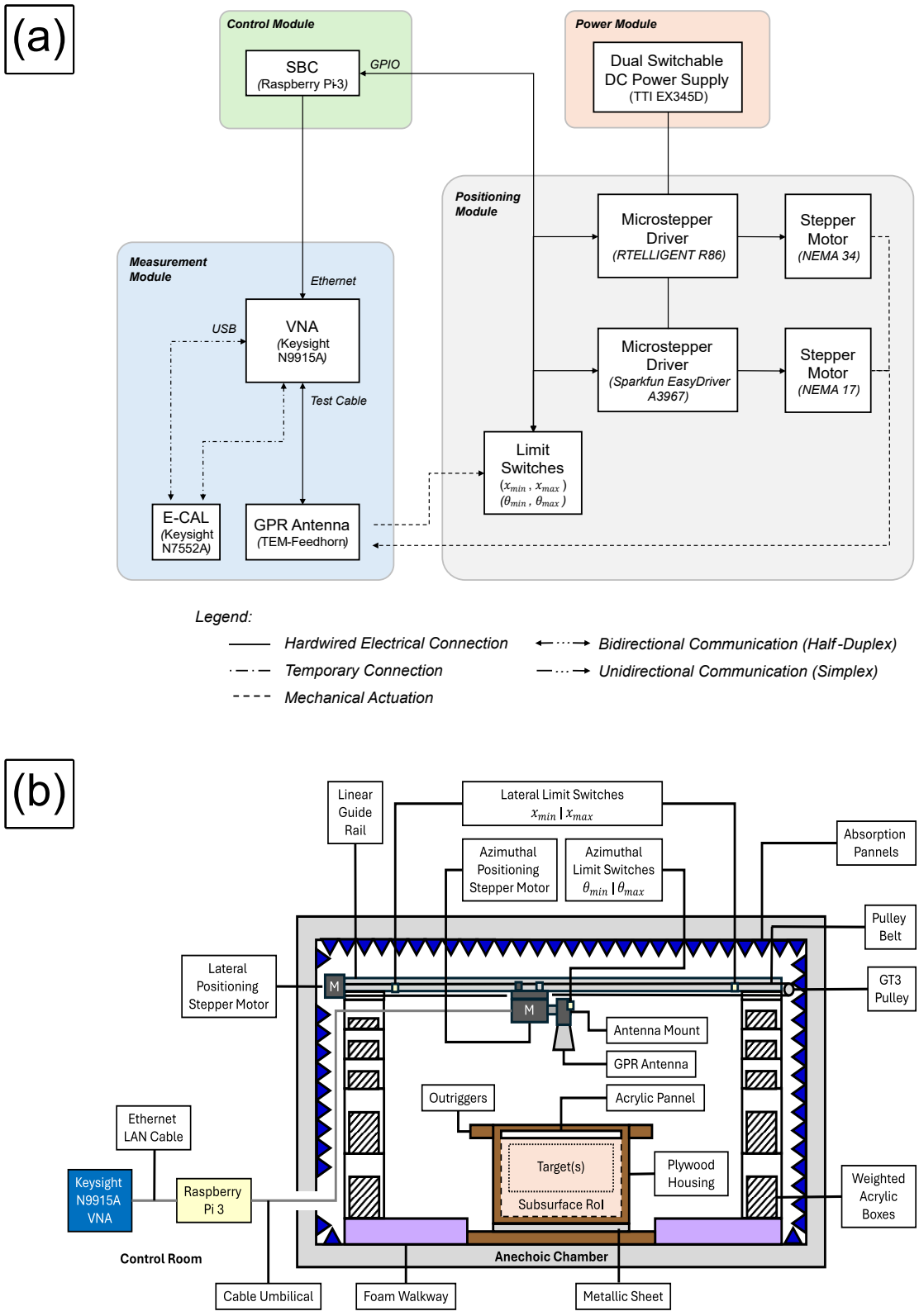


Figure 6.1: Modules (a) and system diagram (b) for hybrid-rotational GPR lab work.

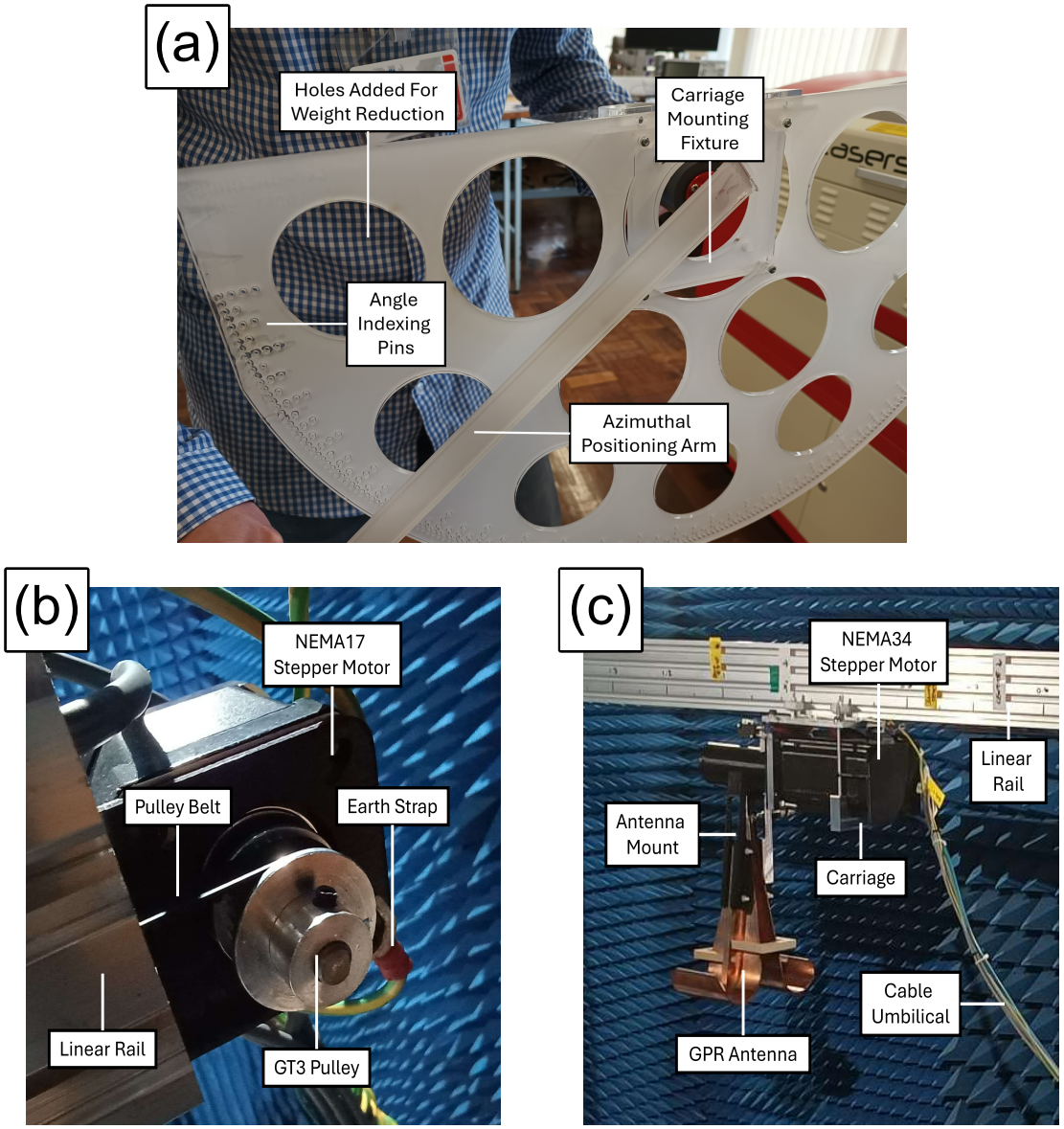


Figure 6.2: Antenna boresight positioning for laboratory hybrid-rotational GPR system. Initial manual positioning (a) was updated to an automated approach. A NEMA17 stepper motor (b) facilitated lateral positioning was achieve, which via a belt drive, advanced the carriage housing a NEMA34 stepper motor (c) for azimuthal positioning.

Precise and repeatable antenna boresight positioning was initially achieved manually using the laser-cut indexing mechanism shown in Figure 6.3a. To improve efficiency, the system was modified to instead utilise two independently controlled bipolar NEMA[2] stepper motors. Azimuthal rotation employed a NEMA34 motor paired with an RTELLIGENT R86 driver, directly driving a custom 3D-printed antenna mount secured to the motor shaft via interference fit and grub screw, as shown in Figure 6.3b. Access slots were included to facilitate tightening of the measurement cable connectors, which doubled as mounting sites for the E-CAL module during VNA calibration. To ensure accurate positioning even at extremal azimuthal limits, it was essential that the motor's holding torque exceeded $4Nm$, which was beyond the typical $3Nm$ upper limit of a standard NEMA23 model [323].

This assembly was mounted on a carriage suspended beneath a 1.2m linear rail spanning the survey area. Lateral movement was achieved via a GT3 pulley belt driven by a NEMA17 motor linked to a Sparkfun EasyDriver (A3967 chipset), as shown in Figure 6.2c. Micro-stepping was enabled on both drivers, providing 40,000 and 3200 steps per revolution for azimuthal and lateral motion, respectively. This increased positioning precision, smoothed carriage movement — reducing strain on the antenna connector — and minimised current spikes during coil excitation, thereby reducing unwanted EM-interference at source.

The separation between the antenna and contact surface was maximised within the available laboratory space (up to approximately 2m), as was the surveyed volume ($0.66m \times 0.34m \times 1.04m$). For this setup, it was not considered necessary to integrate a parabolic reflector, given the reduced maximum survey depth compared to the original feasibility study and the lower expected wavefront energy loss from geometric spreading over the shorter air-launch distance.

Hardwired connections connected the equipment in the anechoic chamber to their respective controllers. A cable umbilical ran 5m from the carriage into a neighbouring room. Current-limited power was delivered to motors through a pair of shielded cables, connected to a TT1 EX345D dual switchable benchtop DC power supply. Positioning feedback was achieved using similar cables, which connected mechanical limit switches — mounted at extrema of the linear rail and antenna mount — to the GPIO pins of Raspberry Pi 3 Single Board Computer (SBC). To reduce line noise, common anode configuration was selected for GPIO hookups.

The SBC master unit controlled both antenna positioning and triggered GPR measurements, the latter performed by a FieldFox N9915A portable VNA interfaced with the SBC via an RJ45 Ethernet connection. The VNA was directly connected to the antenna via a 6mm diameter, super-flexible low loss test cable with dual male Sub-Miniature Version A (SMA) connectors, manufactured by Atlantic Microwave Ltd. It was rated to deliver 81% transmission efficiency for signals up to 26.5GHz, at a minimal bend radius of 25mm.

[2]National Electrical Manufacturers Association (NEMA).

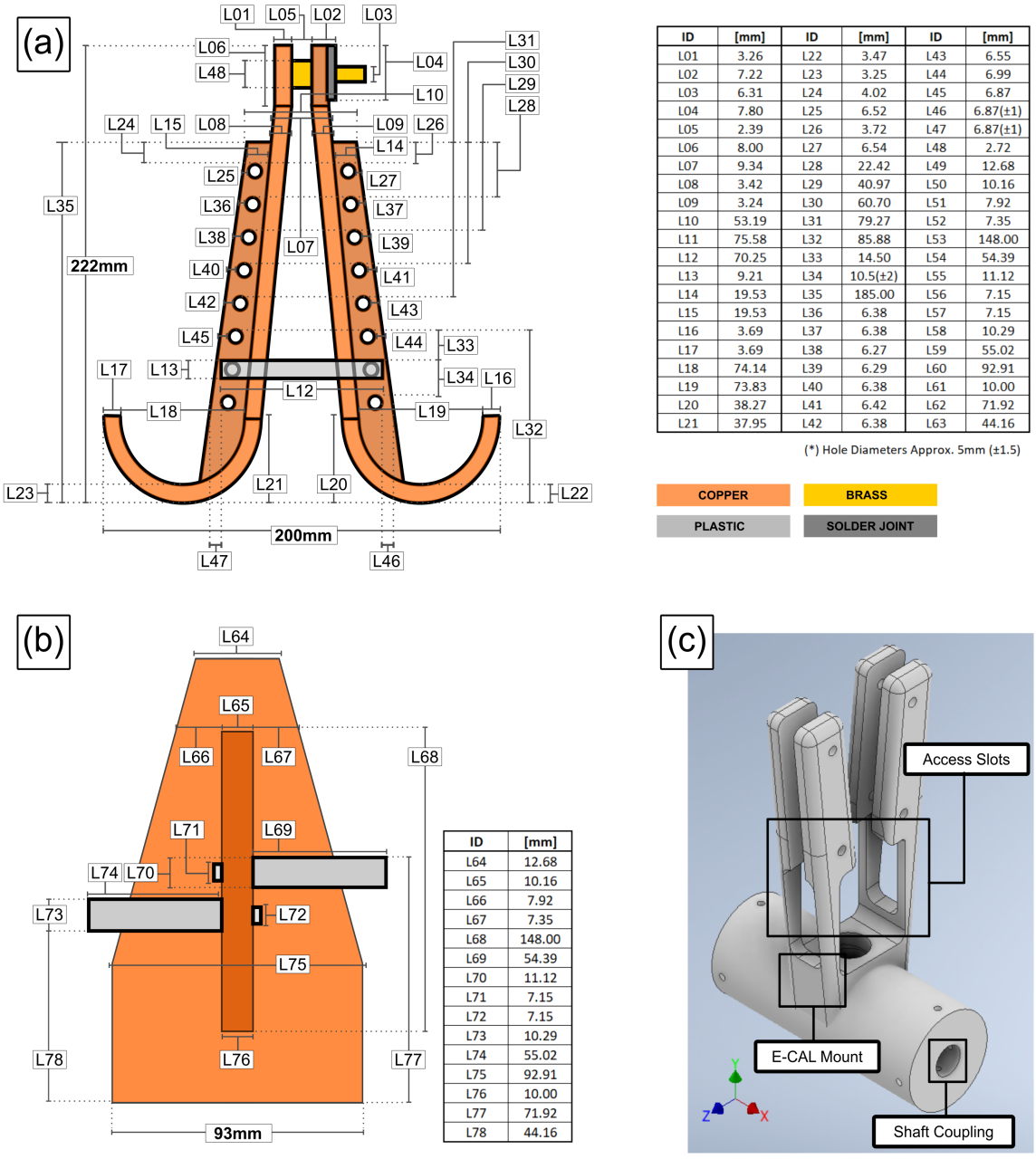


| ID | [mm] | ID | [mm] | ID | [mm] |
|---|---|---|---|---|---|
| L01 | 3.26 | L22 | 3.47 | L43 | 6.55 |
| L02 | 7.22 | L23 | 3.25 | L44 | 6.99 |
| L03 | 6.31 | L24 | 4.02 | L45 | 6.87 |
| L04 | 7.80 | L25 | 6.52 | L46 | 6.87(±1) |
| L05 | 2.39 | L26 | 3.72 | L47 | 6.87(±1) |
| L06 | 8.00 | L27 | 6.54 | L48 | 2.72 |
| L07 | 9.34 | L28 | 22.42 | L49 | 12.68 |
| L08 | 3.42 | L29 | 40.97 | L50 | 10.16 |
| L09 | 3.24 | L30 | 60.70 | L51 | 7.92 |
| L10 | 53.19 | L31 | 79.27 | L52 | 7.35 |
| L11 | 75.58 | L32 | 85.88 | L53 | 148.00 |
| L12 | 70.25 | L33 | 14.50 | L54 | 54.39 |
| L13 | 9.21 | L34 | 10.5(±2) | L55 | 11.12 |
| L14 | 19.53 | L35 | 185.00 | L56 | 7.15 |
| L15 | 19.53 | L36 | 6.38 | L57 | 7.15 |
| L16 | 3.69 | L37 | 6.38 | L58 | 10.29 |
| L17 | 3.69 | L38 | 6.27 | L59 | 55.02 |
| L18 | 74.14 | L39 | 6.29 | L60 | 92.91 |
| L19 | 73.83 | L40 | 6.38 | L61 | 10.00 |
| L20 | 38.27 | L41 | 6.42 | L62 | 71.92 |
| L21 | 37.95 | L42 | 6.38 | L63 | 44.16 |

(*) Hole Diameters Approx. 5mm (±1.5)

COPPER | BRASS | PLASTIC | SOLDER JOINT

| ID | [mm] |
|---|---|
| L64 | 12.68 |
| L65 | 10.16 |
| L66 | 7.92 |
| L67 | 7.35 |
| L68 | 148.00 |
| L69 | 54.39 |
| L70 | 11.12 |
| L71 | 7.15 |
| L72 | 7.15 |
| L73 | 10.29 |
| L74 | 55.02 |
| L75 | 92.91 |
| L76 | 10.00 |
| L77 | 71.92 |
| L78 | 44.16 |

Figure 6.3: Scaled diagrams of TEM-feedhorn antenna front (a) and side (b) elevations, alongside a CAD render of its bespoke mounting fixture (c).

An additional micro USB-B connector supplied 5V power from the VNA to a Keysight N7552A E-CAL module during calibration. A full electrical schematic of the finalised system design is presented in Figure 6.4.

### *6.3.3 Measurement, Automation and Control*

Dedicated Python-based firmware was developed for the SBC to facilitate automated sequential control of antenna boresight positioning and VNA measurement triggering during a scanning pass (Appendix A). The process generated a cylindrical-sector point cloud through the parallel stacking successive rotational transects, which uniformly spanned both the lateral and azimuthal extent of the full survey volume.

Following initial lateral and azimuthal homing, the antenna advanced to a predefined starting position and cycled through increasing azimuth angles (see Figure 6.5) pausing at each to record data. Upon reaching the programmed maximum azimuth, the system rehomed azimuthally, incremented the lateral position, and repeated the process up to and including the maximum lateral position.

To enhance the positional feedback system, a digital debounce subroutine was integrated. Due to the necessary proximity of data and motor power lines within the umbilical — required to avoid obstructing the antenna's rotation plane — there was potential for residual line noise to interfere with limit switch state checks. This could occasionally result in false-positives (unwarranted emergency stops) or false-negatives (missed emergency triggers). Digitally implementing debounce to the limit state read algorithm granted precise control over the activation threshold for state changes, which enabled fine-tuning for improved reliability. This stabilised limit switch performance, prevented fouling and eliminated intermittency.

The scanning process was called using the SBC's terminal interface, which imported pre-defined scan trajectory parameters from a separate ASCII text file (e.g. incrementations, extremal limits, etc.). Parameters for $S_{11}$ trace measurements were manually configured using the VNA's native interface and saved to its onboard SD card. Resulting filenames were prefixed by the concatenation of the current trace and transect indexes, which automatically sorted them ready for data processing. Sequential measurements were triggered independently, via an SCPI[3] packet transmitted over ethernet from the SBC.

[3]Standard Commands for Programmable Instruments (SCPI).

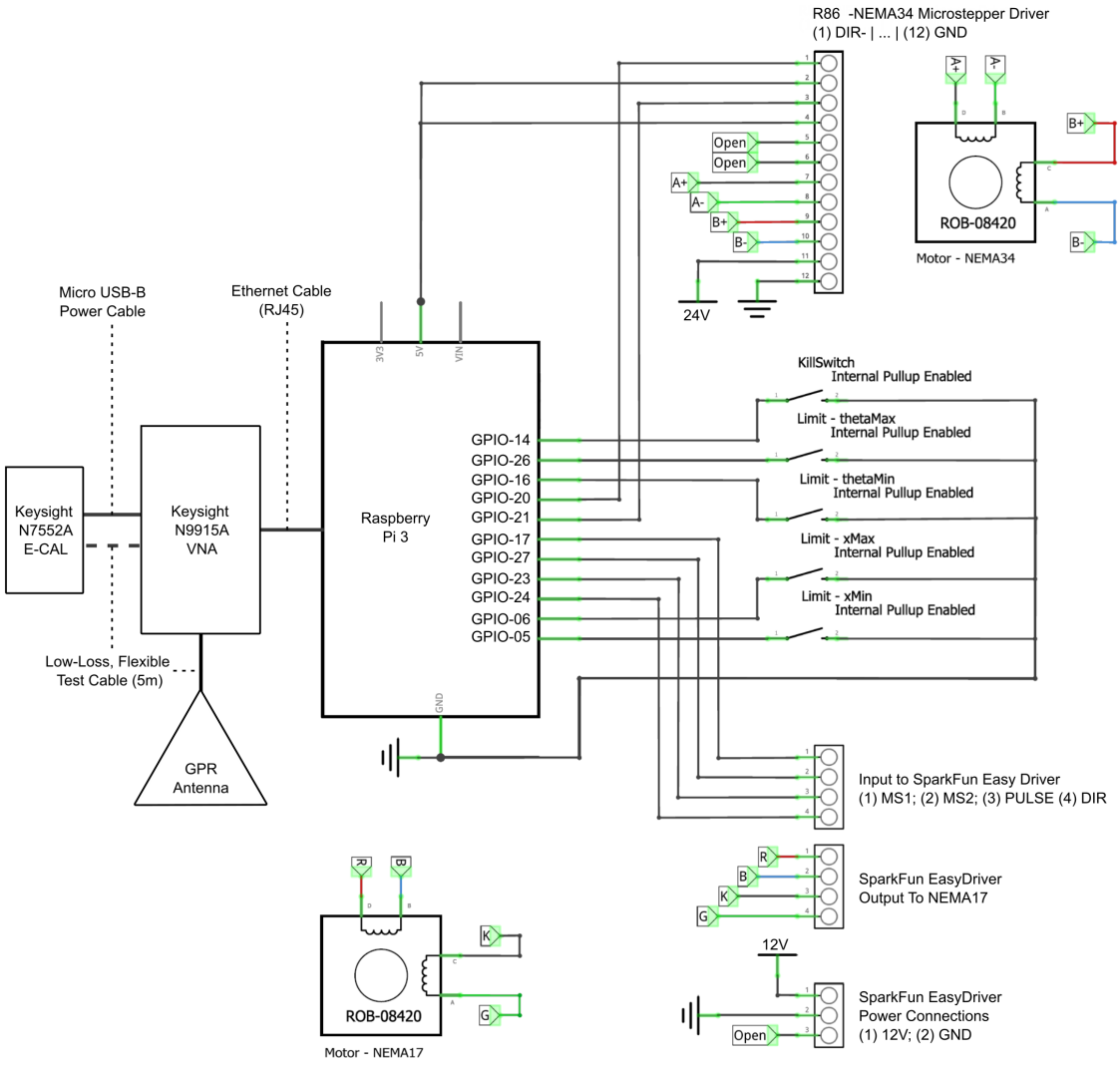


Figure 6.4: Circuit diagram for the finalised laboratory hybrid-rotational GPR system.

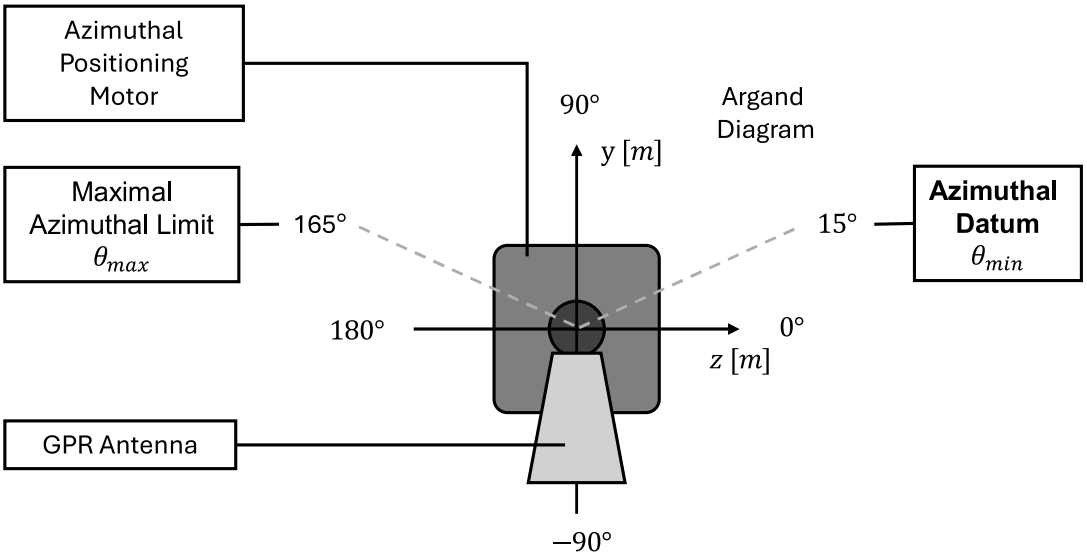


Figure 6.5: Diagram showing azimuthal limits of antenna rotation. When viewed in the direction of lateral advance, values resemble an Argand Diagram, with 0° aligned to the horizontal half-line $z > 0$ intersecting the centre of rotation. Limit switches above the horizontal maximise achievable azimuthal coverage and facilitate practical mounting.

To ensure trace measurement accuracy, VNA calibration was performed to suppress high-intensity internal reflections within the antenna cable, primarily associated with localised impedance mismatches — particularly in the vicinity of sharp bends as shown in Figure 6.6a (e.g. close to the antenna connector). Calibration involved temporarily mounting the E-CAL module to the antenna mount as shown in Figure 6.6b, ensuring both connectors aligned, then executing the VNA's inbuilt 1-Port Short-Open-Load routine to update the internal compensation coefficients. Further details on this standard procedure are available in [329] and [330]. Note that antenna movement during scan passes was observed to have negligible impact on returned measurements, with minimal bend radii consistently exceedingly twice the cable's minimum rating ($r > 50mm$) throughout. This warranted no additional mitigation action to be pursued concerning internal backscatter artifacts.

To suppress backscatter artifacts from the external measurement environment that were not of direct interest to the survey volume (e.g. backfill media, container sidewalls, linear rail), a background calibration was performed. This involved an initial scanning pass without target geometry present followed by subsequent main passes with the geometry in place, as illustrated in Figure 6.6c and Figure 6.6d, respectively. During data processing, the background trace at each boresight position was subtracted from the corresponding trace in the main pass.

Through judicious selection of motor drivers, control over antenna boresight positioning along each axis reduced to regulating the voltage level of just two GPIO pins. One pin set the rotation direction — HIGH for clockwise, LOW for anticlockwise. The other used Pulse Width Modulation (PWM) in four-step coil excitation loop (one per motor coil) to advance the motor through a full rotation. Rotation speed was controlled by adjusting the delay interval between successive excitations, with a minimum interval of $50ms$ required to allow adequate time for coil energisation and de-energisation across each state change.

The system's movement control also required a one-time calibration. It was more intuitive to define the scan parameters in terms of the physical distance metrics associated with lateral and azimuthal positioning, as opposed to dimensionless motor step counts.

Adopting the azimuthal naming convention illustrated in Figure 6.5 — selected to resemble an Argand diagram based on circular polar coordinates in the plane of rotation — orientation values associated with the extremal limits of rotation were first established. The antenna was advanced from its home position to horizontal, with alignment verified using a spirit level. Markers were etched on the surrounding motor housing at both positions. The antenna mount was then removed, and the home angle measured with a protractor, yielding 15°. By symmetry, the corresponding maximal limit of 165° was established.

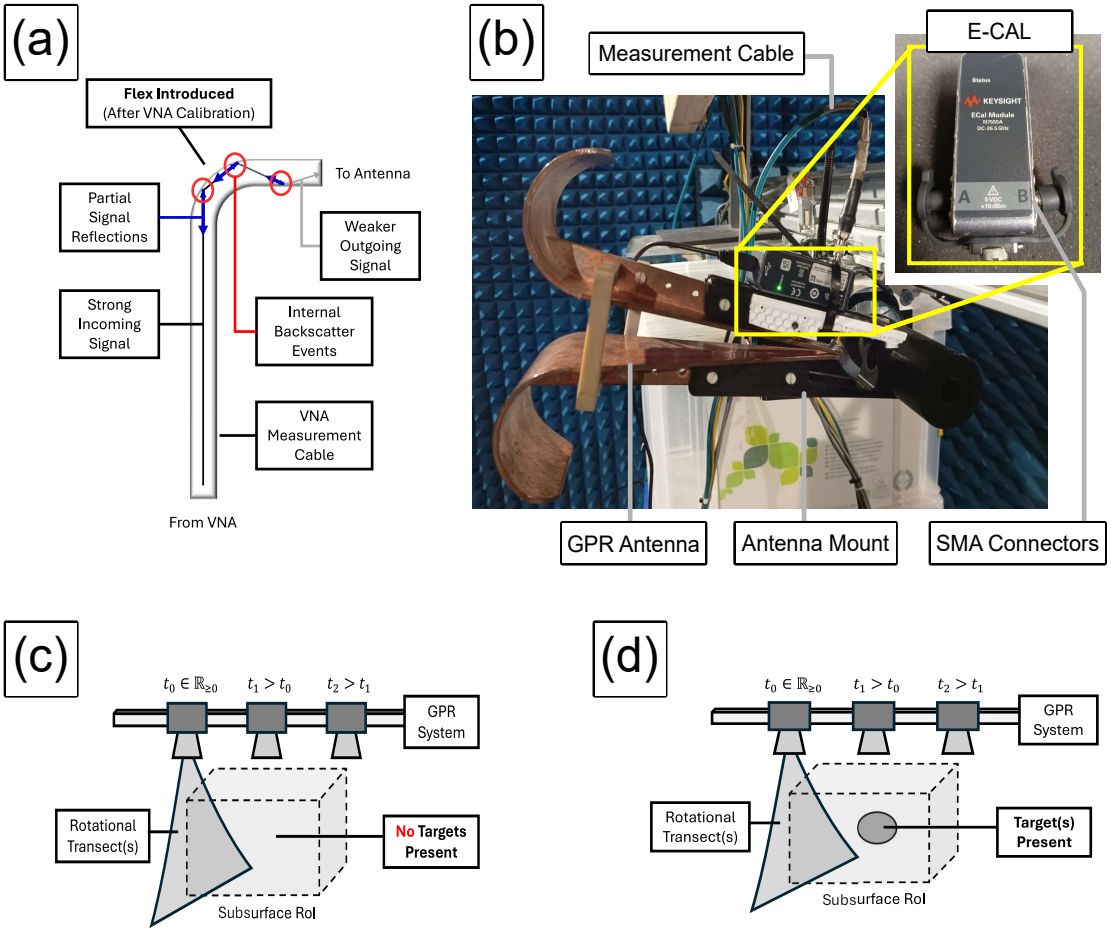


Figure 6.6: System calibration. Measurement cable flex can generate unwanted signal backscatter, especially within the vicinity of sharp bends (a). VNA calibration uses an E-CAL module (b) to suppress these artifacts. Background calibration goes further, subtracting measurements of a scanning pass devoid of target geometry (c) from those with target geometry present (d), this in turn suppresses signal artifacts associated with non-target geometry in the external environment.

The natural mapping to convert degrees of antenna rotation,$\theta$ into a corresponding motor step count was given by

$$N_\theta = \frac{\theta_{\mu_{360}}}{360}, \tag{6.1}$$

where $\mu_{360}$ denotes the number of micro-steps per full revolution of the NEMA34 motor.

A similar mapping would convert the lateral displacement, $x$, of the antenna boresight vector in metres — relative to the lateral datum — to the number of micro-steps advanced by the NEMA17 motor. It was expressed

$$N_x = \frac{x_{\mu_{360}}}{np}, \tag{6.2}$$

where $n = 20$ denotes the number of teeth on the GT3 pulley and $P = 3mm$ denotes the pitch between the teeth (measured centre to centre).

| **Lateral Positioning Calibration** | **Expected Displacement [mm]** | | | |
|---|---|---|---|---|
| | 0.1 | 0.5 | 1.0 | 1.4 |
| Cumulative Absolute Deviation [mm] | 0.5 | 1.0 | 2.0 | 2.5 |
| | 0.5 | 2.0 | 2.5 | 3.0 |
| | 0.0 | 0.5 | 2.0 | 3.0 |
| | 0.5 | 0.5 | 2.0 | 2.5 |
| | 0.5 | 1.5 | 2.5 | 3.0 |
| | 0.5 | 1.5 | 2.5 | 2.5 |
| | 0.5 | 1.5 | 2.0 | 3.0 |
| | 0.5 | 1.0 | 2.0 | 2.5 |
| | 0.5 | 1.5 | 2.5 | 3.0 |
| | 0.5 | 1.5 | 2.0 | 2.5 |
| | 0.5 | 2.0 | 2.5 | 3.0 |
| | 0.5 | 1.5 | 2.5 | 2.5 |
| | 0.5 | 1.5 | 2.5 | 3.0 |
| | 0.5 | 1.5 | 2.5 | 3.0 |
| | 0.5 | 2.5 | 2.5 | 3.5 |
| | 1.0 | 2.0 | 2.5 | 3.0 |
| | 0.5 | 1.0 | 2.0 | 2.5 |
| | 0.5 | 2.0 | 2.5 | 3.0 |
| | 0.5 | 2.0 | 2.5 | 3.0 |
| **Mean [mm]** | 0.48 | 1.53 | 2.33 | 2.85 |

Table 6.1: Hybrid-rotational GPR lateral positioning calibration results.

A preliminary test was designed to calibrate the positioning module and validate both theoretical mappings. It compared observed antenna displacements for multiple target values, each converted to a step-count using the relevant mapping. For lateral positioning calibration, the antenna was advanced sequentially through $x \in [0.1, 0.5, 1.0, 1.4]m$, pausing at each position for observed displacement to be manually recorded using a tape measure. Measurement resolution was to within $\pm 0.5mm$. This process was repeated 20 times, with findings summarised in Table 6.1.

An average 3mm cumulative positioning deviation was consistently observed by $x = 1.4m$, accurate to within 0.25% of the maximal traversal distance. This tolerance was considered more than sufficient to validate lateral positioning accuracy.

| **Azimuthal Positioning Calibration** | **Expected Displacement [deg.]** | | | |
|---|---|---|---|---|
| | 45 | 90 | 135 | 180 |
| Cumulative Absolute Deviation [deg.] | 0.02 | 0.06 | 0.08 | 0.17 |
| | 0.03 | 0.04 | 0.11 | 0.13 |
| | 0.01 | 0.05 | 0.10 | 0.12 |
| | 0.01 | 0.03 | 0.08 | 0.18 |
| | 0.03 | 0.06 | 0.12 | 0.15 |
| | 0.02 | 0.04 | 0.09 | 0.13 |
| | 0.02 | 0.05 | 0.11 | 0.10 |
| | 0.02 | 0.04 | 0.06 | 0.16 |
| | 0.03 | 0.05 | 0.11 | 0.17 |
| | 0.02 | 0.04 | 0.08 | 0.14 |
| | 0.03 | 0.05 | 0.09 | 0.19 |
| | 0.02 | 0.03 | 0.10 | 0.14 |
| | 0.02 | 0.06 | 0.08 | 0.13 |
| | 0.03 | 0.04 | 0.09 | 0.15 |
| | 0.03 | 0.04 | 0.06 | 0.18 |
| | 0.03 | 0.05 | 0.11 | 0.12 |
| | 0.02 | 0.04 | 0.11 | 0.17 |
| | 0.03 | 0.05 | 0.08 | 0.09 |
| | 0.03 | 0.06 | 0.08 | 0.15 |
| **Mean [deg.]** | 0.024 | 0.046 | 0.092 | 0.146 |

Table 6.2: Hybrid-rotational GPR azimuthal positioning calibration results.

A similar process was performed for azimuthal positioning calibration, which sequentially advanced the antenna through $\theta \in [0, 45, 90, 135, 180]°$. Practical measurements of observed displacement involved using a fine black pen to record the angle of the boresight vector on the motor casing at each position. These were compared against similar red indicators denoting the expected angle value (marked using a protractor before starting the test).

Since angular discrepancy was significantly less than 1°, small angle approximation was applied, enabling absolute angular deviation — summarised in Table 6.2 — to be read off a standard digital vernier gauge, accurate to within $\pm 0.01mm$, here equivalent to approximately $\pm 0.0126°$. Averaged findings yielded cumulative absolute deviation of 0.15° (approximately 17 micro-steps), accurate to within 0.17% of a full rotation. As prior, this level of accuracy was considered more than sufficient for the planned investigation.

## 6.4 Aims and Objectives

Having developed a practical hybrid-rotational GPR system for data collection in the laboratory, subsequent benchmarking proceeded as in previous chapters. Primary and secondary aims also carried over, with the former now focused on hybrid-rotational GPR data and the latter now considering segmentation parameter optimisation.

Objectives for this investigation were:

1. To capture a hybrid-rotational GPR background calibration pass of a subsurface volume devoid of target geometry, under controlled conditions.
2. To capture a similar hybrid-rotational GPR scanning pass of the same subsurface volume containing established target geometry.
3. To use the developed workflow to generate 3D visualisations of subsurface anomalies.
4. To quantitatively analyse target detection and mid-centre localisation accuracy, alongside data processing runtime, to gauge the effectiveness of workflow performance.
5. To quantitatively and qualitatively compare returned 3D spatial profiles with those from the previous fixed-directional GPR investigation.

At this stage, it should be emphasised that for workflow performance to be considered sufficiently effective — justifying progression to field testing — anomalies with characteristic length scales of at least 100mm should be accurately resolved. Moreover, the key visual indicator whether the limit of attainable target resolution had been reached would be evidence of coalesced spatial profiles, exhibiting mid-centre agreement within the smallest discernible target's characteristic length scale, relative to the average mid-centre coordinate of all suspected constituent targets.

## 6.5 Experimental Setup and Methods

This section details the experimental setup and methods adopted for data collection using hybrid-rotational GPR in the laboratory. A breakdown of preliminary testing is presented in Section 6.5.1 and Section 6.5.2, validating the efficacy GPR measurements with the proposed equipment setup. This is followed by deconstruction of trace divergence phenomena in Section 6.5.3, wherein a projected lateral separation threshold is derived to inform scanning parameter selection in Section 6.5.4. The practical data collection procedure is finally outlined in Section 6.5.5.

### *6.5.1 Preliminary Test – GPR Frequency Sweep Validation*

Prior to collecting data using the full hybrid-rotational GPR system in the laboratory, a preliminary test was required to validate the accuracy of the GPR measurement equipment.

As shown in Figure 6.7, experimental setup comprised of hardware to be directly integrated to the proposed hybrid-rotational GPR system for laboratory experimentation. The TEM-feedhorn antenna connected was connected to the FieldFox N9915A VNA via the 5m low loss measurement cable. The antenna was connected to a weighted wooden stand and directed at the vertical side wall of the anechoic chamber, lined with EM-absorbing panels to attenuate incoming wavefronts. This suppressed undesirable signal reflections not associated with the target. The target was a large 1m x 0.8m x 2mm, vertically orientated metallic sheet. As a perfect electrical conductor, the majority of incoming energy would be reflected from the contact surface back towards the antenna, making this an ideal target for the validation test.

Planned laboratory and field-testing would involve total signal propagation distances ranging between 1-3m. The separation distances between antenna aperture and target contact surface were chosen to reflect this, in order to validate performance across all anticipated use-cases of the GPR equipment for this work. Separation between antenna aperture and target contact surface was varied between 0.5-2.5m in increments of 0.5m. Note that separations exceeding 2.5m placed the antenna beyond the floorplan of the anechoic chamber. Since the chamber was responsible for supressing external EM-interreferences in measurements, evidence of accuracy between 0.5-2.5m would reasonably imply comparable expected accuracy for measurements recorded at 3m separation.

The preliminary test would also be used to experimentally validate that a 0.5-3GHz linear frequency swept VNA measurements provided an optimal parameter configuration for the GPR antenna. Such a configuration would provide optimal impedance matching, characterised by minimal energy losses across a significant proportion of the swept frequency range during signal exchange with the external environment.

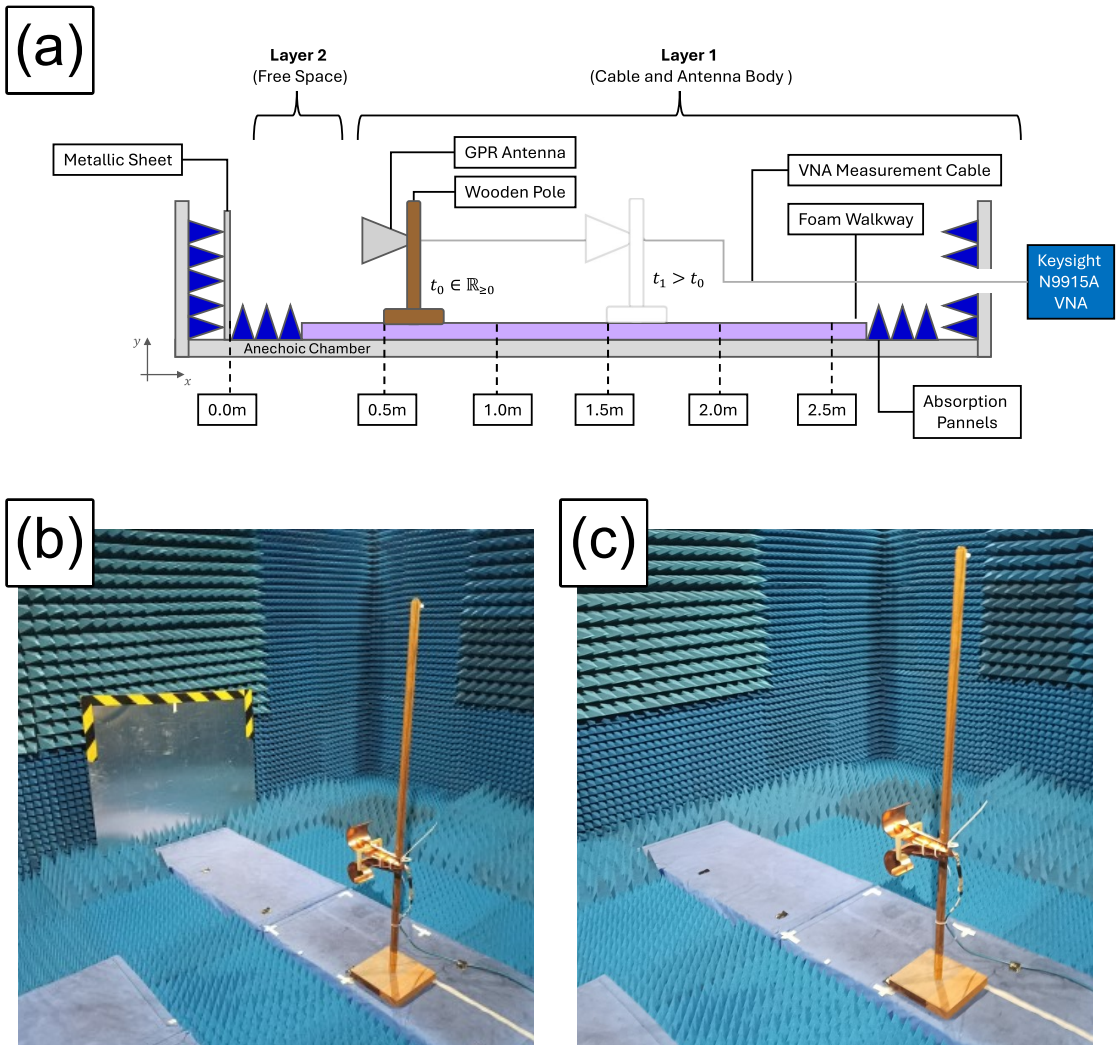


Figure 6.7: Experimental setup for verification of GPR measurement equipment configuration. Separation distances tested span 0.5-2.5m (a), between the antenna and metallic sheet target (b), which is removed during VNA calibration (c).

To achieve this, at each separation position, the target would first be removed, and the E-CAL unit connected to the antenna to calibrate the VNA. The measurement cable was secured to the stand and floor using ties and tape throughout this and later measurements. By minimising cable movement between VNA calibration and GPR measurement events, backscatter events generated at flex-points along the cable were minimised. This combated manifestation of internal backscatter artifacts at source, reducing artifact prevalence within returned trace profiles.

After recording a background trace (i.e. with no target present), the target was re-positioned between two reference markers to ensure positioning consistency. Alignment with the central plane of the antenna was an intuitive selection, informed by the practical simplicity of alignment with the target (requiring only a tape measure and right-square). A further 6 sequential traces were recorded by the VNA using a linear frequency sweep starting at 0.5GHz.

The full measurement cycle was repeated for each separation tested.

In each repeat measurement, the upper limit of the sweep was increased to probe the $S_{11}$ response level in the frequency domain. Defined as the ratio of reflected signal power to transmitted signal power, lower $S_{11}$ values indicate reduced energy losses, corresponding to better impedance matching, and subsequently more effective signal exchange with the external environment.

For a summary of VNA linear frequency sweep configuration parameters[4], see Table 6.3.

| **Parameter** | **Description** | **Value** | **Units** |
|---|---|---|---|
| $f_{min}$ | Sweep starting frequency. | 0.5 | GHz |
| $f_{max}$ | Sweep end frequency. | [3,6,10,15,20] | GHz |
| $P$ | Power level. | -17 | dBm |
| $T_D$ | Dwell time. | 336 | $\mu$s |
| $T$ | Sweep time interval. | 100.186 | ms |
| $N$ | Number of samples recorded. | 201 | 1 |

Table 6.3: Hybrid-rotational GPR preliminary test VNA parameters.

The first aim of the test was to establish that the antenna, VNA and ancillary hardware were correctly configured. Assuming an ideal one-layer signal propagation model, an unobstructed target at a fixed separation from the antenna would be detected a predictable two-way travel time in the temporal domain, given by,

$$t = \frac{2s}{v}, \tag{6.3}$$

where $s$ denotes the signal propagation distance and $v$ denotes the signal propagation velocity.

[4]A units of '1' denotes a dimensionless quantity.

The detection event would manifest in a GPR trace as a significant amplitude peak in the time domain at time $t$, provided the background response in the absence of the target is subtracted across the full time domain.

In practice, signal transmission through the 5m VNA cable was rated to 81% efficiency, yielding $v_1 \approx 0.81c$. In air signal transmission is 99.97% the speed of light in a vacuum. For convenience and in line with common practice, transmission was approximated as lossless, with $v_2 \approx c$.

Therefore, assuming the two-layer model illustrated in Figure 6.7a, the two-way travel time estimate ($\hat{t}$) was expressed piecewise,

$$\hat{t} \approx 2\left(\frac{s_1}{v_1} + \frac{s_2}{v_2}\right), \tag{6.4}$$

where $s_1 = 5$m denotes signal propagation distance between the VNA and antenna aperture, and $s_2 \in [0.5, 1.0, 1.5, 2.0, 2.5]$m denotes signal propagation distance through the air between the antenna aperture and target contact surface. These preliminary estimates are displayed as a dashed vertical line for each respective trace response profile in the temporal domain, across Figure 6.8 and Figure 6.9 respectively.

The frequency-selective fading patterns and temporal response profiles for testing at a 1.5m separation, with frequency sweep 0.5-3GHz, are presented in Figure 6.8.

Of propagation distances tested, 1.5m was considered most relevant to planned laboratory experimentation using the hybrid-rotational GPR system, as the distance between the antenna aperture and RoI volume exit boundary varies with antenna rotation between 1.21m (for vertical downward orientation) and 1.34m (for extremal orientations).

Close agreement to within 3ns was observed between the leading peak of the temporal domain response profile and the preliminary estimate, following subtraction of the background response profile.

On inspection of the background response profile in isolation, the leading peak was found to be significantly broader, associated with $t \ll 5$ns. This was consistent with expected strong internal backscatter events at the VNA measurement port interface, antenna base and antenna aperture, where the signal propagation medium changes. The peak at 13ns was notably not present on the background response profile, further indicative of association with the metallic target.

The addition of the metallic target also significantly altered the frequency-selective fading pattern, introducing a fine-scale periodic variation in the $S_{11}$ response across all measured frequencies. This oscillatory modulation appears superimposed on the antenna's intrinsic response, which largely persists at the macroscale.

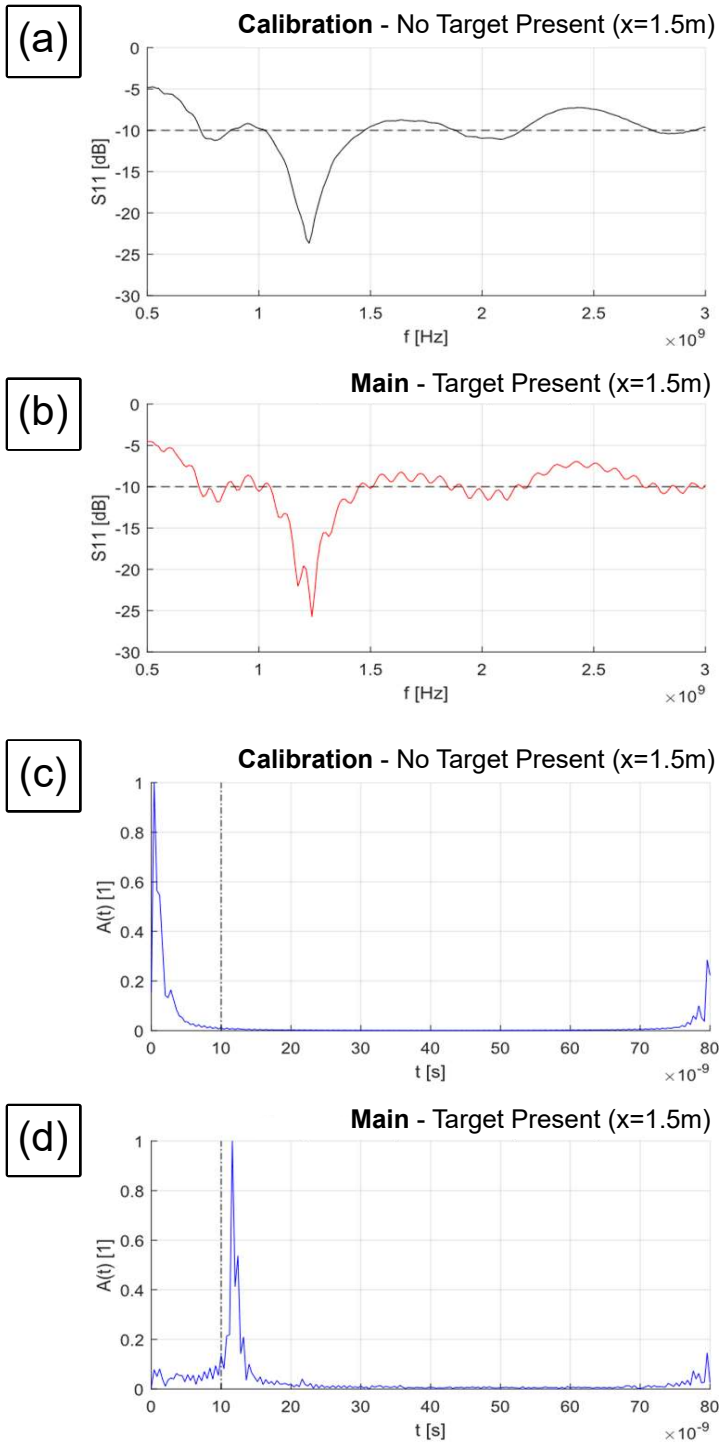


Figure 6.8: Trace measurements confirming detection of the metallic sheet target at 1.5m separation for linear frequency sweep (0.5-3 GHz). The frequency selective fading pattern and corresponding temporal response profiles are shown for VNA calibration with no target present (a, c) and with the target present (b, d).

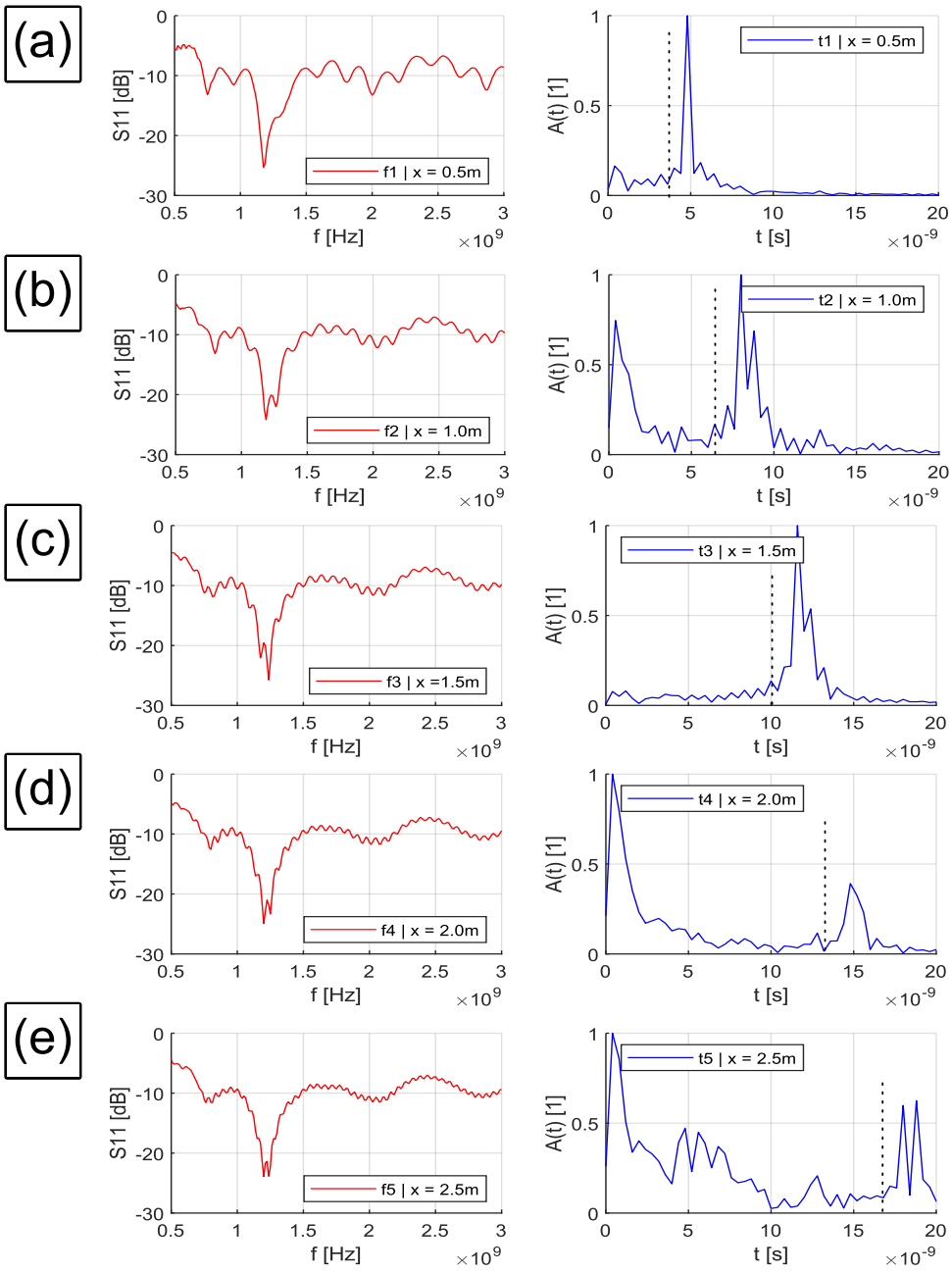


Figure 6.9: Trace measurements evidencing detection of the metallic sheet target at 0.5-2.5m separation (a-e). Dashed vertical lines mark preliminary estimate for target detection two-way travel time. For $S_{11}$ measurements, recall the -10dB reference level for 'good' antenna radiation performance. Frequency and temporal response profiles are denoted by red and blue lines respectively.

Such persistence suggests that the observed changes were due to modification to the external measurement environment rather than intrinsic antenna characteristics. The prevalence and regular periodicity of these oscillations was also consistent with multipath interference and standing wave effects naturally associated with such a highly reflective target.

Moreover, the notable fineness of oscillation periodicity was further suggestive of a sizable separation distance between the target and the antenna, in line with the inherent wavelength-dependence of such interference effects.

In all, results presented across both figures provided strong evidence to suggest the metallic target has been successfully detected and that the GPR measurement equipment is recording accurate environmental measurements.

Similar results were observed for the other tested separation distances, as displayed in Figure 6.10a. The frequency domain response profiles each resembled the background response profile, superimposed with progressively higher frequency sinusoids as the separation distance increased. This would be consistent with the lengthening of signal paths as distance to the target increases, which would lead to greater phase shifting in the reflected signal.

The phenomena would also be coupled with compression of the interference patterns as distance to target increases, as greater propagation distance increases the likelihood of interference interactions. As such, one would expect the sinusoidal oscillations in the $S_{11}$ profile to increase in frequency across the frequency domain, as target separation from the antenna increases. Again, expectation was consistent with observations, and indicative of target detection at each tested separation distance.

Looking closer, the leading peak in each temporal response profile was assumed to be associated with detection of the metallic target, as was the case for separation of 1.5m.

Notably, detection consistently followed the preliminary estimate across all results. Analysis of the absolute deviation is presented in Figure 6.10b. A consistent delay of 1.47ns was observed between the preliminary estimate and observed leading peak for each separation tested. The formulation of two-way travel time in Equation 6.3 was inverted to estimate propagation distance covered, given by,

$$s = \frac{ct}{2}. \tag{6.5}$$

Substituting $t = 1.47$ns returned a propagation distance estimate of 0.22m. This was consistent with the antenna body length, which was grouped with the VNA measurement cable in the first region of the original two-layer model estimate.

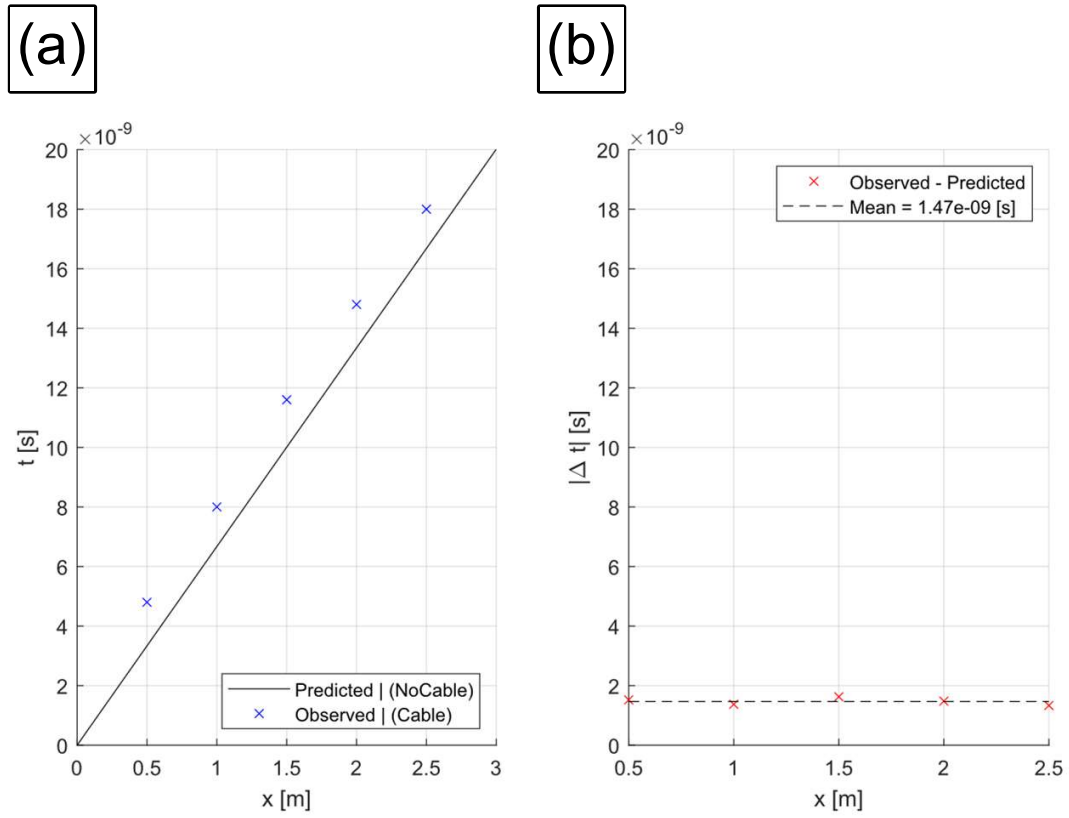


Figure 6.10: Difference between two-way travel time for leading peaks of traces in the time domain for observed data and preliminary estimates (a). Absolute deviation across each separation distance (b) are consistent with offset due to two-way travel time required to traverse the antenna body length.

This observation motivated that the antenna body and measurement cable should be treated as independent layers in future analysis of two-way travel times when working with hybrid-rotational GPR systems. This goes to evidence the significance of the multilayer model integrated into the 3D data alignment procedure in proposed 3D visualisation workflow (see Chapter 3). Here, this justification accounted for the observed offset between preliminary estimations and the observed target backscatter event in temporal response profiles.

In summary, from observed frequency and temporal domain measurements in the preliminary test, it was reasonable to conclude that sufficient evidence existed to verify detection of the metallic sheet target across the separation range 0.5-2.5m. This in turn validated the accuracy of the GPR equipment setup prior to undertaking of laboratory data collection using the hybrid-rotational GPR system.

To address the second aim of the preliminary test, validation was required that the 0.5-3GHz linear frequency swept VNA measurements provided an optimal parameter configuration.

Parameter configurations for which a greater proportion of the total frequency sweep response profile resided below -10dB were associated with better antenna impedance matching. Note that -10dB corresponded to 90% signal transmission efficiency (i.e. 10% energy loss). Therefore, intervals in the linear frequency sweep with associated $S_{11}$ measurements below this threshold indicated that the antennae exhibited more efficient energy exchange with the external environment. In turn, equating to better antenna performance for GPR inspection.

Based results presented in in Figure 6.11, the 0.5-3GHz frequency sweep range was verified to be consistent with optimal performance of the GPR antenna. In each scenario, the 0.5-3GHz interval consistently exhibited an $S_{11}$ response below -10dB. Performance even extended beyond the threshold, reaching -20dB in vicinity of 1-1.5GHz, indicating signal transmission efficiency in excess of 99%.

For 3GHz and above, in all observed scenarios, the resulting $S_{11}$ response profile resided above -10dB, indicating sub-optimal signal transmission performance. This appeared to be a limiting trend, stabilising at approximately -5dB (68.4% signal transmission efficiency) as linear swept frequency approached 15GHz.

Where the maximal frequency exceeded 3GHz, rapidly diminishing returns in antenna performance were observed. This also meant that added frequencies cycled in the linear frequency sweep would offer little practical benefit to GPR measurement.

Subsequently, the 0.5-3GHz linear frequency sweep range presented an optimal parameter selection for VNA measurement, and was therefore adopted for all hybrid-rotational GPR measurements performed for the remainder of this work.

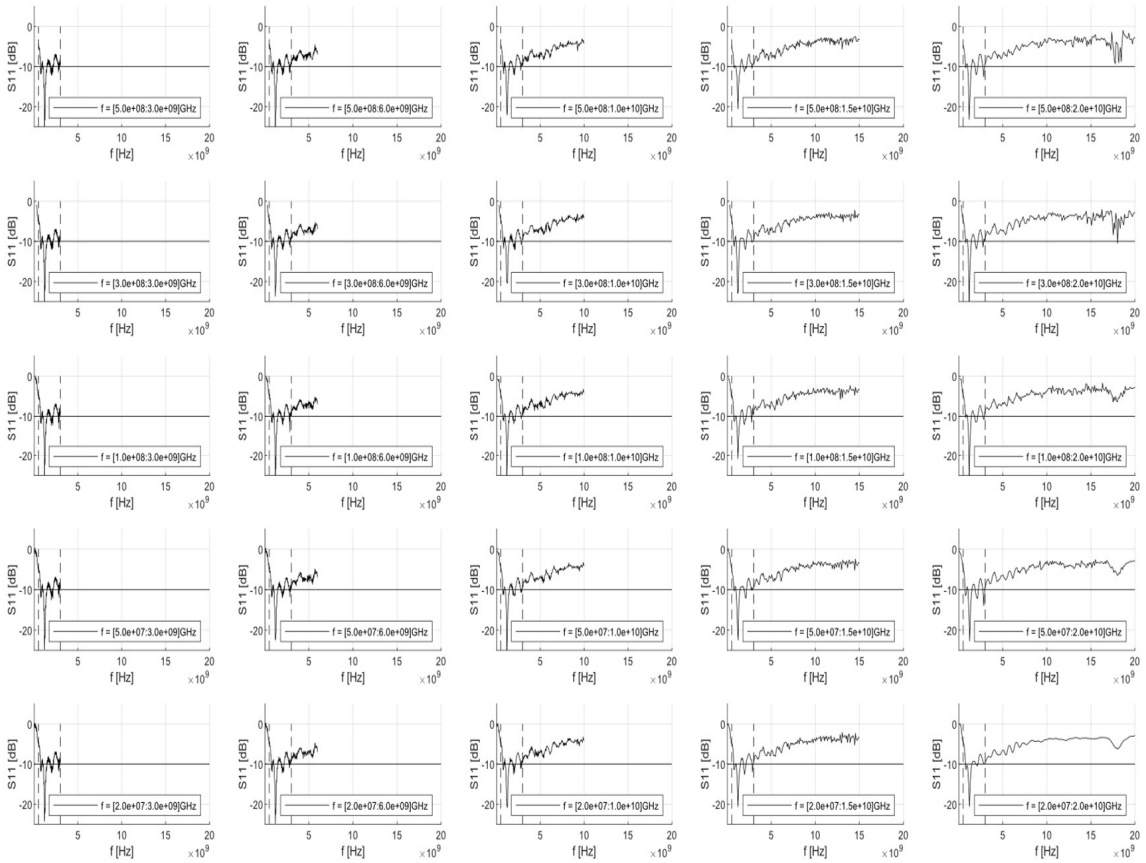


Figure 6.11: Results of antenna frequency sweep validation test. Rows (top to bottom) correspond to 0.5m, 1.0m, ..., 2.5m separations respectively. Columns (left to right) for $f_{max} \in [3, 6, 10, 15, 20]$GHz, respectively. Vertical dashed lines indicate the provisionally selected 0.5-3GHz interval. Horizontal lines highlight -10dB, the adopted reference level for 'good impedance matching'.

### *6.5.2 Preliminary Test – Antenna Radiation Patterns*

To ensure the reproducibility of results from hybrid-rotational GPR investigations presented in this and subsequent chapters, it was necessary to capture the radiation pattern of the bespoke TEM-feedhorn antenna. As prior, practical measurements presented the most direct approach. These measurements would be taken of both the antenna's E-plane and H-plane respectively — see Figure 6.12a — and presented overlayed in a 0dB normalised 2D polar plot, as adopted in similar numerical works [331] and [3].

The measurement process involved placing the antenna under test (AUT) in the centre of the anechoic chamber and connected to Port 1 of the VNA. This is illustrated in Figure 6.12b. The AUT's feed connector marks the origin of the local coordinate system adopted hereon. A comparable calibrated AtlanTecRF AS4771 reference horn antenna was connected to Port 2, orientated to match the AUT, and moved to sequential locations about a circular path. Angular separation was set to 10° increments, placed with its boresight vector, always aligned directly at the AUT. The full process was repeated twice to capture the E-plane and H-plane patterns, shown in Figures 6.12c and 6.12d, respectively. To switch the measurement plane from the starting position in Figure 6.12b, both antennas were rotated by 90° about the $x$-axis[5]. In addition, a background measurement was separately recorded with the AUT removed.

To ensure far-field measurements were recorded, fixed aperture-to-aperture radial separation of $r = 0.43m$ was maintained throughout using a taut cord connected between the angle measure and the antenna stand base. Separation was maximised within the space available and equated to a feed-to-feed separation of over 0.8m. Importantly, this exceeded the necessary $r > 4\lambda_c$ threshold followed by [331], which uniquely presented radiation patterns frequency-averaged across full broadband intervals, more fundamentally relevant to inherently UWB systems like GPR than conventional plots for singular specific frequencies. As such, measurements spanned the full 0.5-3GHz frequency sweep across 401 sample points.

The transmission coefficient ($S_{21}$) provided the most natural measure of power radiated from the AUT in each direction. To plot the antenna radiation pattern, the background response was first subtracted from AUT measurements at each respective. Next, conversion to corresponding frequency-averaged directivity gain, $\tilde{G}(\underline{r})$, was required.

[5]Note that the respective orientations of the E-plane, H-plane and boresight vector are fundamentally associated by the 'Right Hand Rule', and for the geometry of such a horn antenna, the E-plane is always parallel to the long-side of the aperture.

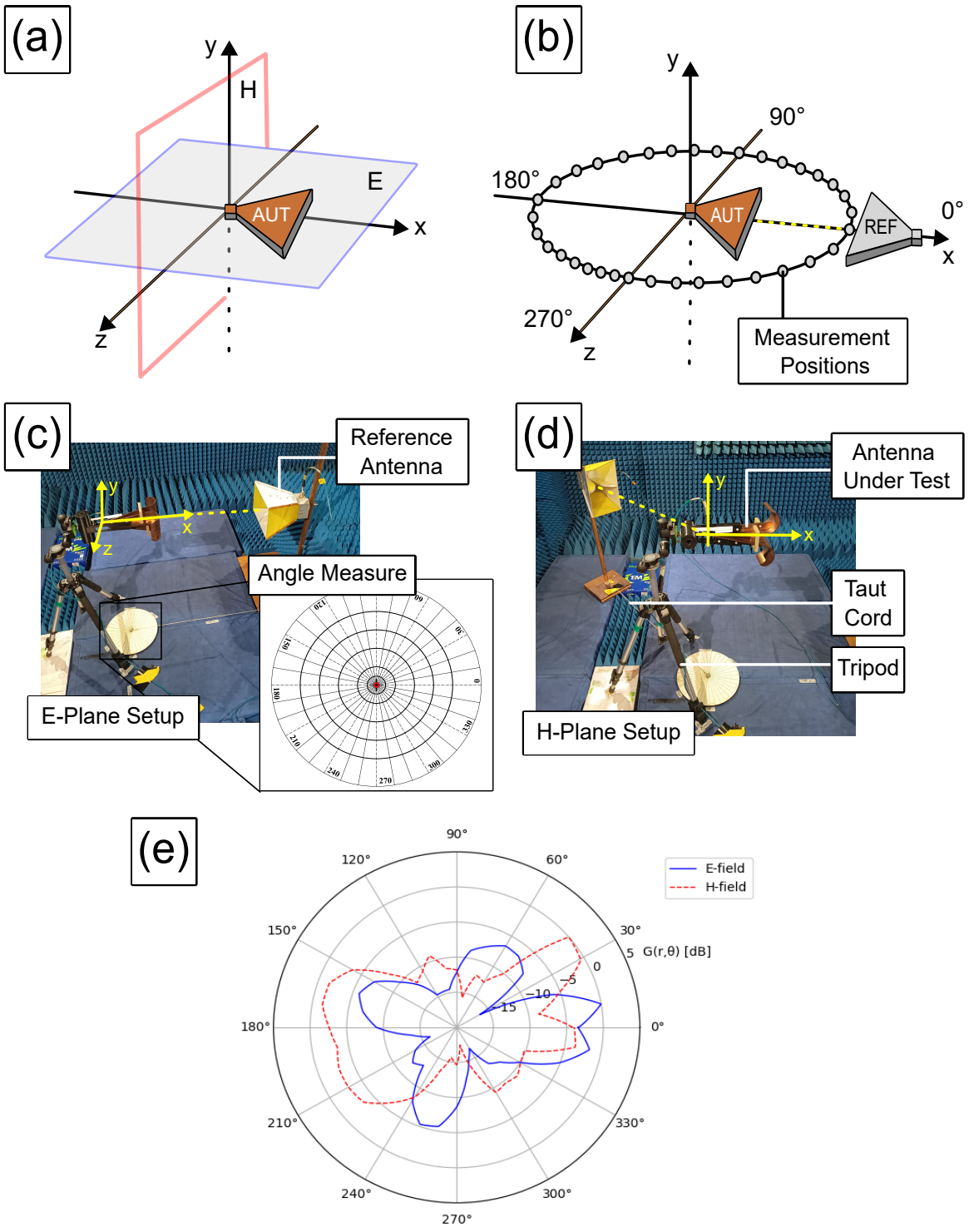


Figure 6.12: E-plane and H-plane (a) radiation pattern(s) of the AUT were captured by taking sequential $S_{21}$ measurements with a calibrated receiver antenna, sequentially placed at 10° angular increments with fixed radial separation $r = 0.43m$ (b). Practical implementation (c, d) returned plots exhibiting a sizable, symmetric main lobe (e).

Equating formulations for the normalised transmitted and received energies between the origin and an arbitrary point in the radiated field, recovered

$$\tilde{G}(\underline{r}) = \frac{(4\pi||\underline{r}||)^2}{(\tilde{\lambda}^2)(f_1 - f_0)} \int_{f_0}^{f_1} |S_{21}(f)|^2 df. \tag{6.6}$$

Here, the full frequency sweep interval spans $f \in [f_0, f_1]$ where $f_1 > f_0$, and $\tilde{\lambda}$ denotes the frequency-averaged wavelength across this interval, given by

$$\tilde{\lambda}^2 = \frac{1}{f_1 - f_0} \int_{f_0}^{f_1} \left(\frac{c}{f}\right)^2 df, \tag{6.7}$$

where $c$ is the speed of light.

For accurate evaluation of the integral, it was essential to convert measured values from exported decibel format ($\hat{S}_{21}$) to dimensionless units, abiding

$$S_{21} = 10^{\frac{\hat{S}_{21}}{10}}. \tag{6.8}$$

The full derivation is presented in Appendix B.

To recover smoother profiles, measurements were up-sampled via linear interpolation by a factor of 20. In turn, the angular separation increment between successive measurements was effectively reduced from 10° to 0.5°.

The recovered radiation patterns presented in Figure 6.12e show a pronounced main lobe at $\theta = 0°$ in the E-plane, along with distinct rear ($\theta \approx 160°$) and side lobes ($\theta \approx [60, 250]°$). This reflects the near-unidirectional behaviour characteristic of an ideal horn antenna, as intended in the GPR design to maximise energy transfer into the subsurface during measurements. Further consistency is observed in the H-plane, which similarly exhibits two symmetric lobes centred around $\theta \approx 0°$ and 180°, with notably broader footprints than those observed in the E-plane.

### *6.5.3 Setup – Trace Divergence and Projected Separation*

The intrinsic interdependencies of GPR parameters is a key challenge for effective survey design, particularly in the selection of optimal trace and transect separations. This complexity is compounded in hybrid-rotational GPR setups owing to emergent trace divergence phenomena (Figure 6.13), which must also be considered.

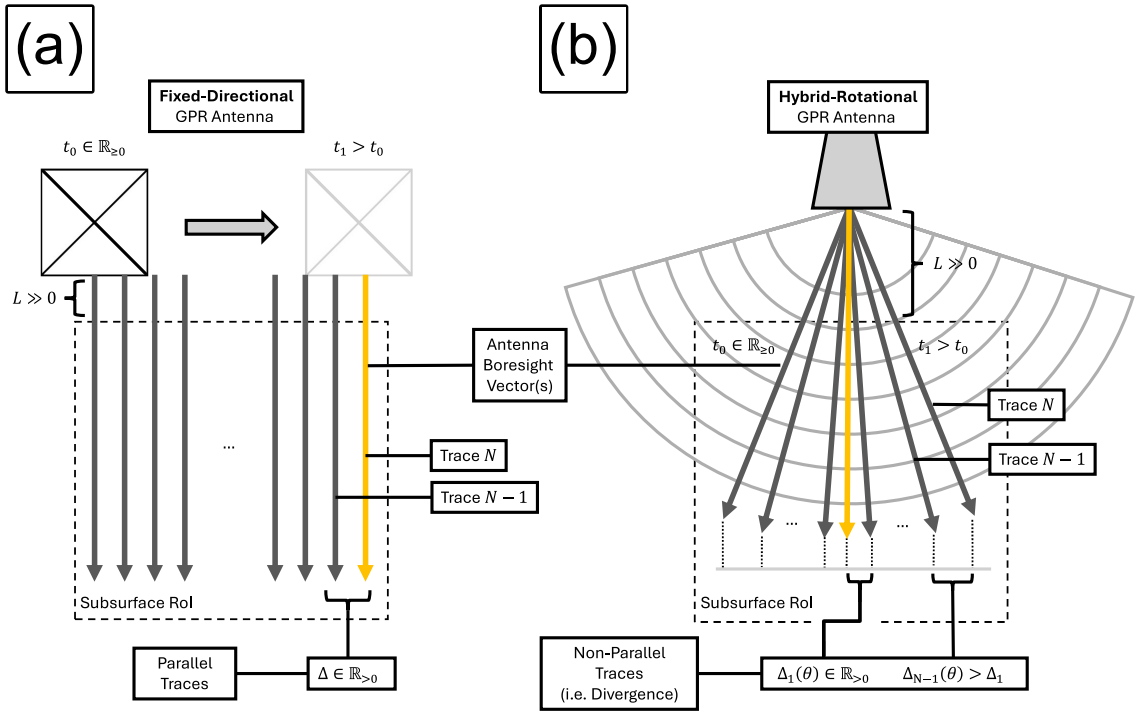


Figure 6.13: Illustration of trace divergence phenomena. Assuming constant lift-off from the contact surface, unlike parallel boresight vectors in fixed-directional GPR antenna (a), boresight vectors from a rotating antenna inherently diverge (b).

Unlike conventional fixed-directional systems, hybrid-rotational setups require the antenna boresight vector to rotate, which leads to a non-uniform spatial sampling density. Specifically, the projected lateral separation ($\Delta z$) between successive the sample points — across successive trace measurements — increases with depth, which can result in sparse measurement regions at extremal depths. On this basis, the estimated maximal value of $\Delta z$ across the full sampling domain, here between traces at extremal depths and azimuth (Figure 6.14), can provide insight into minimal anticipated sampling density, and therein inform survey parameter refinement.

It is important to emphasise that although trace divergence phenomena and the notion of projected lateral separation are closely linked to the attainable 'resolution' of a hybrid-rotational GPR system, these are not equivalent concepts. In fact, conventional reliance on notions range and cross-range formulas to define 'fundamental' resolution[6] break down here, owing to non-uniform spatial sampling density, coupled with the potential for oblique angles between boresight vectors and contact surfaces. Within the scope of this work, trace divergence constrains a hybrid-rotational GPR system's 'effective' resolution[7]. An analogy can be drawn to panoramic photography: even if a camera possesses a high-quality lens (high fundamental resolution), the resulting panorama will suffer if the spacing between constituent images is too sparse or irregular — limiting the effective resolution of the final composite.

This remainder of this section presents the formal derivation of $\max \Delta z$ used to inform parameter selection for investigatory work that follows, starting from the geometry presented in Figure 6.14. A 'pencil-beam' approximation is employed to clarify the geometric interpretation of both trace and transect trajectories, consistent with the standard GPR practice of collapsing trace measurements along the associated boresight vector [152].

Critically, this approximation does not disregard the finite beamwidth of the antenna, which is ultimately responsible for returning the characteristic amplitude peaks and hyperbolic diffraction patterns observed in measurement data. Rather, this interpretation emphasises the significance of the central beam axis in governing the spatial distribution of recorded energy, alongside the observed sampling density of a survey. The reduced dimensionality of this interpretation is particularly beneficial when interpreting measurements in more complex survey scenarios, recorded using non-conventional equipment configurations like hybrid-rotational GPR.

[6] The theoretical minimum resolvable imaging length scale, determined by a system's intrinsic parameters, such as bandwidth and wavelength

[7] The minimum resolvable imaging length scale a system can achieve in practice, notably influenced by sampling density, scan trajectory characteristics, plus the shape and form of ground-truth geometry.

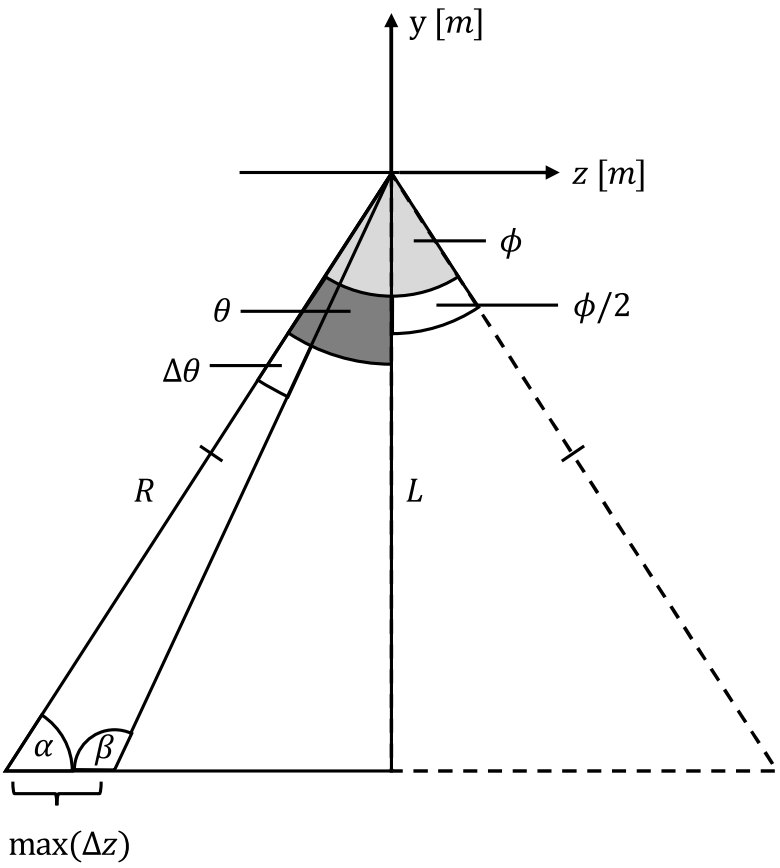


Figure 6.14: Boresight vectors of traces at extremal azimuth within a rotational transect.

For a finite rotational transect, extremal azimuthal limits are assumed to satisfy $0° < \theta < 180°$ where $\phi = \theta_1 - \theta_0$ is the central angle of the transect about the centre of trace rotation. For generalisation to a full revolution, where $0° < \theta_0 < \theta_1 < 360°$, a rotational symmetry argument would be applied, assuming consistent azimuthal separation between successive trace measurements and consistent radial separation between successive sample points within each trace. This rotational transect can be freely re-orientated, enabling $\phi/2$ to be aligned with the downward vertical.

Let $r$ denote the radial displacement of a given sample point from the centre of trace rotation within the rotational transect. Let $\theta$ denote the azimuthal displacement of a trace relative to $\phi/2$. Here extremal survey depth and trace azimuth correspond to the lower internal corners of the RoI volume closest to the floor.

A trace in the rotational transect at extremal azimuth was considered, with $\theta = \phi/2$. As shown in Figure 6.14, a right-angled triangle was formed between this trace and the vertical downward, with associated intersection angle $\theta$.

At the base of the RoI volume in the laboratory, the vertical adjacent side length $L = 1.21$m, corresponded to the cumulative sum of the air-launch distance, $L_2(\beta) = 0.69$m, and RoI volume depth, $L_y = 0.52$m.

By Pythagoras' Theorem, the radial displacement along the extremal trace corresponding to the RoI volume base was given by,

$$R = \frac{L}{\cos(\theta)} = \frac{L}{\cos\left(\frac{\phi}{2}\right)}. \tag{6.9}$$

Next, the immediate neighbouring trace at azimuth $\theta = \phi/2 - \Delta\theta$ was introduced.

The two faces formed the intersecting angle $\Delta\theta$, the side length opposite representing $\max(\Delta z)$. The intersection angle with the trace at extremal azimuth was labelled $\alpha$. The remaining intersection angle with the trace of second extremal azimuth was labelled $\beta$.

By Sine Rule,

$$\frac{R}{\sin(\beta)} = \frac{\max(\Delta z)}{\sin(\Delta\theta)}. \tag{6.10}$$

This rearranged to give,

$$\max(\Delta z) = \sin(\Delta\theta)\left(\frac{R}{\sin(\beta)}\right). \tag{6.11}$$

By Triangle Sum Theorem,

$$\beta = 180 - \alpha - \Delta\theta, \tag{6.12}$$

The periodicity of the sine function was exploited to simplify,

$$\sin\beta = \sin(\alpha + \Delta\theta), \tag{6.13}$$

yielding,

$$\max(\Delta z) = \sin(\Delta\theta)\left(\frac{R}{\sin(\alpha + \Delta\theta)}\right). \tag{6.14}$$

From inspection of the original right-angled triangle, it was noted that,

$$\alpha = 90 - \theta. \tag{6.15}$$

By complementary angle theorem,

$$\sin(\alpha + \Delta\theta) = \sin(90 - \theta + \Delta\theta) = \cos(\theta - \Delta\theta). \tag{6.16}$$

This gave,

$$\max(\Delta z) = R\left(\frac{\sin(\Delta\theta)}{\cos(\theta - \Delta\theta)}\right). \tag{6.17}$$

This was simplified using the reciprocal identity for the secant function, yielding,

$$\max(\Delta z) = R\sin(\Delta\theta)\sec(\theta - \Delta\theta). \tag{6.18}$$

Practically, threshold selection was an inherently subjective process, but was guided by consideration of the characteristic length scale of the smallest target of interest which could be resolved in the RoI volume, namely the 30mm diameter metallic sphere.

Recalling the GPR convention, it is necessary for a target to be intersected by at least 3 sequential traces if it is to be resolved. This warranted selecting hybrid-rotational GPR parameters to satisfy $\max(\Delta z) \leq 10mm$.

### 6.5.4 Setup – Scan Parameter Selection

For laboratory data collection using the hybrid-rotational GPR system, identical RoI ground-truth target geometry was selected to that adopted in the previous chapter. This choice enabled well-defined and more meaningful comparisons to be drawn between performance of the proposed 3D visualisation workflow when applied to both recorded hybrid-rotational and fixed-directional GPR datasets, respectively (see Section 6.6.4).

Parameter settings adopted for hybrid-rotational GPR data collection in the laboratory are presented in Table 6.4.

| **Parameter** | **Description** | **Value** | **Units** |
|---|---|---|---|
| $N_s$ | Number of samples per trace. | 401 | 1 |
| $N_A$ | Number of traces per transect. | 62 | 1 |
| $N_B$ | Number of transects in a full scanning pass. | 67 | 1 |
| $N$ | Number of traces in full scanning pass. | 4154 | 1 |
| $\Delta\theta$ | Trace azimuthal separation. | 0.828 | deg. |
| $\Delta\theta_\mu$ | Azimuthal micro-stepping incrementation. | 0.009 | deg. |
| $\Delta x$ | Trace lateral separation | 10 | mm |
| $x_0$ | Transect initial lateral displacement. | 0.00 | m |
| $x_1$ | Transect final lateral displacement. | 0.66 | m |
| $\theta_0$ | Transect initial boresight vector azimuth. | 79.8 | deg. |
| $\theta_1$ | Transect final boresight vector azimuth. | 130.2 | deg. |
| $f_{min}$ | VNA linear frequency sweep lower limit. | 0.5 | GHz |
| $f_{max}$ | VNA linear frequency sweep upper limit. | 3.0 | GHz |
| $\Delta f$ | VNA linear frequency sweep incrementation. | 6.25 | MHz |
| $L_0$ | VNA measurement cable length. | 5.0 | m |
| $L_1$ | Antenna body length. | 0.222 | m |
| $L_2(\alpha)$ | Lift-off distance for minimal azimuth. | 0.76 | m |
| $L_2(\beta)$ | Lift-off distance for downward vertical azimuth. | 0.69 | m |
| $L_2(\gamma)$ | Lift-off distance for maximal azimuth. | 0.76 | m |
| $\mu_{360}$ | Azimuthal micro-steps per full revolution. | 40,000 | 1 |

Table 6.4: Hybrid-rotational GPR laboratory data collection scan parameters.

The Lateral Positioning Module, Azimuthal Positioning Module and Measurement Control Module each utilised hardware detailed in Section 6.3. This dictated measurement cable length ($L_0$) and antenna body length ($L_1$).

For the VNA, trace measurements were captured using a linear stepped frequency sweep between $f_{min} = 0.5$GHz and $f_{max} = 3.0$GHz, justified through preliminary testing (see Section 6.5). A total of $N_S = 401$ individual samples per trace returned frequency domain stepping incrementation $\Delta f = 6.25$MHz. The FieldFox N9915A portable VNA supported selection of,

$$N_S \in [101, 201, 401, 601, 801, 1001, 1601, 4001, 10001] \tag{6.19}$$

samples per trace. Higher values of $N_S$ selected for frequency domain measurements would increase the maximal span of 'well-defined' two-way signal travel time in corresponding temporal domain response profiles. However, increases to this value would provide diminishing returns for intervals corresponding to equivalent one-way signal propagation distances extending beyond the footprint of the RoI volume. Optimal parameter selection would minimise this potential overshoot whilst maximising the valid range of corresponding temporal response profiles.

The upper limit of the 'well-defined' temporal domain was given by,

$$T = \frac{1}{\Delta f} = \frac{N_s - 1}{f_{\max} - f_{\min}}. \tag{6.20}$$

For $N_S \in [201, 401, 601]$ this equated to two-way travel times of $T \in [80, 160, 240]$ns, respectively. By substituting signal propagation velocity, defined,

$$v = \frac{c}{\sqrt{\epsilon_r}}, \tag{6.21}$$

into Equation 6.3, an estimate of minimal one-way signal propagation distance could be recovered. This assumed minimal anticipated signal propagation velocity, for a one-layer model with the expected relative electrical permittivity of the RoI subsurface, here $\epsilon = 5$. This took the form,

$$s = \frac{ct}{2\sqrt{\epsilon_r}} \approx \frac{cT}{4}, \tag{6.22}$$

yielding $s \in [5.99, 12.0, 18.0]$m respectively.

Recall that signal propagation would need to traverse both $L_0$ and $L_1$ to reach the antenna aperture, a cumulative propagation distance of 5.222m. To reach the RoI contact surface, at extremal azimuthal displacements of $L_2(\alpha)$ and $L_2(\gamma)$, cumulative propagation distance would increase to 5.982m.

Maximal propagation distance to reach the floor of the anechoic chamber was approximated by trigonometry. A right-angled triangle was defined, formed from the antenna boresight vector at extremal azimuth relative to the downward vertical ($\theta_{\perp} = 25.2°$) and the cumulative sum of contact surface lift-off for downward vertical azimuth $L_2(\beta)$, and RoI depth, totalling approximately 1.21m. This estimated a maximal signal propagation distance of 0.75m, resulting in a cumulative total one-way propagation distance of approximately 6m.

This estimate was at the upper limit of the well-defined temporal interval for $N_S = 201$, motivating selection of $N_S \geq 401$ to extend the interval, ensuring all significant backscatter events were recorded before the signal attenuated to the level of ambient background noise. On account of aforementioned diminishing returns expected beyond this threshold, this motivated selection of $N_S = 401$ for laboratory experimentation with the hybrid-rotational GPR system.

For azimuthal positioning, settings for maximal micro-stepping resolution were adopted to maximise achievable boresight vector alignment precision. Namely, DIP configuration for 40,000 micosteps per full revolution, corresponding to a micro-step azimuthal incrementation of $\Delta\theta_{\mu} = 0.009°$. Selection of azimuthal extremals $\theta_0 = 79.8°$ and $\theta_1 = 130.2°$ ensured that coverage of the boresight vector extended beyond the maximal footprint of the RoI volume along the z-axis (see 6.5).

For lateral positioning, similar logic was applied, yielding upper and lower limits of $x_0 = 0$m and $x_1 = 0.66$m respectively. This would ensure x-axis coverage spanned the full extent of the RoI volume.

Finally, it was necessary to select an optimal combination of $N_A$, $N_B$, $\Delta\theta$ and $\Delta x$ settings to balance lateral and azimuthal profiling resolution. This involved estimation of the expected number of unique lateral and azimuthal positions for multiple candidate parameter configurations. An optimal configuration would exhibit the closest similarity of values. Motivation for balancing the frequency of measurements along each axis was akin to maintaining equal separations between transects for fixed-directional GPR area scanning in the previous chapter. It was important to recall that in a transect, a target must be intersected by a minimum of 3-5 traces to be reasonably resolved in GPR output visuals (see Chapter 2).

Identifying an optimal configuration started by considering the constraints governing lateral incrementation between successive transects. For alignment with conducted fixed-directional area scan measurements (see Chapter 5), candidate values for $\Delta x$ were selected to be integer multiples of 5mm – the minimal spatial separation between transects in the area scan grid. To comply with the minimal projected lateral separation requirement $\max(\Delta z) \leq 10$mm (see Section 6.5.3), this restricted candidate values to $\hat{\Delta x} \in [5, 10]$mm.

It followed that the corresponding numbers of independent rotational transects along the x-axis were given by,

$$\hat{N}_x = \frac{x_1 - x_0}{\hat{\Delta x}} + 1. \tag{6.23}$$

The associated number of unique azimuthal positions could in turn be expressed,

$$\hat{N}_\theta = \left\lceil \frac{\hat{N}}{\hat{N}_x} \right\rceil. \tag{6.24}$$

Use of the ceiling function was necessary to return an integer value, and ensure maximal possible azimuthal resolution. The ansatz $\hat{N} \approx 4000$ was selected as a target for the maximal number of individual traces in a full scanning pass. From this, azimuthal separation between successive traces could be computed, given by,

$$\Delta\hat{\theta} = \frac{\theta_1 - \theta_0}{\hat{N}_\theta - 1} \tag{6.25}$$

The resulting parameter configurations are presented in Table 6.5.

| **Candidate Parameters** | | | |
|---|---|---|---|
| $\Delta\hat{x}$ [mm] | $\hat{N}_x$ [1] | $\hat{N}_\theta$ [1] | $\Delta\hat{\theta}$ [deg.] |
| 5 | 133 | 31 | 1.680 |
| 10 | 67 | 62 | 0.826 |

Table 6.5: Candidate configurations for lateral and azimuthal positioning parameters.

Closest agreement between $\hat{N}_x$ and $\hat{N}_\theta$ was within 8% for $\Delta\hat{x} = 10$mm, with associated $\Delta\hat{\theta} = 0.826°$. As a result, scanning trajectories for laboratory experimentation with the hybrid-rotational GPR system would be conducted with: $N_A = N_\theta = 62$; $N_B = N_x = 67$; $\Delta\theta = 0.826°$ and $\Delta x = 10$mm.

### *6.5.5 Method – Data Collection Procedure*

Conducting a hybrid-rotational GPR scanning of an RoI volume first required manual configuration of the RoI volume. The experimentation with hybrid-rotational GPR followed data collection with the fixed-directional GPR system, meaning targets were already in-situ.

To ensure ground-truth geometry was identical in both fixed-directional and hybrid-rotational GPR scanning passes, the background calibration pass (with targets removed) was conducted after the scanning pass with target geometry present. The procedure described below was implemented in both scanning passes. The acrylic sheet present throughout fixed-directional GPR area scanning was also left in place, to ensure consistency of the measurement environment.

Additional mechanical configuration involved elevating the linear rail to the target lift-off separation. This was achieved by first homing the orientation motor, which was then advanced to the vertical downward orientation. After using a spirit level to confirm the carriage was level, the distance between the base of the antenna and RoI contact surface was measured using a tape measure to within sufficient accuracy tolerance of ±5mm. Procurement of a laser distance finder would serve to improve increase resolution to tolerances within ±1mm in future work.

It was important to note that the lateral homing position of the hybrid-rotational GPR system resided behind the RoI volume, at $x = -0.41$m. Prior to data capture, it was necessary to advance the antenna to $x = 0$m to ensure lateral positioning was correctly calibrated. Critically, the operator needed to account for the offset between the lateral positioning reference marker on the carriage wheel and the antenna boresight vector, at 0.1m beyond the marker.

The finalised system configuration for laboratory data collection is presented in Figure 6.15.

Following on, the system was next returned to its datum, homing laterally and azimuthally respectively. In this position, the E-CAL unit was connected to the antenna mount and measurement cable coupled using the supplied 0.9Nm torque wrench to avoid damaging the SMA connections through overtightening. VNA calibration was then performed, and software defined settings updated in the SBC parameter file (see Section 6.3.3). Prior to data capture, the anechoic chamber lights were deactivated to further reduce EM-noise. The chamber door was closed for the full duration of each scanning pass.

By design, the execution of a scanning pass was a single-button push operation. Rotational transects were captured by advancing the antenna boresight vector in azimuthal increments of $\Delta\theta$, pausing for approximately 1 second at each position to allow a single trace measurement to triggered by the SBC. On completion of a full transect, the antenna was azimuthally homed, then laterally advanced by $\Delta x$. This process repeated across the full length of the RoI.

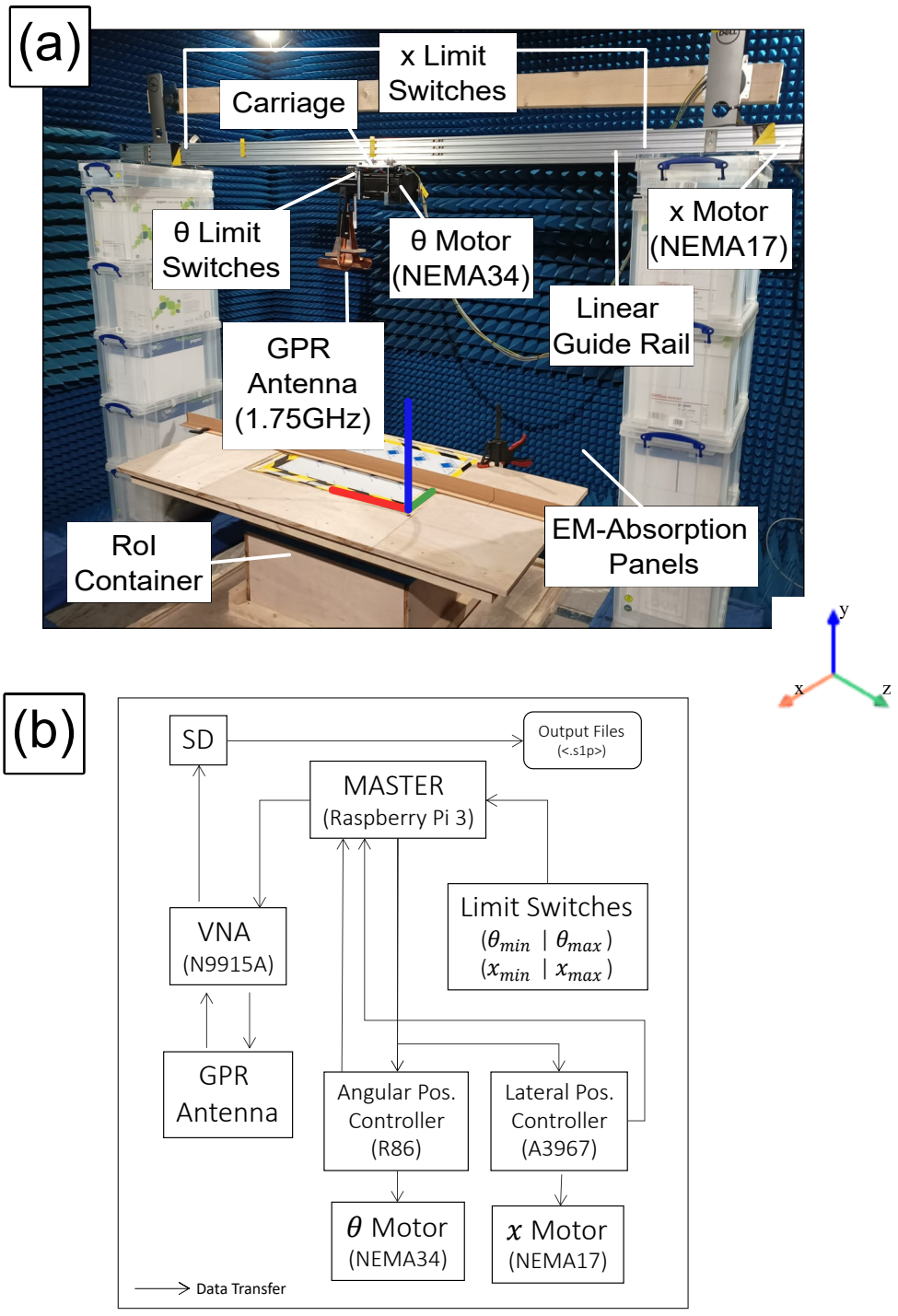


Figure 6.15: Finalised system configuration for physical hybrid-rotational GPR data collection in the laboratory (a). Processes for automatic positioning, data capture and data storage were centrally controlled via the Raspberry Pi (b).

## 6.6 Results and Discussion

This section provides performance analysis of the proposed 3D visualisation workflow applied to a hybrid-rotational GPR dataset recorded in controlled laboratory conditions. Target geometry was identical to that used during the analysis of workflow performance on the fixed-directional GPR dataset to ensure comparisons were well-defined and meaningful (see Chapter 5).

In line with Objectives (1) and (2), both a background calibration and primary measurement dataset were captured. Each dataset was formed through parallel stacking of sequential, laterally incremented rotational transects (see Chapter 2), containing a total of $N_S = 1,665,754$ individual sample points and had a footprint encompassing the full RoI volume. In accordance with Objective (3), the two datasets were passed to the proposed workflow which returned 3D visualisations of detected subsurface anomalies.

To align with Objectives (4) and (5), qualitative visual inspection of rendered 3D spatial profiles was performed against established ground-truth target geometry, with a focus on achieved levels of spatial resolution. The influence of HDBSCAN minimum cluster size and granulation parameter settings on returned 3D visualisations is explored in Section 6.6.1 and Section 6.6.2, respectively. Agreement between mid-centre coordinates of known targets and recovered clusters was quantitatively examined, in conjunction with qualitative visual comparison with cluster characteristics (i.e. shape, size and locale).

Next, in Section 6.6.3, a quantitative analysis of data processing runtimes is performed to gauge workflow efficiency. Finally, in Section 6.6.4, spatial profiles recovered from the hybrid-rotational GPR dataset are directly compared to those recovered from the fixed-directional GPR dataset (see Chapter 5). This served to evidence that 3D visualisations recovered using data from the hybrid-rotational GPR system exhibited comparable levels of effectiveness with those recovered from the fixed-directional GPR system.

### *6.6.1 Influence of Minimal Cluster Size*

Multiple data processing parameters within the proposed workflow could be adjusted to refine the quality of returned 3D visualisations of subsurface anomalies. These included: (i) the amplitude thresholding limit; (ii) selection and scaling of power-based or exponential-based gain; alongside (iii) minimal cluster size and (iv) granularity tuning parameter selection for HDBSCAN clustering, respectively.

The focus was narrowed to consideration of HDBCAN clustering parameters, namely (iii) and (iv). This was in-part motivated by comparably wider scope for parameter variation afforded by HDBSCAN parameters, but more significantly by the more direct fundamental association between segmentation and spatial profile recovery than processing operations (i) and (ii) in earlier phases of the workflow. Intrinsically, unlike amplitude thresholding and gain adjustment, segmentation introduces a notion of proximal locality between subsets of datapoints within an otherwise regular 3D grid, which directly subdivides the collective dataset into smaller, constituent sub-structures, each with associated spatial characteristics. As such, variations to HDBSCAN parameters were expected to have a more noticeable impact on the shape, size and locale of detected structural anomalies. With increased potential for spatial profile variation, greater scope for insight into achieved levels of spatial resolution was also anticipated.

The influence of minimal cluster size ($\hat{N}_\Omega$) on returned 3D visualisations of RoI target geometry within the hybrid-rotational GPR dataset was examined first, with the cluster granularity tuning parameter ($\alpha$) maintained at its default value $\alpha = 1.00$. This partitioned values of $\hat{N}_\Omega$ based on whether successful anomaly detection was observed. Of successful detection events, the value corresponding to the most accurate representation of the ground-truth geometry was in turn selected as the baseline reference for analysing the influence of $\alpha$ variation.

The set of candidate values for $\hat{N}_\Omega$ was based on observations form a preliminary execution of the workflow with the initial ansatz $\hat{N}_\Omega = 5$, based on the HDBSCAN subroutine's native default parameter value. As in previous sections, all workflow performance analyses were conducted on the same consumer-grade PC (see Chapter 4).

When applied, the workflow returned over 100 individual clusters, fully saturating the measurement domain. This indicated candidate values should start from a higher initial limit. The existence of an upper limit for $\hat{N}_\Omega < N_S$ was expected for the trivial segmentation, wherein the largest well-defined cluster would encompass every sample point within the domain, or all points in the domain would be flagged as noise.

To narrow down this range, a maximal limit ansatz of $\hat{N}_\Omega = 250$ was trailed. If a trivial segmentation occurred, the returned 3D visualisation would be saturated. If no well-defined clusters were recovered, and all sample points were flagged a noise, a warning would be displayed, and no render would be produced, as was the case for this ansatz. This identified a working estimate for candidate values of $\hat{N}_\Omega \in (5, 250)$.

This range was refined through iterative bisection, with the new limit passed to the workflow at each stage. Eventually this returned the refined range of candidate values $\hat{N}_\Omega \in [50, 175]$ with incrementation $\Delta\hat{N} = 25$.

Computations were performed with amplitude thresholding $\hat{A}(\underline{x} \in [0.55, 0.85])$ and exponential gain factor $a = 1$. Returned visualisations are presented in Figure 6.16 and Figure 6.17.

Clustering for $\hat{N}_\Omega \leq 100$ exhibited domain saturation, which rapidly converged to two distinct clusters as $\hat{N}_\Omega$ was increased from 125 to 150. The converged clusters exhibited 3D spatial profiles consistent with spherical geometry, subject to deformation. Such deformed spherical profiles were anticipated from more realistic practical experimentation, attributed to more persistent signal artefacts, potentially associated with geometric spreading, trace divergence and residual noise.

Critically, at a high-level, the spherical profiles of both detected anomalies were visually perceivable, with both exhibiting footprints of between 200-300mm, consistent across both XY and XZ projections for $\hat{N}_\Omega \in [150, 175]$ respectively.

Although this was an overestimate of the true diameters the spherical targets, the result was consistent with the levels of accuracy associated with computationally efficient GPR migration operations, including the Stolt method, as adopted here.

Moreover, for practical surveys, it was important to note that it is almost always better practice to overestimate the footprint of a potential structural anomaly when devising a maintenance plan. This rationale, akin to a worst-case estimate for affected surrounding structure, made allowances for potential increased growth between measurement and intervention.

In consideration of achieved levels of spatial resolution, results showed that the recovered spatial profiles of spheres $S_2$ ($D = 60$mm) and $S_3$ ($D = 30$mm) had coalesced into a single cluster in all test cases. Notably, the footprint of the observed cluster for $x < 0.35$m spanned the expected footprints of both $S_2$ and $S_3$. For $\hat{N}_\Omega = 175$ the coalesced cluster mid-centre and geometric mid-point of the ground truth geometry for spheres $S_2$ and $S_3$ were observed to be within 30mm. This was skewed towards the larger sphere $S_2$ along the x-axis, as would be expected, given its larger footprint would exhibit a more notable influence the local GPR response field than the smaller sphere.

Similar agreement and skew towards $S_2$ was also observed for $\hat{N}_\Omega = 150$, which further supported the theory that the cluster observed for $x < 0.35$m was the result of coalesce between the profiles of spheres $S_2$ and $S_3$.

Critically, mid-centre agreement between the coalesced cluster and average mid-centre between $S_2$ and $S_3$ was observed to be within the characteristic length scale of the smallest target (i.e. the 30mm diameter of $S_3$), meeting the requirement formalised in Section 6.4. Therefore, this and similar observations of coalesced targets (across the candidate test values) served as evidence that the limit of spatial resolution had been successfully identified and formally evaluated, residing at an intermediate length scale between 30mm and 60mm.

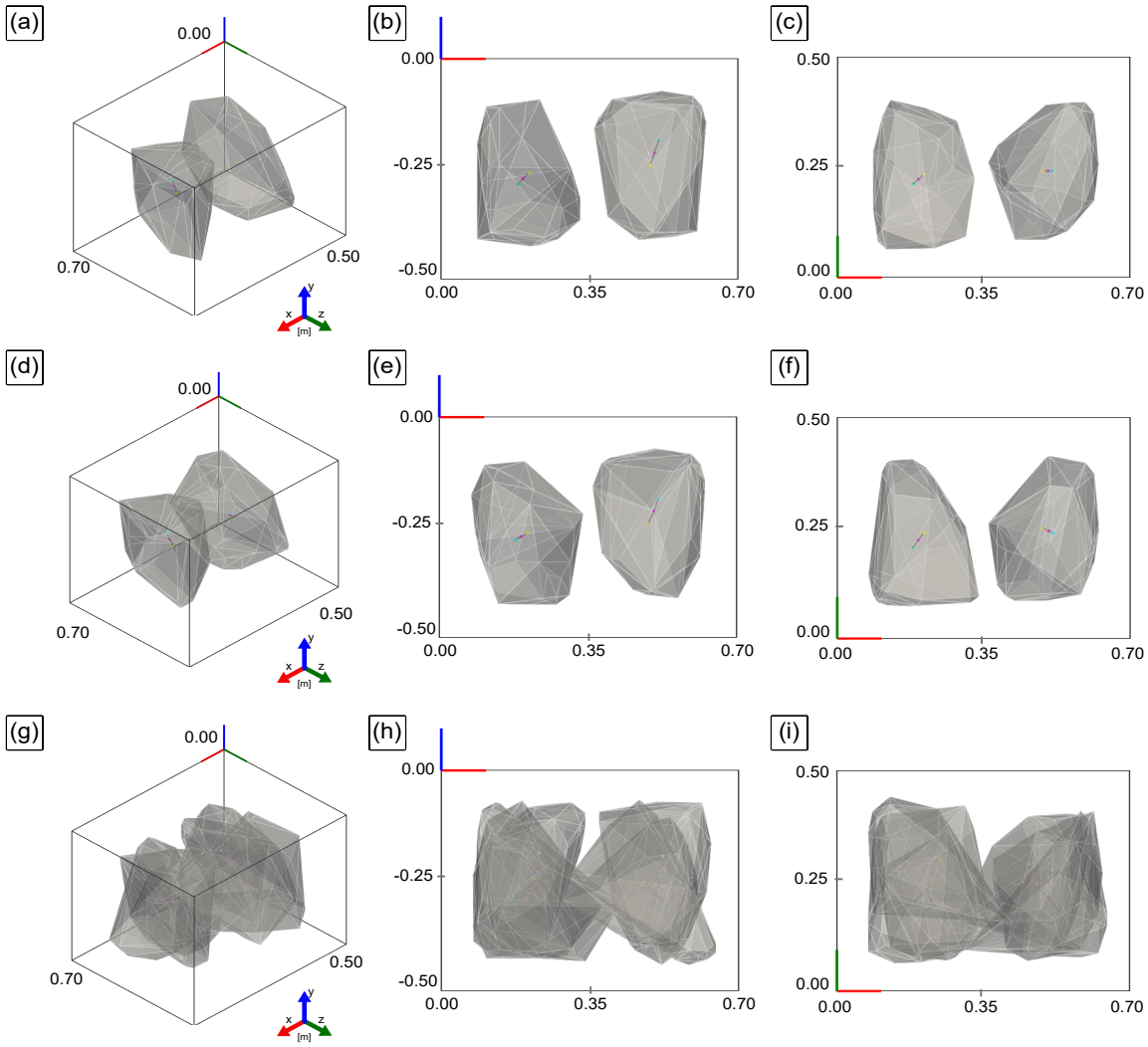


Figure 6.16: Returned visualisations from a hybrid-rotational GPR scan of metallic sphere targets in laboratory RoI volume. Here, HDBSCAN was performed with $\alpha = 1.00$ and (a-c) $\hat{N}_\Omega = 175$; (d-f) $\hat{N}_\Omega = 150$ and (g-i) $\hat{N}_\Omega = 125$, respectively.

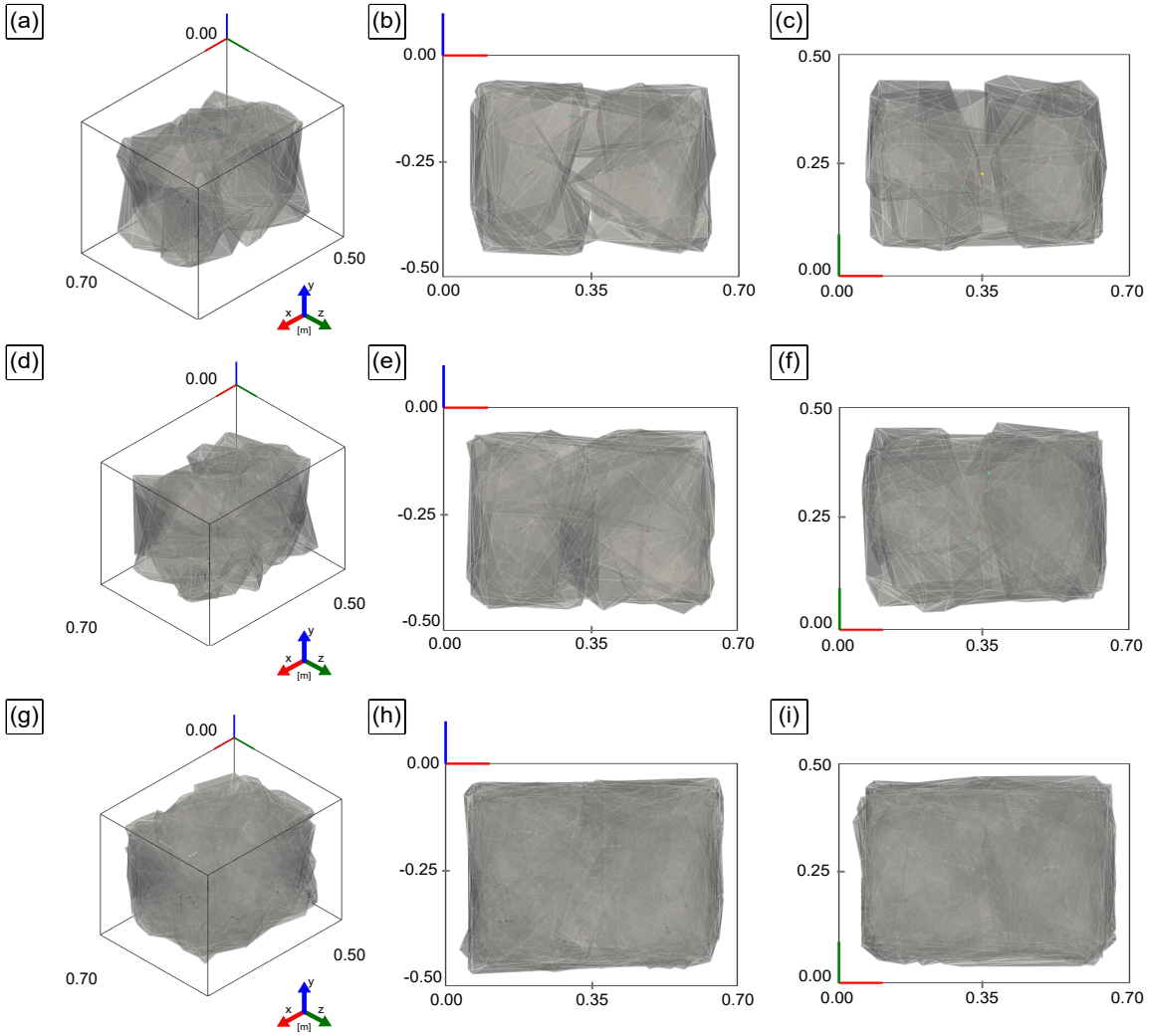


Figure 6.17: Returned visualisations from a hybrid-rotational GPR scan of metallic sphere targets in laboratory RoI volume. Here, HDBSCAN was performed with $\alpha = 1.00$ and (a-c) $\hat{N}_\Omega = 100$; (d-f) $\hat{N}_\Omega = 75$ and (g-i) $\hat{N}_\Omega = 50$, respectively.

Clusters recovered were also observed to exhibit similar vertical coordinates, approximately centred at a depth of 0.254m beneath the contact surface. It was also noted that cluster footprints both started at approximately 0.15m. Given that the mid-centre of the target spheres resided at 0.13m below the contact surface, this was in close agreement with the starting depths of the observed clusters.

It was hypothesised that observed vertical exaggeration of both target footprints was linked to antenna rotation, alongside ringing of the metallic targets.

Ringing of individual targets was anticipated, coupled resonation between neighbouring target, owing to the close proximity of the metallic spheres in the RoI volume. Resultant ringing artifacts would occur later in time and appear at greater depths in the GPR response field, potentially being identified as separate clusters or extensions of the same cluster during HDBSCAN segmentation.

Alongside this, it was suspected rotary motion of the antenna boresight vector would, in principle, change the angle of incidence between incoming radar waves and the targets' leading interfaces. This would increase variability in the length of ray paths and number of intersections between ray paths during scattering.

With increased variability, it was reasonable to assume increased occurrences of constructive and destructive interference phenomena would result. In this case, an increased frequency of constructive interference phenomena was suspected, which alongside with anticipated ringing, would induce vertical exaggeration of target spatial profiles.

The hypothesis that this vertical exaggeration phenomena was the result of a combination of ringing and rotation would be supported if less-pronounced vertical exaggeration was observed during comparison with results from the fixed-directional GPR investigation.

It remained to assess which of the results for $\hat{N}_\Omega \in [150, 175]$ would be adopted as the baseline reference for analysis of $\alpha$ variation. It was decided that $\hat{N}_\Omega = 175$ provided the most accurate representation of ground-truth geometry. From visual inspection of XY and YZ projections, reduced edge sharpness was noted in the XZ projections for $\hat{N}_\Omega = 175$ compared to $\hat{N}_\Omega = 150$, which was more consistent with expected spherical target geometry.

In addition, from comparison of mid-centre coordinate agreement with the ground truth geometry, whilst vertical alignment was comparable to within 0.1mm, results for $\hat{N}_\Omega = 175$ exhibited a small, but not insignificant average positioning accuracy improvement of 0.45% for across both lateral axes, when compared to results for $\hat{N}_\Omega = 150$.

### *6.6.2 Influence of Cluster Granularity Tuning Parameter*

By definition, the cluster granularity tuning parameter modified the stability of feasible clusters formed in the HDBSCAN dendrogram. To examine observed cluster formation trends in hybrid-rotational GPR datasets and identify a suitable baseline reference value ahead of field testing, this test set $\hat{N}_\Omega = 175$ and varied $\alpha \in [0.25, 1.15]$ with incrementation $\Delta\alpha = 0.25$. Computations were performed with amplitude thresholding $\hat{A}(\underline{x}) \in [0.55, 0.85]$ and exponential gain factor $a = 1.$ as prior. Returned visualisations are presented in Figure 6.18 and Figure 6.19.

From visual inspection, spatial profiles exhibited more significant variation in cluster size, shape and frequency when $\alpha \leq 0.55$. By $\alpha = 0.40$ expansion of the spatial profile footprint across all dimensions began to resemble domain saturation, which was fully realised by $\alpha = 0.25$. For $\alpha \geq 0.55$, profile variation was considerably more subtle, effectively negligible when comparing $\alpha = 0.85$ and $\alpha = 0.70$. This observation suggested that although formally integrated as a linear factor in the definition of cluster stability, in practice, variation of $\alpha$ on fixed dataset exhibited a non-linear relationship with the prevalence of clusters at given length scales.

On reflection, this observation was more consistent with the inherent non-linearity of the HDBSCAN clustering method, given the fundamental dependency between hierarchical merging of clusters and the complex interplay of adjacent cluster peripheries, especially in situations where peripheries begin to intersect. Such complex periphery interplay was attributed to the abrupt change in spatial profiles observed between $\alpha = 0.70$ and $\alpha = 0.55$, as the periphery of the cluster for $x < 0.35$m begins to intersect the cluster at $x > 0.35$m.

Evidence of potential ringing artifacts were also observed for $\alpha = 0.55$. As smaller scale clusters began to become more prevalent, it was noted that the first new clusters were approximately centred on the original clusters, with average midpoint coordinate agreement to within 9% across both for $\alpha = 1$. New cluster footprints were also observed to be almost fully contained within the original cluster footprints.

Observations of near-concentric 3D profiles resembled concentric hyperbolae artifacts associated with metallic-target ringing phenomena in 2D transects. Emergence as the value of $\alpha$ reduced was also consistent with this explanation, since ringdown signals from a metal target would be highly attenuated and more likely masked by the stronger initial reflections, requiring a greater level of clustering sensitivity to be more effectively detected.

Comparison between results for increased sensitivity to large-scale structures was performed using results for $\alpha = 1.00$ and $\alpha = 1.15$. Candidates values ranging up to $\alpha = 2.00$ were provisionally tested during early executions of the workflow but returned no well-defined clusters across all candidate values of $\hat{N}_\Omega$ used previously.

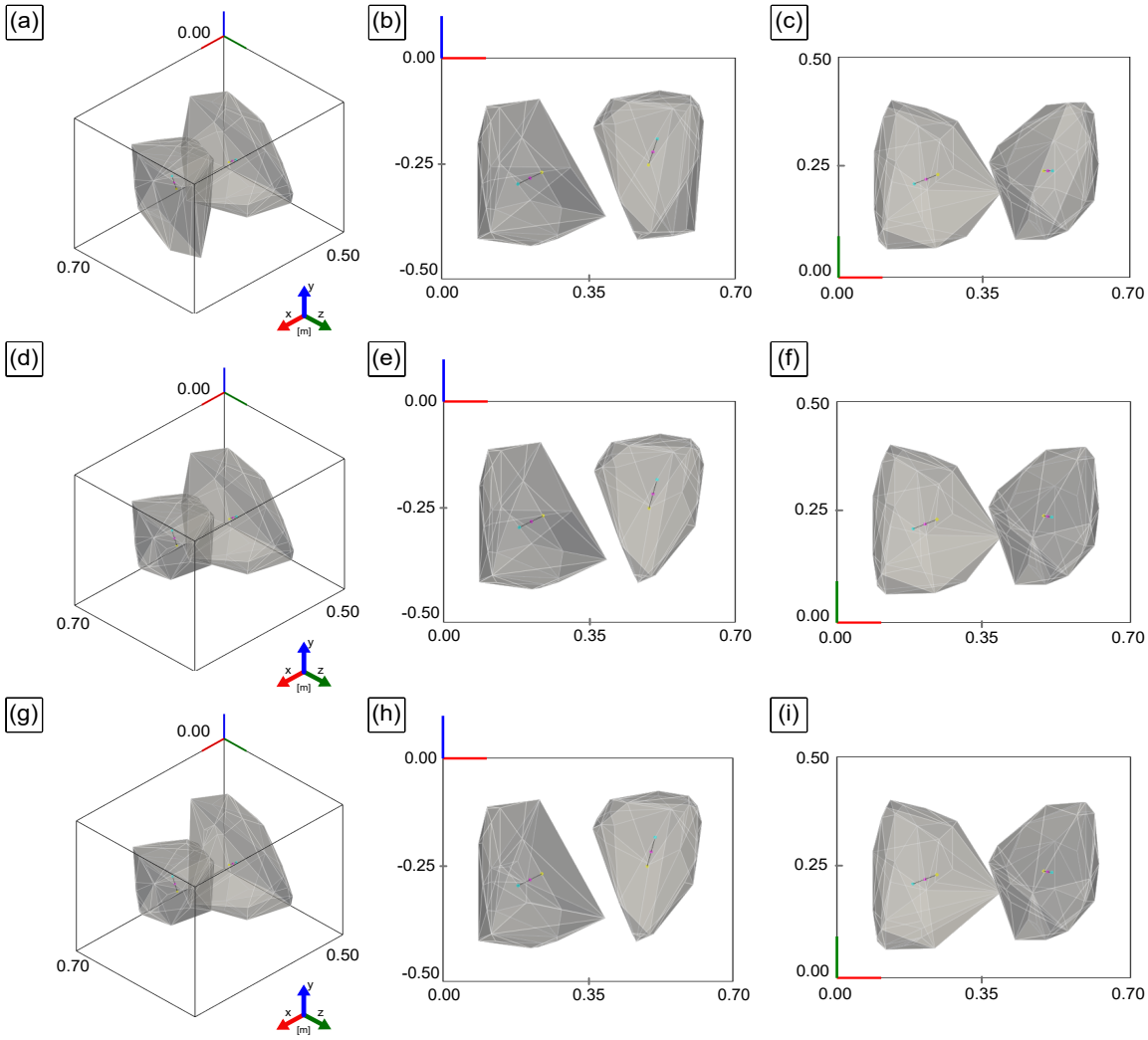


Figure 6.18: Returned visualisations from a hybrid-rotational GPR scan of metallic sphere targets in laboratory RoI volume. Here, HDBSCAN was performed with $\hat{N}_\Omega = 175$ and (a-c) $\alpha = 1.15$, (d-f) $\alpha = 0.85$ and (g-i) $\alpha = 0.70$, respectively.

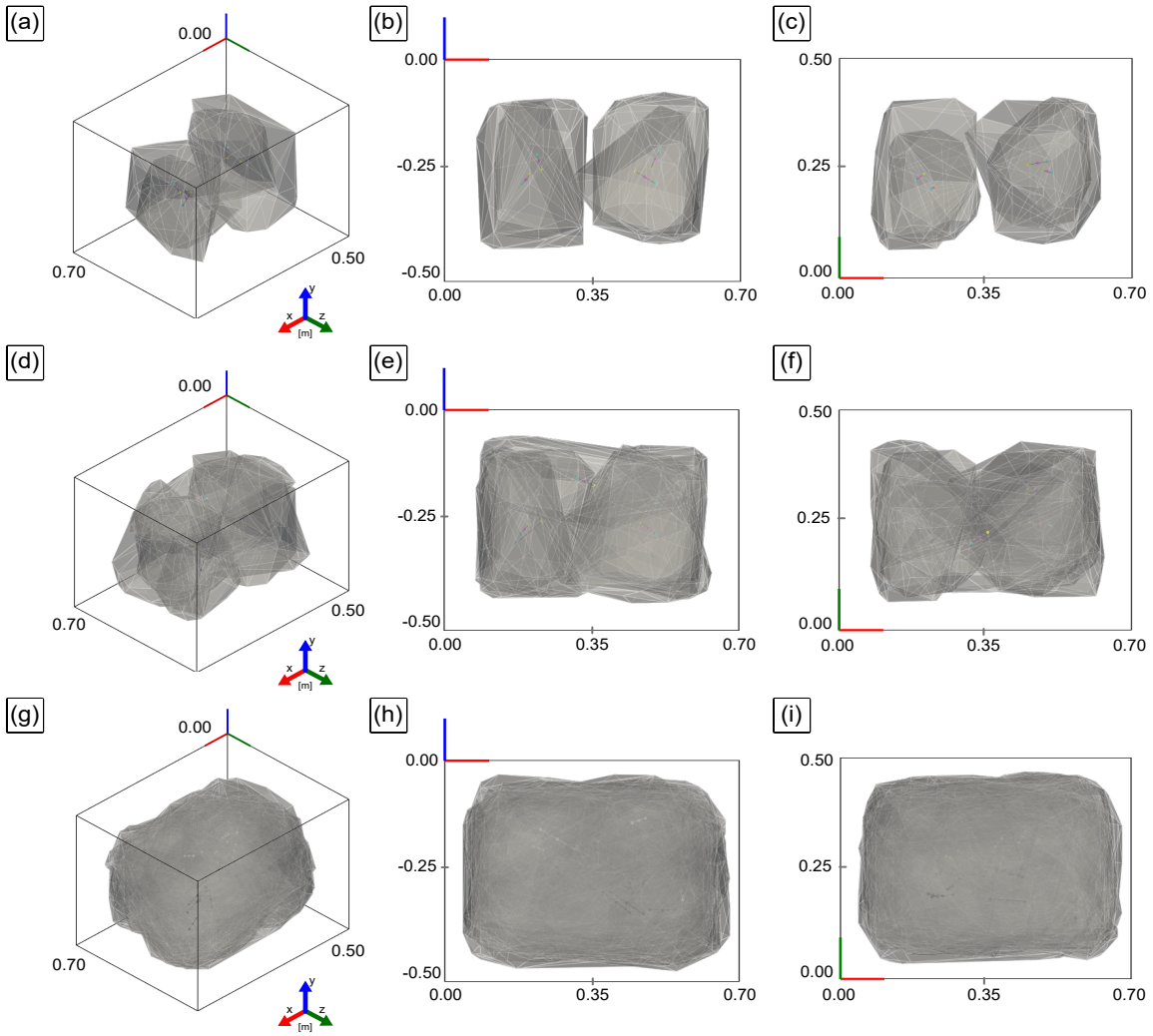


Figure 6.19: Returned visualisations from a hybrid-rotational GPR scan of metallic sphere targets in laboratory RoI volume. Here, HDBSCAN was performed with $\hat{N}_{\Omega} = 175$ and (a-c) $\alpha = 0.55$, (d-f) $\alpha = 0.40$ and (g-i) $\alpha = 0.25$, respectively.

This observation was a promising indicator that the HDBSCAN method was effectively avoiding the influence of smaller-scale features (e.g. associated with residual noise) within the dataset, ensuring that the clustering focus was on more significant and meaningful structures (i.e. subsurface anomalies with the largest characteristic length scales) for values of $\alpha \approx 1$.

Direct comparison of XY and XZ projections for $\alpha = 1$ and $\alpha = 1.15$ highlighted expansion of the footprint associated with spheres $S_2$ and $S_3$. Notably, similar footprint expansion was observed between $\alpha = 1.00$ and $\alpha = 0.85$, however that was also accompanied by reduction of cluster associated with $S_1$ in the XY projection in the region $x > 0.35$m and $y < -0.3$m. Such expansion was consistent with the increased sensitivity to large-scale structures expected from increased values of $\alpha$. Again, similarity in the shape and form of spatial profiles for $\alpha = 1.15$ to the profiles recovered from $\alpha = 1.00$ demonstrated segmentation consistency, reaffirming that the HDBSCAN method was accurately aligning cluster geometry to ground-truth geometry.

Finally, it remained to assess which value for $\alpha \in [1.00, 1.15]$ provided the best quality visualisations across conducted laboratory experimentation. From observed results, cluster profile variation only began to significantly affect the shape and form of detected anomaly spatial profiles for $\alpha \geq 0.55$, below which profiles rapidly approached domain saturation. For $\alpha > 0.85$, observed spatial profile variation was considered negligible. Quantitative analysis followed, which as in previous chapters compared the mid-centre coordinates of recovered clusters with the established ground truth geometry. Notably, for $\hat{N}_\Omega = 175$ and $\alpha = 1.00$ the highest levels of lateral localisation accuracy (to within a 3.4% tolerance) were observed across all candidate parameter combinations tested. From these findings, and to avoid introducing macroscale bias throughs selection of $\alpha > 1.00$, continued use of $\alpha = 1.00$ was selected as the baseline reference value for future tests with the hybrid-rotational GPR system.

### *6.6.3 Elapsed Workflow Runtime*

Elapsed runtime was analysed across 20 independent executions with checkpointing functionality disabled and enabled respectively, as prior (see Chapter 5). Results are presented in Figure 6.20, alongside box and whisker plots summarising the observed extremal and IQRs of measurements.

High levels of computational efficiency were evident from consistent sub-minute runtimes, with the workflow performing considerably more efficiently when importing checkpointed data, averaging approximately 8 seconds elapsed runtime, with standard deviation of 0.98 seconds.

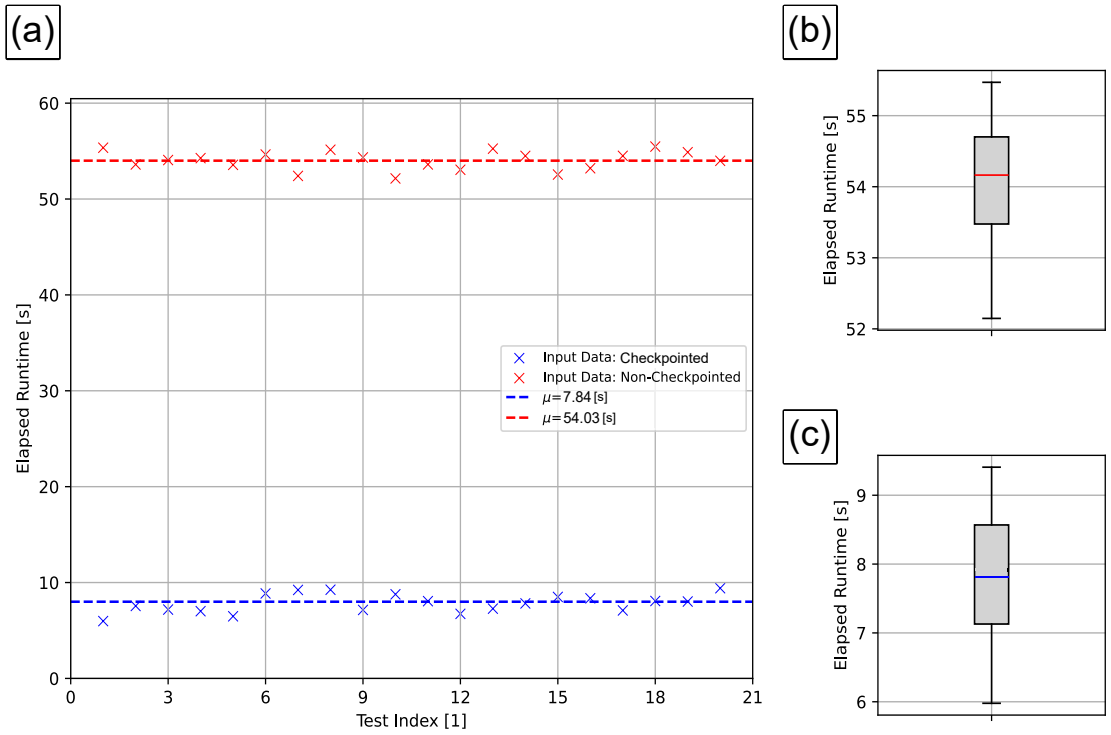


Figure 6.20: Breakdown of elapsed 3D visualisation workflow runtimes averaged over 20 independent executions (a). Runtime duration was measured from program initialisation to final render output. Blue and red markers indicate measurements when the workflow imported checkpointed data, and non-checkpointed data respectively. Box and whisper plots (b,c) follow the same colour coding, relaying the extremal range, mean and IQR of each measurement set respectively.

This marked a significant 85% speed-up compared to direct import for individual `.s1p` trace files, which averaged an elapsed runtime of approximately 54 seconds, with standard deviation of 0.99 seconds. Extremal measurement range spanned approximately 3.5 seconds in both scenarios. The IQR also exhibited close similarity to within 0.21 seconds, at 1.44 and 1.23 seconds respectively.

The similarity of observed extremal ranges and IQRs across both scenarios indicated comparable levels of consistency in observed elapsed runtimes across both scenarios. This also provided evidence indicative of stability in the complexity of data processing operations associated with computational phases of the proposed workflow for laboratory scale datasets (i.e. RoI volumes of the order of $0.5m^3$). Such observations were a promising indication the workflow would scale effectively in application to later field testing on the tunnel subsurface analogue.

### *6.6.4 Comparison to Fixed-Directional GPR*

The final stage of analysis was to compare 3D visualisations of the RoI volume recovered from the proposed workflow using hybrid-rotational GPR and fixed-directional GPR data. To facilitate comparison, a side-by-side comparison of the highest quality output recovered from both respective systems is presented in Figure 6.21.

Prior to analysis, it was necessary to establish that a comparison between the two GPR system setups was justifiable, given that the quality of the returned outputs would inherently depend on not only clustering parameter selection and scan geometry, but would also extend to the established practical differences between experiment setups.

Foremost, it was noted that both system setups operated at optimised lift-off clearances (subject to measurement type and space availability), shared a comparable $O(100mm)$ aperture size and profiled identical survey volumes. This narrowed focus to consideration of operating bandwidths, prospective resolutions and beam characteristics.

The fixed-directional setup, operating with $f_c = 1$GHz with $B \approx 1$GHz and near-zero lift-off, could in principal achieve finer levels of cross-range resolution, advantageous for imaging the small-scale targets between $O(10mm)$ and $O(100mm)$ within the extent of the RoI volume (to a 1m depth). Comparably, the air-launched hybrid-rotational system, operating with $f_c = 1.75$GHz, $B = 2.5$GHz, and a lift-off closer to 1m, had potential to deliver a significantly higher range resolution ($\Delta y \approx 6cm$ compared to $\Delta y \approx 15cm$), subject to possible increased cross-range spatial blur attributed to its inherently broader beam profile at the contact surface. Furthermore, it was also plausible that this system could also produce cleaner response profiles, owing to the inherent noise robustness of longer-duration SFCW measurements.

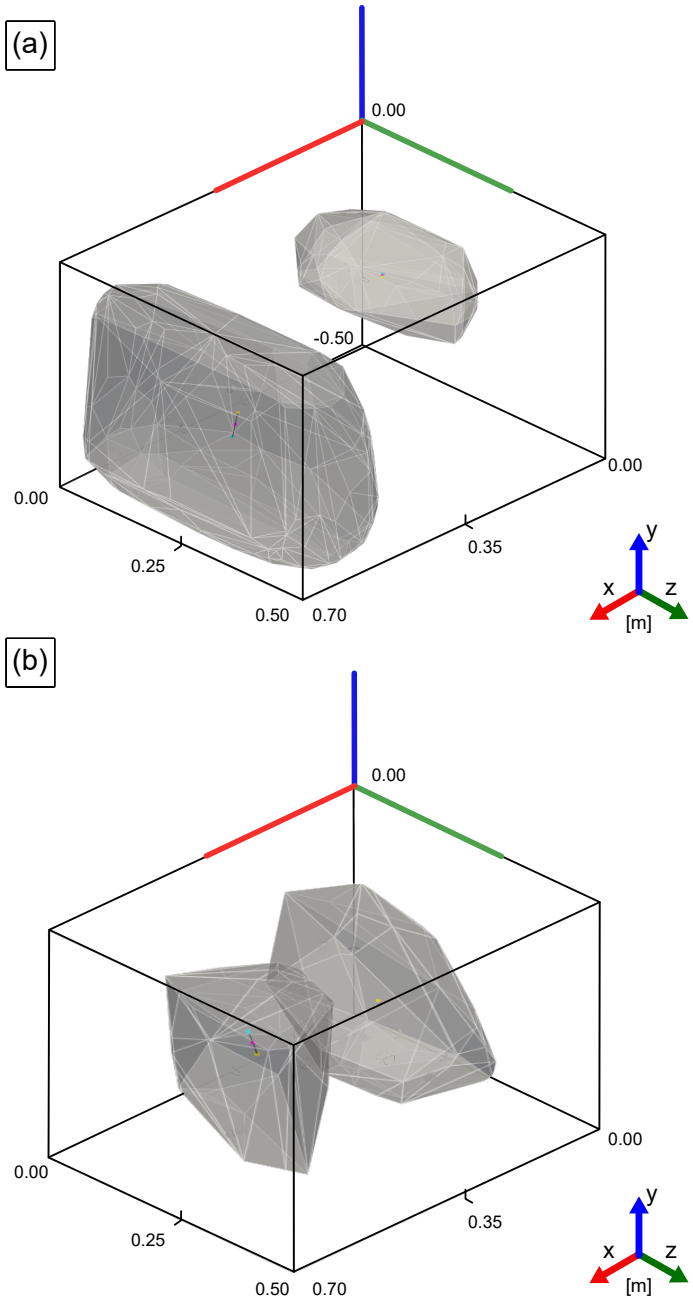


Figure 6.21: Comparison between the most effective 3D output from fixed-directional GPR (a) and hybrid-rotational GPR (b) scans of metallic sphere targets in the laboratory RoI volume. Results shown were obtained with HDBSCAN parameter configurations $N_\Omega = 700$ with $\alpha = 1.00$ (a) and $N_\Omega = 175$ with $\alpha = 1.00$ (b) respectively.

Taken collectively, while the combined influence of these factors would inherently have a non-trivial impact on the quality of returned visuals, no single factor emerged as a decisive limitation that would preclude a meaningful comparison between outputs from the two data collection methods. Therefore, the appraisals which follow are made with the caveat that observed differences could be reasonably, but not exclusively, linked to the influence of cluster parameter selection and scan geometry.

Output for hybrid-rotational GPR was observed to more faithfully capture the spherical nature of the targets, in particular the larger sphere $S_1$ (with $D = 100$mm).

The cuboidal form of the spatial profile associated with $S_1$ recovered from the fixed-directional GPR dataset resembled profiles associated with domain saturation, observed during refinement of $\hat{N}_\Omega$ and $\alpha$ parameter selection for the hybrid-rotational GPR dataset. It was feasible that due to the short propagation distance between the signal source and leading target interface, the fixed-directional GPR system was able to deliver sufficient energy to $S_1$ to result in localised domain saturation from the intensity of initial backscattering. The delivery of a high energy wavefront could also induce prolonged and potentially more rapid ringdown of the response profile. If the case, these mechanisms would in turn extend clusters returned from the HDBSCAN method, laterally and vertically accordingly. As this phenomenon was observed, the theory was supported.

There was also observed curtailing of lateral cluster expansion towards the centre of the RoI volume for $S_1$. This was consistent with the proposed theory, which would also anticipate the abrupt change in backscatter intensity when the wavefront from $S_1$ collided with the combined wavefront of initial backscatter from $S_2$ and $S_3$. The natural result for HDBSCAN clustering would have been a distinct lateral partition in clusters either side of $x \approx 0.35$m, as observed.

The more consistent spherical profiles observed for both $S_1$ and the coalesced profiles of $S_2$ and $S_3$ suggested that a similar saturation event did not occur in the hybrid-rotational GPR dataset. By similar logic, it was feasible that the greater propagation distance associated with the air-launched setup resulted in comparably lower levels of energy arriving at $S_1$, evidently sufficient to still clearly profile the subsurface (given multiple targets were successfully resolved), but sufficiently low as to prevent initial backscatter from fully saturating the localised domain in the immediate vicinity of $S_1$.

Inspection of cluster shape and form identified vertical exaggeration of expected spherical profiles in visualisations of both targets within the hybrid-rotational GPR data. However, for the fixed-directional GPR data, vertical exaggeration of target geometry was observed to be significantly less prevalent in the coalesced cluster for spheres $S_2$ and $S_3$. This observation supported the hypothesis proposed earlier, namely, that the underlying mechanism was a result of the combined influence of ringing *and* rotation.

In addition to performance of the workflow for 3D visualisation recovery, the performance of the hybrid-rotational GPR system and fixed-directional GPR system were also compared based on data collection efficiency. Completion of the fixed-directional GPR area scan totalled 8 hours across two working days, averaging 2 minutes per transect. The hybrid-rotational GPR system was able to complete a full scanning pass of the RoI volume within 3.6 hours over a single working day and involved only one button to be pressed to begin the scanning pass. Automation of data capture and antenna movement in turn significantly reduced operator workload compared to manual execution for fixed-directional GPR data collection.

Overall, the findings in this section highlight the effectiveness of the proposed 3D visualisation workflow on hybrid-rotational GPR data, demonstrating accurate anomaly detection and localisation, coupled with high computational efficiency. Moreover, visual outputs returned showed notably enhanced levels of fidelity compared to those recovered using fixed-directional GPR. From an equipment perspective, the new hybrid-rotational GPR data collection system proved both efficient and reliable throughout the investigation, justifying its adoption as the basis for subsequent field tests presented in Chapter 7.

## 6.7 Summary

In this chapter, a dedicated hybrid-rotational GPR system was developed for laboratory data collection of a controlled RoI volume. System design was based on an automated 3D polar plotter, and consisted of modules for power, measurement and control, alongside lateral and azimuthal positioning of the antenna boresight vector. This was achieved through the design, implementation and refinement of constituent mechanical and electrical subsystems, alongside the development of bespoke firmware for automated measurement and positioning control.

This work was followed by 3D visualisation of subsurface structural anomalies in a controlled laboratory environment using the proposed data processing workflow, based on an input dataset recovered using the developed hybrid-rotational GPR system. Target geometry mirrored that used for analysis of workflow performance on practical fixed-directional GRP data presented in Chapter 5. This approach enabled comparative assessment of the quality of returned 3D visualisations and validated the effectiveness of the developed system as a basis for laboratory-based experimentation.

Preliminary testing validated the efficacy of configured SFCW GPR measurement equipment for target detection. This was followed by selection and justification of hybrid-rotational GPR scanning parameters (e.g. projected lateral separation), method choices (e.g. use of rotational transects) and contingency measures.

The effectiveness of returned 3D visualisations for the detection and localisation of subsurface structural anomalies was subsequently analysed.

Qualitative assessment of the shape, form and locale of returned spatial profiles successfully identified target coalescence phenomena, evidencing that returned visualisations exhibited spatial resolution to within 60mm to 30mm. Quantitative analysis of cluster mid-centre coordinates also evidenced high levels of lateral localisation accuracy were achieved, with returned spatial profiles within a 3.4% tolerance of established ground truth geometry.

Further investigation of HDBSCAN minimal cluster size and granularity tuning parameter influence on the quality of returned 3D visualisations identified an optimal parameter configuration of $\hat{N}_{\Omega} = 175$ with $\alpha = 1.00$ for the dataset recovered from laboratory experimentation. Quantitative analysis of elapsed workflow runtimes evidenced high computational efficiency, averaging an initialisation to render runtime within 8 seconds on a consumer-grade PC with input data checkpointing functionality enabled.

Finally, performance comparison between fixed-directional GPR and hybrid-rotational was performed, evidencing improved runtime efficiency and spatial profile fidelity with respect to ground-truth target geometry.

# Chapter 7. Field Testing – Hybrid-Rotational GPR

In this chapter, two field tests based on hybrid-rotational GPR are performed, utilising practical datasets gathered from realistic structural analogues. The first test analyses the performance of the developed 3D visualisation workflow from a survey practitioner's perspective. The second test explores refinement of the workflow, investigating the capabilities of Combined Processing Methodology (CPM) for spatial resolution enhancement.

## 7.1 Introduction

The next stage of investigatory work transitioned from small-scale laboratory benchmarking to larger-scale field tests. These tests would examine the practical performance of the developed workflow on real-world hybrid-rotational GPR datasets, and explore opportunities for refinement in its future iterations.

## 7.2 Motivation

Two separate tests were designed. One to assess performance of the current workflow on practical survey data, the second to focus on its refinement potential. This approach would enable performance analysis across various structures and targets, providing greater insight into workflow versatility and robustness. Naturally, as the emergent survey solution, both tests would be based on hybrid-rotational GPR data.

As in previous chapters, tests required more precise knowledge of ground-truth geometry than available from survey records of in-service infrastructure, motivating the use of structural analogues. Masonry tunnels and retaining walls, as common embedded structures, provided a natural structural basis for the tests, and closely aligned with the earlier feasibility study (see Chapter 2). Similarly, the target basis was updated from solid steel spheres to the use of hollow cylindrical plastic targets and metallic strip reflectors — representing utility pipes and electrical conduits, respectively — providing added realism for this more practical survey data.

Practically, constructing a fully enclosed tunnel subsurface analogue was beyond the scope of this investigation. A tunnel floor analogue was ultimately pursued, which also ensured operator safety. Its scale was maximised within the available testing environment, achieving a subsurface volume approximately 60 times larger than possible in the laboratory.

Through the same rotational symmetry argument employed in the laboratory, findings returned for this sectoral analogue could be reasonably generalised to an arbitrary quadrant of a tunnel's full cross section.

At a fundamental level, the structural analogues updated the idealised laboratory setup, to better represent a practical survey environment. Likewise, it was equally important to update the approach for workflow performance analysis to more closely align with the priorities of a real-world survey practitioner. Through dialogues opened with industry practitioners across rail and wider modalities, alongside academics in civil engineering, key priorities were identified in order of importance:

1. **Detection Vs Localisation**: The primary priority identified was accurately detecting anomaly presence within a survey quadrant to determine which regions of the structure require the most urgent attention. This took precedence over pinpointing an anomaly's exact location within a specific quadrant, as the quadrant's unique index within the routine partitioning of the full structure would innately localise any suspected anomalies to within the quadrant boundary[1].

2. **Lateral Vs Vertical Localisation**: When localising a suspected anomaly in 3D space, lateral accuracy (parallel to the rails) was favoured over vertical accuracy (perpendicular to the intrados, into the walls). Since quadrants resemble 'slab' cuboids[2], prioritising lateral accuracy inherently minimises the volume of healthy tunnel subsurface potentially disturbed during maintenance.

3. **Processing Efficiency**: Ultimately assuming accurate insight into subsurface structure can be obtained, a shorter delay between survey collection and the availability of findings would expedite report generation and maintenance strategy planning, thereby reducing the risk of anomaly growth before intervention.

## 7.3 Application I – Subsurface Inspection of a Tunnel Analogue

This section details the first field test, performed on a large-scale tunnel subsurface analogue. Aims and objectives are outlined in Section 7.3.1 and a breakdown of experimental setup and methods is provided in Section 7.3.2. Findings are summarised in Section 7.3.3.

[1]This boundary is not standardised and frequently varies, even within individual surveys. As an example, in [23] quadrants spanning the surveyed tunnel spanned (on average) approximately $10m^2$ when projected onto the intrados.

[2]Where for a quadrant's cuboidal volume, the lateral span significantly exceeds its depth.

### 7.3.1 Aims and Objectives

The primary aim of this investigation was to analyse the performance of the developed 3D visualisation workflow when applied to hybrid-rotational GPR datasets of survey quadrants captured across the tunnel subsurface analogue. As in benchmarking, anomaly detection and localisation accuracy would be considered, alongside computational runtime. Objectives for this investigation were:

1. To capture a hybrid-rotational GPR background calibration scan for the tunnel subsurface analogue, devoid of target geometry.
2. To capture hybrid-rotational GPR scan(s) spanning the tunnel subsurface analogue, containing known ground-truth geometry.
3. To generate 3D visualisations of subsurface anomalies detected within individual survey quadrants, using the developed workflow.
4. To both quantitatively and qualitatively analyse the effectiveness of workflow performance from the viewpoint of a survey practitioner.

### 7.3.2 Experimental Setup and Methods

The tunnel subsurface analogue was formed from a railway locomotive inspection pit as shown in Figure 7.1, which measured 10m long by approximately 1.2m deep.

A pair of steel railway tracks were recessed into the floor of the locomotive works and straddled the pit. The width across the pit was approximately the gauge of the rails, at 1.435m. This corresponded to an approximate total RoI volume of $17.2m^3$. In early plans, the pit would have been manually backfilled with individual clay bricks to emulate layers of masonry in a real tunnel, a slow and highly involved operation. This approach was revised to the use of ballast backfill loaded with an excavator — both readily available onsite. This proved the more pragmatic approach.

From a GPR measurement perspective, both backfill media exhibited a degree of heterogeneity across length scales the order of millimetres, but both could be considered effectively homogeneous at length scales the order of metres (i.e. across the full RoI volume). Moreover, the relative electrical permittivity of both backfill media were considered comparable, with $\epsilon_r \in [2, 6]$ for dry clay (i.e. brick) and $\epsilon_r \in [4, 6]$ for granite (i.e. ballast) [42].

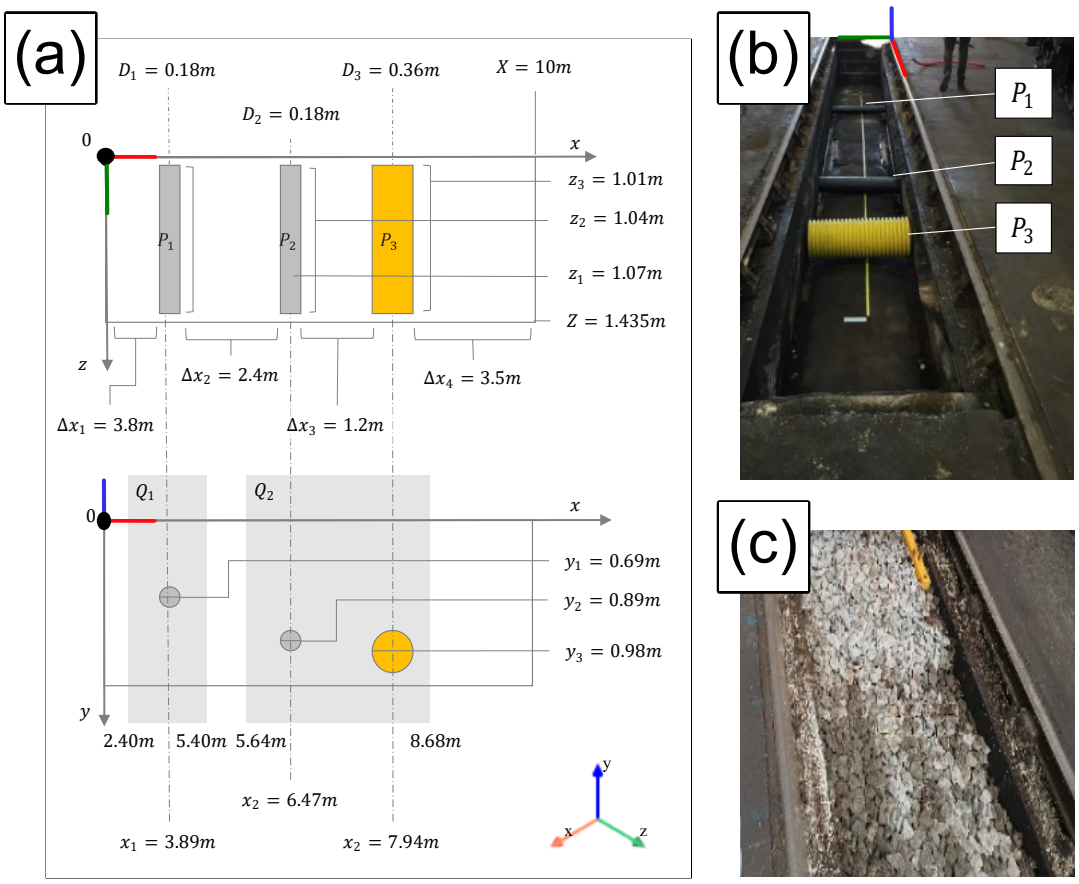


Figure 7.1: The ground truth geometry (a) for the tunnel subsurface analogue for the hybrid-rotational GPR field test was subdivided into two principal quadrants $Q_1$ and $Q_2$ containing hollow plastic utility pipes (b) and ballast backfill (c).

The global coordinate system was aligned to resemble conventions adopted in the previous chapters. Akin to the laboratory setup, the origin was aligned to the upper vertex of the RoI volume, as shown in Figure 7.1b.

The origin was to the left of the centre line when facing the direction of lateral advance and marked on the rail top using chalk. The lateral x-axis was aligned parallel to rails, with the z-axis orthogonal, extending outward from the origin for $z > 0$. The y-axis also intersected the origin, extending vertically upward for $y > 0$. The contact surface for this test was the uppermost surface of the ballast backfill. To simplify target depth measurements, the global origin was vertically aligned with this surface.

Prior to backfill, plastic utility pipes were placed into the pit to serve as targets for detection and localisation. Early plans proposed the addition of voids — similar to ring separation events — using hollow 3D printed targets. The selection was revised to plastic utility pipes, which proved more robust, better withstanding the weight of the surrounding backfill without deforming[3]. Pipes also provided contextually relevant targets, as common subsurface anomalies in GPR-based rail infrastructure surveys, particularly in tunnels for drainage. The hollow cylindrical structure — compared to the solid spheres used for laboratory benchmarking — would also provide insight into how well the proposed 3D visualisation workflow processed more complex RoI target geometry.

A detailed breakdown of ground-truth geometry is presented in Figure 7.1a. In total three plastic utility pipes, $P_{1-3}$ were concealed, with associated diameters $D_1 = 0.18$m, $D_2 = 0.18$m and $D_3 = 0.36$m, respectively.

It was of interest if potential ringdown artifacts associated with the hollow nature of the targets would have an influence on HDBSCAN clustering. Therefore, $P_1$ was placed at a reduced depth compared to $P_2$ and $P_3$ to increase the likelihood a ringdown artifact would be captured within the RoI volume.

Owing to the extensive lateral span of the inspection pit, the full RoI volume was subdivided into two principal quadrants of interest which were analysed independently. As shown in Figure 7.1a, quadrant $Q_1$ encompassed $P_1$ and quadrant $Q_2$ encompassed $P_2$ and $P_3$.

The hybrid-rotational GPR data collection system was based on the system developed in the previous chapter for laboratory benchmarking. The main augmentation made was to mount the system on a former rail inspection pushcart, which replaced the linear rail configuration formerly adopted for the lateral positioning module.

[3]It was noted that the development of a more robust physical analogue of a ring separation event, or digital analogue generator for proposed simulation of hybrid-rotational GPR, presented an opportunity for future work, albeit beyond the scope of this project.

This proved a more practical solution than extending the linear rail to span 10m, which would have deflected under its own weight and required support structures, presenting an obstruction to the carriage. Repositioning a shorter 5m or 2m linear rail was also considered, however repositioning a pushcart mounted system presented the more efficient approach.

As shown in Figure 7.2, the rotating antenna mount was directly mounted to a bespoke glass fibre reinforced polymer superstructure. The strength and rigidity afforded by glass fibre polymer, coupled with its low weight, allowed the displacement between the antenna and metal pushcart frame to be increased without significant deflection. Moreover, as a non-conductive material, the use of glass fibre polymer also avoided introducing unnecessary metallic structures within close proximity of the antenna. This suppressed potential sources of EM-interference at source.

In addition, the superstructure was designed with an integrated pin indexing system. The functionality was incorporated to maximise the versatility of the system. It allowed the centre of antenna rotation to be adjusted between experiments in an accurate and repeatable manner, relative to the RoI volume. Such adjustment provided scope for measurements to be offset laterally from the RoI centreline by up to $\pm 0.5$m in $z$, up to $\pm 0.5$m in $x$, and for contact surface lift off to be set up to almost 2m. In this test, the centre of rotation was aligned to the RoI centre line as in laboratory benchmarking. The contact surface lift off was maximised to provide more a realistic level of clearance with the structure, necessary to mitigate the risk of collision with the catenary of a real tunnel (see Section 2.4.2).

The positioning control, measurement control and power modules were directly transplanted from laboratory system. The superstructure was designed with a two-tier workbench at the working height of the operator to accommodate this equipment, with power supplied to the pushcart via an extension cable connected to the mains.

The pushcart was manually advanced by the operator, as opposed to motorised. This significantly simplified the design process, and the human-in-the-loop approach granted the operator adequate control over lateral positioning. To maximise achievable lateral positioning accuracy and reliability, provisional tests had the operator attempt to advance the pushcart by the shortest possible distance from a reference marker on the rail. It was found that a human operator could comfortably control the movement of the pushcart to within $\pm 20$mm, starting from rest and returning to rest. Doubled for tolerance, this informed the minimal lateral advance of $\Delta x = 40$mm between rotational transects adopted for the field test. This would also ensure that more than 3 rotational transects would intersect each pipe, as required to ensure the pipes had potential to be resolved.

A laser dot mounted on the pushcart projected onto the floor (Figure 7.3). It aligned with 40mm markers etched onto a custom 2m aluminium measure, placed parallel with the pit edge, which was progressively advanced forward to provided a precise lateral position reference.

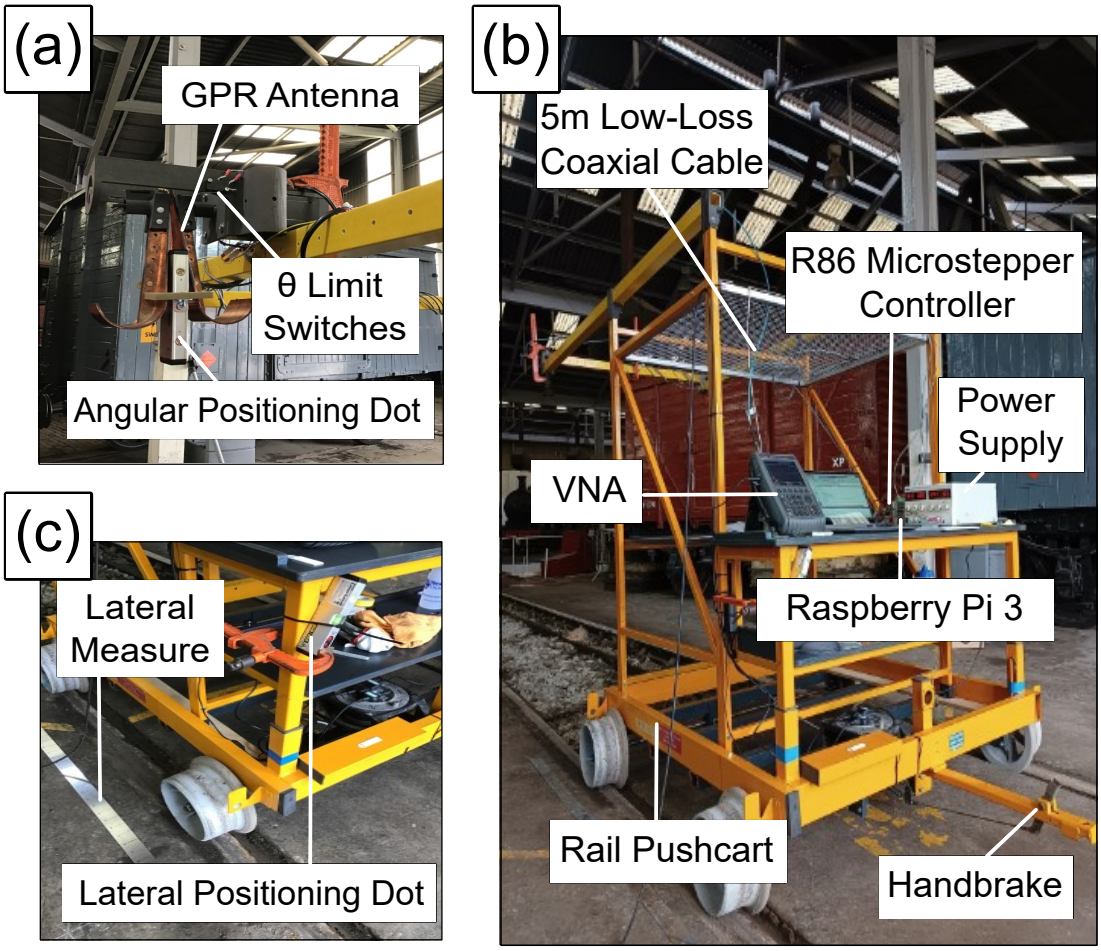


Figure 7.2: Hybrid-rotational GPR data collection system used for field test of tunnel subsurface analogue. The azimuthal positioning module (a) from the laboratory system was mounted on a manually driven rail inspection pushcart (b) that utilised a laser dot (c) to achieve lateral positioning to within ±5mm.

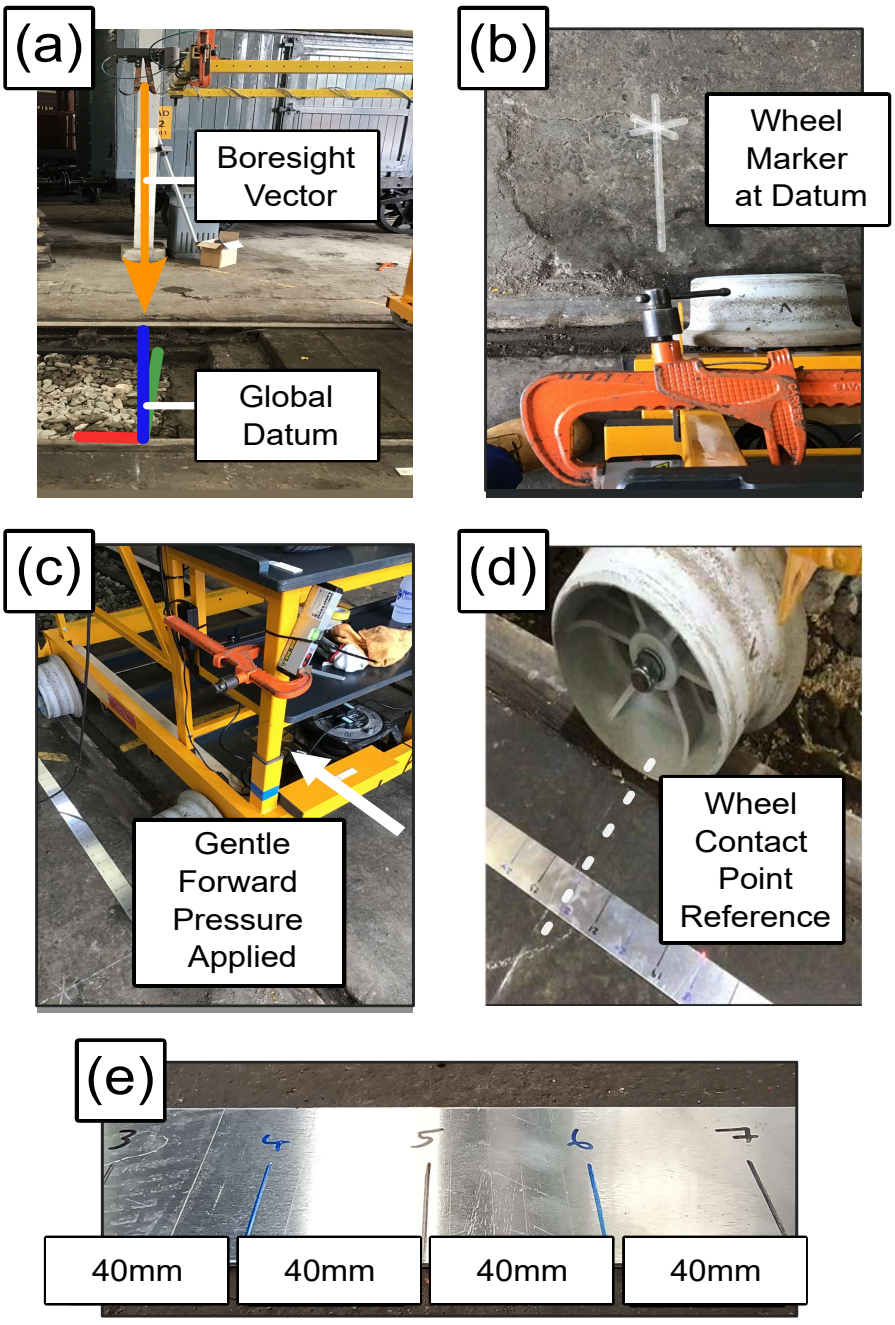


Figure 7.3: Breakdown of lateral positioning during inspection of the tunnel subsurface analogue. The lateral datum aligned with the leading edge of the inspection pit, marked by a chalk line on the floor at the corresponding wheel position (b). Gentle pressure on the frame allowed the pushcart to advance in 40mm increments with relative ease (c). A bespoke 40mm measure (d, e) provided reference markers for the laser dot, enabling accurate and reliable positioning across the full pit length.

Once in position, the pushcart handbrake was applied to prevent the system from moving during data collection. The measure was progressively advanced along the pit when the pushcart reached the end marker. To make repositioning more efficient and accurate, five sets of corner markers were pre-marked on the floor beside the pit using chalk prior to data collection.

The creation of a bespoke measure was necessary on three grounds: clarity, stability, and safety. The aluminium measure was wider than a conventional tape measure (affording larger font) and contained no additional subdivisions. This made it significantly easier for the operator to see when stood advancing the pushcart. To further aid clarity, sequential markers alternated between blue and black, with a red marker highlighting the midpoint. This reduced the cognitive load on the operator, as the 'next' lateral position could be associated with a colour change, as opposed to the recollection of a specific marker index. It also significantly reduced the likelihood of a rotational transect being recorded at the wrong lateral displacement. With regards stability, the measure was fabricated from a flat strip of 2mm thick aluminium. Unlike a regular tape measure, this provided sufficient weight and friction to prevent the measure from moving when the wind gusted through the locomotive works. Safety was also a factor, as the low profile and rigid form did not pose a significant trip hazard.

The azimuthal positioning module closely resembled that used for laboratory benchmarking. The antenna mount was modified to accommodate a sleeve. It passed over the superstructure and housed the vertical indexing pin, which set the desired contact surface lift off. This update required the azimuthal limit switches to be repositioned, which changed the location of the azimuthal datum. Therefore, it was necessary to recalibrate the system to ensure azimuthal displacement (in degrees) was accurately mapped to the equivalent number of microsteps from the azimuthal datum. At over 1.5m above the ground, it was not practical to use visual markers on the antenna motor casing to determine downward vertical alignment, unlike in the laboratory.

The solution devised utilised the laser dot, as shown in Figure 7.4.

The laser was temporarily affixed to the antenna using a threaded bolt, which connected to the laser dot body through a hole in the centre of the supporting struts of the antenna. This fixed the laser dot in alignment with the boresight vector of the antenna, which extended radially outward from the centre of the aperture. The antenna was then iteratively advanced by the operator, using a subroutine which printed the current number of microsteps from the datum to the Python terminal. A spirit level was placed across the rails directly in the vertical plane of the rotational transect. When the vertical downward orientation was reached, the laser dot intersected a marker at the centre of the spirt level, which was aligned to the pit centreline. This approach successfully located the vertical downward at 8459 microsteps from the new azimuthal datum.

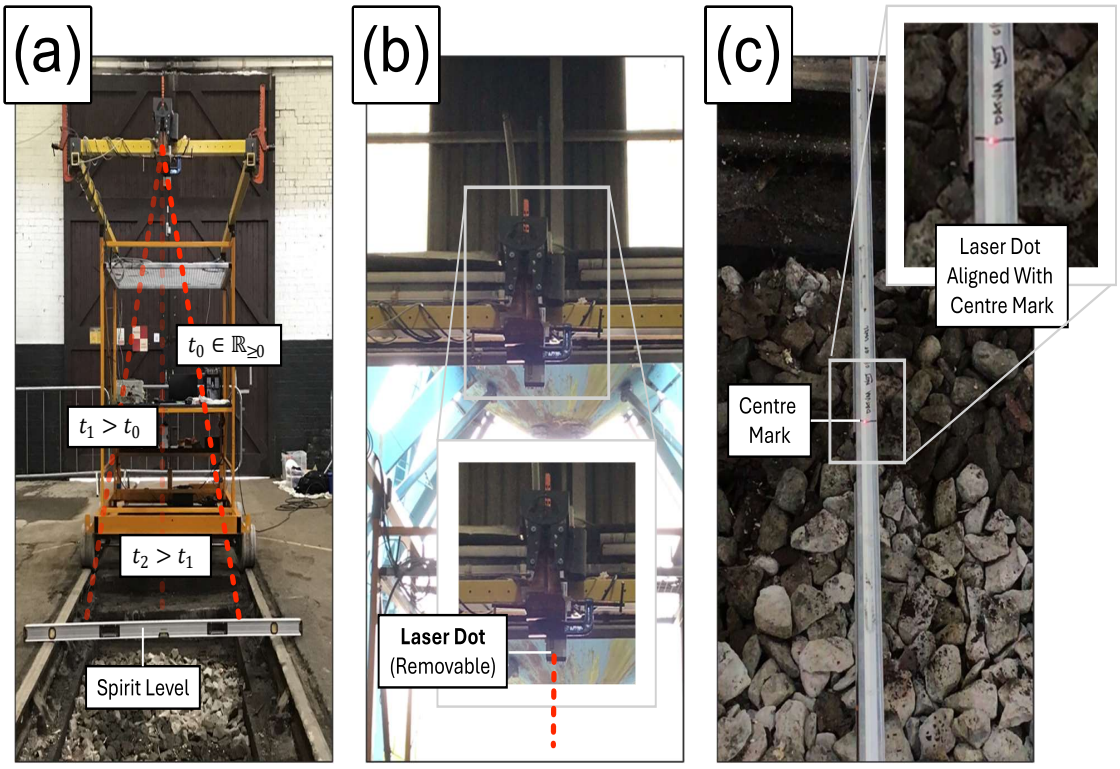


Figure 7.4: Breakdown of azimuthal positioning calibration for inspection of the tunnel subsurface analogue. It was necessary to verify the number of microsteps associated with the downward vertical (a) after updating limit switch placement. This was achieved through manual, iterative updates to the azimuthal displacement (b), using a laser dot and pit centre marker etched on a spirit level (c).

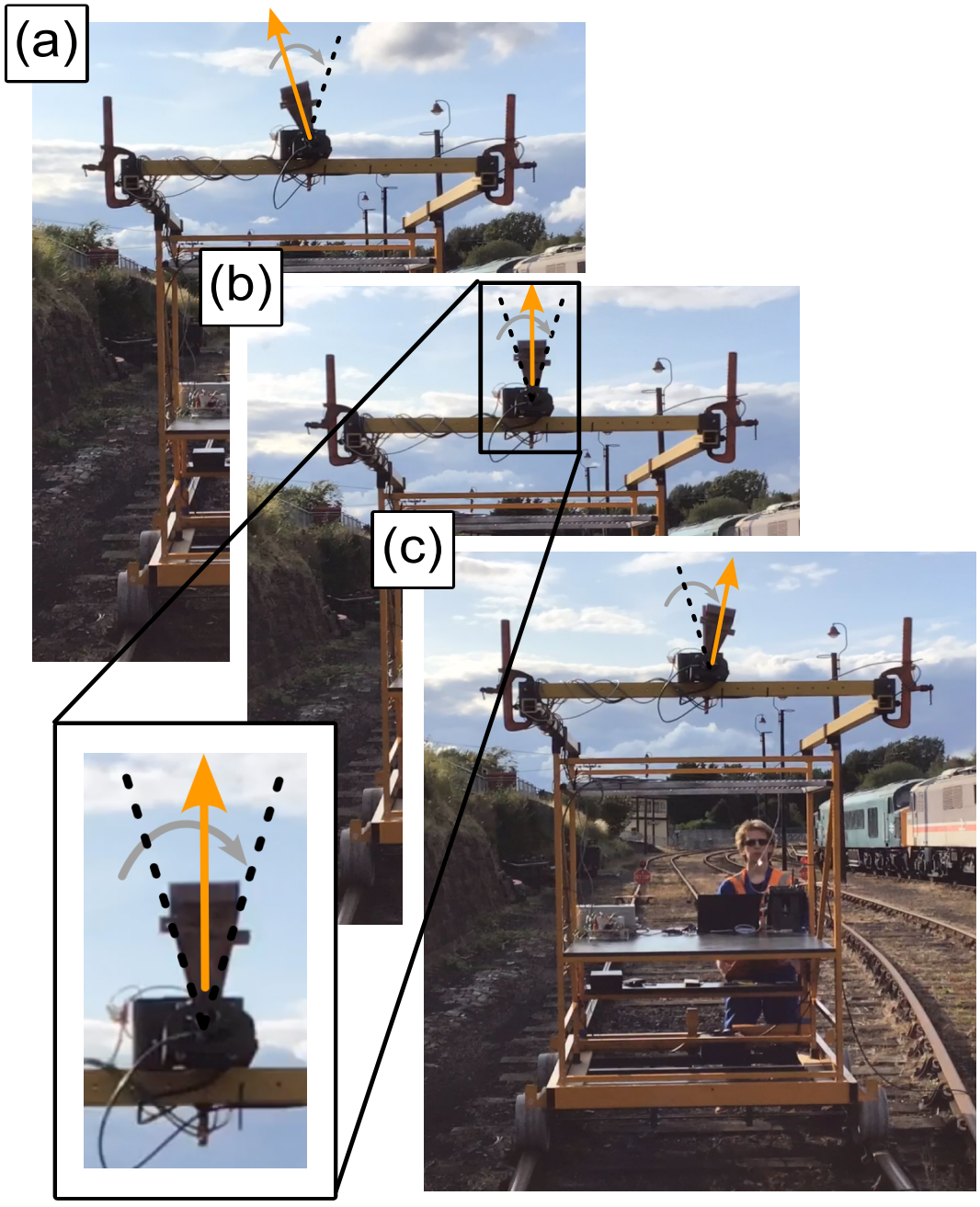


Figure 7.5: Background calibration of hybrid-rotational GPR data collection system prior to scanning tunnel subsurface analogue. This process captured a full rotational transect with a skyward-directed antenna (a-c).

In accordance with Objective (1), VNA calibration followed, as detailed in the previous chapter. Subsequent background calibration captured a rotational transect with the antenna directed skyward, as shown in Figure 7.5.

It was not practically feasible to remove targets from the backfilled inspection pit and record a scanning pass of an empty RoI volume to suppress both internal sources of backscatter and external background geometry (i.e. the backfill). The next most effective strategy was to focus on suppression of internal backscatter, principally attributed to cable flex with advancing azimuthal displacement. To achieve this, the pushcart was moved outside beneath an overhead metal water tower. The underside of the water tower was between 4-6m above the antenna. This region was devoid of any significant sources of backscatter. The antenna was directed skyward and a full rotational transect was recorded. To achieve background calibration, recovered temporal response profiles were subtracted from each trace of corresponding azimuthal displacement recorded during the later recorded full scanning pass of the tunnel subsurface analogue. The water tower served as an effective safety guard, which significantly attenuated the radar signal once it passed into the external environment.

Calibration was followed by the main scanning pass of the tunnel subsurface analogue, in line with Objective (2). The operator manually advanced the pushcart to the required displacement as previously described. The operator then triggered a rotational transect with a keystroke on the PC. Here, the data collection procedure for each transect was identical to that described in the previous chapter. On completion, the operator disengaged the handbrake and laterally advanced the pushcart. This process was repeated across the full length of the tunnel subsurface analogue.

Parameter settings adopted for the field test are presented in Table 7.1.

A single dataset of maximal sample point density would be recorded to provide the most comprehensive analysis possible. The number of sample point per trace was increased from $N_S = 401$ (used in laboratory benchmarking) to $N_S = 1001$ to reflect this, which also ensured that the temporal response interval significantly exceeded 60ns, ensuring that backscatter associated with the extremal limits of the RoI volume (at maximal depth) could be detected.

It remained to optimise the trade-off between the number of unique lateral and azimuthal displacements recorded.

To ensure the full RoI volume was spanned, boresight vectors were aligned to intersect the rail tops at extremal azimuthal displacement. This yielded a total azimuthal displacement of 32.076° across a full rotational transect. It was further recalled that lateral incrementation was set at 40mm. This required a total of 251 rotational transects across the full tunnel subsurface analogue.

| Parameter | Description | Value | Units |
|---|---|---|---|
| $N_S$ | Number of samples per trace. | 1001 | 1 |
| $N_A$ | Number of traces per transect. | 109 | 1 |
| $N_B$ | Number of transects in a full scanning pass. | 251 | 1 |
| $N$ | Number of traces in full scanning pass. | 27359 | 1 |
| $\Delta\theta$ | Trace azimuthal separation. | 0.297 | deg. |
| $\Delta\theta_\mu$ | Azimuthal micro-stepping incrementation. | 0.009 | deg. |
| $\Delta x$ | Trace lateral separation. | 40 | mm |
| $x_0$ | Transect initial lateral displacement. | 0.00 | m |
| $x_1$ | Transect final lateral displacement. | 10.00 | m |
| $\theta_0$ | Transect initial boresight vector azimuth. | 73.962 | deg. |
| $\theta_1$ | Transect final boresight vector azimuth. | 106.038 | deg. |
| $f_{min}$ | VNA linear frequency sweep lower limit. | 0.5 | GHz |
| $f_{max}$ | VNA linear frequency sweep upper limit. | 3.0 | GHz |
| $\Delta f$ | VNA linear frequency sweep incrementation. | 2.50 | MHz |
| $L_0$ | VNA measurement cable length. | 5.0 | m |
| $L_1$ | Antenna body length. | 0.222 | m |
| $L_2(\alpha)$ | Lift-off distance for minimal azimuth. | 0.76 | m |
| $L_2(\beta)$ | Lift-off distance for downward vertical azimuth. | 1.846 | m |
| $L_2(\gamma)$ | Lift-off distance for maximal azimuth. | 1.921 | m |
| $\mu_{360}$ | Azimuthal micro-steps per full revolution. | 40,000 | 1 |

Table 7.1: Hybrid-rotational GPR field test parameters (tunnel subsurface analogue).

The selection of 109 traces per transect was informed by dividing the number of rotational transects into an estimate of the maximal number of trace measurements which could be recorded during the available $T = 21$ hour data collection window. This value was estimated at $N \approx 27300$ individual traces by calculating:

$$N = \frac{3600T}{t_A} \tag{7.1}$$

where $t_A \approx 2.76$ was a 50% overestimate of the observed average duration of a trace measurement at VNA setting to $N_S = 1001$, which provided a reasonable allowance for antenna re-positioning delay between successive trace measurements. This choice also satisfied the projected lateral separation condition $\Delta z \leq 17$mm at the base of the pit for traces of extremal azimuthal displacement (see Section 6.5.3).

### *7.3.3 Results and Discussion*

In accordance with Objective (3), datasets recorded for quadrants $Q_1$ and $Q_2$ were independently processed by the proposed 3D visualisation workflow.

Target Detection and Localisation:

The 3D visualisation workflow was applied in its current state, to both principal quadrants with amplitude thresholding $\hat{A}[\underline{x} \in [0.55, 0.85]$, exponential gain factor $a = 1$, minimal cluster variation across $\hat{N_\Omega} \in [400, 700]$ with $\Delta\hat{N_\Omega} = 50$ and granulation parameter $\alpha \in [0.10, 1.00]$ with $\Delta\alpha = 0.15$.

As in laboratory benchmarking, the selection of suitable $\hat{N_\Omega}$ and $\alpha$ was a subjective process of iterative refinement. Quadrants in the tunnel subsurface analogue were approximately 40 times greater than the RoI volume used in laboratory benchmarking. Moreover, the minimal characteristic target length scale (i.e. the diameter) was only between 2-3 times greater than 100mm sphere used in the laboratory benchmarking. However, it was also noted that the minimal target volume was approximately 65 times greater owing to the length of the pipes. Therefore, it was anticipated the minimal cluster size would need to be increased from $\hat{N_\Omega} = 175$ to reflect this. To achieve this, minimal cluster sizes trailed were approximately doubled to $\hat{N_\Omega} = 400$ and quadrupled to $\hat{N_\Omega} = 700$.

Through iterative refinement, it was found the $\hat{N_\Omega} = 700$ returned optimal output for both quadrants. As in laboratory benchmarking, the influence of variation to $\alpha$ was found to be of negligible significance to recovered spatial profile geometry until $\alpha \ll 0.70$, which rapidly saturated the RoI volume. Output for both quadrants presented in Figure 7.6 was recovered with $\alpha = 1$ and $\alpha = 0.70$ for $Q_1$ and $Q_2$ respectively.

The returned 3D output clearly revealed two sizeable anomalies in $Q_2$, consistent with targets $P_2$ and $P_3$. The average vertical mid-centre coordinates were found to be accurate to within 5.4%, approximately 45mm deeper than the ground truth. Lateral mid-centre localisation was also within 3% for both spatial profiles, averaging 25mm ahead of the ground truth. These values were considered more than acceptable tolerances, given the smallest pipe's minimum characteristic radius (90 mm) was significantly larger than both observed offsets.

Additionally, $Q_1$ also demonstrated successful anomaly detection. The average vertical mid-centre coordinates were accurate to within 7.3%, residing approximately 50mm above the ground truth. The average lateral mid-centre coordinates of each cluster exhibited 42mm forward offset, which notably remained well within the acceptable tolerance.

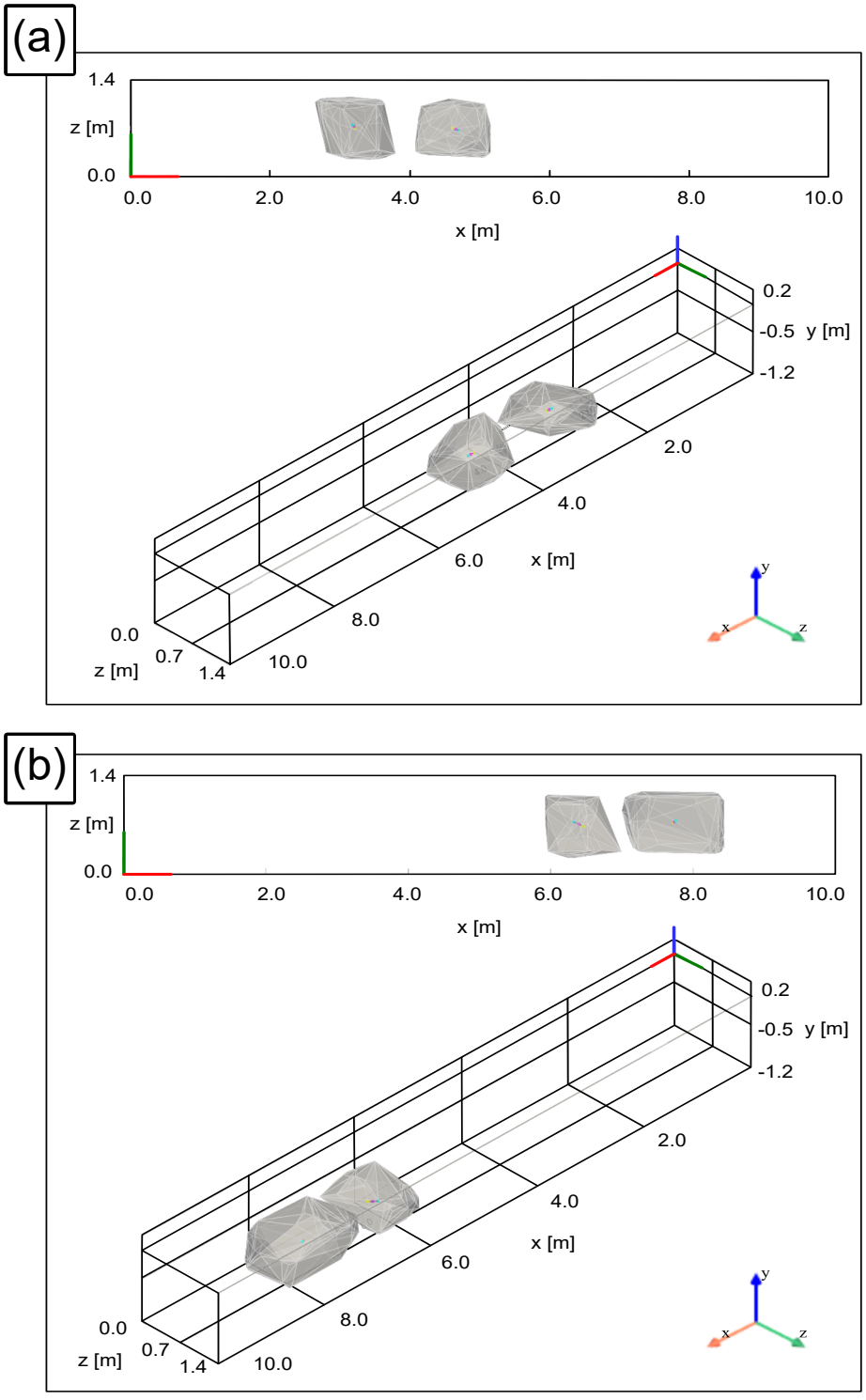


Figure 7.6: Hybrid-rotational GPR scan XZ plane projections (upper inserts) and isometric projections (lower inserts) of 3D visualisation output successfully detected known targets within quadrants $Q_1$ (a) and $Q_2$ (b).

Owing to the reduced depth of $P_1$ compared to $P_2$ and $P_3$, and that it is a hollow target, it was suspected that ringdown occurred within dataset $Q_1$ between -1m $< y < -0.69$m, an artifact attributed to resonation of backscatter within the hollow interior of the pipe. It was proposed that such an artifact, occurring at greater depth than the backscatter event associated with the uppermost interface of the pipe, would exhibit a wider lateral spatial profile but still be in sufficiently close vertical proximity to the original backscatter event to remain within the RoI volume — unlike potential resonation of the significantly deeper targets $P_2$ and $P_3$.

Noting from Chapter 3 that by formulation, migration most accurately resolves the front and rear interfaces of a suspected target[4], it was reasonable that HDBSCAN clustering had identified the ringdown artefact as a candidate rear interface, thereby extending the lateral range over which the clusters were considered, and therein fragmenting the target into the two observed clusters recovered for $Q_1$. Therefore, in reducing the depth of $P_1$ relative to $P_2$ and $P_3$, this had provided valuable insight into the potential influence of ringdown on returned 3D visualisations.

In future work, it would be of interest to trial a selection of more sophisticated migration techniques (e.g. Reverse Time Migration [286,332]) to recover the spatial profile of interfaces with enhanced accuracy. The incorporation an explicit proximity threshold also had potential to aid the discrimination of principal backscatter from the leading interface of a subsurface structural anomaly from its ringdown artifacts.

Critically, in line with Objective (4), this field test had evidenced successful detection of macroscopic structural anomalies requiring follow-up in both quadrants, as would be primarily desired by a surveyor to deliver an effective structural survey of the tunnel subsurface analogue. Subject to fragmentation, observations also further highlighted that significant levels of lateral and vertical localisation had also been achieved, in accordance with identified secondary and tertiary surveyor priorities, respectively.

Computational Performance:

As shown in Figure 7.7, computational runtime for 3D visualisation output averaged 16.8 minutes for $Q_1$ and 14.6 minutes for $Q_2$. This reduced by 2.97% to 16.3 minutes for $Q_1$ and by 3.21% to 14.1 minutes for $Q_2$ when importing merged checkpointed data.

It was recalled that the circumference of the archetypical UK rail tunnel examined in the feasibility study was approximately 16m. Moreover, that masonry tunnels encountered in the literature review (see Chapter 2) contained up to 15 concentric layers of brickwork, extending approximately 1m into the tunnel subsurface[5].

[4]Since GPR ray paths which intersect the sides of targets typically exhibit angles of incidence which reflect them away from the receiver antenna.

[5]This estimate was based on red clay brick and mortar joint dimensions (see Section 3.2.5), with individual bricks orientated with longest side parallel to the centreline of the tunnel.

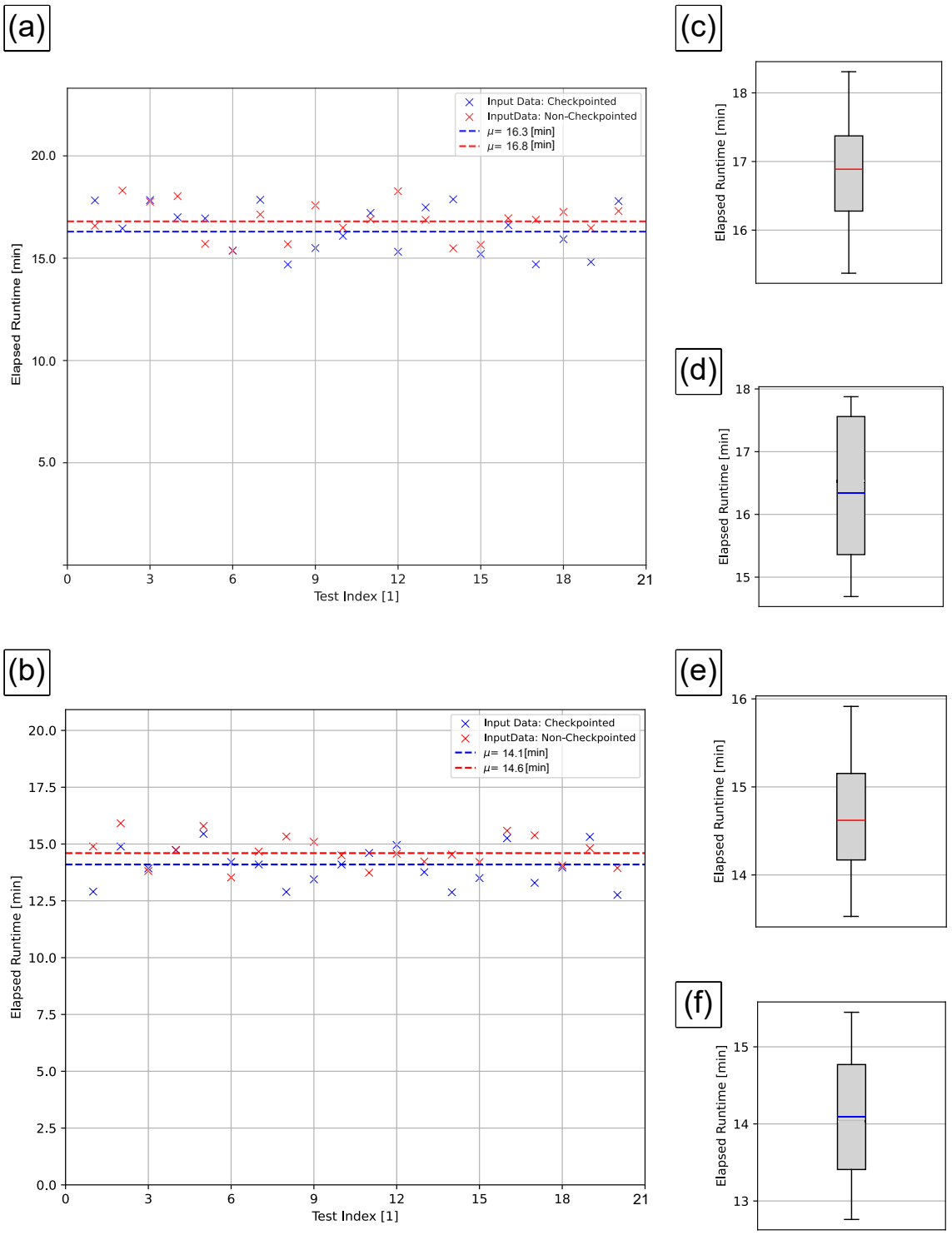


Figure 7.7: Breakdown of elapsed 3D visualisation workflow runtimes for quadrants $Q_1$ (a) and $Q_2$ (b), averaged over 20 independent executions. Box and whisker plots relay the extremal range, mean and IQR of each measurement set for $Q_1$ (c, d) and $Q_2$ (e, f).

Aforementioned dialogue with transport representatives highlighted that structural anomalies which presented the most significant risk were often located in closest proximity to the intrados contact surface. For a 500m long tunnel, the corresponding RoI volume was estimated at $8000m^3$. This equated to approximately 1600 partitioned quadrants.

With an average computational processing time of 15 minutes per quadrant, this approach would require approximately 17 days to generate a full-scale 3D subsurface visualisation. Given the absence of alternative technologies capable of producing comparably comprehensive datasets in tunnel environments, its relatively short turnaround time —significantly faster than the month-long closures required for repairing failed structures —demonstrated sufficient levels of efficiency to be considered practical feasible for future application to surveys of working tunnels.

In practice, reimplementation of this workflow in a compiled language (e.g. C++), as opposed to the interpreted Python language, presents a direct and viable strategy for reducing processing time by several orders of magnitude. Additionally, optimisation for distributed computing, particularly through parallelisation of computationally intensive tasks such as 3D spatial alignment and temporal response recovery, would further improve efficiency. Development of a lightweight quadrant 'culling' tool could also expedite processing by filtering out datasets without significant structural anomalies, or reprioritising considered datasets to prioritise those containing the most potentially significant anomalies.

## 7.4 Application II – Subsurface Inspection of a Wall Analogue

This section details the second field test which explored spatial resolution enhancement for hybrid-rotational GPR data on a large-scale masonry retaining wall analogue. As prior, aims and objectives are first outlined in Section 7.4.1. The CPM algorithm is then formally formulated in Section 7.4.2. Following this, experimental setup and methods are detailed in Section 7.4.3. Finally, results and discussion are presented in Section 7.4.4.

The work presented in this section was summarised and disseminated in [21].

### *7.4.1 Aims and Objectives*

This investigation marked the first application of the CPM algorithm to hybrid-rotational GPR datasets. The primary aim was to assess the viability of the CPM algorithm as a practical basis for spatial resolution enhancement in a future refinement of the proposed 3D visualisation workflow.

In the initial iteration of the proposed workflow, utilised throughout the previous chapters, the data extraction phase is based on the IFFT algorithm. As a fundamental operation in digital signal processing, Fourier Transforms are extensively utilised across the field of GPR analysis [333–335], and can recover the temporal response profiles from trace measurements directly recorded in the frequency domain [336,337].

The MUSIC algorithm can also be utilised for this purpose, albeit far less commonly adopted for GPR analysis. It is capable of recovering trace temporal profiles with higher spatial-temporal resolution than IFFT (i.e. sharper peaks), but inherently yields reduced comparative amplitude precision.

The CPM algorithm, first proposed in [338] and elaborated upon in [138], innovatively combines the more advantageous characteristics of both IFFT and MUSIC, for exclusively 1D datasets. In principal, returning trace temporal response profile with improved spatial resolution compared to IFFT, and higher amplitude precision than MUSIC.

At this stage of research, focus had shifted from initial validation to refining the hybrid-rotational GPR data processing workflow. It was noted that increased fidelity (through spatial resolution enhancement) could be achieved by using CPM for data extraction, instead of sole reliance on IFFT. In fact, direct integration of the full CPM algorithm had been considered for the workflow's first iteration.

However, IFFT was ultimately prioritised due to its broader adoption across encountered literature, which made it the most natural starting point for developing the full 3D visualisation workflow. Its more direct numerical implementation — compared to MUSIC — further supported IFFT as more pragmatic choice, enabling greater focus on the more complex second and third phase processes (i.e. regularisation, post-processing, segmentation, and rendering).

For CPM to be considered a viable basis for spatial resolution enhancement of hybrid-rotational GPR data, performance analysis would be required as in previous chapters. A key area of interest would be the degree of agreement between the established target placements and the observed locations of amplitude peaks across all returned temporal response profiles. This would serve as an indicator of whether the formulation and numerical implementation of CPM had been performed accurately.

Further insights would be gained through direct comparison of the amplitude peak precision and sharpness of the temporal response profiles between CPM and MUSIC, as well as between CPM and IFFT. This comparison would serve to analyse how effectively the CPM algorithm synthesised the advantageous attributes of each respective method.

Objectives for this investigation were:

- To consolidate, and explicitly formulate a standalone, tractable mathematical framework for the practical implementation of the IFFT, MUSIC and CPM algorithms.
- To capture a rotational transect of a large-scale retaining wall analogue devoid of target geometry for background calibration, using a hybrid-rotational GPR data collection system.
- To capture a rotational transect of a large-scale retaining wall analogue containing known ground-truth geometry, using a hybrid-rotational GPR data collection system.
- To validate effective operation of the hybrid-rotational GPR data collection system through quantitative analysis of contact surface detection events, alongside qualitative trends observed in signal noise spectra.
- To analyse the accuracy of temporal response profiles recovered from CPM, based on agreement between known ground-truth geometry and the observed two-way travel time of trace amplitude peaks in the temporal domain.
- To analyse the effectiveness of CPM for spatial resolution enhancement of hybrid-rotational GPR traces, based on observed comparative temporal response amplitude precision (relative to MUSIC) and amplitude peak sharpness (compared to IFFT).

### *7.4.2 Combined Processing Methodology (CPM)*

In this section, the numerical implementation of the CPM algorithm is presented for a 1D GPR trace dataset, $X[f]$. This dataset was separately passed to the algorithms for IFFT and MUSIC, respectively. For a comprehensive deconstruction of each algorithm, see Appendix C.

Here, let application of IFFT convert $X[f] \rightarrow X[t]$. Similarly, let application of MUSIC convert $X[f] \rightarrow Y[t]$. Taking the absolute magnitudes $|X[t]|$ and $|Y[t]|$ recovered the observable temporal response profiles, which were subsequently normalised to the range [0,1], which combatted skew attributed to dissimilar temporal response magnitudes during merger. For brevity, let the normalised observable temporal responses be denoted $x(t)$ and $y(t)$ respectively.

For an ideal merger, it was sought to preserve the advantageous characteristics of both temporal response profiles. In reality, combining both profiles fundamentally resulted in a trade-off. This meant that the CPM temporal response profile was expected to reside between $x(t)$ and $y(t)$ throughout the temporal domain, and would provided a useful visual sanity-check during numerical implementations, particularly during the early stages of program development.

The relation for the CPM temporal response profile, $z[t]$, was intuitively derived by considering the desired characteristics of the temporal response profile when either close or far away from a peak associated with a strong backscatter event.

Close proximity to a peak was indicated by a considerably sharper increase in $y(t)$ than $x(t)$, owing to the higher spatial resolution of the MUSIC response compared to the IFFT response. In this region, the CPM response requires the highest level of amplitude accuracy, associated with $x(t)$. Note that compounded approximations were performed during the MUSIC algorithm, which would inherently limit the comparable amplitude accuracy of $y(t)$. It was further recalled that peaks corresponded to high magnitude gradients in temporal response profiles. Therefore, this condition could be formulated in terms of partial derivatives as,

$$\frac{\partial y}{\partial t} \gg \frac{\partial x}{\partial t} \implies z[t] \to x[t]. \tag{7.2}$$

In contrast, when far from a peak, the MUSIC response was near flat compared to the IFFT response, owing to its improved noise suppression. Here, it was desired that the CPM response more closely resemble $y(t)$ to incorporate the higher levels of noise suppression achieved by MUSIC and maintain sharp peaks. Framed in terms of partial derivatives,

$$\frac{\partial x}{\partial t} \gg \frac{\partial y}{\partial t} \implies z[t] \to y[t]. \tag{7.3}$$

From these conditions, the CPM relation was formulated, in line with Objective (1). The initial form resembled a weighted average of both responses, re-standardised through division by the magnitude of the weighting coefficients, which were determined by asymptotic fit subject to the two identified conditions associated with the partial derivatives. The full formulation can be expressed as

$$z[t] = \frac{x\left|\frac{\partial y}{\partial t}\right| + y\left|\frac{\partial x}{\partial t}\right|}{\sqrt{\left|\frac{\partial x}{\partial t}\right|^2 + \left|\frac{\partial y}{\partial t}\right|^2}}. \tag{7.4}$$

Computation of the first-order partial derivatives was achieved using the fourth-order central differencing approximations,

$$\begin{aligned} \frac{\partial x[t_k]}{\partial t} &= \frac{x[t_{k-2}] - 8x[t_{k-1}] + 8x[t_{k+1}] - x[t_{k+2}]}{12\Delta t} + O(\Delta t^4) \\ \frac{\partial y[t_k]}{\partial t} &= \frac{y[t_{k-2}] - 8y[t_{k-1}] + 8y[t_{k+1}] - y[t_{k+2}]}{12\Delta t} + O(\Delta t^4) \end{aligned} \tag{7.5}$$

where $\Delta t = T/N$ is the temporal incrementation value.

Ghost-points were defined to enforce physically grounded boundary conditions for recovered temporal response profiles. Considering $t = 0$, the *fixed* boundary condition $x = y = 0$ was enforced for ghost points at $t_{-2}$ and $t_{-1}$. It was reasoned that as no signal backscatter could occur without sufficient elapsed time for the transmission signal to propagate to a subsurface anomaly interface, backscatter from it, and return to the receiver antenna. In addition, considering $t = T$, a further *periodic* boundary condition was implemented for ghost-points defined at $t_{N-1}$ and $t_N$:

$$\begin{aligned} x[t_N] &= x[t_0] \\ y[t_N] &= y[t_0] \\ x[t_{N+1}] &= x[t_1] \\ y[t_{N+1}] &= y[t_1] \end{aligned} \tag{7.6}$$

In reality, attenuation, and signal scattering within the subsurface would eventually attenuate backscatter amplitude intensity to the level of background noise. However, in the finite temporal interval of the VNA measurement, exactly when the return signal fully attenuated to this point was inherently ambiguous. When considered at the low-level, this was due to continual presence of background noise and the intrinsic randomness of its associated contribution to observed return signal magnitude. Alternatively, when considered from a high-level, the VNA measurement was effectively considering a small sample of a much longer duration signal. This motivated selection of a periodic boundary condition.

For the full numerical implementation utilised in this study, see Appendix A.

### *7.4.3 Experimental Setup and Methods*

Data utilised in this study was obtained using a hybrid-rotational GPR system to capture a rotational transect of a large-scale masonry retaining wall analogue.

The IFFT, MUSIC and CPM algorithms were applied to constituent traces recorded across a range of azimuthal displacements. To suppress spectral leakage artifacts, a Kaiser–Bessel window with $\alpha = 3$ was applied within the IFFT algorithm (see Appendix C.3). Similarly, the MSSP technique was incorporated into the MUSIC algorithm to mitigate artifacts arising from coherent return signals (see Appendix C.5).

Alongside facilitating comparative analysis between performance of IFFT, MUSIC and CPM on isolated traces, varying the azimuthal displacement of traces across the rotational transect provided further insight into the influence of antenna rotation in each case.

As in previous chapters, a rotational symmetry argument was applied to reduce the total number of unique antenna azimuthal displacements required during data collection, therein simplifying the design and operation of the data collection system.

The global coordinate system was aligned to resemble conventions adopted in the previous chapters. As in the previous investigation, the origin was naturally associated with the centre of antenna rotation, approximately located at the base of the rotating antenna, aligned with the centre of the motor shaft. The lateral x-axis was aligned parallel to the long side of the retaining wall, with the z-axis orthogonal, extending outward from the origin for $z > 0$. The y-axis also intersected the origin, extending vertically upward for $y > 0$.

| **Trace Index [1]** | **Contact Surface Lift Off [m]** | **Azimuthal Disp. [deg.]** |
|---|---|---|
| 00 | 0.170 | 59.015 |
| 01 | 0.153 | 61.880 |
| 02 | 0.137 | 65.317 |
| 03 | 0.137 | 71.047 |
| 04 | 0.127 | 75.057 |
| 05 | 0.137 | 80.787 |
| 06 | 0.132 | 84.224 |
| 07 | 0.150 | 90.000 |
| 08 | 0.151 | 93.438 |
| 09 | 0.176 | 98.594 |
| 10 | 0.183 | 102.032 |
| 11 | 0.214 | 106.043 |
| 12 | 0.224 | 108.908 |
| 13 | 0.261 | 112.918 |
| 14 | 0.276 | 115.783 |
| 15 | 0.316 | 118.648 |
| 16 | 0.333 | 120.940 |

Table 7.2: Summary of contact surface lift off and azimuthal displacement for each constituent trace within the rotational transect of the retaining wall.

The rotational transect was aligned to the XZ plane for orthogonal intersection with the wall, and throughout data collection the lateral position of the antenna was maintained (relative to a reference marker etched on the wall). Together, these selections ensured that the returned transect provided a clear cross section of the retaining wall subsurface for comparison with the known ground truth geometry.

In line with Objective (3), a total of 17 distinct traces formed the transect, recorded with the antenna boresight vector at azimuthal displacements presented in Table 7.2.

As in earlier chapters, when viewed in the YZ plane, orientation angles resembled an Argand Diagram, with azimuth $\theta = 0°$ aligned with the horizontal half-line for $z > 0$. Displacements were measured relative to a fixed azimuthal datum aligned with the downward vertical half-line for $y < 0$. Total azimuthal displacement spanned 62°. To ensure maximal coverage was achieved, extremal limits of antenna rotation were selected such that the antenna boresight vector directly intersected the extremal interfaces of the retaining wall.

| **Parameter** | **Description** | **Value** | **Units** |
|---|---|---|---|
| $N_S$ | Number of samples per trace. | 201 | 1 |
| $N_A$ | Number of traces per transect. | 17 | 1 |
| $N_B$ | Number of transects in a full scanning pass. | 1 | 1 |
| $N$ | Number of traces in full scanning pass. | 17 | 1 |
| $\Delta\theta$ | Trace azimuthal separation. | [2.30,5.80] | deg. |
| $\Delta\theta_\mu$ | Azimuthal micro-stepping incrementation. | 0.009 | deg. |
| $x_0$ | Transect initial lateral displacement. | 0.00 | m |
| $x_1$ | Transect final lateral displacement. | 0.00 | m |
| $\theta_0$ | Transect initial boresight vector azimuth. | 59.015 | deg. |
| $\theta_1$ | Transect final boresight vector azimuth. | 120.940 | deg. |
| $f_{min}$ | VNA linear frequency sweep lower limit. | 0.5 | GHz |
| $f_{max}$ | VNA linear frequency sweep upper limit | 3.0 | GHz |
| $\Delta f$ | VNA linear frequency sweep incrementation. | 12.5 | MHz |
| $L_0$ | VNA measurement cable length. | 0.91 | m |
| $L_1$ | Antenna body length. | 0.222 | m |
| $L_2(\alpha)$ | Lift-off distance for minimal azimuth. | 0.170 | m |
| $L_2(\gamma)$ | Lift-off distance for maximal azimuth. | 0.333 | m |
| $\mu_{360}$ | Azimuthal micro-steps per full revolution. | 40,000 | 1 |

Table 7.3: Hybrid-rotational GPR field test parameters (retaining wall analogue).

As in Section 7.3, the hybrid-rotational GPR data collection system was an augmented version of that used for laboratory benchmarking. To ensure consistency, the system configuration for the retaining wall was based on the same positioning motor and TEM-feedhorn GPR antenna, cycling linear frequency sweeps of 0.5-3GHz to record trace measurements.

A Hewlett-Packard HP8753D VNA was made available for this test. Trace measurement automation was successfully achieved using SCPI commands, transmitted over a 1m USB cable through a National Instruments GPIB-USB interface adapter. The antenna was connected to the VNA via a 0.91m measurement cable.

Parameter settings used for data collection are provided in Table 7.3, and a visual summary of the system configuration is shown in Figure 7.8a.

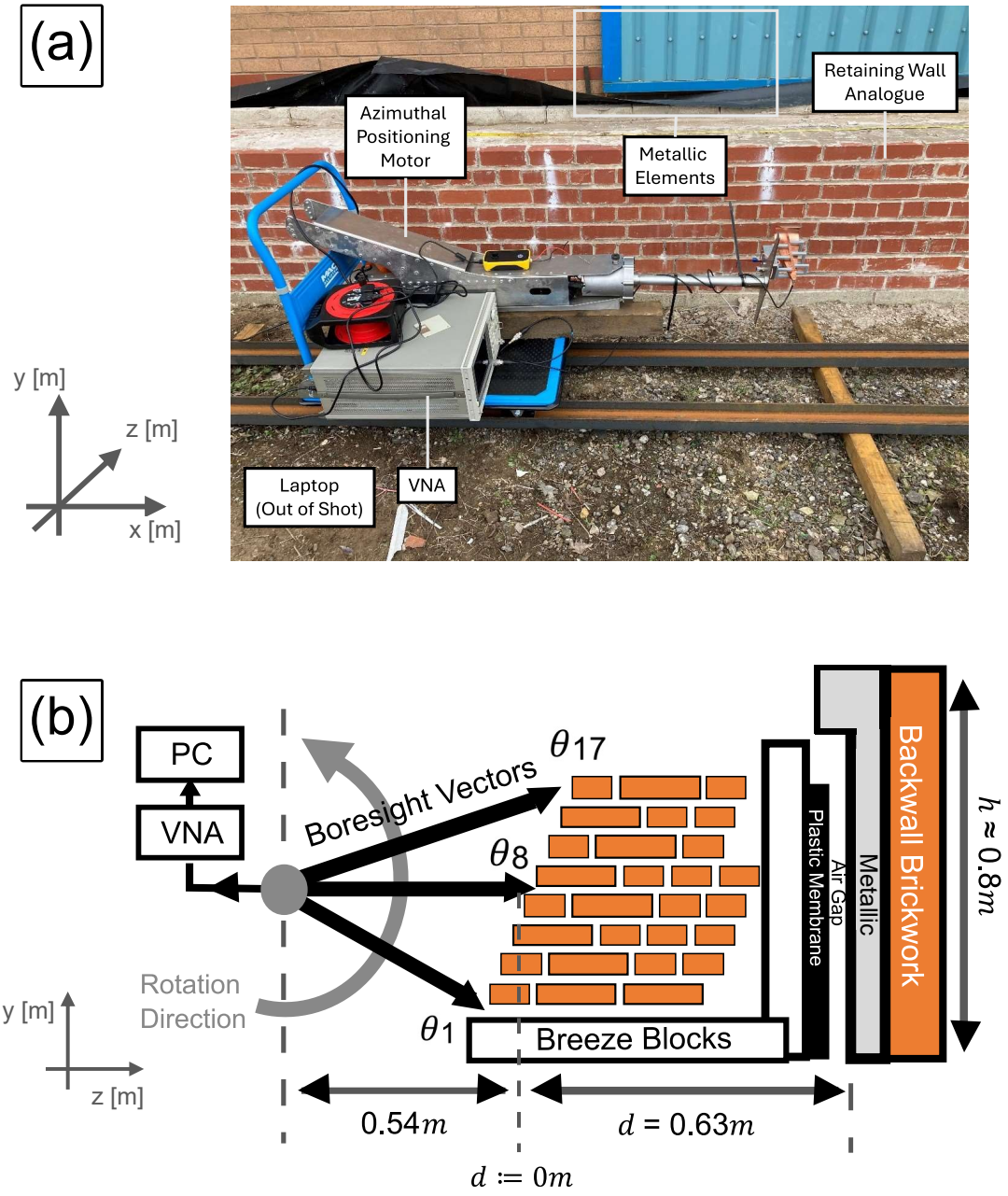


Figure 7.8: Experimental setup for hybrid-rotational GPR data collection on the retaining wall analogue (a) with associated ground truth geometry (b).

The retaining wall analogue was comprised red clay bricks bounded by mortar stacked atop a level base of breeze blocks partially sunken into the ground. Individual bricks measured approximately 215mm in $x$, 65mm in $y$ and 103mm in $z$, separated by 10mm mortar joints on all sides. In keeping with historic masonry infrastructure encountered during the literature review (see Chapter 2), the retaining wall analogue was constructed to be 8 layers tall and 5 layers deep. A single layer of breeze blocks supported the rear of the wall, backed by a plastic water-resistant membrane. It was separated from the sidewall of an adjacent warehouse by a narrow air gap less than 0.1m wide. As in laboratory benchmarking, it was decided that the first tests involving CPM on hybrid-rotational GPR data should feature more a more idealised homogeneous subsurface composition similar to earlier simulation work (see Chapter 4), therefore, the air gap was not backfilled up to the retaining wall analogue for this investigation.

Metallic cladding was attached to the adjacent wall, stopping within 0.1m of the top of the retaining wall. A metallic strip was also present, which overlapped the metallic cladding by approximately 130mm and extended the full height of the retaining wall to the ground. Figure 7.8b provides a visual breakdown of the ground-truth geometry.

Prior to data collection, VNA calibration was performed using Keysight 85052D Mechanical Calibration Standards (i.e. short, open and load). Background calibration followed. To effectively assess the performance of the CPM algorithm, it was necessary to ensure temporal response profiles exhibited multiple amplitude peaks. Such peaks would be expected from the successive interfaces of the masonry layers and metallic targets at the rear.

Therefore, in this context it was desired that backscatter events associated with external environment geometry should be preserved wherever possible during background calibration. Henceforth, the suppression of internal backscatter events (i.e. between VNA output and antenna aperture) was prioritised. In accordance with Objective (2), this was achieved by recording a trace measurement with the antenna directed skyward ($\theta = 180°$). A metal roof canopy was located approximately 5m above the retaining wall, sufficiently high as not to interfere with measurements of the wall, whilst still providing suitable weather protection for the experimental apparatus. The canopy also served as a safety guard, which significantly attenuated the radar signal during background calibration after wavefronts crossed the antenna aperture and entered the external environment. Once the background calibration trace was recorded, the IFFT and MUSIC algorithms were applied to this and each trace in the rotational transect. The final step each algorithm performed was the subtraction of the background calibration trace, prior to the data being passed to the CPM algorithm.

System automation was achieved using MATLAB throughout this test, as its Instrument Control Toolbox readily supported interfacing via the GPIB-USB adapter. MATLAB was also selected as the basis for IFFT, MUSIC and CPM data processing in this study.

Here, it should be noted that the focus of research in this study began to lean more heavily into the refinement of this new generation of hybrid-rotational GPR technology, whereas in previous sections, the focus was centred on benchmarking and the validation of effective performance in the field. The focus-shift towards refinement afforded a greater flexibility in the choice of approaches this study could select from. For example, it was decided MATLAB would be provisionally trailed in place of Python for data processing in this study. This was motivated by the more direct resemblance between syntax in MATLAB and the mathematics underpinning developed programs. The higher level of abstraction in MATLAB syntax had potential to allow for a more intuitive and effective implementation of both the MUSIC and CPM algorithms, especially in the initial development phase.

Importantly, flexibility would still exist to switch back to development in Python if required. Since MATLAB and Python were both high level programming languages based on imperative control structures[6], a program developed in MATLAB could be converted into equivalent Python syntax with relative ease. This flexibility was also of great potential benefit for future research efforts subject to both possible outcomes of this trial, whether it was found that the higher level of abstraction had not proved of significant benefit to the numerical implementation of MUSIC and CPM, or that this approach had provided significant benefit. In the latter case, being able to port any developed programs to a non-proprietary programming language would increase the accessibility and usability of developed programs among the wider research collective.

### *7.4.4 Results and Discussion*

The rotational transect was contextualised through 3D alignment of the XZ measurement plane in Figure 7.9, alongside the overlay of the retaining wall contact surface and physical data collection system in Figure 7.10.

The observable temporal response profiles were recovered by taking the absolute magnitude of the returned GPR signal. To aid comparison, profiles were normalised to the range [0,1]. High intensity initial backscatter from the contact surface of the wall dominated raw temporal response profiles, therefore a threshold of 0.25 was applied to the temporal response profiles to increase the clarity of lower intensity peaks in the immediate vicinity. The resultant increase in achieved contrast is shown in Figure 7.11.

Trace measurements from the rotational transect are presented side by side on separate axes in Figure 7.12 to facilitate closer analysis of contact surface detection events and associated noise spectra, in accordance with Objective (4).

[6]Sequences of operations performed as a run of conditionals (e.g. `if`,`else`) and loops (e.g. `for`,`while`), rather than declarative or functional control structures.

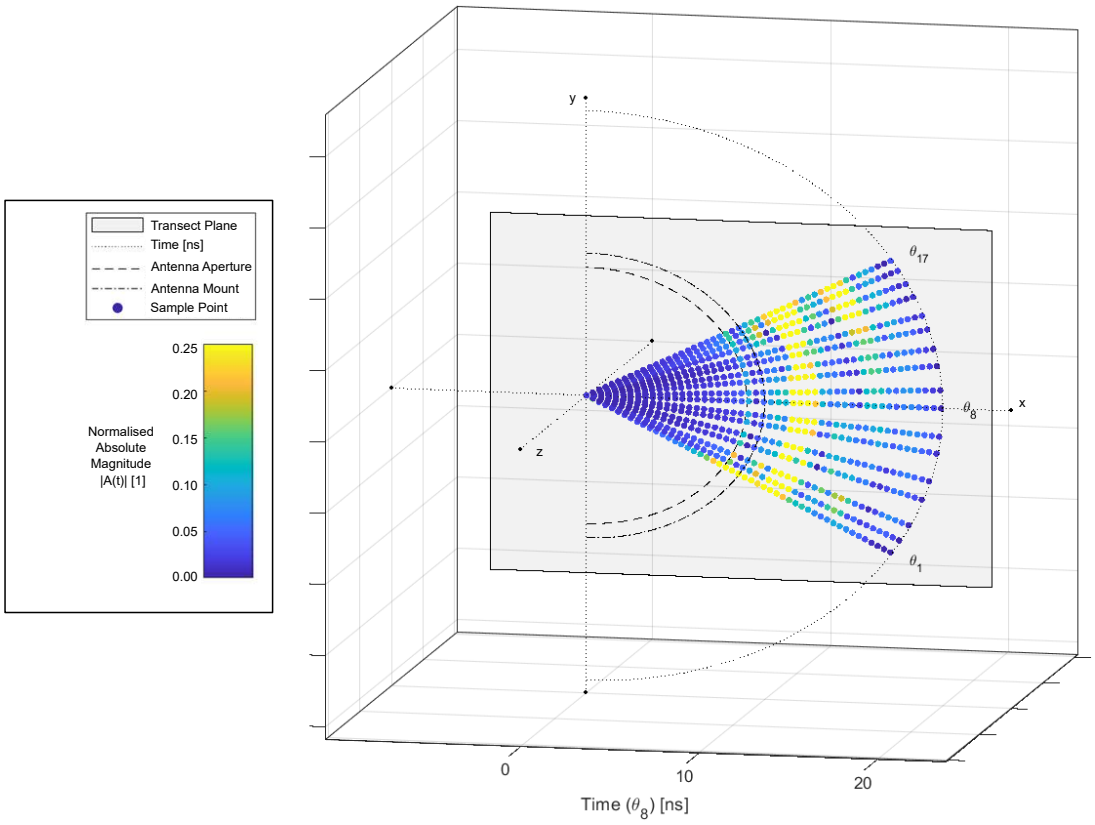


Figure 7.9: Rotational transect of the retaining wall analogue aligned in 3D space, captured using the hybrid-rotational GPR data collection system.

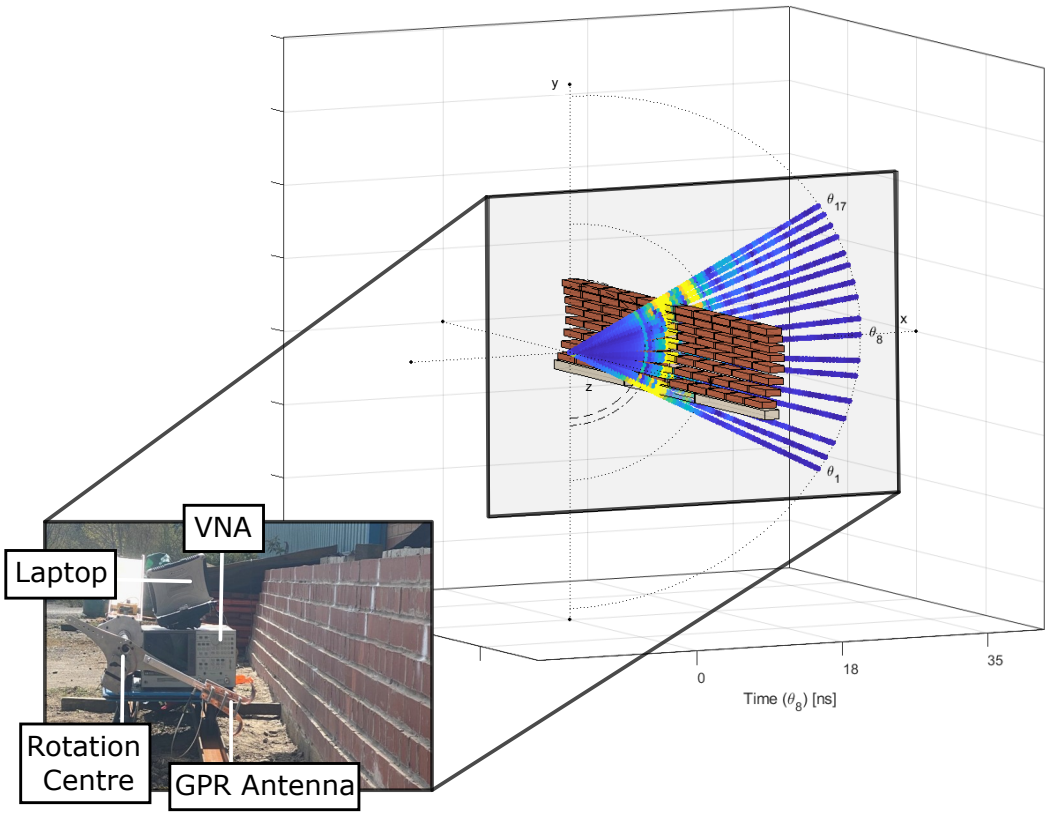


Figure 7.10: Overlay of contact surface geometry and the hybrid-rotational GPR data collection system for contextualisation of the 3D-aligned rotational transect.

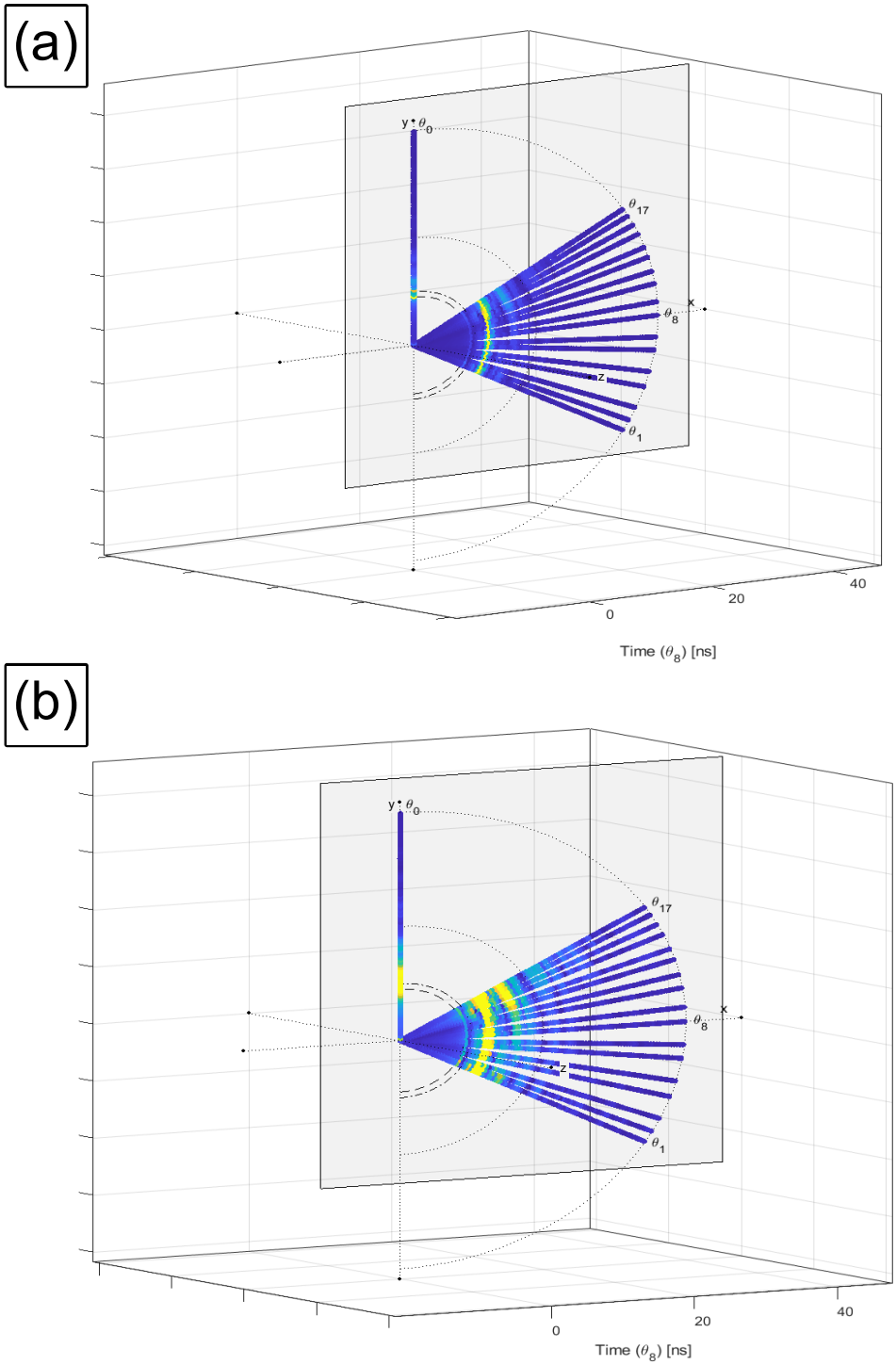


Figure 7.11: Comparison of threshold value impact on transect contrast. Reducing the threshold from 1 (a) to 0.25 (b) highlighted more subtle variations within the subsurface.

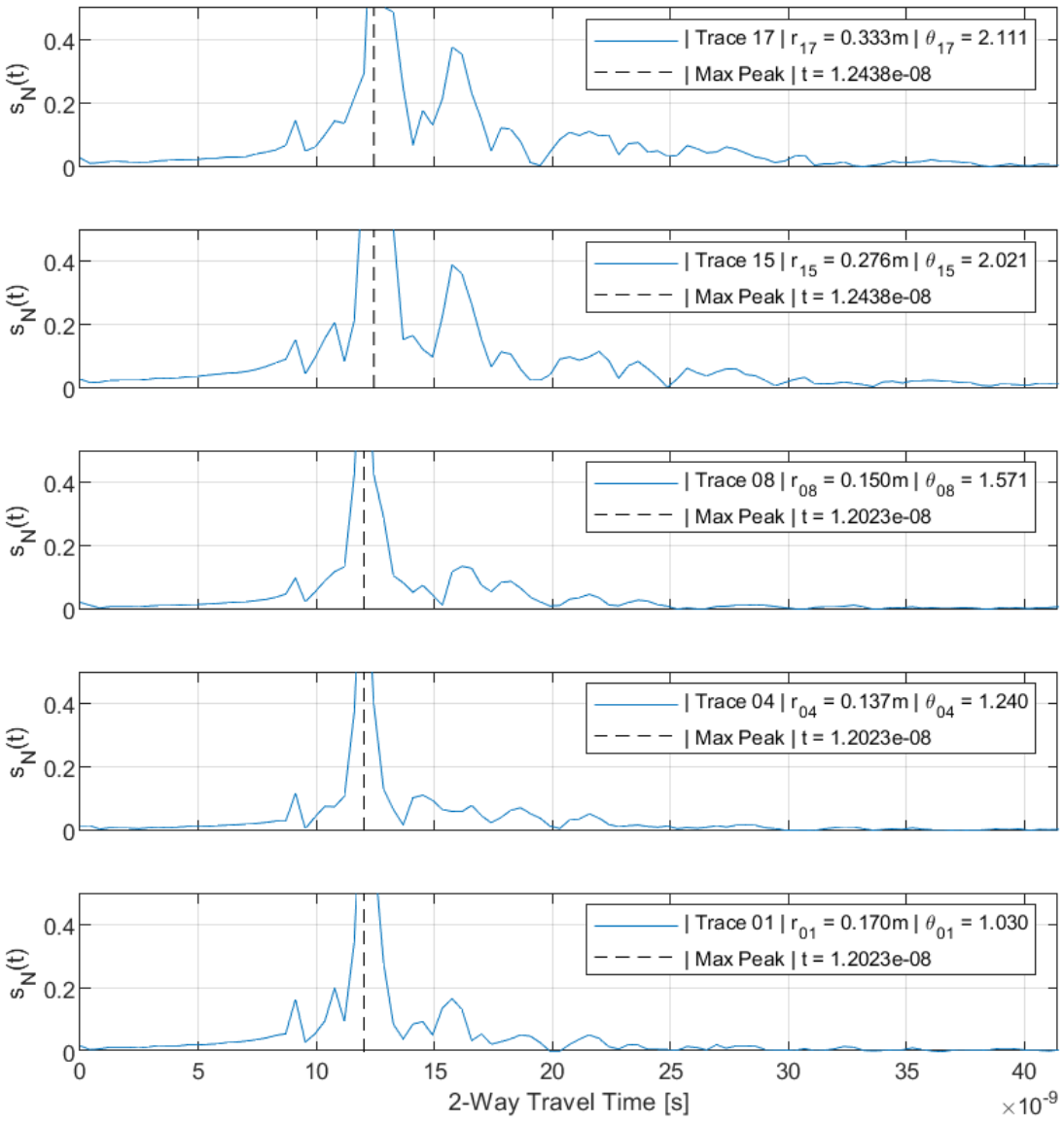


Figure 7.12: Signal magnitude peak variation in temporal response profiles (recovered via IFFT) subject to increased azimuthal displacement on the retaining wall analogue.

Peaks of maximal intensity were observed to occur at later two-way travel times as the azimuth of the antenna boresight vector increased. Associated displacements exhibited close agreement within 3.9% of expected contact surface lift off listed in Table 7.3. This observation evidenced that the hybrid-rotational GPR hardware was correctly configured and accurately detecting the ground-truth geometry of the retaining wall.

Evidence of the onset of noise dominance within the temporal response profile was also observed for $t \gg 40$ns, shown in Figure 7.13.

Eventually, the return signal magnitude was expected to attenuate to a level where background levels of residual noise[7] dominated the temporal response profile. These hallmarks were clearly identifiable for $t \gg 40$ns, beyond the retaining wall RoI volume. The mean average percentage variation was 0.005%, very close to a typical Gaussian white noise profile characterised by a mean of zero. Noise analysis therefore also evidenced that the hybrid-rotational GPR system was correctly configured and returning measurements consistent with expected signal behaviour.

The impact of CPM, MUSIC and CPM processing was visually compared using plots presented in Figure 7.14.

It was noted that the CPM temporal response profile was consistently bounded between the temporal response profiles recovered from IFFT and MUSIC. This was consistent with the accuracy check proposed earlier in this section.

The significantly increased spatial resolution of the MUSIC algorithm was immediately evident from visual inspection of the trace overlays, especially compared to the broad bases of the IFFT peaks. The extremely close agreement between the FWHM of CPM and MUSIC peaks was further apparent, in conjunction with comparable levels of agreement demonstrated between the absolute magnitudes of the CPM and IFFT peaks. More in-depth inspection revealed the FWHM of CPM peaks to be between 1-3ns wider on average than for MUSIC, and amplitude agreement with IFFT to be on average within an approximate 8.7% average tolerance in the vicinity of the main peaks. This was consistent with the inherent trade-off between amplitude precision and spatial resolution enhancement which underpinned the CPM strategy. Collectively, these observations provided strong supporting evidence that the CPM algorithm had been precisely formulated and accurately numerically implemented.

In line with Objective (5), the level of agreement between known ground-truth geometry and peaks in the observed CPM temporal response profiles was examined.

[7] Characterised by stochastic random intensity fluctuations (see Chapter 2).

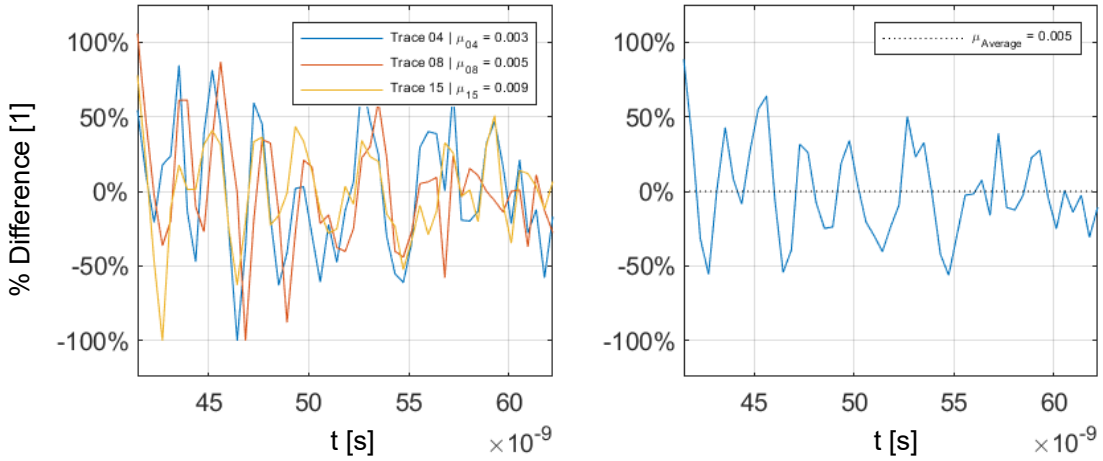


Figure 7.13: Highly attenuated temporal response profiles for $t \gg 40$ns. Noise dominated observed profiles in this region, evidenced by the stochastic random nature of amplitude variation in both raw amplitude data (a) and averaged amplitude data (b).

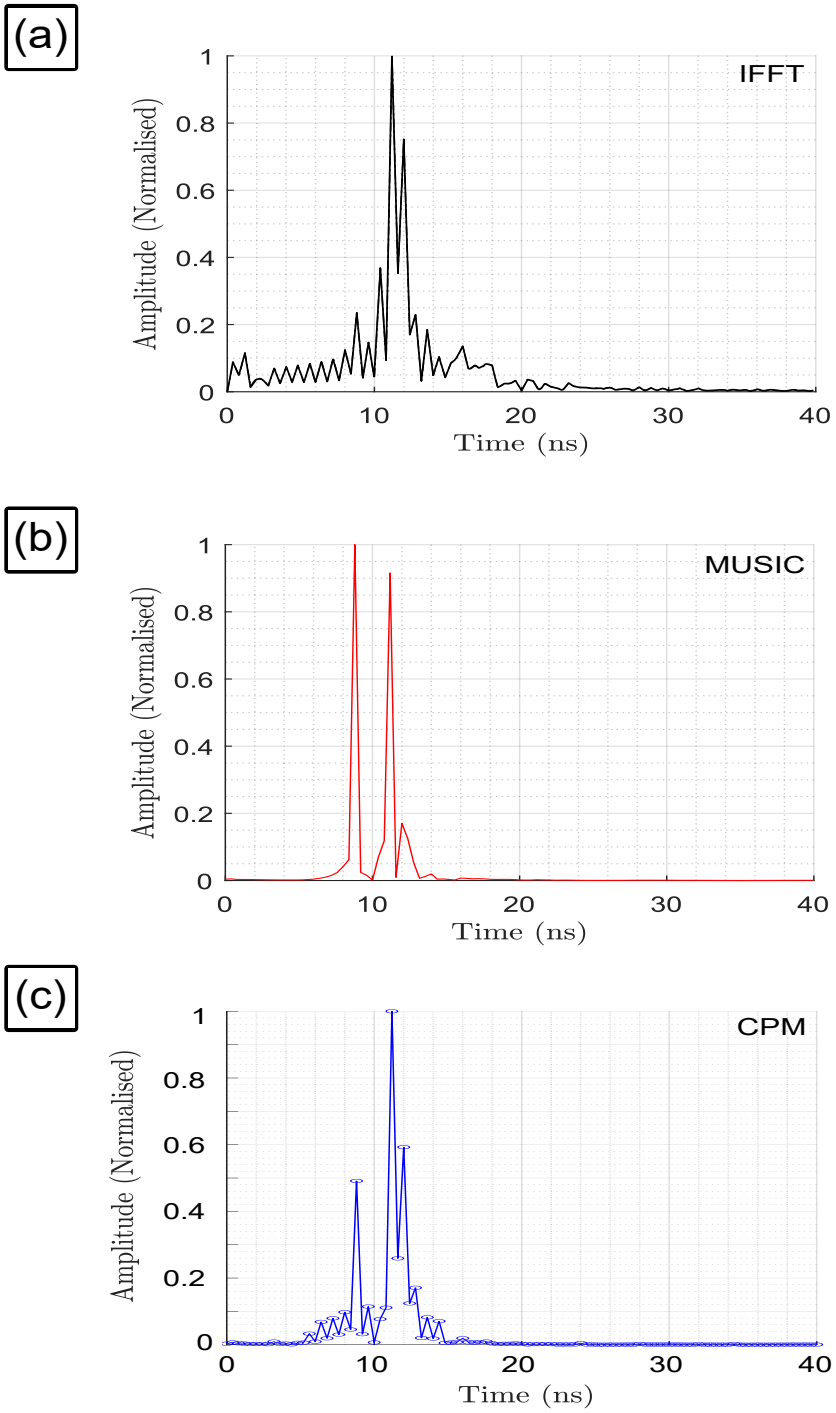


Figure 7.14: Comparison of temporal response profiles recovered for the rotational transect with azimuthal displacement $\theta_7 = 90°$ (i.e. horizontal). Data processing utilises: (a) IFFT with Kaiser-Bessel windowing; (b) MUSIC subject to MSSP and (c) CPM.

In the temporal response displayed in Figure 7.14, high amplitude peaks near $t = 9$ns, $t = 12$ns and $t = 13$ns indicated the occurrence of strong backscatter events. Initial backscatter from the contact surface of the retaining wall air-wall marked the first significant backscatter event. This compared to the expected two-way travel time, expressed as,

$$t \approx \frac{2}{c}(s_0 + s_1 + s_2) \approx 9.7\,\text{ns}, \tag{7.7}$$

here $s_0$ was the length of measurement cable, $s_1$ was the length of the antenna body and $s_2$ was the lift off from the retaining wall contact surface for $\theta = \theta_7$. This estimate was consistent with the observed location of the leading peak in temporal response amplitude.

In regard to the close proximity air void and metallic structures at the rear of the retaining wall analogue, at depths of 0.52m and 0.63m relative to the contact surface, the expected two-way travel times for expected peaks were,

$$\begin{aligned} t &\approx \frac{2}{c}\,(s_0 + s_1 + s_2 + 0.52) \approx 12.0ns \\ t &\approx \frac{2}{c}\,(s_0 + s_1 + s_2 + 0.63) \approx 12.8ns \end{aligned} \tag{7.8}$$

which further agreed with corresponding peaks preset in the CPM temporal response profile. These observations evidenced successful detection and discrimination of the close proximity targets, for which similar analysis notably ambiguous interpretations for the IFFT and MUSIC responses when considered in isolation.

A subsequent point of consideration was the nature of the six peaks recorded between the contact surface and air void backscatter events. The peak at approximately 12ns of moderate amplitude aligned with the established location of the plastic membrane. Between $t = 10.5$ns and $t = 11.5$ns, two significant peaks occurred, with a third lower amplitude central peak enclosed. This was suggestive of a wide object, for which the leading and rear material interfaces would generate higher intensity backscatter, whilst multiple partial reflections from within the structure would amount to a lower amplitude — but still significant — set of central peaks, notably consistent with the vertical backing breeze blocks.

Finally, between the breeze blocks and contact surface, 4-5 sequential peaks of similar magnitude were observed in the temporal response profile between $t = 9 - 11$ns, which was consistent with the individual layers of brickwork in this region.

In these results, hybrid-rotational GPR with CPM spatial resolution enhancement had demonstrated potential to accurately detect and localise subsurface structural anomalies to a specific layer within historic masonry infrastructure, a noteworthy improvement upon levels of precision achieved in laboratory benchmarking. In practical surveys of in-service infrastructure, this added precision would afford significantly more insight for surveyors and infrastructure managers when devising maintenance strategies.

To address Objective (6), comparative performance of the CPM algorithm was analysed relative to standalone temporal response profiles recovered by IFFT and MUSIC, respectively.

The formal assessment of magnitude precision achieved by CPM was achieved through quantitative comparison with the magnitude precision achieved by MUSIC. The IFFT temporal response as a comparative baseline for each trace in the rotational transect.

Root Mean Square Deviation (RMSD) was calculated using magnitudes extracted from both MUSIC and CPM temporal response profiles to compute respective residuals (see Figure 7.15a). Subsequent recovery of absolute percentage difference between RMSD output for each trace facilitated calculation of a representative mean average measure of magnitude accuracy (see Figure 7.15b). It should be remarked that a higher absolute percentage difference equated to a temporal response more closely aligned with the IFFT profile.

Average observed percentage reduction in RMSD across all 17 compared traces was found to be 52.7%. This indicated that CPM exhibited effectively half the amplitude deviation experienced by MUSIC. An apparent rise-fall trend in alignment variation was also observed across the rotational transect, with magnitude deviation about the horizontal trace 20-30% lower (i.e. higher absolute percentage difference) than at extremal azimuthal displacements.

A potential explanation for this observation was that the boresight vectors of traces with extremal azimuth, when extended, did not predominantly reside within the retaining wall itself. Instead, boresight vectors passed into the ground for $\theta_{i\leq 2}$ and out of the top of the wall back into free space for $\theta_{i\geq 15}$. Notably, both regions contained fewer significant sources of backscatter were present. By Equation 7.4, deviation between $y[t]$ and $z[t]$ was lowest when the return signal exhibited very few significant peaks, corresponding to encounters with the fewest sources of backscatter. Moreover, the approximate 5% greater percentage difference between traces of low and high azimuth would also agree with their respective extension into the ground, rather than back into free space. More low amplitude peaks would be returned by ground-entering signals as this medium exhibited greater inhomogeneity than free space. Despite their low amplitude, such peaks could still cause $z[t]$ to marginally less closely resemble $y[t]$, feasibly resulting in the percentage difference offset observed against the traces with high azimuthal displacement.

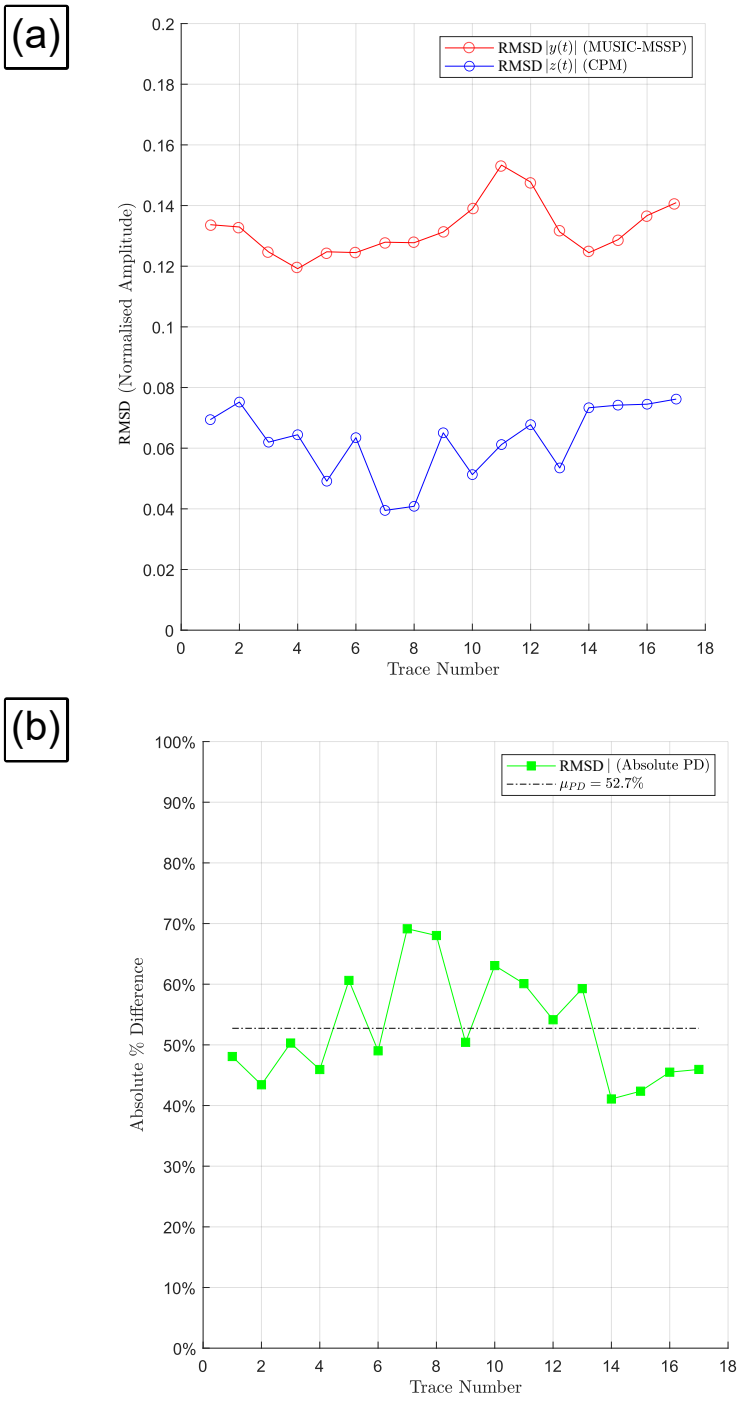


Figure 7.15: Amplitude deviation comparison between MUSIC (with MSSP) and CPM temporal responses. (a) Temporal response RMSD calculated from a predictive baseline provided by IFFT. (b) Absolute percentage difference of RMSD by trace.

Critically, the rise-fall trend did not undermine that the results attained by CPM in this study consistently evidence at least a 40% increase in observed amplitude precision compared to exclusive application the MUSIC algorithm. Refining consideration to non-extremal traces $\theta_{i\in[3,4,...,14]}$ this improvement increased to 55.2%.

Comparison between the levels of achieved spatial resolution by CPM and IFFT required a means of quantifying the sharpness of returned peaks in the temporal response profiles. By definition, data processing which enhanced the spatial resolution of a temporal response profile would result in a new profile containing a higher proportion of sharp peaks. This implied that the median frequency of the profile would also increase.

The median frequency of the temporal response profile returned by IFFT was denoted $\tilde{x}$ and by $\tilde{z}$ for CPM, respectively. Performing FFT and comparing $\tilde{x}$ and $\tilde{z}$ across axes standardised by sampling frequency provided a suitable indirect quantitative measure of signal spatial resolution. Examples of recovered spectra are presented in Figure 7.16.

From analysis of spectra obtained across all 17 responses, it was found $\tilde{z}$ was an average of 152% greater than the $\tilde{x}$ baseline for the equivalent trace.

In all, results across comparative analysis with standalone application of the IFFT and MUSIC algorithms served to evidence the effectiveness of CPM for the practical spatial resolution enhancement of hybrid-rotational GPR data. This provided strong motivation for future research efforts to pursue the full integration of the CPM algorithm into the data extraction phase of the visualisation workflow, thereby enhancing the spatial resolution of constituent 1D traces, with the potential to subsequently enhance the fidelity of returned 3D spatial profiles in the process.

Extension of the CPM algorithm also offers a promising avenue for further development. Here, the effectiveness of the 1D formulation has been evidenced for direct application to individual traces. Generalisation of the CPM mathematical formulation to higher dimensional forms presents an interesting development opportunity from an academic standpoint, and practically, would serve to further increase the application potential of the strategy. For example, a 2D formulation could be implemented transect-by-transect as a pre-processing algorithm. Equally, implementation of a 3D formulation as a post-processing algorithm could (in principal) facilitate direct enhancement of recovered 3D spatial profiles, without the need for modification to constituent trace data input.

Of note, this study was originally planned to extend to the derivation and testing of a 3D extension of CPM. The algorithm would have been integrated into the ETL workflow as a post-processing module, which could be subsequently applied to the 3D spatial profiles recovered in the previous chapters. However, as this conceptually extensive work rapidly began to exceed the scope of the PhD project, it was deferred to future research so that focus could be better maintained and resource allocation optimised.

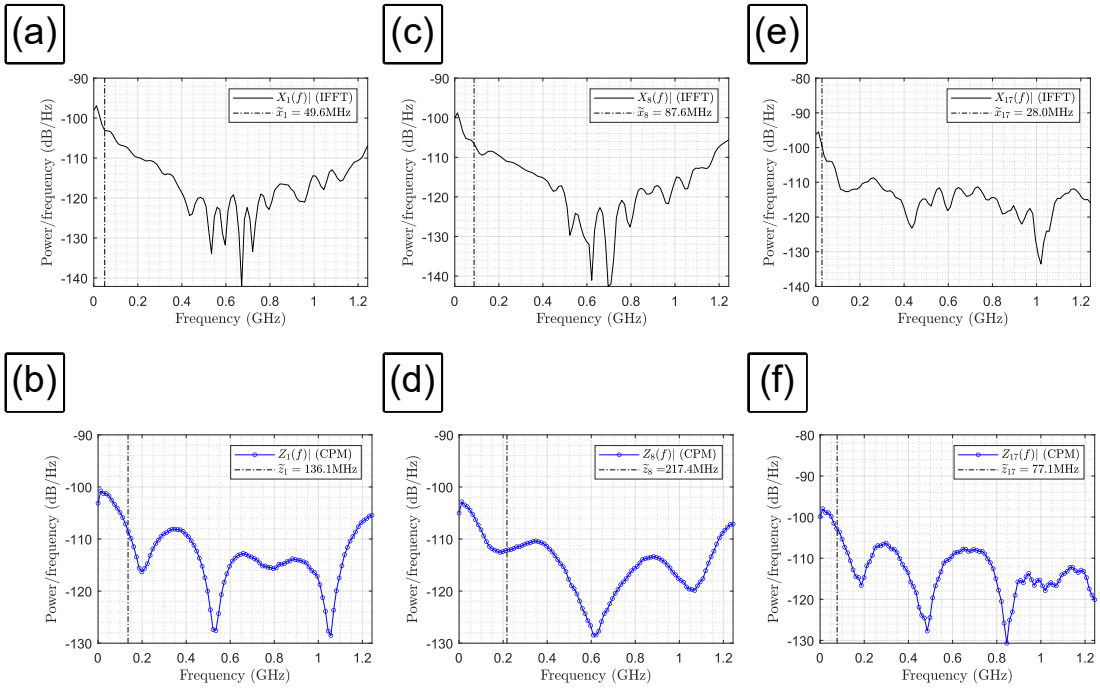


Figure 7.16: Spatial resolution enhancement quantified by consideration of the relative difference between median frequency of the IFFT and CPM temporal response profiles, respectively. Power spectra are presented for rotational traces at azimuthal displacements (a,b) $\theta_0$, (c,d) $\theta_7$ and (e,f) $\theta_{16}$.

On reflection, the decision to focus on applying CPM as a 1D trace pre-processing procedure (instead of a 3D post-processing procedure) enabled a more thorough, experiment-led study, to be completed *in full* and subsequently disseminated.

## 7.5 Summary

In this chapter, two field tests were conducted to assess the effectiveness of the proposed 3D visualisation workflow in more realistic survey environments and explore approaches for potential future innovation. Both tests utilised augmented versions of the hybrid-rotational GPR data collection system for the laboratory presented in the previous chapter.

The first field test analysed the effectiveness of the 3D visualisation workflow from the perspective of a surveyor conducting a practical tunnel survey. Utility pipes served as targets for detection and localisation within a large-scale tunnel subsurface analogue, based on a backfilled railway inspection pit. Findings from the test were consistent with performance achieved during laboratory benchmarking, successfully detecting all known targets across both survey quadrants and localising spatial profiles to within decimetre length scales over reasonable durations, feasibly scalable to full surveys of in-service infrastructure. Of note, observed cluster fragmentation provided valuable insight into a viable mechanism by which ringdown artifacts from hollow structural anomalies could influence the HDBSCAN clustering algorithm, therein motivating integration of an explicit proximal threshold for ringdown discrimination in a future refinement of the workflow.

The second field test narrowed focus to older masonry railway structures, in close alignment with the original feasibility study. The effectiveness of the CPM algorithm for was analysed for the spatial resolution enhancement of hybrid-rotational GPR data. A rigorous, formalised mathematical framework was devised for the full, practical numerical implementation of the CPM algorithm. This served to address a significant knowledge gap in the field, principally resulting from ambiguity surrounding the practical numerical implementation of the MUSIC algorithm, and by extension, the CPM algorithm itself.

In practical application to a rotational transect of the retaining wall analogue, traces recovered using CPM exhibited highly effective performance. Results demonstrated an average 52% reduction in amplitude deviation from those recovered by the MUSIC algorithm, whilst spatial resolution was observed to have significantly increased by an average of over 150% on the baseline set by the IFFT algorithm. These findings collectively motivated direct integration of the CPM algorithm into future refinements of the proposed 3D visualisation workflow for hybrid-rotational GPR, and generalisation of its mathematical formulation to facilitate application to higher dimensional datasets — principally, those based on rotational and helical transects.

# Chapter 8. Conclusions and Future Work

This chapter summarises the key work and findings presented in this thesis. Section 8.1 provides concluding remarks, highlighting the most significant and quantifiable findings. Section 8.2 reflects on the alignment between the initial research objectives and the work conducted. Finally, Section 8.3 outlines recommendations for future research.

## 8.1 Concluding Remarks

The novel work presented in this thesis has significantly advanced the capabilities of emerging hybrid-rotational ground penetrating radar (GPR) technology. Critically, this work has developed the first effective framework for end-to-end 3D visualisation of concealed structural anomalies in its datasets. Key innovations include both the design of compact measurement apparatus for pioneering lab-based testing and development of a bespoke data processing workflow based on a 3-phase extract-transform-load architecture. Amongst open source GPR processing solutions, this workflow is also uniquely capable of visualising datasets generated by numerical simulations (gprMax) and fixed-directional commercial GPR hardware. Further achievements include the successful recovery of distinct GPR hallmarks for blind shafts in a historic working UK railway tunnel, utilising data captured using a pioneering large-scale hybrid-rotational GPR prototype.

In benchmarking the developed workflow, novel area scan functionality (exploiting shell scripting) was developed and applied to numerical simulations of fixed-directional GPR using 100mm, 60mm and 30mm metallic spheres as concealed targets. Robust accuracy was demonstrated, with the workflow successfully detecting all decimetre-scale targets within 30mm, and returning 3D spatial profiles localising target mid-centres to within an impressive 4.2% tolerance of the established ground-truth geometry. Notable runtime efficiency was also observed, with full end-to-end processing completed in just 5 seconds across 20 independent runs, with a low interquartile range (IQR) of 0.53 seconds.

Applying the workflow to practical datasets from the laboratory using a fixed-directional GPR system and novel miniaturised hybrid-rotational GPR apparatus, further evidenced its high levels of lateral and vertical target localisation accuracy. Observed alignment to within a 3.4% tolerance of ground truth geometry was observed in returned 3D spatial profiles. Refinement of segmentation parameters explored the influence of minimum cluster size, $N_{\Omega}$, and the granularity tuning parameter, $a$, on the quality of recovered 3D spatial profiles.

Resulting recurrent observation of domain saturation for $N_\Omega \leq 100$ and $a \ll 0.55$ in turn informed an optimised parameter configuration for $N_\Omega = 175$ and $a = 1$, providing a basis for segmentation configuration for subsequent investigations. In conjunction, runtime efficiency was further improved by the addition of checkpoint during data extraction, yielding a significant 12% average reduction in overall processing runtime and sizable 60% reduction in observed IQR variation.

Progression to field testing saw the 3D visualisation workflow maintain high levels of subsurface anomaly detection and localisation. All hollow targets within a large tunnel subsurface analogue were successfully identified, with returned 3D profiles exhibiting mid-centre agreement with to within a 3% tolerance ground-truth geometry, consistent with laboratory benchmarking results. Moreover, a viable mechanism for an observed instance of cluster fragmentation was also proposed, drawing links to the potential influence of hollow-target ringdown phenomena at depths between 0.69m and 1m in the first quadrant.

Further workflow refinements were also explored. Combined Processing Methodology (CPM) was applied for the first time to hybrid-rotational GPR traces, recorded through practical scanning of a masonry retaining wall analogue. The use of CPM significantly improved the sharpness of returned traces across the full 60° azimuthal range examined, increasing the median frequency component of the recovered temporal response profiles by 152% compared to IFFT. It also considerably reduced root mean square amplitude deviation by almost 50% relative to profiles recovered using MUSIC — both compared against the same IFFT baseline. This work also disseminated comprehensive documentation detailing practical numerical implementation of CPM which was notably lacking from encountered literature.

In all, work conducted throughout this thesis has significantly enhanced the accessibility of both CPM processing and the 3D visualisation of hybrid-rotational GPR datasets for future researchers. Looking to the future, a logical next step in this field would be the optimisation of new helical transects for 3D data acquisition, which could further improve the 3D subsurface visualisation capability of this technology and expand its applicability across a broader range of transport infrastructure and research disciplines.

## 8.2 Reflection on Research Objectives

In all, the work conducted has served to address each research objective outlined in Chapter 2.

In line with Objective (1), a pool of GPR datasets were generated through the feasibility study, laboratory benchmarking, and field tests, utilising multiple hybrid-rotational GPR systems. Area scan simulations recovered using gprMax and fixed-directional commercial GPR systems further expanded the pool, in turn supporting workflow testing and refinement.

The conception, design, and iterative refinement of the proposed data processing workflow provided valuable insights into both conventional and advanced GPR processing algorithms, alongside 3D dataset visualisation techniques, addressing Objectives (2)-(4). Finally, performance analysis of the workflow and its associated elements (e.g. data collection hardware, CPM enhancement, etc.) across all investigatory work conducted has rigorously compared returned outputs against established ground truth geometry, fulfilling Objective (5).

## 8.3 Recommendations for Future Work

Work conducted has highlighted multiple routes for potential high impact future research and development. This extends to refinement of the 3D visualisation workflow itself and extending the functionality of hybrid-rotational GPR data collection systems. Moreover, opportunity for further scientific investigations has been identified, alongside scope for application beyond rail infrastructure.

Branches of innovation identified have been subdivided into short-term and long term. Short term research avenues present timely opportunities, either currently under development or, in principal, directly implementable based on the current state of developments in GPR research at the time of writing. Key opportunities identified include:

- Knowledge transfer from 3D visualisation of hybrid-rotational GPR data for critical rail infrastructure structural inspection to increase the resilience of critical infrastructure in other transport modalities. For example, work presented in this thesis already underpins the development of a novel automated subsurface inspection radar system for structural anomaly detection and localisation within lock chamber walls as part of the Horizon Europe project 'Climate Resilient and Environmentally Sustainable Transport Infrastructure, with a Focus on Inland Waterways' (CRISTAL) [339].

- The development of a robust numerical simulation for hybrid-rotational GPR would significantly increase the efficiency of future experimentation, more readily facilitating adjustment of ground truth geometry between test scenarios. It would also enable generation of the sizable volumes of training data necessary to train machine learning tools in subsequent research projects. A primary route to achieve this would be the augmentation of gprMax to rotate and translate environmental geometry about a stationary antenna model to emulate fixed-directional, rotational, and helical transect acquisition respectively.

- The direct integration of Reverse Time Migration [286], edge-preserving Bilateral Filtering [340] and 1D CPM to future refinements of the 3D visualisation workflow would serve to increase the fidelity of returned spatial profiles. Moreover, further scope for innovation would include the generalisation of the CPM algorithm for direct application to higher dimensional 2D and 3D GPR datasets, alongside continued research into the reliable automation of noise subsurface partitioning.

- Investigation into the optimisation and integration of an effective 3D spatial interpolation technique, such as Radial Basis Functions [341], Hemisphere Harmonics [342] or Kriging [343] would serve to improve amplitude estimation relative to current 3D grid regularisation in sparser hybrid-rotational GPR datasets, particularly at greater penetration depths in the vicinity of diverging trace extremals.

- Improvements to processing efficiency extend to workflow reimplementation in a compiled language (e.g. C++); parallelisation of workflow processes (e.g. 3D spatial alignment and temporal amplitude recovery), and the development and integration of a suitably lightweight 'culling' algorithm to filter out lower-priority healthy quadrants in larger infrastructure surveys.

- The incorporation of a proximal threshold parameter between candidate clusters generated via HDBSCAN, in addition to the existing granularity tuning parameter, could be used to explicitly define the minimal separation between neighbouring clusters. This would increase control over cluster fragmentation and the fidelity of recovered 3D spatial profiles.

- The application of machine learning also presents multiple avenues for development, including but not limited to: (i) increasing achievable levels of anomaly detection and localisation accuracy [344]; (ii) cluster characterisation through the addition of labels (e.g. asset/defect discrimination, material type) [39, 345] and structural health metrics (e.g. Tunnel Condition Monitoring Index) [86, 279]; (iii) automated ranking of quadrant maintenance priority and (iv) the automated consolidation of quadrant survey results into formal summary reports, using development platforms such as Microsoft Power BI [346], IBM Congos Analytics [347], or Google LookerStudio [348].

Avenues for longer-term research are associated with innovation that is dependent on work identified above. Scope extends to other sensing technologies or pertains to evolution of the visualisation framework into a practically deployable tool for real surveys within the transport sector or beyond. Several key routes identified include:

- Investigation into the optimisation of scan parameters for helical transect acquisition would serve to increase the practical functionality of current hybrid-rotational GPR systems. This would provide more efficient, uninterrupted system motion, whilst maintaining effective data capture with sufficient sample point density for accurate 3D visualisations to be recovered. A natural route based on this work's practical datasets would be judicious extraction of rotational transects to facilitate controllable artificial reduction of sample point density. Equally, analysis of full 360-degree helical trajectories and increased variation in trailable lateral and azimuthal movement speeds, afforded post-development of a hybrid-rotational GPR simulation tool, may offer a more robust and versatile foundation for such an investigation.

- Hybridisation between hybrid-rotational GPR and datasets from state-of-the-art Terrestrial Laser Scanning (TLS) technology [349] or Close Range Photogrammetry (CRP) [278] would have potential to consolidate records surface and subsurface condition across full-scale transport infrastructure. This would yield more comprehensive survey records, which could significantly increase levels of insight available to infrastructure managers and provide a backbone for the generation of immersive virtual survey environments using Extended Reality technology as in [263] and serve as key feeder data for digital twins of the infrastructure [239, 350].

- Fusion of the proposed workflow with the functionality of gprMax and GPRPy would have potential to realise a seamless, fully open access software application for the GPR research community. This would combine state-of-the-art numerical simulation, 2D and 3D visualisation of both virtual and practical GPR datasets, an important step towards creating an accessible development platform for practical surveying and for researchers to test new analysis techniques.

- The development of a fully integrated transport infrastructure subsurface inspection tool, based on a refined iteration of the work presented in this thesis, presents a significant development opportunity to better aid survey practitioners and infrastructure managers in the current transport sector. From a physical systems standpoint, one area to consider would be the automation of lateral positioning, similar to the automated rail trolleys presented in [115,351]. Equally, the design of a more adaptable system that could also be mounted to an unmanned ground vehicle (e.g. Huskey [352]) or portable linear rail configuration, thereby extending usability beyond the rail modality, similar to [353]. From a cyber-physical perspective, development of a multi-platform application (akin to [139] and [354]) would synthesise physical data collection system and virtual data processing workflow, centralising control of scan parameter settings, measurement and movement of the data collection system, data storage, local or cloud-based data processing and synchronisation of survey results with digital twins of the infrastructure.

# Bibliography


[1] P. Bevelacqua. (2024) Antenna types. Organisation Website. Antenna Theory. Accessed 04 March 2025. [Online]. Available: https://www.antenna-theory.com/antennas/main.php

[2] Sensors & Software. (2025) Understanding GPR resolution and target detection. Organisation Website. Sensors & Software. Accessed 04 March 2025. [Online]. Available: https://www.sensoft.ca/blog/understanding-gpr-resolution-and-target-detection/

[3] C. Warren, "Numerical modelling of high-frequency ground-penetrating radar antennas," phdthesis, The University of Edinburgh, 2009, accessed 27 April 2025. [Online]. Available: http://hdl.handle.net/1842/4074

[4] G. Developers. (2017) Geophysics for practicing geoscientists. Organisation Website. GPG. Accessed 30 August 2021. [Online]. Available: https://gpg.geosci.xyz/index.html

[5] D. Daniels, *Ground penetrating radar*, 2nd ed., ser. IET Radar, Sonar, Navigation and Avionics Series, D. Daniels, Ed. Institution of Engineering and Technology, 2004, vol. 15. [Online]. Available: https://books.google.co.uk/books?hl=en&lr=&id=16PV-fhKasoC&oi=fnd&pg=PR15&dq=Daniels,+D.+J.+(2004).+Ground+Penetrating+Radar+(2nd+ed.).+IET.&ots=u09HYkS8qe&sig=6933QdvGNfzaOsHHV55eqtEbazM&redir_esc=y#v=onepage&q=Daniels,D.J.(2004).GroundPenetratingRadar(2nded.).IET.&f=false

[6] ScanTech Geoscience. (2025, Mar.) About GPR. Organisation Website. ScanTech Geoscience. Accessed 03 March 2025. [Online]. Available: https://scantech.ie/scantech-about-gpr.html

[7] Proceq, *Proceq GPR ground penetrating radar user manual*, Screaning Eagle Technologies, Jun. 2024, accessed 23 July 2024. [Online]. Available: https://media.screeningeagle.com/asset/Downloads/Proceq%20GPR%20GP8000_GP8100_GP8800%20User%20Manual%20v1.0%201.pdf

[8] H. Sun, Z. Xu, L. Yao, R. Zhong, L. Du, and H. Wu, "Tunnel monitoring and measuring system using mobile laser scanning: Design and deployment," *Remote Sensing*, vol. 12, p. 730, 2020. [Online]. Available: https://doi.org/10.3390/rs12040730

[9] R. Olmi, L. Palombi, S. Durazzani, D. Poggi, N. Renzoni, F. Costantino, S. Durazzani, G. Frilli, and V. Raimondi, "Integrating thermographic images in a user-friendly platform to support inspection of railway bridges," *Proceedings*, vol. 27, no. 1, 2019. [Online]. Available: https://www.mdpi.com/2504-3900/27/1/12

[10] L. Iampoli, A. Calvi, and F. D'Amico, "Railway ballast monitoring by GPR: A test-site investigation," *Remote Sensing*, vol. 11, no. 20, p. 2381, 2019. [Online]. Available: https://doi.org/10.3390/rs11202381

[11] N. Šarlah, T. Podobnikar, T. Ambrožič, and B. Mušič, "Application of kinematic GPR-TPS model with high 3D georeference accuracy for underground utility infrastructure mapping: A case study from urban sites in Celje, Slovenia," *Remote Sensing*, vol. 12, no. 8, p. 1228, 2020. [Online]. Available: https://doi.org/10.3390/rs12081228

[12] S. Zhang, L. Zhang, W. He, T. Ling, Z. Deng, and G. Fu, "Three-dimensional quantitative recognition of filler materials ahead of a tunnel face via time-energy density analysis of wavelet transforms," *Minerals*, vol. 12, no. 2, p. 234, 2022. [Online]. Available: https://doi.org/10.3390/min12020234

[13] M. Coli, A. L. Ciuffreda, E. Marchetti, D. Morandi, G. Luceretti, and Z. Lippi, "3D HBIM model and full contactless GPR tomography: An experimental application on the historic walls that support Giotto's mural paintings, Santa Croce Basilica, Florence, Italy," *Heritage*, vol. 5, pp. 2534–2546, 2022. [Online]. Available: https://doi.org/10.3390/heritage5030132

[14] F. Hou, X. Liu, X. Fan, and Y. Guo, "DL-aided underground cavity morphology recognition based on 3D GPR data," *Mathematics*, vol. 10, no. 15, p. 2806, 2022. [Online]. Available: https://doi.org/10.3390/math10152806

[15] T. Iwamoto, T. Enaka, and K. Tada, "Development of testing machine for tunnel inspection using multi-rotor UAV," *Journal of Physics: Conference Series*, vol. 842, no. 1, p. 012068, 2017. [Online]. Available: https://dx.doi.org/10.1088/1742-6596/842/1/012068

[16] A. Mosaddek, H. K. R. Kommula, and F. Gonzalez, "Design and testing of a recycled 3D printed and foldable unmanned aerial vehicle for remote sensing," in *2018 International Conference on Unmanned Aircraft Systems (ICUAS)*, 2018, pp. 1207–1216.

[17] Y.-J. Cheng, W.-G. Qiu, and D.-Y. Duan, "Automatic creation of as-is building information model from single-track railway tunnel point clouds," *Automation in Construction*, vol. 106, p. 102911, 2019. [Online]. Available: https://www.sciencedirect.com/science/article/pii/S0926580519300585

[18] M. Soilán, A. Sánchez-Rodríguez, P. Del Río-Barral, C. Pérez-Collazo, P. Arias, and B. Riveiro, "Review of laser scanning technologies and their applications for road and railway infrastructure monitoring," *Infrastructures*, vol. 4, p. 58, 2019. [Online]. Available: https://doi.org/10.3390/infrastructures4040058

[19] H. Xiong, G. Su, C. Zhang, B. Li, and W. Wentao, "A train-mounted gpr system for operating railway tunnel inspection," in *Proceedings of the 7th International Symposium on Innovation Sustainability of Modern Railway*, 2020. [Online]. Available: https://ebooks.iospress.nl/volume/ismr-2020-proceedings-of-the-7th-international-symposium-on-innovation-amp-sustainability-of-modern-railway

[20] L. Wei, D. R. Magee, and A. G. Cohn, "An anomalous event detection and tracking method for a tunnel look-ahead ground prediction system," *Automation in Construction*, vol. 91, pp. 216–225, 2018. [Online]. Available: https://www.sciencedirect.com/science/article/pii/S0926580517307537

[21] T. McDonald, M. Robinson, and G. Tian, "Spatial resolution enhancement of rotational-radar subsurface datasets using combined processing method," *Journal of Physics: Conference Series*, vol. 2090, no. 1, p. 012001, nov 2021. [Online]. Available: https://dx.doi.org/10.1088/1742-6596/2090/1/012001

[22] ——, "T-Vision: A hybrid subsurface radar inspection system for intelligent asset management of railway tunnels," *Transportation Research Procedia*, vol. 72, pp. 3466–3473, 2023, tRA Lisbon 2022 Conference Proceedings Transport Research Arena (TRA Lisbon 2022),14th-17th November 2022, Lisboa, Portugal. [Online]. Available: https://www.sciencedirect.com/science/article/pii/S2352146523010669

[23] AMEY, "Structures detailed examination report," Network Rail, Tech. Rep., 2020, accessed 12 October 2021.

[24] T. McDonald, M. Robinson, and G. Tian, "Developments in 3D visualisation of the rail tunnel subsurface for inspection and monitoring," *Applied Sciences*, vol. 12, no. 22, p. 11310, 2022.

[25] R. Montero, J. Victores, S. Martinez, A. Jardón, and C. Balaguer, "Past, present and future of robotic tunnel inspection," *Autom. Constr.*, vol. 59, pp. 99–112, 2015. [Online]. Available: https://doi.org/10.1016/j.autcon.2015.02.003

[26] B. Farahani, F. Barros, P. Sousa, P. Cacciari, P. Tavares, M. Futai, and P. Moreira, "A coupled 3D laser scanning and digital image correlation system for geometry acquisition and deformation monitoring of a railway tunnel," *Tunn. Undergr. Space Technol.*, vol. 91, p. 102995, 2019. [Online]. Available: https://doi.org/10.1016/j.tust.2019.102995

[27] N. University. (2024) Search techniques. Organisation Website. Newcastle University. Accessed 16 March 2021. [Online]. Available: https://www.ncl.ac.uk/academic-skills-kit/information-and-digital-skills/finding-information/search-techniques/

[28] Proceq. (2025, Apr.) What is the frequency of GPR? Organisation Website. Screaning Eagle. Accessed 27 April 2025. [Online]. Available: https://www.screeningeagle.com/en/academy/faq/what-is-the-frequency-of-gpr

[29] M. Frid and V. Frid, "A case study of the integration of ground-based and drone-based ground-penetrating radar (gpr) for an archaeological survey in Hulata (Israel): Advancements, challenges, and applications," *Applied Sciences*, vol. 14, no. 10, p. 4280, May 2024.

[30] SPH Engineering. (2025, Apr.) Detailed subsurface data with universal GPR systems. Organisation Website. SPH Engineering. Accessed 27 April 2025. [Online]. Available: https://www.sphengineering.com/integrated-systems/technologies/gpr

[31] D. Goodman, "Ground-penetrating radar simulation in engineering and archaeology," *Geophysics*, vol. 59, no. 2, pp. 176–315, Feb. 1994.

[32] M. Garcia-Fernandez, G. Alvarez-Narciandi, Y. A. Lopez, and F. Las-Heras, "Array-based ground penetrating synthetic aperture radar on board an unmanned aerial vehicle for enhanced buried threats detection," *IEEE Transactions on Geoscience and Remote Sensing*, vol. 61, pp. 1–18, May 2023.

[33] MALA Guideline Geo. (2024) MALA Guideline Geo. Organisation Website. MALA Guideline Geo. Accessed 18 August 2024. [Online]. Available: https://www.guidelinegeo.com/mala-ground-penetrating-radar-gpr/

[34] GSSI Geophysical Survey Systems Inc. (2024) GSSI Geophysical Survey Systems Inc. Organisation Website. GSSI Geophysical Survey Systems Inc. Accessed 18 August 2024. [Online]. Available: https://www.geophysical.com/

[35] Sensors and Software. (2024) Sensors and Software from RADIODETECTION. Organisation Website. Sensors and Software. Accessed 18 August 2024. [Online]. Available: https://www.sensoft.ca/

[36] Hexagon Leica Geosystems. (2024) Hexagon Leica Geosystems. Organisation Website. Hexagon Leica Geosystems. Accessed 18 August 2024. [Online]. Available: https://leica-geosystems.com/en-gb/

[37] RadarSystemsInc. (2024) Radar Systems Inc. Organisation Website. RadarSystemsInc. Accessed 18 August 2024. [Online]. Available: https://www.radsys.lv/en/index/

[38] Hexagon Leica Geosystems, *C-thrue all-in-one ground penetrating radar (GPR) for non-destructive testing of concrete surfaces user manual*, Hexagon Leica Geosystems, 2017, accessed 18 August 2024. [Online]. Available: https://shop.leica-geosystems.com/sites/default/files/2021-07/C-ThrueUserManual_0.pdf?srsltid=AfmBOormRJY8N4MKIy5xrrHhSXCI9x2Izo5R7nBoGjzm1-sgwpyP5ylN

[39] N. Kim, S. Kim, Y.-K. An, and J.-J. Lee, "A novel 3D GPR image arrangement for deep learning-based underground object classification," *International Journal of Pavement Engineering*, vol. 22, no. 6, pp. 740–751, May 2021. [Online]. Available: https://doi.org/10.1080/10298436.2019.1645846

[40] Sensors and Software. (2015) Concrete scanning with GPR guidebook. Online Document. Sensors and Software. Accessed 16 March 2021. [Online]. Available: https://www.sensoft.ca/wp-content/uploads/2015/11/Concrete-Scanning-with-GPR-book.pdf

[41] Proceq. (2022) Demo Proceq GP8000 grid scan. Organisation Website. Screaning Eagle Technologies. Accessed 16 March 2021. [Online]. Available: https://www.youtube.com/watch?v=vYDIfYZejzQ

[42] G. S. Baker, T. E. Jordan, and J. Pardy, "An introduction to ground penetrating radar (GPR)," in *Stratigraphic Analyses Using GPR*. Geological Society of America, 01 2007. [Online]. Available: https://doi.org/10.1130/2007.2432(01)

[43] R. B. Marks, "A multiline method of network analyzer calibration," *IEEE Transactions on Microwave Theory and Techniques*, vol. 39, no. 7, pp. 1205–1215, 1991.

[44] Rohde and Schwarz UK Ltd. (2024) Getting started with vector network analyzers (VNAs). Online Document. Rohde and Schwarz UK Ltd. Accessed 08 May 2024. [Online]. Available: https://www.rohde-schwarz.com/uk/products/test-and-measurement/analyzers/network-analyzers/fundamentals-of-vector-network-analysis_253352.html?form=INRED_PremiumDownload_cca89713-c9e5-4794-b7ec-038cd9ff111a

[45] Commission of the European Communities. (2006, Dec.) Communication from the commissionon a european programme for critical infrastructure protection. Online Document. European Commission. Accessed 03 May 2024. [Online]. Available: https://eur-lex.europa.eu/LexUriServ/LexUriServ.do?uri=COM:2006:0786:FIN:EN:PDF

[46] E. J. Palin, I. Stipanovic Oslakovic, K. Gavin, and A. Quinn, "Implications of climate change for railway infrastructure," *Wiley Interdisciplinary Reviews: Climate Change*, vol. 12, no. 5, 2021.

[47] T. Wang, Z. Qu, Z. Yang, T. Nichol, G. Clarke, and Y.-E. Ge, "Climate change research on transportation systems: Climate risks, adaptation and planning," *Transportation Research Part D: Transport and Environment*, vol. 88, p. 102553, 2020. [Online]. Available: https://www.sciencedirect.com/science/article/pii/S1361920920307409

[48] D. Beil and L.-M. Putz, "Modal shift measures to increase the use of eco-friendly transport modes: a literature review," *Transportation Research Procedia*, vol. 72, pp.

4279–4286, 2023. [Online]. Available: https://www.sciencedirect.com/science/article/pii/S2352146523006403

[49] S. A. Mitoulis, M. Domaneschi, J. R. Casas, G. P. Cimellaro, N. Catbas, B. Stojadinovic, and D. M. Frangopol, "Editorial: The crux of bridge and transport network resilience - advancements and future-proof solutions," *Proceedings of the Institution of Civil Engineers - Bridge Engineering*, vol. 175, no. 3, pp. 133–137, Aug. 2022. [Online]. Available: https://doi.org/10.1680/jbren.2022.175.3.133

[50] Eurpoean Sources Online. (2024, Jan.) Commission recommendation (EU) 2024/236 on means to address the impact of automation and digitalisation on the transport workforce. Online Document. European Commission. Accessed 16 August 2024. [Online]. Available: https://eur-lex.europa.eu/eli/reco/2024/236/oj

[51] F. Liu, T. Ma, C. Tang, X. Liu, and F. Chen, "A case study of collapses at the Yangshan tunnel of the coal transportation channel from the Western Inner Mongolia to the central China," *Tunnelling and Underground Space Technology*, vol. 92, p. 103063, 2019. [Online]. Available: https://www.sciencedirect.com/science/article/pii/S0886779818305133

[52] RTL Today. (2022, Sep.) No trains to operate between Kautenbach and Wilwerwiltz until end of the year. Organisation Website. RTL Today. Accessed 16 August 2024. [Online]. Available: https://today.rtl.lu/news/luxembourg/a/1961104.html

[53] J. Perry. (2024, Jun.) Tunnels and cuttings. Organisation Website. Forgotten Relics of an Enterprising Age. Accessed 18 March 2021. [Online]. Available: http://www.forgottenrelics.org/tunnels/

[54] Cannal and River Trust. (2020, Nov.) Tunnels. Organisation Website. Cannal and River Trust. Accessed 18 March 2021. [Online]. Available: https://canalrivertrust.org.uk/things-to-do/canal-history/canal-heritage-and-architecture/tunnels

[55] D. M. Z. Islam, R. Jackson, T. H. Zunder, and A. Burgess, "Assessing the impact of the 2011 EU transport white paper - a rail freight demand forecast up to 2050 for the EU27," *European Transport Research Review*, vol. 7, no. 3, p. 22, 2015. [Online]. Available: https://doi.org/10.1007/s12544-015-0171-7

[56] J. Perry. (2024, Jun.) Tunnel construction. Organisation Website. Forgotten Relics of an Enterprising Age. Accessed 16 August 2024. [Online]. Available: http://www.forgottenrelics.org/tunnels/construction/

[57] C. Atkinson, C. Paraskevopoulou, and R. Miller, "Investigating the rehabilitation methods of Victorian masonry tunnels in the UK," *Tunnelling and Underground Space Technology*,

vol. 108, p. 103696, 2021. [Online]. Available: https://www.sciencedirect.com/science/article/pii/S0886779820306507

[58] Network Rail. (2018) Asset management policy January 2018. Online Document. Network Rail. Accessed 25 July 2021. [Online]. Available: https://www.networkrail.co.uk/wp-content/uploads/2019/10/Asset-Management-Policy-2018.pdf

[59] H. J. Pragnell, "Early british railway tunnels: The implications for planners, landowners and passengers between 1830 and 1870," PhD thesis, University of York, 2016. [Online]. Available: https://etheses.whiterose.ac.uk/16826/

[60] P. Taylor, "Search for hidden construction shafts within the welsh railway tunnels," in *Proceedings of the XVII ECSMGE-2019 Geotechnical Engineering Foundation of the Future*, Reykjavik, Iceland, 2019, pp. 1–6. [Online]. Available: https://www.ecsmge-2019.com/uploads/2/1/7/9/21790806/0215-ecsmge-2019_taylor.pdf

[61] R. Khan, M. Emad, and B. Jo, "Tunnel portal construction using sequential excavation method: A case study," in *Proceedings of the MATEC Web of Conferences*, vol. 138. EDP Sciences, 2017, p. 04002. [Online]. Available: https://doi.org/10.1051/matecconf/201713804002

[62] J. Spinks, "Strengthening of heritage tunnel portals," in *Proceedings of the 12th Australia New Zealand Conference on Geomechanics*, G. Ramsey, Ed. Wellington, New Zealand: SIMSG ISSMGE, 2015, accessed 25 July 2021. [Online]. Available: https://www.issmge.org/publications/publication/strengthening-of-heritage-tunnel-portals

[63] N. Fletcher, M. Brown, and T. Sadek, "Great Western Railway electrification, UK: Patchway tunnels," *Proceedings of the Institution of Civil Engineers - Civil Engineering*, vol. 173, no. 6, pp. 37–45, Jun. 2020. [Online]. Available: https://doi.org/10.1680/jcien.20.00021

[64] P. Zhang, Z. Huang, S. Liu, and T. Xu, "Study on the control of underground rivers by reverse faults in tunnel site and selection of tunnel elevation," *Water*, vol. 11, no. 5, p. 889, 2019. [Online]. Available: https://doi.org/10.3390/w11050889

[65] POLYPIPE. (2014) Rail construction solutions. Online Document. POLYPIPE. Accessed 28 July 2021. [Online]. Available: https://www.polypipe.com/sites/default/files/Rail_Construction_Solutions_Dec2014.pdf

[66] H. Hui, Z. Bowen, Z. Yanyan, Z. Chunmei, W. Yize, and G. Zeng, "The mechanism and numerical simulation analysis of water bursting in filling karst tunnel," *Geotechnical and Geological Engineering*, vol. 36, no. 2, pp. 1197–1205, 2018. [Online]. Available: https://doi.org/10.1007/s10706-017-0386-6

[67] Y. Zhou, X. Zhang, L. Wei, S. Liu, B. Zhang, and C. Zhou, "Experimental study on prevention of calcium carbonate crystallizing in drainage pipe of tunnel engineering," *Advances in Civil Engineering*, vol. 2018, pp. 1–11, 2018, accessed on 25 July 2021. [Online]. Available: https://www.hindawi.com/journals/ace/2018/9430517/

[68] C. Atkinson, C. Paraskevopoulou, and R. Miller, "Investigating the rehabilitation methods of Victorian masonry tunnels in the UK," *Tunnelling and Underground Space Technology*, vol. 108, p. 103696, 2021.

[69] J. Parrott and J. Lahra. (2014) Masonry arch bridges and tunnels repair and strengthening: a case study. Online Document. Goldhawk. Accessed 12 November 2021. [Online]. Available: https://bridgerestoration.co.uk/wp-content/uploads/2019/10/Underpass-strengthening.pdf

[70] H.-M. Chen, H.-S. Yu, and M. J. Smith, "Physical model tests and numerical simulation for assessing the stability of brick-lined tunnels," *Tunnelling and Underground Space Technology*, vol. 53, pp. 109–119, 2016. [Online]. Available: https://www.sciencedirect.com/science/article/pii/S0886779816300232

[71] P. Anbazhagan, P. Dixit, and T. Bharatha, "Identification of type and degree of railway ballast fouling using ground coupled GPR antennas," *Journal of Applied Geophysics*, vol. 126, pp. 183–190, 2016.

[72] S. Cafiso, B. Capace, C. D'Agostino, E. Delfino, and A. Di Graziano, "Application of NDT to railway track inspections," in *Proceedings of the 3rd International Conference on Traffic and Transport Engineering (ICTTE)*, Lucerne, Switzerland, 2016. [Online]. Available: https://www.researchgate.net/publication/309385327_Application_of_NDT_to_railway_track_inspections

[73] L. Gao, W. Zhao, B. Hou, and Y. Zhong, "Analysis of influencing mechanism of subgrade frost heave on vehicle-track dynamic system," *Applied Sciences*, vol. 10, no. 22, p. 8097, 2020.

[74] S. Akagawa, M. Hori, and J. Sugawara, "Frost heaving in ballast railway tracks," *Procedia Engineering*, vol. 189, pp. 547–553, 2017. [Online]. Available: https://www.sciencedirect.com/science/article/pii/S1877705817322129

[75] Y. Luo and J. Chen, "Research status and progress of tunnel frost damage," *Journal of Traffic and Transportation Engineering (English Edition)*, vol. 6, no. 3, pp. 297–309, 2019. [Online]. Available: https://www.sciencedirect.com/science/article/pii/S2095756417302556

[76] BBC. (2020) Flood-prone Crick Railway Tunnel repairs will reduce delays. Organisation Website. BBC. Accessed 22 November 2021. [Online]. Available: https://www.bbc.co.uk/news/ukengland-northamptonshire-56354714

[77] Rail Accident Investigation Branch, "Partial failure of a structure inside Balcombe Tunnel, West Sussex," Department for Transport, techreport 13-2013, Sep. 2023, accessed 22 November 2021. [Online]. Available: https://www.gov.uk/raib-reports/partial-failure-of-a-structure-inside-balcombe-tunnel-west-sussex

[78] A. Bahadori-Jahromi, A. Rotimi, and A. Roxan, "Sustainable conditional tunnel inspection: London Underground, UK," *Infrastruct. Asset Manag.*, vol. 5, pp. 22–31, 2018. [Online]. Available: https://doi.org/10.1680/jinam.17.00011

[79] S. Liu, Q. Wang, and Y. Luo, "A review of applications of visual inspection technology based on image processing in the railway industry," *Transp. Saf. Environ.*, vol. 1, pp. 185–204, 2019. [Online]. Available: https://doi.org/10.1093/tse/tdz007

[80] S. Stent, C. Girerd, P. Long, and R. Cipolla, "A low-cost robotic system for the efficient visual inspection of tunnels," in *International Symposium on Automation and Robotics in Construction*, vol. 32. Oulu, Finland: IAARC Publications, 2015, accessed 13 July 2021. [Online]. Available: http://mi.eng.cam.ac.uk/~cipolla/archive/Publications/inproceedings/2015-ISARC-tunnel-inspection.pdf

[81] L. Attard, C. J. Debono, G. Valentino, and M. D. Castro, "Image mosaicing of tunnel wall images using high level features," in *Proceedings of the 10th International Symposium on Image and Signal Processing and Analysis*, 2017, pp. 141–146.

[82] D. Tannant, "Review of photogrammetry-based techniques for characterization and hazard assessment of rock faces," *Int. J. Georesour. Environ. IJGE*, vol. 1, pp. 76–87, 2015. [Online]. Available: https://doi.org/10.15273/ijge.2015.02.009

[83] C. Krisada, K. Tae-Kyun, V. Fabio, C. Roberto, and S. Kenichi, "Distortion-free image mosaicing for tunnel inspection based on robust cylindrical surface estimation through structure from motion," *J. Comput. Civ. Eng.*, vol. 30, p. 04015045, 2016. [Online]. Available: https://doi.org/10.1061/(ASCE)CP.1943-5487.0000516

[84] M. D. Jenkins, T. Buggy, and G. Morison, "An imaging system for visual inspection and structural condition monitoring of railway tunnels," in *2017 IEEE Workshop on Environmental, Energy, and Structural Monitoring Systems (EESMS)*, 2017, pp. 1–6.

[85] Y. Xue, S. Zhang, M. Zhou, and H. Zhu, "Novel SfM-DLT method for metro tunnel 3D reconstruction and visualization," *Undergr. Space*, vol. 6, pp. 134–141, 2021. [Online]. Available: https://doi.org/10.1016/j.undsp.2020.01.002

[86] N. Aleksieva, C. H. Carrasco, A. Brown, R. Dean, A. Carolin, B. Täljsten, F. A. García-Villena, and F. J. Morales-Gamiz, "Inspection and monitoring techniques for tunnels and bridges," European Commission, Tech. Rep., 2019, accessed 25 September 2021.

[87] N. J. McCormick, A. Najimi, D. Jonas, and S. A. Kimkeran, "Assessing the condition of railway assets using DIFCAM: Results from tunnel examinations," in *Proceedings of the 6th IET Conference on Railway Condition Monitoring (RCM 2014)*, Singapore, 2014. [Online]. Available: https://doi.org/10.1049/cp.2014.1002

[88] NPL Management Ltd. (2021) DIFCAM Evolution. Organisation Website. NPL Management Ltd. Accessed 13 July 2021. [Online]. Available: https://gtr.ukri.org/projects?ref=971711

[89] Y. Xue and S. Zhang, "A fast metro tunnel profile measuring method based on close-range photogrammetry," in *Information Technology in Geo-Engineering*, A. G. Correia, J. Tinoco, P. Cortez, and L. Lamas, Eds. Cham: Springer International Publishing, 2020, pp. 57–69. [Online]. Available: https://link.springer.com/chapter/10.1007/978-3-030-32029-4_5#citeas

[90] E. Leonidas and Y. Xu, "The development of an automatic inspection system used for the maintenance of rail tunnels," in *2018 24th International Conference on Automation and Computing (ICAC)*, 2018, pp. 1–6.

[91] T. A. C. Garcia, A. M. G. Tommaselli, L. F. Castanheiro, and M. B. Campos, "A photogrammetric approach for real-time visual SLAM applied to an omnidirectional system," *The Photogrammetric Record*, vol. 39, no. 187, pp. 577–599, Apr. 2024.

[92] IOWA State University. (2021) The speed of sound in other materials. Organisation Website. IOWA State University. Accessed 15 June 2021. [Online]. Available: https://www.ndeed.org/Physics/Sound/speedinmaterials.xhtml

[93] TWI Ltd. (2021) What is ultrasonic testing and how does it work? Organisation Website. TWI Ltd. Accessed 17 June 2021. [Online]. Available: https://www.twiglobal.com/technical-knowledge/faqs/ultrasonic-testing

[94] R. Whitlow, R. Haskins, S. Mccomas, C. Crane, I. Howard, and M. Mckenna, "Remote bridge monitoring using infrasound," *J. Bridge Eng.*, vol. 24, p. 04019023, 2019. [Online]. Available: https://doi.org/10.1061/(ASCE)BE.1943-5592.0001375

[95] J. White, K. Wieghaus, M. Karthik, P. Shokouhi, S. Hurlebaus, and A. Wimsatt, "Nondestructive testing methods for underwater tunnel linings: Practical application at Chesapeake Channel Tunnels," *J. Infrastruct. Syst.*, vol. 23, p. B4016011, 2017. [Online]. Available: https://doi.org/10.1061/(ASCE)IS.1943-555X.0000350

[96] E. Menendez, J. Victores, R. Montero, S. Martínez, and C. Balaguer, "Tunnel structural inspection and assessment using an autonomous robotic system," *Autom. Constr.*, vol. 87, pp. 117–126, 2018. [Online]. Available: https://doi.org/10.1016/j.autcon.2017.12.001

[97] E. Protopapadakis, C. Stentoumis, N. Doulamis, A. Doulamis, K. Loupos, K. Makantasis, G. Kopsiaftis, and A. Amditis, "Autonomous robotic inspection in tunnels," *ISPRS Ann. Photogramm. Remote Sens. Spat. Inf. Sci.*, vol. 5, pp. 167–174, 2016. [Online]. Available: https://doi.org/10.5194/isprsannals-III-5-167-2016

[98] ROBOSPECT. (2021) Robotic system with intelligent vision and control for tunnel structural inspection and evaluation. Organisation Website. ROBOSPECT. Accessed 18 July 2021. [Online]. Available: http://www.robo-spect.eu/index.php/project

[99] A. Watanabe, J. Even, L. Y. Morales, and C. Ishi, "Robot-assisted acoustic inspection of infrastructures - cooperative hammer sounding inspection," in *2015 IEEE/RSJ International Conference on Intelligent Robots and Systems (IROS)*, 2015, pp. 5942–5947.

[100] A. Jamshidi, S. Faghih Roohi, A. Núñez, R. Babuska, B. De Schutter, R. Dollevoet, and Z. Li, "Probabilistic defect-based risk assessment approach for rail failures in railway infrastructure," *IFAC-PapersOnLine*, vol. 49, pp. 73–77, 2016. [Online]. Available: https://doi.org/10.1016/j.ifacol.2016.07.013

[101] H. Fujii, A. Yamashita, and H. Asama, "Defect detection with estimation of material condition using ensemble learning for hammering test," in *2016 IEEE International Conference on Robotics and Automation (ICRA)*, 2016, pp. 3847–3854.

[102] J. Y. Louhi Kasahara, A. Yamashita, and H. Asama, "Acoustic inspection of concrete structures using active weak supervision and visual information," *Sensors*, vol. 20, p. 629, 2020. [Online]. Available: https://doi.org/10.3390/s20030629

[103] S. Nakamura, A. Yamashita, F. Inoue, D. Inoue, Y. Takahashi, N. Kamimura, and T. Ueno, "Inspection test of a tunnel with an inspection vehicle for tunnel lining concrete," *Journal of Robotics and Mechatronics*, vol. 31, pp. 762–771, 2019. [Online]. Available: https://doi.org/10.20965/jrm.2019.p0762

[104] F. Moreu, E. Ayorinde, J. Mason, C. Farrar, and D. Mascarenas, "Remote railroad bridge structural tap testing using aerial robots," *International Journal of Intelligent Robotics and Applications*, vol. 2, pp. 67–80, 2018. [Online]. Available: https://doi.org/10.1007/s41315-017-0041-7

[105] D. Lattanzi and G. Miller, "Review of robotic infrastructure inspection systems," *Journal of Infrastructure Systems*, vol. 23, no. 1, pp. 1–15, 2017. [Online]. Available: https://doi.org/10.1061/(ASCE)IS.1943-555X.0000353

[106] T. Sugimoto, K. Sugimoto, I. Uechi, N. Utagawa, and C. Kuroda, "Efficiency improvement of outer wall inspection by noncontact acoustic inspection method using sound source mounted type UAV," in *2019 IEEE International Ultrasonics Symposium (IUS)*, 2019, pp. 2091–2094.

[107] M. Arastounia, "Automated as-built model generation of subway tunnels from mobile LIDAR data," *Sensors*, vol. 16, no. 9, p. 1486, 2016. [Online]. Available: https://doi.org/10.3390/s16091486

[108] Zoller and Fröhlich. (2014) Z+F Profiler 6007 Duo. Online Document. Zoller and Fröhlich. Accessed 16 July 2021. [Online]. Available: https://www.zf-laser.com/fileadmin/editor/Broschueren/Broschuere_PROFILER_6007_duo_E_compr.pdf

[109] H. Cui, X. Ren, Q. Mao, Q. Hu, and W. Wang, "Shield subway tunnel deformation detection based on mobile laser scanning," *Automation in Construction*, vol. 106, p. 102889, 2019.

[110] L. Gézero and C. Antunes, "Automated three-dimensional linear elements extraction from mobile LIDAR point clouds in railway environments," *Infrastructures*, vol. 4, p. 46, 2019. [Online]. Available: https://doi.org/10.3390/infrastructures4030046

[111] D. Kemp. (2016) 3D Crossrail tunnel scan unwrapped into 2D for first time. Online Document. CN Construction News. Accessed 19 July 2021. [Online]. Available: https://www.constructionnews.co.uk/tech/3d-crossrailtunnel-scan-unwrapped-into-2d-for-first-time-03-08-2016/#Tunnel_slice

[112] K. Tan, X. Cheng, and Q. Ju, "Combining mobile terrestrial laser scanning geometric and radiometric data to eliminate accessories in circular metro tunnels," *Journal of Applied Remote Sensing*, vol. 10, p. 030503, 2016. [Online]. Available: https://doi.org/10.1117/1.JRS.10.030503.short

[113] K. Mccrory. (2020) Case study of Llandudno Junction Station survey. Online Document. Scantech International Ltd. Accessed 16 July 2021. [Online]. Available: https://scantechinternational.com/case_study/llandudno-junction-station

[114] Scantech International Ltd. (2021) Railway surveys. Organisation Website. Scantech International Ltd. Accessed 24 July 2021. [Online]. Available: https://scantechinternational.com/sectors/railway-surveys

[115] X. Cheng, X. Hu, K. Tan, L. Wang, and L. Yang, "Automatic detection of shield tunnel leakages based on terrestrial mobile LiDAR intensity images using deep learning," *IEEE Access*, vol. 9, pp. 55 300–55 310, 2021.

[116] Zoller and Fröhlich. (2016) Case study: Train mounted laser survey of Birmingham New Street area resignalling phase 7. Online Document. Zoller and Fröhlich. Accessed 16 July 2021. [Online]. Available: https://www.zf-laser.com/fileadmin/editor/Case_studies/Case_Study_omnicom_E_comp.pdf

[117] E. Heinz, M. Mettenleiter, H. Kuhlmann, and C. Holst, "Strategy for determining the stochastic distance characteristics of the 2D laser scanner Z+F Profiler 9012a with special focus on the close range," *Sensors*, vol. 18, p. 2253, 2018. [Online]. Available: https://doi.org/10.3390/s18072253

[118] F. Yamazaki, H. Ueda, and W. Liu, "Basic study on detection of deteriorated RC structures using infrared thermography camera," *Engineering Journal*, vol. 22, pp. 233–242, 2018. [Online]. Available: https://engj.org/index.php/ej/article/view/2442

[119] B. Farahani, "Innovative methodology for railway tunnel inspection," Ph.D. dissertation, Ghent University, Sep. 2019. [Online]. Available: http://hdl.handle.net/1854/LU-01H086BAZDP6DXAYKKKMQB4GWX

[120] M. Ishikawa, M. Koyama, H. Kasano, N. Ogasawara, Y. Yamada, H. Hatta, R. Fukui, Y. Nishitani, and S. Utsunomiya, "Inspection of concrete structures using the active thermography method with remote heating apparatuses," in *Proceedings of the 15th Asia Pacific Conference for Non-Destructive Testing (APCNDT2017)*, Singapore, 2017. [Online]. Available: https://www.ndt.net/events/APCNDT2017/app/content/Paper/41_Ishikawa.pdf

[121] X. Lu, G. Tian, J. Wu, B. Gao, and P. Tian, "Pulsed air-flow thermography for natural crack detection and evaluation," *IEEE Sensors Journal*, vol. 20, pp. 8091–8097, 2020. [Online]. Available: https://doi.org/10.1109/JSEN.2020.2982556

[122] Z. Liu, B. Gao, and G. Tian, "Natural crack diagnosis system based on novel L-shaped electromagnetic sensing thermography," *IEEE Transactions on Industrial Electronics*, vol. 67, pp. 9703–9714, 2020. [Online]. Available: https://doi.org/10.1109/TIE.2019.2952782

[123] S. Konishi, K. Kawakami, and M. Taguchi, "Inspection method with infrared thermometry for detecting void in subway tunnel lining," *Procedia Engineering*, vol. 165, pp. 474–483, 2016. [Online]. Available: https://doi.org/10.1016/j.proeng.2016.11.723

[124] A. Afshani and H. Akagi, "Investigate the detection rate of defects in concrete lining using infrared-thermography method," in *Proceedings of the 7th Japan-China Geotechnical Symposium*, Sanya, China, 2018, pp. 1005–1016, accessed on 14 July 2021. [Online]. Available: http://www.scopus.com/inward/record.url?scp=85048987585&partnerID=8YFLogxK

[125] F. Liu and S. Seipel, "Infrared-visible image registration for augmented reality-based thermographic building diagnostics," *Visual Computing*, vol. 3, p. 16, 2015. [Online]. Available: https://doi.org/10.1186/s40327-015-0028-0

[126] A. Afshani, K. Kawakami, S. Konishi, and H. Akagi, "Study of infrared thermal application for detecting defects within tunnel lining," *Tunnelling and Underground Space Technology*, vol. 86, pp. 186–197, 2019.

[127] Scintrex. (1995) CG-3/3M autograv automated gravity meter operator manual, 5 ed. Online Document. Scintrex. Accessed 27 November 2021. [Online]. Available: https://scintrexltd.com/support/product-manuals/cg3-manual/

[128] D. Butler. (2008) Detection and characterization of cavities, tunnels, and abandoned mines. Online Document. The University of South Florida. Accessed 14 November 2020. [Online]. Available: https://digital.lib.usf.edu//content/SF/S0/05/54/94/00001/K26-05045-Butler--ICEEG_Presentation_on_Cavities_and_Tunnels.pdf

[129] B. Fores, C. Champollion, N. Lesparre, S. Pasquet, A. Martin, and F. Nguyen, "Variability of the water stock dynamics in karst: Insights from surface-to-tunnel geophysics," *Hydrogeology Journal*, vol. 29, pp. 2077–2089, 2021. [Online]. Available: https://doi.org/10.1007/s10040-021-02365-5

[130] V. Blecha and D. Mašín, "Observed and calculated gravity anomalies above a tunnel driven in clays: implication for errors in gravity interpretation," *Near Surface Geophysics*, vol. 11, pp. 569–578, 2013.

[131] P. Zahorec, J. Papčo, P. Vajda, and S. Szabó, "High-precision local gravity survey along planned motorway tunnel in the Slovak karst," *Contributions to Geophysics and Geodesy*, vol. 49, pp. 207–227, 2019. [Online]. Available: https://journal.geo.sav.sk/cgg/article/view/203

[132] E. Bloedau, "Assessment of change to gravity field due to underground railroad tunnel construction," Ph.D. dissertation, University of Stuttgart, Stuttgart, Germany, 2021, accessed 14 June 2021. [Online]. Available: https://elib.uni-stuttgart.de/handle/11682/11296

[133] R. Han, W. Li, R. Cheng, F. Wang, and Y. Zhang, "3D high-precision tunnel gravity exploration theory and its application for concealed inclined high-density ore deposits," *Journal of Applied Geophysics*, vol. 180, p. 104119, 2020.

[134] A. Alani and F. Tosti, "GPR applications in structural detailing of a major tunnel using different frequency antenna systems," *Construction and Building Materials*, vol. 158, pp. 1111–1122, 2018.

[135] W. Lai, X. Derobert, and P. Annan, "A review of ground penetrating radar application in civil engineering: A 30-year journey from locating and testing to imaging and diagnosis," *NDTE International*, vol. 96, pp. 58–78, 2018.

[136] Sensors and Software. (2020) What is ground penetrating radar. Online Document. Sensors and Software. Accessed 17 November 2020. [Online]. Available: https://www.sensoft.ca/blog/what-is-gpr/

[137] M. Solla, V. Pérez-Gracia, and S. Fontul, "A review of GPR application on transport infrastructures: troubleshooting and best practices," *Remote Sensing*, vol. 13, no. 4, p. 672, 2021. [Online]. Available: https://doi.org/10.3390/rs13040672

[138] S. M. Shrestha and I. Arai, "Signal processing of ground penetrating radar using spectral estimation techniques to estimate the position of buried targets," *EURASIP Journal on Advances in Signal Processing*, vol. 2003, no. 12, p. 970543, 2003. [Online]. Available: https://doi.org/10.1155/S1110865703307036

[139] Proceq, *Proceq GPR Live*, Screaning Eagle Technologies, Apr. 2018, accessed 10 March 2024. [Online]. Available: https://media.screeningeagle.com/asset/Downloads/Proceq%20GPR%20Live%20Quick%20Start%20Guide.pdf

[140] GSSI Geophysical Survey Systems Inc. (2017) StructureScan Mini XT. Online Document. GSSI Geophysical Survey Systems Inc. Accessed 21 July 2021. [Online]. Available: https://www.geophysical.com/wp-content/uploads/2018/01/GSSI-StructureScanMiniXTBrochure.pdf

[141] T. Dawood, Z. Zhu, and T. Zayed, "Deterioration mapping in subway infrastructure using sensory data of GPR," *Tunnelling and Underground Space Technology*, vol. 103, p. 103487, 2020.

[142] 3D-RADAR. (2019) GEOSCOPE MK IV: High-speed 3D GPR with high-resolution and deep penetration. Online Document. 3D-RADAR. Accessed 18 June 2021. [Online]. Available: http://3d-radar.com/wp-content/uploads/2019/10/3DRadar_GeoScope_ProductSheet_2019.pdf

[143] Zetica Rail. (2021) Zetica Advanced Rail Radar (ZARR) solution to augment inspection trains. Organisation Website. Zetica Rail. Accessed 04 July 2021. [Online]. Available: https://zeticarail.com/systems-software/zarr/

[144] IDS GeoRadar. (2021) SRS SafeRailSystem: safe railway ballast inspections with ground penetrating radar. Organisation Website. IDS GeoRadar. Accessed 04 July 2021. [Online]. Available: https://idsgeoradar.com/products/ground-penetratingradar/srs-saferailsystem

[145] Y. Zan, Z. Li, G. Su, and X. Zhang, "An innovative vehicle-mounted GPR technique for fast and efficient monitoring of tunnel lining structural conditions," *Case Studies in Nondestructive Testing and Evaluation*, vol. 6, pp. 63–69, 2016. [Online]. Available: https://doi.org/10.1016/j.csndt.2016.10.001

[146] X. Han, J. Jin, M. Wang, W. Jiang, L. Gao, and L. Xiao, "A review of algorithms for filtering the 3D point cloud," *Signal Processing: Image Communication*, vol. 57, pp. 103–112, 2017. [Online]. Available: https://doi.org/10.1016/j.image.2017.05.009

[147] F. I. Rial and U. Uschkerat, "Improving SCR of underground target signatures from air-launched GPR systems based on scattering center extraction," in *2017 18th International Radar Symposium (IRS)*, 2017, pp. 1–10.

[148] Z. Xiang, A. Rashidi, and G. Ou, "States of practice and research on applying GPR technology for labelling and scanning constructed facilities," *Journal of Performance of Constructed Facilities*, vol. 33, p. 03119001, 2019. [Online]. Available: https://doi.org/10.1061/(ASCE)CF.1943-5509.0001313

[149] Y. Lyu, H. Wang, and J. Gong, "GPR detection of tunnel lining cavities and reverse-time migration imaging," *Applied Geophysics*, vol. 17, no. 1, pp. 1–7, 2020. [Online]. Available: https://doi.org/10.1007/s11770-019-0831-9

[150] V. Bugarinović, L. Pajewski, A. Ristić, M. Vrtunski, M. Govedarica, and M. Borisov, "On the introduction of canny operator in an advanced imaging algorithm for real-time detection of hyperbolas in ground-penetrating radar data," *Electronics*, vol. 9, no. 3, p. 541, 2020. [Online]. Available: https://doi.org/10.3390/electronics9030541

[151] C. Li, S. Xing, S. E. Lauro, Y. Su, S. Dai, J. Feng, B. Cosciotti, F. D. Paolo, E. Mattei, Y. Xiao, C. Ding, and E. Pettinelli, "Pitfalls in GPR data interpretation: False reflectors detected in lunar radar cross sections by Change-3," *IEEE Transactions on Geoscience and Remote Sensing*, vol. 56, no. 3, pp. 1325–1335, 2018.

[152] G. Johnston. (2018) The basics of interpreting GPR data - part 2. Organisation Website. Sensors and Software. Accessed 16 November 2020. [Online]. Available: https://www.sensoft.ca/trainingevents/webinars/interpreting-gpr-data-part2/

[153] G. Kilic and L. Eren, "Neural network based inspection of voids and karst conduits in hydroelectric power station tunnels using GPR," *Journal of Applied Geophysics*, vol. 151, pp. 194–204, 2018. [Online]. Available: https://doi.org/10.1016/j.jappgeo.2018.02.026

[154] X. Wang, S. Sun, J. Wang, A. Yarovoy, B. Neducza, and G. Manacorda, "Real GPR signal processing for target recognition with circular array antennas," in *2016 URSI International Symposium on Electromagnetic Theory (EMTS)*, 2016, pp. 818–821.

[155] R. Sjödin, "Interpolation and visualization of sparse GPR data," Master's thesis, Umeå University, Umeå, Sweden, 2020, accessed 30 July 2021. [Online]. Available: https://www.diva-portal.org/smash/record.jsf?pid=diva2:1431027&dswid=8251

[156] Golden Software LLC. (2015) Voxler4: 3d well and volumetric data visualization. Online Document. Golden Software LLC. Accessed 12 December 2020. [Online]. Available: https://downloads.goldensoftware.com/guides/Voxler4UserGuide.pdf

[157] MALA Guideline Geo. (2021) MALA Vision user manual. Online Document. MALA Guideline Geo. Accessed 02 December 2021. [Online]. Available: https://www.guidelinegeoc.cdn.triggerfish.cloud/uploads/2021/03/MALA-Vision-User-Manual-July-2021.pdf

[158] X. Núñez-Nieto, M. Solla, F. J. Prego, and H. Lorenzo, "Assesing the applicability of GPR method for tunnelling inspection characterization and volumetric reconstruction," in *2015 8th International Workshop on Advanced Ground Penetrating Radar (IWAGPR)*, 2015, pp. 1–4.

[159] A. Simi and G. Manacorda, "The NeTTUN project: Design of a GPR antenna for a TBM," in *2016 16th International Conference on Ground Penetrating Radar (GPR)*, 2016, pp. 1–6.

[160] F. Garcia-Garcia, A. Valls-Ayuso, J. Benlloch-Marco, and M. Valcuende-Paya, "An optimization of the work disruption by 3D cavity mapping using GPR: A new sewerage project in Torrente (Valencia, Spain)," *Construction and Building Materials*, vol. 154, pp. 1226–1233, 2017. [Online]. Available: https://www.sciencedirect.com/science/article/pii/S0950061817312527

[161] S. Kadioglu and Y. K. Kadioğlu, "Determining buried remains under the Ala Gate Road of Anavarza ancient city in the southern turkey with interactive transparent 3D GPR data imaging," in *Proceedings of the International Multidisciplinary Scientific GeoConference: SGEM*, vol. 19, no. 1.1, 2019, pp. 773–779. [Online]. Available: https://www.proquest.com/openview/a405c1443ce97bab63fa781fe76c2c56/1?pq-origsite=gscholar&cbl=1536338

[162] M. Grasmueck and D. Viggiano, "PondView: Intuitive and efficient visualization of 3D GPR data," in *2018 17th International Conference on Ground Penetrating Radar (GPR)*, 2018, pp. 1–6.

[163] P. Agrafiotis, K. Lampropoulos, A. Georgopoulos, and A. Moropoulou, "3D Modelling the invisible using ground penetrating radar," *International Archives of the Photogrammetry, Remote Sensing and Spatial Information Sciences*, vol. XLII-2/W3, pp. 33–37, 2017. [Online]. Available: https://doi.org/10.5194/isprs-archives-XLII-2-W3-33-2017

[164] Z. Tong, J. Gao, and H. Zhang, "Recognition, location, measurement, and 3D reconstruction of concealed cracks using convolutional neural networks," *Construction and Building Materials*, vol. 146, pp. 775–787, 2017. [Online]. Available: https://www.sciencedirect.com/science/article/pii/S095006181730747X

[165] K. Chen, M. Kamezaki, T. Katano, T. Kaneko, K. Azuma, T. Ishida, M. Seki, K. Ichiryu, and S. Sugano, "Compound locomotion control system combining crawling and walking for multi-crawler multi-arm robot to adapt unstructured and unknown terrain," *ROBOMECH Journal*, vol. 5, no. 1, p. 2, 2018. [Online]. Available: https://doi.org/10.1186/s40648-018-0099-5

[166] W. Neubauer, A. Bornik, M. Wallner, and G. Verhoeven, "Novel volume visualisation of GPR data inspired by medical applications," in *New Global Perspectives on Archaeological Prospection: 13th International Conference on Archaeological Prospection*, J. Bonsall, Ed. Sligo, Ireland: Archaeopress, 2019, pp. 309–312. [Online]. Available: https://doi.org/10.2307/jj.15135979.83

[167] Y. Liu, J. Qiao, T. Han, L. Li, and T. Xu, "A 3D image reconstruction model for long tunnel geological estimation," *Journal of Advanced Transportation*, vol. 2020, p. 8846955, 2020. [Online]. Available: https://doi.org/10.1155/2020/8846955

[168] J. Feng, L. Yang, H. Wang, Y. Song, and J. Xiao, "GPR-based subsurface object detection and reconstruction using random motion and DepthNet," in *2020 IEEE International Conference on Robotics and Automation (ICRA)*, 2020, pp. 7035–7041.

[169] J. Feng, L. Yang, E. Hoxha, D. Sanakov, S. Sotnikov, and J. Xiao, "GPR-based model reconstruction system for underground utilities using GPRNet," in *2021 IEEE International Conference on Robotics and Automation (ICRA)*, 2021, pp. 845–851.

[170] K. Dinh, N. Gucunski, K. Tran, A. Novo, and T. Nguyen, "Full-resolution 3D imaging for concrete structures with dual-polarization GPR," *Automation in Construction*, vol. 125, p. 103652, 2021. [Online]. Available: https://www.sciencedirect.com/science/article/pii/S0926580521001035

[171] M. Pereira, D. Burns, D. Orfeo, Y. Zhang, L. Jiao, D. Huston, and T. Xia, "3D multistatic ground penetrating radar imaging for augmented reality visualization," *IEEE Transactions on Geoscience and Remote Sensing*, vol. 58, no. 8, pp. 5666–5675, 2020.

[172] S. Wu, L. Hou, and G. K. Zhang, "Integrated application of BIM and extended reality technology: a review, classification and outlook," in *Proceedings of the 18th International Conference on Computing in Civil and Building Engineering*, E. Toledo Santos and S. Scheer, Eds. Cham: Springer International Publishing, 2021, pp. 1227–1236. [Online]. Available: https://link.springer.com/chapter/10.1007/978-3-030-51295-8_86#citeas

[173] E. Karaaslan, U. Bagci, and F. Catbas, "Artificial intelligence assisted infrastructure assessment using mixed reality systems," *Transportation Research Record*, vol. 2673, pp. 413–424, 2019. [Online]. Available: https://doi.org/10.1177/0361198119839988

[174] J. Childs, D. Orfeo, D. Burns, D. Huston, and T. Xia, "Enhancing ground penetrating radar with augmented reality systems for underground utility management," in *Virtual, Augmented, and Mixed Reality (XR) Technology for Multi-Domain Operations*, vol. 11426. Bellingham, WA, USA: International Society for Optics and Photonics, 2020, p. 1142608. [Online]. Available: https://doi.org/10.1117/12.2561042.short

[175] R. Jin, "Developing a mixed-reality based application for bridge inspection and maintenance," in *Proceedings of the 20th International Conference on Construction Applications of Virtual Reality (CONVR 2020)*, Middlesbrough, UK, September 30–October 2 2020. [Online]. Available: https://openresearch.lsbu.ac.uk/item/8qyzx

[176] D. Hu, F. Hou, J. Blakely, and S. Li, "Augmented reality based visualization for concrete bridge deck deterioration characterized by ground penetrating radar," in *Construction Research Congress 2020*. Reston, VA: American Society of Civil Engineers, March 2020, pp. 1156–1164.

[177] ESCAP. (2019) Inspection and monitoring of railway infrastructure using aerial drones. Online Document. ESCAP. Accessed 01 July 2021. [Online]. Available: https://www.unescap.org/sites/default/files/TARWG_4E_Inspectionandmonitoring.pdf

[178] C. H. Tan, D. S. b. Shaiful, W. J. Ang, S. K. H. Win, and S. Foong, "Design optimization of sparse sensing array for extended aerial robot navigation in deep hazardous tunnels," *IEEE Robotics and Automation Letters*, vol. 4, no. 2, pp. 862–869, 2019.

[179] S. Jordan, J. Moore, S. Hovet, J. Box, J. Perry, K. Kirsche, D. Lewis, and Z. Tse, "State-of-the-art technologies for UAV inspections," *IET Radar, Sonar & Navigation*, vol. 12, pp. 151–164, 2018. [Online]. Available: https://doi.org/10.1049/iet-rsn.2017.0251

[180] L. Galtarossa, L. F. Navilli, and M. Chiaberge, "Visual-inertial indoor navigation systems and algorithms for UAV inspection vehicles," in *Industrial Robotics*, A. Grau and Z. Wang, Eds. Rijeka: IntechOpen, 2020. [Online]. Available: https://doi.org/10.5772/intechopen.90315

[181] F. Azevedo, A. Oliveira, A. Dias, J. Almeida, M. Moreira, T. Santos, A. Ferreira, A. Martins, and E. Silva, "Collision avoidance for safe structure inspection with multirotor UAV," in *2017 European Conference on Mobile Robots (ECMR)*, 2017, pp. 1–7.

[182] Q. Quan, R. Fu, M. Li, D. Wei, Y. Gao, and K. Y. Cai, "Practical distributed control for VTOL UAVs to pass a virtual tube," *IEEE Transactions on Intelligent Vehicles*, vol. 7, no. 2, pp. 342–353, 2022.

[183] M. Petrlík, T. Báča, D. Heřt, M. Vrba, T. Krajník, and M. Saska, "A robust UAV system for operations in a constrained environment," *IEEE Robotics and Automation Letters*, vol. 5, no. 2, pp. 2169–2176, 2020.

[184] M. Moletta, "Path planning for autonomous aerial robots in unknown underground zones optimized for vertical tunnels exploration," Master's thesis, KTH Royal Institute of Technology, Stockholm, Sweden, 2020, accessed 18 March 2021. [Online]. Available: https://www.diva-portal.org/smash/record.jsf?pid=diva2:1499089&dswid=5052

[185] T. Elmokadem and A. Savkin, "A method for autonomous collision-free navigation of a quadrotor UAV in unknown tunnel-like environments," *Robotica*, vol. 40, no. 4, pp. 1–27, 2021. [Online]. Available: https://doi.org/10.1017/S0263574721000849

[186] A. Falcone and G. Vaccarino. (2020) Primary level UAV for tunnel inspection: The PLUTO project. Online Document. Semantic Scholar. Accessed 18 July 2020. [Online]. Available: https://www.semanticscholar.org/paper/Primary-Level-UAVfor-Tunnel-Inspection:-the-PLUTO-Falcone-Vaccarino/32a694d6dbe4f7dba61181c54d8681fbe7503245

[187] T. Özaslan, S. Shen, Y. Mulgaonkar, N. Michael, and V. Kumar, "Inspection of penstocks and featureless tunnel-like environments using micro UAVs," in *Field and Service Robotics: Results of the 9th International Conference*, L. Mejias, P. Corke, and J. Roberts, Eds. Cham: Springer International Publishing, 2015, pp. 123–136. [Online]. Available: https://doi.org/10.1007/978-3-319-07488-7_9

[188] M. Sakuma, Y. Kobayashi, T. Emaru, and A. A. Ravankar, "Mapping of pier substructure using UAV," in *2016 IEEE/SICE International Symposium on System Integration (SII)*, 2016, pp. 361–366.

[189] W. Wu, M. A. Qurishee, J. Owino, I. Fomunung, M. Onyango, and B. Atolagbe, "Coupling deep learning and UAV for infrastructure condition assessment automation," in *2018 IEEE International Smart Cities Conference (ISC2)*, 2018, pp. 1–7.

[190] S. Dorafshan, M. Maguire, N. V. Hoffer, and C. Coopmans, "Challenges in bridge inspection using small unmanned aerial systems: Results and lessons learned," in *2017 International Conference on Unmanned Aircraft Systems (ICUAS)*, 2017, pp. 1722–1730.

[191] Hovering Solutions Ltd. (2020) Case studies: Penstock inspections and mapping by using autonomous flying robots. Organisation Website. Hovering Solutions Ltd. Accessed 19 April 2021. [Online]. Available: http://www.hoveringsolutions.com/aboutus/penstocks-mapping

[192] C. Tan, M. N, D. Shaiful, S. Win, W. Ang, S. Yeung, H. Lim, M. Do, and S. Foong, "A smart unmanned aerial vehicle (UAV) based imaging system for inspection of deep hazardous tunnels," *Water Practice and Technology*, vol. 13, pp. 991–1000, 2018.

[193] Hovering Solutions Ltd. (2017) Case studies: London crossrail tunnels are scanned using drones. Organisation Website. Hovering Solutions Ltd. Accessed 19 April 2021. [Online]. Available: http://www.hoveringsolutions.com/about-us/crossrailtunnels-3d-mapping-using-drones

[194] R. S. Pahwa, K. Y. Chan, J. Bai, V. B. Saputra, M. N. Do, and S. Foong, "Dense 3D reconstruction for visual tunnel inspection using unmanned aerial vehicle," in *2019 IEEE/RSJ International Conference on Intelligent Robots and Systems (IROS)*, 2019, pp. 7025–7032.

[195] P. Cwiakala, W. Gruszczynski, T. Stoch, E. Puniach, D. Mrochen, W. Matwij, K. Matwij, M. Nedzka, P. Sopata, and A. Wojcik, "UAV applications for determination of land deformations caused by underground mining," *Remote Sensing*, vol. 12, no. 11, p. 1733, 2020. [Online]. Available: https://doi.org/10.3390/rs12111733

[196] M. García-Fernandez, Y. Alvarez-Lopez, B. Gonzalez-Valdés, A. Arboleya-Arboleya, Y. Rodríguez-Vaqueiro, F. L. Heras, and A. Pino, "UAV-mounted GPR for NDT applications," in *2018 15th European Radar Conference (EuRAD)*, 2018, pp. 2–5.

[197] M. Garcia-Fernandez, Y. Alvarez-Lopez, F. L. Heras, B. Gonzalez-Valdes, Y. Rodriguez-Vaqueiro, A. Pino, and A. Arboleya-Arboleya, "GPR system onboard a UAV for non-invasive detection of buried objects," in *2018 IEEE International Symposium on Antennas and Propagation & USNC/URSI National Radio Science Meeting*, 2018, pp. 1967–1968.

[198] K. Lamsters, J. Karušs, M. Krievāns, and J. Ješkins, "High-resolution surface and bed topography mapping of Russell Glacier (SW Greenland) using UAV and GPR," *ISPRS Annals of the Photogrammetry, Remote Sensing and Spatial Information Sciences*, vol. II-2, pp. 757–763, 2020. [Online]. Available: https://doi.org/10.5194/isprs-annals-II-2-757-2020

[199] MALA Guideline Geo. (2021) MALA Geodrone 80 technical specification. Online Document. MALA Guideline Geo. Accessed 02 December 2021. [Online]. Available: https://www.guidelinegeoc.cdn.triggerfish.cloud/uploads/2020/01/MALA-GeoDrone-80-Technical-Specification-2020-04-27.pdf

[200] Q. Delamare, "Algorithms for estimation and control of quadrirotors in physical interaction with their environment," Ph.D. dissertation, Université de Rennes, 2019, nNT : 2019REN1S099. [Online]. Available: https://tel.archives-ouvertes.fr/tel-02895102v2

[201] Q. Delamare, P. R. Giordano, and A. Franchi, "Toward aerial physical locomotion the contact-fly-contact problem," *IEEE Robotics and Automation Letters*, vol. 3, no. 3, pp. 1514–1521, 2018.

[202] P. Sanchez-Cuevas, P. Ramon-Soria, B. Arrue, A. Ollero, and G. Heredia, "Robotic system for inspection by contact of bridge beams using UAVs," *Sensors*, vol. 19, no. 2, p. 305, 2019. [Online]. Available: https://doi.org/10.3390/s19020305

[203] B. Kocer, T. Tjahjowidodo, M. Pratama, and G. Seet, "Inspection-while-flying: An autonomous contact-based nondestructive test using UAV-tools," *Automation in Construction*, vol. 106, p. 102895, 2019. [Online]. Available: https://doi.org/10.1016/j.autcon.2019.102895

[204] PRODRONE Co Ltd. (2021) PD6-CI-L. Organisation Website. PRODRONE Co Ltd. Accessed 19 July 2021. [Online]. Available: https://www.prodrone.com/products/pd6-ci-l/

[205] S. Mahmood, S. Bakhy, and M. Tawfik, "Propeller-type wall-climbing robots: a review," in *IOP Conference Series: Materials Science and Engineering*, vol. 1094. Baghdad, Iraq: IOP Publishing, 2021, p. 012106. [Online]. Available: https://doi.org/10.1088/1757-899X/1094/1/012106/meta

[206] T. Ikeda, S. Yasui, M. Fujihara, K. Ohara, S. Ashizawa, A. Ichikawa, A. Okino, T. Oomichi, and T. Fukuda, "Wall contact by octo-rotor UAV with one DoF manipulator for bridge inspection," in *2017 IEEE/RSJ International Conference on Intelligent Robots and Systems (IROS)*, 2017, pp. 5122–5127.

[207] G. Jiang, R. M. Voyles, and J. J. Choi, "Precision fully-actuated UAV for visual and physical inspection of structures for nuclear decommissioning and search and rescue," in *2018 IEEE International Symposium on Safety, Security, and Rescue Robotics (SSRR)*, 2018, pp. 1–7.

[208] L. Brown, R. Clarke, A. Akbari, U. Bhandari, S. Bernardini, P. Chhabra, O. Marjanovic, T. Richardson, and S. Watson, "The design of Prometheus: A reconfigurable UAV for subterranean mine inspection," *Robotics*, vol. 9, p. 95, 2020. [Online]. Available: https://doi.org/10.3390/robotics9040095

[209] G. Ecker, B. Zagar, C. Schwab, F. Saliger, T. Schachinger, and M. Stur, "Conceptualising an inspection robot for tunnel drainage pipes," in *IOP Conference Series: Materials Science and Engineering*, vol. 831. Melbourne, Australia: IOP Publishing, 2020, p. 12016. [Online]. Available: https://doi.org/10.1088/1757-899X/831/1/012016/meta

[210] N. Naclerio, A. Karsai, M. Murray-Cooper, Y. Ozkan-Aydin, E. Aydin, D. Goldman, and E. Hawkes, "Controlling subterranean forces enables a fast, steerable, burrowing soft robot," *Science Robotics*, vol. 6, no. 53, p. eabe2922, 2021.

[211] X. Xiao and R. Murphy, "A review on snake robot testbeds in granular and restricted maneuverability spaces," *Robotics and Autonomous Systems*, vol. 110, pp. 160–172, 2018. [Online]. Available: https://www.sciencedirect.com/science/article/pii/S0921889018300861

[212] J. Liu, Y. Tong, and J. Liu, "Review of snake robots in constrained environments," *Robotics and Autonomous Systems*, vol. 141, p. 103785, 2021. [Online]. Available: https://www.sciencedirect.com/science/article/pii/S0921889021000701

[213] M. Ghazali and H. Mohamad, "Monitoring subsurface ground movement using fibre optic inclinometer sensor," in *IOP Conference Series: Materials Science and Engineering*, vol. 527. Kuala Lumpur, Malaysia: IOP Publishing, 2019, p. 012040. [Online]. Available: https://doi.org/10.1088/1757-899X/527/1/012040/meta

[214] F. Ciocca, L. Bodet, N. Simon, R. Karaulanov, A. Clarke, C. Abesser, S. Krause, A. Chalari, and M. Mondanos. (2017) Towards the wetness characterization of soil subsurface using fibre optic distributed acoustic sensing. Online Document. AGU Fall Meeting Abstracts. Accessed 19 July 2021. [Online]. Available: https://agu.confex.com/agu/fm17/meetingapp.cgi/Paper/270785

[215] R. Guzman, R. Navarro, M. Beneto, and D. Carbonell, "Robotnik professional service robotics applications with ROS," in *Robot Operating System (ROS): The Complete Reference (Volume 1)*, A. Koubaa, Ed. Cham: Springer International Publishing, 2016, pp. 253–288. [Online]. Available: https://doi.org/10.1007/978-3-319-26054-9_10

[216] A. Brunete, A. Ranganath, S. Segovia, J. P. de Frutos, M. Hernando, and E. Gambao, "Current trends in reconfigurable modular robots design," *International Journal of Advanced Robotic Systems*, vol. 14, no. 3, 2017.

[217] M. Zou, H. Bai, Y. Wang, and S. Yu, "Mechanical design of a self-adaptive transformable tracked robot for cable tunnel inspection," in *2016 IEEE International Conference on Mechatronics and Automation*, 2016, pp. 1096–1100.

[218] L. Bruzzone, P. Fanghella, and G. Quaglia, "Experimental performance assessment of MANTIS 2, hybrid leg-wheel mobile robot," *International Journal of Automation Technology*, vol. 11, pp. 396–403, 2017.

[219] X. Zhang, Y. Jiang, and S. Sugimoto, "Seismic damage assessment of mountain tunnel: A case study on the Tawarayama tunnel due to the 2016 Kumamoto Earthquake,"

*Tunnelling and Underground Space Technology*, vol. 71, pp. 138–148, 2018. [Online]. Available: https://www.sciencedirect.com/science/article/pii/S0886779816306472

[220] A. A. Calderón, J. C. Ugalde, J. C. Zagal, and N. O. Pérez-Arancibia, "Design, fabrication and control of a multi-material-multi-actuator soft robot inspired by burrowing worms," in *2016 IEEE International Conference on Robotics and Biomimetics (ROBIO)*, 2016, pp. 31–38.

[221] H. Ahmadzadeh, E. Masehian, and M. Asadpour, "Modular robotic systems: Characteristics and applications," *Journal of Intelligent & Robotic Systems*, vol. 81, pp. 317–357, 2016. [Online]. Available: https://doi.org/10.1007/s10846-015-0237-8

[222] X. Zhang, T. Pan, H. L. Heung, P. W. Y. Chiu, and Z. Li, "A biomimetic soft robot for inspecting pipeline with significant diameter variation," in *2018 IEEE/RSJ International Conference on Intelligent Robots and Systems (IROS)*, 2018, pp. 7486–7491.

[223] E. Kopperger, J. List, S. Madhira, F. Rothfischer, D. Lamb, and F. Simmel, "A self-assembled nanoscale robotic arm controlled by electric fields," *Science*, vol. 359, pp. 296–301, 2018. [Online]. Available: https://www.science.org/doi/full/10.1126/science.aao4284

[224] Y. Amir, A. Abu-Horowitz, J. Werfel, and I. Bachelet, "Nanoscale robots exhibiting quorum sensing," *Artificial Life*, vol. 25, pp. 227–231, 2019. [Online]. Available: https://doi.org/10.1162/artl_a_00293

[225] J. Dong, M. Wang, Y. Zhou, C. Zhou, and Q. Wang, "DNA-based adaptive plasmonic logic gates," *Angewandte Chemie*, vol. 132, pp. 15 148–15 152, 2020. [Online]. Available: https://doi.org/10.1002/ange.202006029

[226] J. Romanishin. (2018) Creating modular robotic systems which can reconfigure themselves in order to create new robots. Organisation Website. MIT. Accessed 20 July 2021. [Online]. Available: https://www.csail.mit.edu/research/m-blocksmodular-robotics

[227] NBS Enterprises Ltd. (2021) What is building information modelling BIM. Organisation Website. NBS Enterprises Ltd. Accessed 12 July 2021. [Online]. Available: https://www.thenbs.com/knowledge/what-is-buildinginformation-modelling-bim

[228] V. Kupriyanovsky, O. Pokusaev, A. Klimov, and A. Volodin, "BIM on the way to IFC5-alignment and development of IFC semantics and ontologies with UML and OWL for road and rail structures, bridges, tunnels, ports, and waterways," *International Journal of Open Information Technologies*, vol. 8, pp. 69–78, 2020. [Online]. Available: https://www.investigo.biblioteca.uvigo.es/xmlui/handle/11093/1896

[229] M. Soilán, A. Nóvoa, A. Sánchez-Rodríguez, B. Riveiro, and P. Arias, "Semantic segmentation of point clouds with PointNet and KPConv architectures applied to railway tunnels," *ISPRS Annals of the Photogrammetry, Remote Sensing and Spatial Information Sciences*, vol. V-2-2020, pp. 281–288, 2020. [Online]. Available: https://doi.org/10.5194/isprs-annals-V-2-2020-281-2020

[230] T. Nuttens, V. De Breuck, R. Cattoor, K. Decock, and I. Hemeryck, "Using BIM models for the design of large rail infrastructure projects: Key factors for a successful implementation," *International Journal of Sustainable Development and Planning*, vol. 13, no. 1, pp. 77–89, 2018. [Online]. Available: https://doi.org/10.2495/SDP-V13-N1-73-83

[231] ERA LEARN. (2018) Eurostars 2 project operation oriented tunnel inspection system. Organisation Website. ERA LEARN. Accessed 17 July 2021. [Online]. Available: https://www.era-learn.eu/networkinformation/networks/eurostars-2/eurostars-cut2013off-9/operation-oriented-tunnel-inspection-system

[232] R. Sorge, D. Buttafoco, J. Debenedetti, A. Menozzi, G. Cimino, F. Maltese, and B. Tiberi, "BIm implementation - Brenner Base Tunnel project," in *Tunnels and Underground Cities. Engineering and Innovation Meet Archaeology, Architecture and Art.* CRC Press, 2019, pp. 3122–3131. [Online]. Available: https://www.taylorfrancis.com/chapters/edit/10.1201/9780429424441-331/bim-implementation-brenner-base-tunnel-project-sorge-buttafoco-debenedetti-menozzi-cimino-maltese-tiberi

[233] K. Tijs, "Digital tunnel twin: Enriching the maintenance and operation of dutch tunnels," Master's thesis, Delft University of Technology, Delft, The Netherlands, 2020, accessed 1 July 2021. [Online]. Available: http://resolver.tudelft.nl/uuid:9cbf5ecf-66ce-4dde-9306-16bd8ccfdb9d

[234] O. Schneider, A. Prokopová, F. Modetta, and V. Petschen, "The use of artificial intelligence for a cost-effective tunnel maintenance," in *Tunnels and Underground Cities: Engineering and Innovation Meet Archaeology, Architecture and Art.* CRC Press, 2019, pp. 3050–3059. [Online]. Available: https://hagerbach.ch/fileadmin/user_upload/ch323_OliverSchneider.pdf

[235] G. Kapogiannis and A. Mlilo, "Digital construction strategies and BIM in railway tunnelling engineering," in *Tunnel Engineering*, M. Sakellariou, Ed. Rijeka: IntechOpen, 2019. [Online]. Available: https://doi.org/10.5772/intechopen.87942

[236] Z. Song, G. Shi, J. Wang, H. Wei, T. Wang, and G. Zhou, "Research on management and application of tunnel engineering based on BIM technology," *Journal of Civil*

*Engineering and Management*, vol. 25, no. 8, pp. 785–797, 2019. [Online]. Available: https://doi.org/10.3846/jcem.2019.11056

[237] R. Monica, J. Aleotti, M. Zillich, and M. Vincze, "Multi-label point cloud annotation by selection of sparse control points," in *2017 International Conference on 3D Vision (3DV)*, 2017, pp. 301–308.

[238] C. Xu, B. Wu, Z. Wang, W. Zhan, P. Vajda, K. Keutzer, and M. Tomizuka, "SqueezeSegV3: Spatially-adaptive convolution for efficient point-cloud segmentation," in *Computer Vision - ECCV 2020*, A. Vedaldi, H. Bischof, T. Brox, and J.-M. Frahm, Eds. Cham: Springer International Publishing, 2020, pp. 1–19.

[239] S. Kaewunruen, S. Peng, and O. Phil-Ebosie, "Digital twin aided sustainability and vulnerability audit for subway stations," *Sustainability*, vol. 12, no. 19, p. 1873, 2020.

[240] V. Singh and K. Willcox, "Engineering design with digital thread," *AIAA Journal*, vol. 56, pp. 4515–4528, 2018. [Online]. Available: https://doi.org/10.2514/1.J057255

[241] P. Shi, D. Zhang, J. Pan, and W. Liu, "Geological investigation and tunnel excavation aspects of the weakness zones of Xiang'an subsea tunnels in China," *Rock Mechanics and Rock Engineering*, vol. 49, no. 12, pp. 4853–4867, 2016. [Online]. Available: https://doi.org/10.1007/s00603-016-1076-z

[242] S. Zhou, Z. Tian, H. Di, P. Guo, and L. Fu, "Investigation of a loess-mudstone landslide and the induced structural damage in a high-speed railway tunnel," *Bulletin of Engineering Geology and the Environment*, vol. 79, no. 5, pp. 2201–2212, 2020. [Online]. Available: https://doi.org/10.1007/s10064-019-01711-y

[243] A. Ghezzi, A. Schettino, P. P. Pierantoni, L. Conyers, L. Tassi, L. Vigliotti, E. Schettino, M. Melfi, M. Gorrini, and P. Boila, "Reconstruction of a segment of the UNESCO world heritage Hadrian villa tunnel network by integrated GPR, magnetic–paleomagnetic, and electric resistivity prospections," *Remote Sensing*, vol. 11, no. 15, p. 1739, 2019.

[244] S. Moghaddam, A. Azadi, and E. Sadeghi, "Detection of landslide geometry using ERT, a case study: the tunnel of Kermanshah-Khosravy Railway," in *Proceedings of the 19th Iranian Geophysical Conference.* Iranian National Geophysical Society, 2020, pp. 68–71, accessed on 30 November 2021. [Online]. Available: http://www.nigsconference.ir/article_4094.pdf

[245] MALA Guideline Geo. (2017) User manual Terrameter LS2. Online Document. MALA Guideline Geo. Accessed 03 December 2021. [Online]. Available: https://www.guidelinegeoc.cdn.triggerfish.cloud/uploads/2017/08/Terrameter-LS-2-User-Manual-2017-08-14-1.pdf

[246] J. Lataste and J. Bruneau, "Geophysical investigations of a landslide to interpret the distortion of a railway tunnel," in *Proceedings of the NSG2021 27th European Meeting of Environmental and Engineering Geophysics*, vol. 2021. Kosterijland 48, 3981 AJ Bunnik, The Netherlands: EarthDoc: EAGE, 2021, pp. 1–5.

[247] N. Rhayma, A. Talon, P. Breul, and P. Goirand, "Mechanical investigation of tunnels: risk analysis and notation system," *Structure and Infrastructure Engineering*, vol. 12, no. 3, pp. 381–393, Mar. 2016. [Online]. Available: https://doi.org/10.1080/15732479.2015.1019892

[248] M. Futai, P. Cacciari, J. Monticeli, and V. Cantarella, "Study of an old railway rock tunnel: site investigation, laboratory tests, weathering effects and computational analysis," in *Proceedings of the 19th International Conference on Soil Mechanics and Geotechnical Engineering*. Seoul, Korea: ISSMGE, COEX Convention Centre, 2017, accessed on 25 July 2021. [Online]. Available: https://www.issmge.org/publications/publication/study-ofan-old-railway-rock-tunnel-site-investigation-laboratorytests-weathering-effects-and-computational-analysis

[249] L. F. Thompson, J. P. Stowell, S. J. Fargher, C. A. Steer, K. L. Loughney, E. M. O'Sullivan, J. G. Gluyas, S. W. Blaney, and R. J. Pidcock, "Muon tomography for railway tunnel imaging," *PRRESEARCH*, vol. 2, no. 2, p. 023017, Apr. 2020. [Online]. Available: https://link.aps.org/doi/10.1103/PhysRevResearch.2.023017

[250] R. Han, Q. Yu, Z. Li, J. Li, Y. Cheng, B. Liao, L. Jiang, S. Ni, Z. Yi, T. Liu, and Z. Wang, "Cosmic muon flux measurement and tunnel overburden structure imaging," *Journal of Instrumentation*, vol. 15, no. 06, p. P06019, 2020. [Online]. Available: https://dx.doi.org/10.1088/1748-0221/15/06/P06019

[251] M. D. Castro, M. L. B. Tambutti, M. Ferre, R. Losito, G. Lunghi, and A. Masi, "i-TIM: A robotic system for safety, measurements, inspection and maintenance in harsh environments," in *2018 IEEE International Symposium on Safety, Security, and Rescue Robotics (SSRR)*, 2018, pp. 1–6.

[252] C. Shi, H. Che, H. Hu, W. Wang, X. Xu, and J. Li, "Research on laser positioning system of a underground inspection robot based on signal reflection principle," in *2019 3rd International Conference on Robotics and Automation Sciences (ICRAS)*, 2019, pp. 58–62.

[253] R. Vithanage, C. Harrison, and A. Desilva, "Importance and applications of robotic and autonomous systems (RAS) in railway maintenance sector: A review," *Computers*, vol. 8, no. 3, p. 56, 2019. [Online]. Available: https://doi.org/10.3390/computers8030056

[254] Lincseek. (2021) Rail-mounted robot. Organisation Website. Lincseek. Accessed 02 July 2021. [Online]. Available: http://en.launchdigital.net/product.aspx?t=25

[255] M. Ziegler and S. Loew, "Investigations in the new TBM-excavated belchen highway tunnel," in *Program, Design and Installations (Part 1)*. Zürich, Switzerland: Techreport, ETH Zürich, 2017, accessed on 25 November 2021. [Online]. Available: https://www.researchgate.net/publication/333653106_Investigations_in_the_new_TBM-excavated_Belchen_highway_tunnel_-_Program_design_and_installations_Part_1

[256] T.-Y. Zhang, B. Shi, C.-C. Zhang, T. Xie, J. Yin, and J.-P. Li, "Tunnel disturbance events monitoring and recognition with distributed acoustic sensing (DAS)," *IOP Conference Series: Earth and Environmental Science*, vol. 861, no. 4, p. 042034, 2021. [Online]. Available: https://dx.doi.org/10.1088/1755-1315/861/4/042034

[257] W. Lienhart, F. Buchmayer, F. Klug, and C. M. Monsberger, "Distributed fibre-optic sensing applications at the Semmering Base Tunnel, Austria," *Proceedings of the Institution of Civil Engineers - Smart Infrastructure and Construction*, vol. 172, no. 4, pp. 148–159, Dec. 2019. [Online]. Available: https://doi.org/10.1680/jsmic.20.00006

[258] Y. El Masri and T. Rakha, "A scoping review of non-destructive testing (NDT) techniques in building performance diagnostic inspections," *Construction and Building Materials*, vol. 265, p. 120542, 2020. [Online]. Available: https://www.sciencedirect.com/science/article/pii/S0950061820325472

[259] L. Zou, L. Yi, and M. Sato, "On the use of lateral wave for the interlayer debonding detecting in an asphalt airport pavement using a multistatic GPR system," *IEEE Transactions on Geoscience and Remote Sensing*, vol. 58, no. 6, pp. 4215–4224, 2020.

[260] J. H. Han, Y. C. Cho, H. G. Lee, H. S. Yang, W. J. Jeong, and Y. S. Moon, "Crack detection method on surface of tunnel lining," in *2019 34th International Technical Conference on Circuits/Systems, Computers and Communications (ITC-CSCC)*, 2019, pp. 1–3.

[261] S. Hou, B. Dong, H. Wang, and G. Wu, "Inspection of surface defects on stay cables using a robot and transfer learning," *Automation in Construction*, vol. 119, p. 103382, 2020. [Online]. Available: https://www.sciencedirect.com/science/article/pii/S0926580520309626

[262] N. Gagarin, J. R. Mekemson, and D. Goulias, "Second-generation analysis approach for condition assessment of transportation infrastructure using step-frequency (SF) ground-penetrating-radar (GPR) array system," in *Bearing Capacity of Roads, Railways and Airfields*. CRC Press, 2017, pp. 1573–1581. [Online]. Available: https://www.taylorfrancis.com/chapters/edit/10.1201/9781315100333-209/second-generation-analysis-approach-condition-assessment-transportation-infrastructure-using-step-frequency-sf-ground-penetrating-radar-gpr-array-system-gagarin-mekemson-goulias

[263] M. Insa-Iglesias, M. D. Jenkins, and G. Morison, "3D visual inspection system framework for structural condition monitoring and analysis," *Automation in Construction*, vol. 128, p. 103755, 2021. [Online]. Available: https://www.sciencedirect.com/science/article/pii/S0926580521002065

[264] K. Makantasis, E. Protopapadakis, A. Doulamis, N. Doulamis, and C. Loupos, "Deep convolutional neural networks for efficient vision based tunnel inspection," in *2015 IEEE International Conference on Intelligent Computer Communication and Processing (ICCP)*, 2015, pp. 335–342.

[265] M. Nasrollahi, N. Bolourian, and A. Hammad, "Concrete surface defect detection using deep neural network based on lidar scanning," in *Proceedings of the CSCE Annual Conference*, Laval, Greater Montreal, QC, Canada, June 2019, pp. 12–15. [Online]. Available: https://legacy.csce.ca/elf/apps/CONFERENCEVIEWER/conferences/2019/pdfs/PaperPDFversion_32_0409032519.pdf

[266] M. Arbabsiar, M. Farsangi, and H. Mansouri, "Fuzzy logic modelling to predict the level of geotechnical risks in rock tunnel boring machine (TBM) tunnelling," *Mining-Geology-Petroleum Engineering Bulletin*, vol. 35, no. 2, pp. 1–14, 2020, accessed on 27 July 2021. [Online]. Available: https://hrcak.srce.hr/ojs/index.php/rgn/article/view/9979

[267] L. El-khateeb, E. Mohammed Abdelkader, A. Al-Sakkaf, and T. Zayed, "A hybrid multi-criteria decision making model for defect-based condition assessment of railway infrastructure," *Sustainability*, vol. 13, no. 13, p. 7186, 2021. [Online]. Available: https://doi.org/10.3390/su13137186

[268] S. Sajid, A. Taras, and L. Chouinard, "Defect detection in concrete plates with impulse-response test and statistical pattern recognition," *Mechanical Systems and Signal Processing*, vol. 161, p. 107948, 2021. [Online]. Available: https://www.sciencedirect.com/science/article/pii/S0888327021003435

[269] J. Nielsen. (2006) Progressive disclosure. Organisation Website. Nielsen Norman Group. Accessed 09 November 2020. [Online]. Available: https://www.nngroup.com/articles/progressive-disclosure/

[270] S. Vi, T. S. da Silva, and F. Maurer, "User experience guidelines for designing hmd extended reality applications," in *Human-Computer Interaction - INTERACT 2019*, D. Lamas, F. Loizides, L. Nacke, H. Petrie, M. Winckler, and P. Zaphiris, Eds. Cham: Springer International Publishing, 2019, pp. 319–341.

[271] A. Fast-Berglund, L. Gong, and D. Li, "Testing and validating extended reality XR technologies in manufacturing," *Procedia Manufacturing*, vol. 25, pp. 31–38, 2018. [Online]. Available: https://www.sciencedirect.com/science/article/pii/S2351978918305730

[272] S. Chuah, "Why and who will adopt extended reality technology literature review, synthesis, and future research agenda," *Lit. Rev. Synth. Future Res. Agenda*, pp. 1–55, 2018. [Online]. Available: https://doi.org/10.2139/ssrn.3300469

[273] L. H. Hansen, S. C. S. Wyke, and E. Kjems, "Combining reality capture and augmented reality to visualise subsurface utilities in the field," in *Proceedings of the 37th International Symposium on Automation and Robotics in Construction (ISARC 2020): From Demonstration to Practical Use-To New Stage of Construction Robot*. The International Symposium on Automation and Robotics in Construction, 2020, pp. 703–710. [Online]. Available: https://vbn.aau.dk/ws/portalfiles/portal/401875244/Combining_Reality_Capture_and_Augmented_Reality_to_Visualise_Subsurface_Utilities_in_the_Field.pdf

[274] J. Du, Z. Zou, Y. Shi, and D. Zhao, "Simultaneous data exchange between BIM and VR for collaborative decision making," in *Proceedings of Computing in Civil Engineering 2017*. American Society of Civil Engineers (ASCE), 2017, pp. 1–8. [Online]. Available: https://ascelibrary.org/doi/10.1061/9780784480830.001

[275] F.-Z. Wang, H.-C. Sui, W.-D. Kong, and H. Zhong, "Application of BIM and VR technology in immersed tunnel construction," *IOP Conference Series: Earth and Environmental Science*, vol. 798, no. 1, p. 012019, 2021. [Online]. Available: https://dx.doi.org/10.1088/1755-1315/798/1/012019

[276] G. Cosma, E. Ronchi, and D. Nilsson, "Way-finding lighting systems for rail tunnel evacuation: A virtual reality experiment with Oculus Rift," *Journal of Transportation Safety & Security*, vol. 8, no. sup1, pp. 101–117, Jun. 2016. [Online]. Available: https://doi.org/10.1080/19439962.2015.1046621

[277] S. Arias, S. La Mendola, J. Wahlqvist, O. Rios, D. Nilsson, and E. Ronchi, "Virtual reality evacuation experiments on way-finding systems for the future circular collider," *Fire Technology*, vol. 55, no. 6, pp. 2319–2340, 2019. [Online]. Available: https://doi.org/10.1007/s10694-019-00868-y

[278] M. I. Iglesias, M. Jenkins, and G. Morison, "An enhanced photorealistic immersive system using augmented situated visualization within virtual reality," in *2021 IEEE Conference on Virtual Reality and 3D User Interfaces Abstracts and Workshops (VRW)*, 2021, pp. 514–515.

[279] Network Rail. (2019, Jun.) Capability assessment tool for tunnel masonry linings. Online Document. Network Rail. Accessed 08 May 2021. [Online]. Available: https://www.networkrail.co.uk/wp-content/uploads/2019/06/Challenge-Statement-Tunnels-Capability-assessment-tool-for-tunnel-masonry-linings.pdf

[280] ——. (2024) Our business areas. Organisation Website. Network Rail. Accessed 19 July 2024. [Online]. Available: https://www.networkrail.co.uk/careers/our-business-areas/

[281] ——. (2020) Careers search. Organisation Website. Network Rail. Accessed 19 July 2021. [Online]. Available: https://www.networkrail.co.uk/careers/careers-search/

[282] MTI. (2021) Tunnel mesh - long range nodes. Organisation Website. MTI. Accessed 23 November 2021. [Online]. Available: https://mti-technology.com/products/long-range-nodes/

[283] ——. (2020) Mining and tunnelling communication systems - tunnel mesh. Organisation Website. MTI. Accessed 23 November 2021. [Online]. Available: https://mti-technology.com/product_category/tunnelmesh/

[284] V. Singh and K. E. Willcox, "Engineering design with digital thread," *Aiaa Journal*, vol. 56, no. 11, pp. 4515–4528, 2018.

[285] Zetica Rail. (2017) ZARR Zetica Advanced Rail Radar. Online Document. Zetica Rail. Accessed 13 July 2021. [Online]. Available: https://zeticarail.com/wp-content/uploads/2017/02/English-International-Flyer.pdf

[286] H. Liu, Y. Yue, Y. Lian, X. Meng, Y. Du, and J. Cui, "Reverse-time migration of GPR data for imaging cavities behind a reinforced shield tunnel," *Tunnelling and Underground Space Technology*, vol. 146, p. 105649, 2024. [Online]. Available: https://www.sciencedirect.com/science/article/pii/S0886779824000671

[287] Y. Zan, Z. Li, G. Su, and X. Zhang, "An innovative vehicle-mounted GPR technique for fast and efficient monitoring of tunnel lining structural conditions," *Case Studies in Nondestructive Testing and Evaluation*, vol. 6, pp. 63–69, 2016. [Online]. Available: https://www.sciencedirect.com/science/article/pii/S2214657116300363

[288] PENETRADAR. (2024) Ground penetrating radar inspeciton vehicles. Organisation Website. PENETRADAR. Accessed 16 August 2024. [Online]. Available: http://penetradar.com/new/?page_id=525

[289] P. Bevelacqua. (2024) Directivity. Organisation Website. Antenna Theory. Accessed 12 February 2025. [Online]. Available: https://www.antenna-theory.com/basics/directivity.php

[290] H. Pragnell, "Tunnels in arcadia: Isambard Kingdom Brunel's portal designs for the great western railway," *Architectural History*, vol. 63, pp. 143–169, 2020. [Online]. Available: https://www.cambridge.org/core/product/F61B7FE53CB234C0EE336F5E6A684E98

[291] Office of Rail and Road. (2017, Dec.) Quarters 1-2 of Year 4 of CP51 April 2017 to 14 October 2017. Online Document. Office of Rail and Road. Accessed 20 March 2021. [Online]. Available: https://www.orr.gov.uk/sites/default/files/om/network-rail-monitor-2017-18-q1-2.pdf

[292] ——. (2020, Jul.) Annual assessment of Network Rail April 2020 to March 2021. Online Document. Office of Rail and Road. Accessed 20 March 2021. [Online]. Available: https://www.orr.gov.uk/sites/default/files/2021-07/annual-assessment-of-network-rail-2020-21.pdf

[293] COWI UK LTD, "Tunnel management strategy desk study," Network Rail, Tech. Rep., 2017, accessed 20 March 2021.

[294] T. McDonald, A. Plattner, C. Warren, M. Robinson, and G. Tian, "3D visualization of new hybrid-rotational ground-penetrating radar for subsurface inspection of transport infrastructure," *IEEE Transactions on Geoscience and Remote Sensing*, vol. 63, pp. 1–13, Jan. 2025.

[295] COMSOL, "RF Module," September 2024. [Online]. Available: https://www.comsol.com/rf-module

[296] GPR-SURVEY, "GPR-SIM," Sep. 2024. [Online]. Available: https://www.gpr-survey.com/gprsim.html

[297] C. Warren, A. Giannopoulos, and I. Giannakis, "gprMax Open source software to simulate electromagnetic wave propagation for ground penetrating radar," *Computer Physics Communications*, vol. 209, pp. 163–170, 2016. [Online]. Available: https://www.sciencedirect.com/science/article/pii/S0010465516302533

[298] Wienerberger. (2021, Apr.) Weinerberger technical guidance - brickwork dimensions table - standard UK brick. Online Document. Wienerberger. Accessed 18 December 2022. [Online]. Available: https://www.wienerberger.co.uk/content/dam/wienerberger/united-kingdom/marketing/documents-magazines/technical/brick-technical-guidance-sheets/UK_MKT_DOC_BrickworkDimensionTables.pdf

[299] A. P. Annan and N. Diamanti, "A step towards quantitative target analysis for GPR," in *2016 16th International Conference on Ground Penetrating Radar (GPR)*, 2016, pp. 1–5.

[300] A. C. Gürbüz, T. Counts, K. Kim, J. H. McClellan, and W. R. S. Jr., "Application of multistatic inversion algorithms to landmine detection," in *Proceedings of SPIE*, vol. 6217, may 2006, p. 621724. [Online]. Available: https://doi.org/10.1117/12.666367

[301] Z. Idriss, R. G. Raj, and R. M. Narayanan, "A wideband method of moments target modeling and feature extraction approach for GPR imaging," in *2021 IEEE International Geoscience and Remote Sensing Symposium IGARSS*, 2021, pp. 2258–2261.

[302] H. Jung and K. Kim, "Iteration strategy for autofocusing metric evaluation in GPR imaging," in *2018 International Symposium on Antennas and Propagation (ISAP)*, 2018, pp. 1–2. [Online]. Available: https://ieeexplore.ieee.org/abstract/document/8627650?casa_token=Pjr_0YVCDdUAAAAA:bYDmkwH59rpmwtqZKEhPTw5vUnZ91rLfpYyinM8cTpEVMOxiTm4ncr_fIKj4_YICESKUll6IbNs

[303] F. Soldovieri, I. Catapano, P. M. Barone, S. E. Lauro, E. Mattei, E. Pettinelli, G. Valerio, D. Comite, and A. Galli, "GPR Estimation of the geometrical features of buried metallic targets in testing conditions," *Progress In Electromagnetics Research B*, vol. 49, pp. 339–362, 2013.

[304] A. M. Plattner, "GPRPy open-source ground-penetrating radar processing and visualization software," *The Leading Edge*, vol. 39, no. 5, pp. 332–334, May 2020. [Online]. Available: https://doi.org/10.1190/tle39050332.1

[305] MALA Guideline Geo. (2021, Mar.) Appendix 1 – Detailed description of RD3, RD7 and RAD formats. Online Document. MALA Guideline Geo. Accessed 05 August 2022. [Online]. Available: https://wwwguidelinegeoc.cdn.triggerfish.cloud/uploads/2021/03/MALA-formats-rd3-and-rd7.pdf

[306] GSSI Geophysical Survey Systems Inc, *RADAN 7 Manual MN43-199 Rev G*, GSSI Geophysical Survey Systems Inc, 2011, accessed 04 February 2021. [Online]. Available: https://www.geophysical.com/wp-content/uploads/2017/10/GSSI-RADAN-7-Manual.pdf

[307] Sensors and Software Inc, *EKKO View2 user's guide*, Sensors and Software Inc, 2008, accessed 10 March 2024. [Online]. Available: https://www.sensoft.ca/wp-content/uploads/2015/11/EKKO_View.compressed.pdf

[308] RadarSystemsInc, *Prism2 version 2.7x user's manual rev.*, RadarSystemsInc, Mar. 2022, accessed 13 March 2023. [Online]. Available: https://www.radsys.lv/userfiles/files/prism2manual.pdf

[309] Keysight Technologies. (2024) SnP (Touchstone) File Format. Organisation Website. Keysight Technologies. Accessed 09 June 2021. [Online]. Available: https://helpfiles.keysight.com/csg/N1930xB/FilePrint/SnP_File_Format.htm

[310] Center for Research in Earth and Space Science (CREWES), "CREWES freeware," September 2024. [Online]. Available: https://www.crewes.org/ResearchLinks/FreeSoftware/

[311] Scikit-Learn Developers. (2024) HDBSCAN. Organisation Website. Scikit Learn. Accessed 14 November 2023. [Online]. Available: https://scikit-learn.org/stable/modules/generated/sklearn.cluster.HDBSCAN.html

[312] J. Rubia, "Rice University Rule to determine the number of bins," *Open Journal of Statistics*, vol. 14, pp. 119–149, 2024.

[313] H. Shimazaki and S. Shinomoto, "A method for selecting the bin size of a time histogram," *Neural Comput*, vol. 19, no. 6, pp. 1503–1527, Jun. 2007. [Online]. Available: https://doi.org/10.1162/neco.2007.19.6.1503

[314] L. McInnes, J. Healy, and S. Astels. (2016) How HDBSCAN works. Organisation Website. hdbscan. Accessed 11 January 2022. [Online]. Available: https://hdbscan.readthedocs.io/en/latest/how_hdbscan_works.html

[315] P. Berba. (2020, Jan.) Understanding HDBSCAN and density-based clustering. Organisation Website. Github. Accessed 05 October 2020. [Online]. Available: https://pberba.github.io/stats/2020/01/17/hdbscan/

[316] B. Sullivan and A. Kaszynski, "PyVista: 3D plotting and mesh analysis through a streamlined interface for the Visualization Toolkit (VTK)," 2024. [Online]. Available: https://doi.org/10.5281/zenodo.12792244

[317] P. Virtanen and R. e. a. Gommers, "SciPy 1.0: fundamental algorithms for scientific computing in Python," *Nature Methods*, vol. 17, no. 3, pp. 261–272, 2020. [Online]. Available: https://doi.org/10.1038/s41592-019-0686-2

[318] C. B. Barber, D. P. Dobkin, and H. T. Huhdanpaa, "The Quickhull algorithm for convex hulls," *ACM Transactions on Mathematical Software*, vol. 22, no. 4, pp. 469–483, Dec. 1996. [Online]. Available: http://www.qhull.org

[319] J. Geng and H. Ye, "Revers time migration method of ground penetrating radar based on gprMax," in *2022 International Applied Computational Electromagnetics Society Symposium (ACES-China)*, 2022, pp. 1–3.

[320] S. J. Savita and A. Pallavi, "Modeling of GPR using gprMax simulation," in *2022 IEEE International Conference on Distributed Computing and Electrical Circuits and Electronics (ICDCECE)*, 2022, pp. 1–4.

[321] U. Akhaury, I. Giannakis, C. Warren, and A. Giannopoulos, "Machine learning based forward solver: an automatic framework in gprMax," in *2021 11th International Workshop on Advanced Ground Penetrating Radar (IWAGPR)*, 2021, pp. 1–6.

[322] C. Warren and A. Giannopoulos. (2024) gprMax - guidance on GPR modelling. Organisation Website. gprMax. Accessed 28 July 2024. [Online]. Available: https://docs.gprmax.com/en/latest/gprmodelling.html#guidance

[323] K. M. Barry, D. A. Cavers, and C. W. Kneale, "Recommended standards for digital tape formats," *Geophysics*, vol. 40, no. 2, pp. 344–352, Apr. 1975. [Online]. Available: https://doi.org/10.1190/1.1440530

[324] Equinor, "SEGYIO," September 2024. [Online]. Available: https://github.com/equinor/segyio

[325] M. A. Baker, "SEGPY," September 2024. [Online]. Available: https://pypi.org/project/segpy/

[326] L. Yang, "SGY2TXT," September 2018. [Online]. Available: https://github.com/lyc11776611/SGY2TXT/blob/master/SGY2TXT.py

[327] Y. A. Lopez, M. Garcia-Fernandez, G. Alvarez-Narciandi, and Andres, "Unmanned aerial vehicle-based ground-penetrating radar systems: A review," *IEEE Geoscience and Remote Sensing Magazine*, vol. 10, no. 2, pp. 66–86, 2022.

[328] G. EMC, *3m compliant EMC anechoic test chambers (semi)*, GLOBAL EMC, 2024, accessed 30 May 2023. [Online]. Available: https://globalemc.co.uk/download/86223/?tmstv=1708420907

[329] Keysight Technologies. (2024) VNA help - calibration wizard. Organisation Website. Keysight Technologies. Accessed 02 September 2021. [Online]. Available: https://helpfiles.keysight.com/csg/N52xxB/S3_Cals/Calibration_Wizard.htm

[330] T. Reveyrand, S. Hernández, S. Mons, and E. Ngoya, "SOLT and SOLR calibration methods using a single multiport thru standard connection," in *2020 95th ARFTG Microwave Measurement Conference (ARFTG)*, 2020, pp. 1–4.

[331] N. Diamanti and A. P. Annan, "Characterizing the energy distribution around GPR antennas," *Journal of Applied Geophysics*, vol. 99, pp. 83–90, 2013. [Online]. Available: https://www.sciencedirect.com/science/article/pii/S0926985113001511

[332] Z. Chen, H. Liu, X. Meng, Y. Yue, B. Zhang, L. Zou, and Y. Du, "Internal decay inspection of tree trunks using 3D point cloud and reverse time migration of ground

penetrating radar data," *NDT & E International*, vol. 137, p. 102853, 2023. [Online]. Available: https://www.sciencedirect.com/science/article/pii/S0963869523000683

[333] G. Serbin and D. Or, "Frequency-domain analyses of GPR waveforms : Enhancing near-surface observational capabilities," in *Predictions in ungauged basins (promise and progress)*, vol. 1. IAHS, Wallingford, 2006, pp. 274–285. [Online]. Available: http://pascal-francis.inist.fr/vibad/index.php?action=getRecordDetail&idt=18578204

[334] A. D. Strange, "A systematic method for characterizing the time-range performance of ground penetrating radar," *J Geophys Eng*, vol. 10, no. 3, p. 034001, Jun. 2013. [Online]. Available: https://doi.org/10.1088/1742-2132/10/3/034001

[335] G. Marasco, M. M. Rosso, S. Aiello, A. Aloisio, G. Cirrincione, B. Chiaia, and G. C. Marano, "Ground penetrating radar fourier pre-processing for deep learning tunnel defects automated classification," in *Engineering Applicationsof Neural Networks*, ser. International Conference on Engineering Applications of Neural Networks, F. Joaquim, Ed., vol. 1600, Communications in Computer and Information Science. Cham, Switzerland: Springer International Publishing, Jun. 2022, pp. 165–176.

[336] D. Paredes-Palacios, F. Mota-Toledo, B. Biosca, L. Arévalo-Lomas, and J. Díaz-Curiel, "Optimization of dominant frequency and bandwidth analysis in multi-frequency 3D GPR signals to identify contaminated areas," *Sensors*, vol. 22, no. 24, p. 9851, Dec. 2022.

[337] P. Smogavec, B. Pongrac, A. Sarjaš, V. Kafedziski, N. Dončov, and D. Gleich, "Comparative study of GPR acquisition methods for shallow buried object detection," *Remote Sensing*, vol. 16, no. 21, p. 3931, Oct. 2024.

[338] S. M. Shrestha, I. Arai, T. Miwa, and Y. Tomizawa, "Signal processing of ground penetrating radar using super resolution technique," in *Proceedings of the 2001 IEEE Radar Conference (Cat. No.01CH37200)*, 2001, pp. 300–305.

[339] CORDIS. (2022, Jun.) Climate resilient and environmentally sustainable transport infrastructure, with a focus on inland waterways. Organisation Website. European Commission. Accessed 15 August 2023. [Online]. Available: https://cordis.europa.eu/project/id/101069838

[340] A. Bornik and W. Neubauer, "3D Visualization techniques for analysis and archaeological interpretation of GPR data," *Remote Sensing*, vol. 14, no. 7, p. 1709, 2022.

[341] S. B. Iryanto, F. H. Muttaqien, and R. Sadikin, "Irregular grid interpolation using radial basis function for large cylindrical volume," *Jurnal Ilmu Komputer dan Informasi*, vol. 13, no. 1, pp. 17–23, Mar. 2020. [Online]. Available: https://jiki.cs.ui.ac.id/index.php/jiki/article/view/805

[342] Z. Qin, X. Li, and Y. Gu, "Hemisphere harmonics basis a universal approach to remote sensing BRDF approximation," *IEEE Transactions on Geoscience and Remote Sensing*, vol. 62, pp. 1–12, 2024.

[343] T. Zhang, D. Zhang, D. Zheng, X. Guo, and W. Zhao, "Construction waste landfill volume estimation using ground penetrating radar," *Waste Manag Res*, vol. 40, no. 8, pp. 1167–1175, Jan. 2022. [Online]. Available: https://doi.org/10.1177/0734242X221074114

[344] N. Smitha and V. Singh, "Target detection using supervised machine learning algorithms for GPR data," *Sensing and Imaging*, vol. 21, no. 1, p. 11, 2020. [Online]. Available: https://doi.org/10.1007/s11220-020-0273-8

[345] N. Barkataki, A. J. Kalita, and U. Sarma, "Automatic material classification of targets from gpr data using artificial neural networks," in *2022 IEEE Silchar Subsection Conference (SILCON)*, 2022, pp. 1–5.

[346] M. Ignite. (2024, Nov.) Power BI documentation. Online Document. Microsoft Ignite. Accessed 14 January 2024. [Online]. Available: https://learn.microsoft.com/en-us/power-bi/

[347] IBM. (2024) IBM Cognos analytics manuals. Online Document. IBM. Accessed 27 April 2024. [Online]. Available: https://www.ibm.com/docs/en/cognos-analytics/12.0.0?topic=manuals

[348] G. Cloud. (2024) Looker product family documentation. Online Document. Google. Accessed 05 June 2024. [Online]. Available: https://cloud.google.com/looker/docs

[349] ELAG, *OPTIMESS laser distance sensor Type M analog-output operating manual*, ELAG, May 2009, accessed 21 March 2024. [Online]. Available: http://www.optimess.cn/UploadFiles/Others/20140726233714_21282.pdf

[350] R. Schneider, L. Prokopová, P. Modetta, and J. Petschen, *Use of artificial intelligence for cost-effective tunnel maintenance.* Taylor and Francis, 2024, ch. 23, pp. 323–339. [Online]. Available: https://www.taylorfrancis.com/chapters/edit/10.1201/9780429424441-323/use-artificial-intelligence-cost-effective-tunnel-maintenance-schneider-prokopov%C3%A1-modetta-petschen

[351] P. Urda, J. F. Aceituno, S. Muñoz, and J. L. Escalona, "Measurement of railroad track irregularities using an automated recording vehicle," *Measurement*, vol. 183, p. 109765, 2021. [Online]. Available: https://www.sciencedirect.com/science/article/pii/S026322412100720X

[352] CLEARPATH ROBOTICS, *HUSKEY Unmanned ground vehicle user manual*, CLEARPATH ROBOTICS, Aug. 2020, accessed 04 February 2021. [Online]. Available: https://levelfivesupplies.com/wp-content/uploads/2020/08/Husky-UGV-User-Manual.pdf

[353] H. Liu, M. Rahman, M. Rahimi, A. Starr, I. Durazo-Cardenas, C. Ruiz-Carcel, A. Ompusunggu, A. Hall, and R. Anderson, "An autonomous rail-road amphibious robotic system for railway maintenance using sensor fusion and mobile manipulator," *Computers and Electrical Engineering*, vol. 110, p. 108874, 2023. [Online]. Available: https://www.sciencedirect.com/science/article/pii/S0045790623002987

[354] U. Jasnoch. (2021, Oct.) Optimize your asset management with a digital twin. Organisation Website. Haxagon. Accessed 17 December 2022. [Online]. Available: https://sigblog.hexagon.com/optimize-your-asset-management-with-a-digital-twin/

[355] P. Bevelacqua. (2024) The Friis equation. Organisation Website. Antenna Theory. Accessed 12 February 2025. [Online]. Available: https://www.antenna-theory.com/basics/friis.php

[356] S. M. Shrestha, Y. Tomizawa, and I. Arai, "Detection of buried pipes under road surfaces using high-resolution frequency GPR," *Journal of the Japan Society of Remote Sensing*, vol. 28, no. 3, pp. 231–245, 2008.

[357] A. S. Turk, P. Ozkan-Bakbak, L. Durak-Ata, M. Orhan, and M. Unal, "High-resolution signal processing techniques for through-the-wall imaging radar systems," *International Journal of Microwave and Wireless Technologies*, vol. 8, no. 6, pp. 855–863, 2016. [Online]. Available: https://www.cambridge.org/core/product/C2543A23E7B6BB93C2F58B731F8ECDAC

[358] S. B. Thomas and L. P. Roy, "Thin coal layer thickness estimation using MUSIC algorithm," in *2017 IEEE Microwaves, Radar and Remote Sensing Symposium (MRRS)*, 2017, pp. 99–104.

[359] L. Li, C. Yu, Z. Han, and T. Sun, "Automatic identification of the rock-soil interface and solution fissures from optical borehole images based on color features," *IEEE Journal of Selected Topics in Applied Earth Observations and Remote Sensing*, vol. 12, no. 10, pp. 3862–3873, 2019.

[360] MathWorks, "pmusic - Pseudospectrum using MUSIC algorithm," September 2023. [Online]. Available: https://uk.mathworks.com/help/instrument/

[361] M. Wachowiak, "music-aoa-estimation-py," Feb. 2021. [Online]. Available: https://github.com/MarcinWachowiak/music-aoa-estimation-py

[362] V. Slobodyan, "MUSIC - Multiple Signal Classification," November 2017. [Online]. Available: https://github.com/vslobody/MUSIC

[363] T. Spadin, "pyArgus," September 2023. [Online]. Available: https://pypi.org/project/pyargus/

[364] SIEMENS. (2020, Jul.) Digital signal processing: Sampling rates, bandwidth, spectral lines, and more.... Organisation Website. SIEMENS. Accessed 15 October 2022. [Online]. Available: https://community.sw.siemens.com/s/article/digital-signal-processing-sampling-rates-bandwidth-spectral-lines-and-more

[365] J. W. Cooley and J. W. Tukey, "An algorithm for the machine calculation of complex fourier series," *Mathematics of Computation*, vol. 19, no. 90, pp. 297–301, 1965.

[366] W. M. Gentleman and G. Sande, "Fast fourier transforms for fun and profit," in *Proceedings of the November 7-10, 1966, Fall Joint Computer Conference*, ser. AFIPS '66 (Fall). New York, NY, USA: Association for Computing Machinery, 1966, p. 563–578. [Online]. Available: https://doi.org/10.1145/1464291.1464352

[367] A. E. Lanman, J. C. Pober, N. S. Kern, E. de Lera Acedo, D. R. DeBoer, and N. Fagnoni, "Quantifying EoR delay spectrum contamination from diffuse radio emission," *Mon Not R Astron Soc*, vol. 494, no. 3, pp. 3712–3727, May 2020. [Online]. Available: https://doi.org/10.1093/mnras/staa987

[368] R. Zhang, K. Xu, Y. Quan, S. Zhu, and M. Xing, "Signal subspace reconstruction for DOA detection using quantum-behaved particle swarm optimization," *Remote Sensing*, vol. 13, no. 13, p. 2560, 2021.

[369] M. E. Kotanchek, "Stability exploitation and subspace array processing," Ph.D. dissertation, The Pennsylvania State University, 1995. [Online]. Available: https://www.proquest.com/openview/39b3dbcaa125682ebc237fcac7a88842/1?pq-origsite=gscholar&cbl=18750&diss=y

[370] M. Parker, *Digital Signal Processing 101*, 2nd ed., T. Pitts, Ed. Oxford, United Kingdom: Jonathan Simpson, Jun. 2017. [Online]. Available: https://brownsbfs.co.uk/Product/Parker-Michael-Senior-DSP-Technical-Marketing-Manager-Altera-Corpor/Digital-Signal-Processing-101/9780128114537

[371] C. Benoit, "Note on a method for solving normal equations arising from the application of the least squares method to a system of linear equations with fewer equations than unknowns - application of the method to solving a defined system of linear equations," *Bulletin géodésique*, vol. 2, no. 1, pp. 67–77, 1924. [Online]. Available: https://doi.org/10.1007/BF03031308

[372] C. B. Moler and G. W. Stewart, "An algorithm for generalized matrix eigenvalue problems," *SIAM Journal on Numerical Analysis*, vol. 10, no. 2, pp. 241–256, 1973. [Online]. Available: http://www.jstor.org/stable/2156353

[373] C.-Q. Miao, "On Chebyshev-Davidson method for symmetric generalized eigenvalue problems," *Journal of Scientific Computing*, vol. 85, no. 3, p. 53, 2020. [Online]. Available: https://doi.org/10.1007/s10915-020-01360-4

[374] K. S. Al-Kharabsheh, I. M. AlTurani, A. M. I. AlTurani, and N. I. Zanoon, "Review on sorting algorithms a comparative study," *International Journal of Computer Science and Security (IJCSS)*, vol. 7, no. 3, pp. 120–126, 2013. [Online]. Available: https://www.academia.edu/download/83532208/research-paper-lecture-5-bubble-sort-4.pdf

[375] M. Marcellino, D. W. Pratama, S. S. Suntiarko, and K. Margi, "Comparative of advanced sorting algorithms (quick sort, heap sort, merge sort, intro sort, radix sort) based on time and memory usage," in *2021 1st International Conference on Computer Science and Artificial Intelligence (ICCSAI)*, vol. 1, 2021, pp. 154–160.

[376] G. Liu, H. Chen, X. Sun, and R. C. Qiu, "Modified MUSIC algorithm for DOA estimation with Nyström approximation," *IEEE Sensors Journal*, vol. 16, no. 12, pp. 4673–4674, 2016.

[377] E. D. D. Claudio, R. Parisi, and G. Jacovitti, "Space time MUSIC consistent signal subspace estimation for wideband sensor arrays," *IEEE Transactions on Signal Processing*, vol. 66, no. 10, pp. 2685–2699, 2018.

# Appendices

# Appendix A. Code and Dataset Availability

The research in this thesis has been consolidated and disseminated in [294].

To ensure transparency, all relevant codes and datasets have been openly published in publicly accessible repositories. Given the extensive nature of the developed programs, a code and dataset access statement with relevant links is provided in this thesis in lieu of a full code appendix. These repositories contain all materials necessary to reproduce the main results presented in this thesis.

For visual access links, see Figure A.1.

---

Full source code can be accessed via the GitHub repository:

| https://github.com/TMc-DevTools/3D_Visualisation_Hybrid-Rotational_GPR.git |
|---|

Released code and relevant documentation includes:

- (Python) Scripts enabling gprMax Area Scan functionality.
- (Python) Firmware for operation of developed Hybrid-Rotational GPR hardware.
- (Python) Toolbox for implementation of the developed 3D visualisation workflow.
- (MATLAB) Scripts for CPM data processing on 1D traces.

---

Key datasets have been publicly released in the IEEE DataPort repository:

| http://ieee-dataport.org/documents/3d-visualisation-new-hybrid-rotational-ground-penetrating-radar-subsurface-inspection |
|---|

Content includes:

- (Chapter 4) Data from gprMax area scan simulations.
- (Chapter 5) Data from physical lab-based fixed-directional GPR measurements.
- (Chapter 6) Data from physical lab-based hybrid-rotational GPR measurements.
- (Chapter 7) Data from physical hybrid-rotational GPR field testing.

(a)

(b)

Figure A.1: Links to publicly available source code (a) and key datasets (b).

# Appendix B. Frequency-Averaged Directivity Gain

This section derives the frequency-averaged directivity gain relation used to extract the antenna radiation patterns in Chapter 6.

For practical purposes, the formulation is applied within the horizontal 2D measurement plane surrounding the AUT, with feed connector centred at the local coordinate system's origin. While a similar approach can be generalised through additional integrals to evaluate frequency-averaged directivity gain at arbitrary point in the inherently 3D radiation field of the AUT, such an involved derivation extends beyond the scope of this research project.

As practical measurements involve orbiting a reference antenna about the AUT on a circular path, a 2D polar coordinate system convention is adopted. Let $\underline{r} = (r, \theta)$ denote an arbitrary point in space beyond the footprint of the AUT in the horizontal measurement plane and residing in the far field of the AUT. Typically, this critical separation distance is expressed as:

$$R_{ff} > \frac{2D^2}{\lambda_{max}}, \tag{B.1}$$

where $D$ represents the largest characteristic length scale of the antenna aperture and $\lambda_{max} = c/f_0$ denotes the longest characteristic wavelength involved, with $c$ denoting the speed of light. Longer wavelengths are considered owing to their longevity over propagation, compared to more rapidly attenuating shorter wavelengths (i.e. higher frequency components).

However, as put forward by [331],

$$R_{ff} > 4\lambda_c \tag{B.2}$$

presents a more realistic estimation in the context of *broadband* measurements, including GPR. Here, $\lambda_c$ denotes the wavelength associated with the centre frequency of the measured bandwidth, given by

$$\lambda_c = \frac{c}{f_c} = \frac{2c}{f_0 + f_1}. \tag{B.3}$$

Returning to consideration of the measurement plane, the AUT's directivity gain $G(\underline{r})$ at any well-defined location — with given fixed $\theta \in [0, 360]^\circ = [0, 2\pi]$ — can be expressed in terms of the power transmission coefficient $S_{21}(f) \in \mathbb{R}_{\geq 0}$, where the AUT connects to VNA measurement Port 1. Assume frequency swept measurements are recorded across the well-defined bandwidth interval $B = [f_0, f_1] \subset \mathbb{R}$ where $f_0 < f_1$ and $f_0 f_1 > 0$.

Since GPR fundamentally involves broadband signals, typically with relative beamwidth exceeding 10%, the conventional approach of recovering measures of directivity gain at a fixed frequency value can generate misleading results. Moreover, the significant variability possible in antenna radiation efficiency across such a bandwidth can also lead to misrepresentation if a fixed transmission efficiency is assumed, especially if only subset of full bandwidth is considered. Therefore, akin to the approach adopted by [331], here the normalised transmitted energy between $\underline{r}$ and the origin is considered, obtained by computing

$$\tilde{\epsilon} = \left(\frac{1}{f_1 - f_0}\right) \int_{f_0}^{f_1} |S_{21}(f)|^2 df. \tag{B.4}$$

Essentially, this formulation computes area under the $S_{21}$ response curve — which more accurately representing total transmitted energy. To alleviate dependency on the specific bandwidth physically measured, the result is normalised by its span. It should be noted that the integral requires a dimensionless measure of $S_{21}$, requiring more commonly adopted decibel units to be converted to linear form prior to evaluation.

Assuming the far-field condition holds, and that free-space exclusively separates the AUT and reference antenna (located at $\underline{r}$), *received power* at this point would be,

$$P_{rx}(\underline{r}, f) = P_{tx}(f)|S_{21}(f)|^2, \tag{B.5}$$

where $P_{tx}(f) \in (0, 1]$ is the scaling factor denoting the efficiency of power transfer (at any given frequency) between both points. By Equation B.4, this expression can be generalised to account for frequency-averaging across the full measurement bandwidth, which yields,

$$\tilde{P}_{rx} = \tilde{P}_{tx}\tilde{\epsilon}. \tag{B.6}$$

At this point, consider the Friis transmission equation [355], noting that the received power at $\underline{r}$ can also be expressed as,

$$P_{rx}(\underline{r}, f) = P_{tx}(f)G(\underline{r}, f)\left(\frac{\lambda(f)}{4\pi R}\right)^2, \tag{B.7}$$

where: $R = ||\underline{r}||$ denotes the absolute displacement of the measurement point from the origin; $\lambda = c/f$ is the associated wavelength and $G$ is the directivity gain value at the considered point in the field.

Substituting corresponding frequency-averaged terms, as prior, gives

$$\tilde{P}_{rx} = \tilde{P}_{tx}\tilde{G}(\underline{r})\left(\frac{\tilde{\lambda}}{4\pi R}\right)^2, \tag{B.8}$$

where $\tilde{G}$ denotes frequency-averaged directivity gain, defined as:

$$\tilde{G}(\underline{r}) = \left(\frac{1}{f_1 - f_0}\right)\int_{f_0}^{f_1} G(\underline{r}, f)df. \tag{B.9}$$

At this point, note that the value of frequency-averaged wavelength ($\tilde{\lambda}^2$) can be directly evaluated over the full bandwidth, yielding

$$\tilde{\lambda}^2 = \left(\frac{1}{f_1 - f_0}\right)\int_{f_0}^{f_1}\left(\frac{c}{f}\right)^2 df = \frac{c^2}{f_0 f_1}, \tag{B.10}$$

which can be back-substituted into Equation B.8 to return

$$\tilde{P}_{rx} = \tilde{P}_{tx}\tilde{G}(\underline{r})\left(\frac{c^2}{f_0 f_1 (4\pi R)^2}\right). \tag{B.11}$$

Now, recalling Equation B.6, further substitution for $\tilde{P}_{rx}$ yields,

$$\tilde{P}_{tx}\tilde{\epsilon} = \tilde{P}_{tx}\tilde{G}(\underline{r})\left(\frac{c^2}{f_0 f_1 (4\pi R)^2}\right). \tag{B.12}$$

Since the power transmission coefficient is both real-valued and greater than zero (by definition and narrative context), the above can be reduced to,

$$\tilde{\epsilon} = \tilde{G}(\underline{r}) \left( \frac{c^2}{f_0 f_1 (4\pi R)^2} \right), \tag{B.13}$$

which, as $f_0 f_1 R > 0$, can be rearranged in terms of directivity gain,

$$\tilde{G}(\underline{r}) = \left( \frac{f_0 f_1 (4\pi R)^2}{c^2} \right) \tilde{\epsilon}. \tag{B.14}$$

The desired final formulation of normalised frequency-averaged directivity gain — expressed in terms of $S_{21}(f)$ — can be now recovered by substituting the form for $\tilde{\epsilon}$ from Equation B.4,

$$\tilde{G}(\underline{r}) = \left( \frac{f_0 f_1 (4\pi R)^2}{c^2 (f_1 - f_0)} \right) \int_{f_0}^{f_1} |S_{21}(f)|^2 df. \tag{B.15}$$

# Appendix C. Breakdown of IFT and MUSIC

This section provides further details on the *practical numerical* implementation of the IFT and MUSIC algorithms, which underpin the CPM algorithm discussed in Chapter 7.

## C.1 Implementing CPM – An Overlooked Knowledge Gap

In researching the CPM algorithm, this work identified multiple mathematical inconsistencies in the debut publication of the CPM algorithm [338]. No individual issue was of significant merit to fully undermine the robustness of the presented rationale. However, collectively they were more than sufficient to considerably limit the accessibility of the algorithm, particularly to researchers new to the field or attempting a numerical implementation.

Consultation of relevant associated literature encountered few subsequent works that directly utilised CPM to enhance practical GPR datasets, whether simulated or experimentally derived. Prior to this investigation, the only direct follow up application of CPM was aligned with GPR for infrastructure inspection concerned utility pipe detection beneath gravel roads in Japan [356], notably led by the original authors. Where subsequently referenced in independent works, they were principally consulted for details concerning the mathematics behind CPM's dependant algorithms — especially MUSIC [357–359]. These works often contained detailed but highly abstract mathematical justifications of *why* the MUSIC algorithm could achieve spatial resolution enhancement. Yet, no study encountered that numerically implemented the MUSIC algorithm provided a tractable, standalone recount of the exact sequence of practical steps involved in *how* the computations were actually performed.

Similarly, practical details on the numerical implementation of windowed IFT were often omitted — likely for brevity — given the availability of built-in functions in most high-level programming languages. Furthermore, when references to other works were provided, the mathematics presented would commonly employ differing terminology and notation, complicating interpretation and limiting accessibility, especially for non-specialist researchers.

Based on these observations, it was suspected that ambiguity surrounding the practical implementation of the MUSIC algorithm (and to a lesser but non-trivial extent, windowed IFT) were the key contributors to the limited research uptake of the CPM algorithm.

To further probe this theory and provide a more complete review, standalone software solutions for the practical implantation of the MUSIC algorithm were also considered.

One noteworthy contribution was the `pmusic()` subroutine, developed for MATLAB [360]. This proprietary subroutine returned the frequency domain pseudospectrum associated with a known time domain signal input. Scope for application to this investigation was found to be limited, as `pmusic()`did not natively support the conversion of signal responses from the frequency domain to the temporal domain. Moreover, as a proprietary subroutine, the tractability of the numerical implementation was extremely limited, and therein any subsequent opportunity for augmentation.

Open-source implementations encountered were exclusively Python-based [361,362]. The pyArgus package [363] was found to provide the most comprehensive implementation of the MUSIC algorithm. It featured multiple subroutines to implement MUSIC for signal 'angle of arrival' estimation, applied to both single and multi-dimensional input signals. However, although source code was accessible, the traceability of the algorithm was impaired due to insufficient documentation, especially in the form of clear in-line comments devoid of complex programmatical terminology.

Collectively, these findings reinforced the initial inference, highlighting an important but overlooked knowledge gap in the field. To address the gap effectively, it was essential to increase the accessibility of the CPM algorithm to a broader audience. Addressing this gap required improving the accessibility of the CPM algorithm for a wider audience. To this end, a consolidated and tractable summary was required to comprehensively detail the practical implementation of both windowed-IFT and the MUSIC algorithm.

## C.2 Algorithm – Windowed-IFT

This section deconstructs the practical computation of an Inverse Fourier Transform (IFT), performed in the context of GPR temporal response recovery, with application of a suitable windowing function to suppress spectral leakage artifacts.

Consider a typical 1D GPR trace. To warrant conversion to the temporal domain, assume that the trace was directly recorded in the frequency domain, using a linear frequency sweep containing $N$ sample points, cycled through $f \in [f_{min}, f_{max}]$, with $f \subset \mathbb{R}_{>0}$ and $0 < f_{min} < f_{max}$. Sample measurements were finite and discretised, indexed by integer values $n \in [0, 1, \ldots, N-1]$. Note that zero-based indexing is adopted to match the indexing conventions of the programming languages encountered during exploration of software solutions discussed in the previous section.

The first stage of numerical implementation is to recover the two-way travel times (in the temporal domain) associated with each sample point in the frequency domain.

Starting from the associated frequency incrementation,

$$\Delta f = \frac{f_{\max} - f_{\min}}{N-1}, \tag{C.1}$$

the maximal two-way travel time (i.e. 'temporal interval', 'frame-size') is given by,

$$T = \frac{1}{\Delta f}. \tag{C.2}$$

From this, incrementation between sample points in the time domain,

$$\Delta t = \frac{T}{N-1}, \tag{C.3}$$

facilitates direct computation of associated two-way travel times,

$$t = n\Delta t, \tag{C.4}$$

where $t \in [0, T] \subset \mathbb{R}_{\geq 0}$.

The next stage of numerical implementation is to recover the temporal response profile, $X[t]$, from the observed frequency response profile $X[f]$. Note that amplitudes of both responses are inherently complex-valued because the VNA directly records variation in the $S_{11}$ reflection coefficient, which is fundamentally related to the complex impedance of the measurement environment — most significantly the GPR antenna (see Chapter 2).

To increase computational efficiency and stability during numerical implementation of IFT, $X[f] \in \mathbb{C}$ is converted from Cartesian form,

$$X[f] = x + iy, \tag{C.5}$$

where $x \in \mathbb{R}$ denotes the real component and $y \in \mathbb{R}$ denotes the imaginary component, with $i = \sqrt{-1}$, to exponential form,

$$X[f] = |A|e^{i\theta}, \tag{C.6}$$

where $|X| \in \mathbb{R}_{\geq 0}$ is the absolute magnitude in dimensionless units (i.e. the modulus), and $\theta \in (-\pi, \pi] \subset \mathbb{R}$ is the principal argument in radians.

For $X[f]$ returned from the VNA in Cartesian format[1], conversion to exponential format follows,

$$\begin{aligned} |X| &= \sqrt{x^2 + y^2} \\ \theta &= \arctan 2(y, x) \end{aligned} \tag{C.7}$$

where the two-argument arctangent function is defined,

$$\theta = \text{arctan2}(y, x) = \begin{cases} \arctan\left(\frac{y}{x}\right) & \text{if } x > 0, \\ \arctan\left(\frac{y}{x}\right) + \pi & \text{if } x < 0 \text{ and } y \geq 0, \\ \arctan\left(\frac{y}{x}\right) - \pi & \text{if } x < 0 \text{ and } y < 0, \\ +\frac{\pi}{2} & \text{if } x = 0 \text{ and } y > 0, \\ -\frac{\pi}{2} & \text{if } x = 0 \text{ and } y < 0, \\ \text{NaN} & \text{if } x = 0 \text{ and } y = 0. \end{cases} \tag{C.8}$$

For $X[f]$ returned from the VNA in exponential format[2], magnitude requires conversion from decibels ($|X|_{dB}$) to dimensionless units ($|X|$). The relationship is given by,

$$|X| = 10^{\frac{|X|_{\text{dB}}}{20}}. \tag{C.9}$$

Magnitude is accompanied by frequency response phase, $\phi \in \mathbb{R}$, in units of degrees.

The corresponding argument is recovered by conversion to radians,

$$\tilde{\theta} = \phi\left(\frac{\pi}{180}\right) \in \mathbb{R}, \tag{C.10}$$

followed by the mapping $\tilde{\theta} \to (-\pi, \pi]$ to recover the principal value.

Having recovered $X[f]$ in dimensionless exponential form, it is necessary to apply a suitable windowing function $W[n]$ to combat spectral leakage (see [364] for further details). To effectively combat spectral leakage, one can apply the Kaiser-Bessel Window to $A[f]$ prior to performing IFT. For a breakdown of common window functions, see Section C.3.

[1]Specified by data format RI (i.e. real-imaginary) in an `.s1p` file header.
[2]Specified by data format DB (i.e. decibels) in an `.s1p` file header.

In accordance with Convolution Theorem, the window is applied in the frequency domain via the convolution,

$$X_w[f_n] = W[n] \cdot X[f_n] = \sum_{m=1}^{N} W[m] X\left[f_{n-m+1}\right], \tag{C.11}$$

where $f_n$ denotes sequentially indexed excitation frequencies associated with the GPR trace.

The temporal domain response profile is subsequently recovered via IFT. Specifically Inverse Discrete Fourier Transform (IDFT), formulated,

$$X[t_k] = \frac{1}{N} \sum_{n=0}^{N-1} X_w[f_n] \exp\left(\frac{2\pi i}{N} n t_k\right), \tag{C.12}$$

where $k \in [0, 1, \ldots, N-1]$ indexes aforementioned discretised two-way travel times in the temporal domain.

Note that the computational complexity of IDFT is $O(N^2)$, which would limit the scalability of this approach to larger hybrid-rotational GPR datasets associated with real working infrastructure. Therefore, in this work, practical computation is achieved using the more efficient IFFT (Inverse Fast Fourier Transform) algorithm, which reduces computational complexity to at most $O(N \log N)$.

The IFFT algorithm is a divide-and-conquer method, which effectively reformulates the computation of $N = n_1 n_2$ independent IFT operations — where $n_2, n_2 \in \mathbb{N}_{\leq N}$ is a recursive sequence of $n_1$ equivalent Discrete Fourier Transforms (DFTs) of size $n_2$. Here, DFT computations are based on the Cooley-Tukey algorithm for Fast Fourier Transform (FFT) [365]. Briefly summarised, the algorithm is based on the following relationship,

$$X[t_n] = \mathrm{IFFT}(X[f_n]) = \frac{1}{N} \mathrm{FFT}(X^*[f_n])^*, \tag{C.13}$$

where $X^*$ denotes the complex conjugate of signal response amplitude. This relationship leverages the conjugate, periodic and antiperiodic (i.e. odd-even) symmetry of the complex exponential weighting factors (i.e. complex roots of units, also dubbed 'twiddle factors') to reduce the number of unique computations involved, thereby increasing computational efficiency [366].

## C.3 Window Formulations

This section provides a summary of windowing functions integrated into the developed 3D visualisation workflow, including relevant mathematical formulations and insights into their respective contextual applications.

The Rectangular (None) Window is presented in Section C.3.1 followed by the Hamming and Hanning Windows in Section C.3.2 and Section C.3.3, respectively. Details of the Blackman Window are provided in Section C.3.4, alongside the Blackman-Harris variation in Section C.3.5. The Kaiser-Bessel Window is detailed in Section C.3.6, followed by an overview of the Nuttall Window follows in Section C.3.7. Finally, details on the Tapered Cosine (Turkey) Window are presented in Section C.3.8.

### *C.3.1 Rectangular (None) Window*

The Rectangular (None) Window is given by,

$$W[n] = 1 \tag{C.14}$$

**Usage**: This is fundamentally the simplest window to implement, since it applies a uniform weighting factor across all frequency components. It is typically applied in scenarios where spectral leakage is negligible, not a concern, or when theoretical analysis is prioritised over practical considerations (e.g. in textbook examples or idealised simulations). However, due to its comparatively poor spectral characteristics — particularly its high sidelobe levels — it is rarely used in practical signal processing applications, where more sophisticated formulations are preferred to reduce leakage and improve frequency resolution.

### *C.3.2 Hamming Window*

The Hamming Window is given by,

$$W[n] = a - (1 - a)\cos\left(\frac{2\pi n}{N}\right), \tag{C.15}$$

with $0 \leq n < N$ and $a = 25/46$.

**Usage**: This window is used to provide moderate levels of sidelobe attenuation.

### C.3.3 Hanning Window

The Hanning Window is given by,

$$W[n] = a - (1-a)\cos\left(\frac{2\pi n}{N}\right), \tag{C.16}$$

with $0 \leq n < N$ and $a = 1/2$.

**Usage**: This window is similar to the Hamming Widow, but used to provide smoother sidelobe attenuation. It is often applied to particularly noisy signals.

### C.3.4 Blackman Window

The Blackman Window is given by,

$$W[n] = a_0 - a_1\cos\left(\frac{2\pi n}{N}\right) + a_2\cos\left(\frac{4\pi n}{N}\right) \tag{C.17}$$

with $0 \leq n < N$.

For the truncated form,

$$a_0 = \frac{1-\alpha}{2}, \quad a_1 = \frac{1}{2}, \quad a_2 = \frac{\alpha}{2} \quad \text{with } \alpha = 0.16. \tag{C.18}$$

For the exact form,

$$\begin{aligned} a_0 &= 7938/18608 \\ a_1 &= 9240/18608 \\ a_2 &= 1430/18608 \end{aligned} \tag{C.19}$$

**Usage**: This window is used when high sidelobe attenuation is critical and some frequency resolution can be sacrificed (e.g. high dynamic range spectral analysis in radio astronomy [367]).

### C.3.5 Blackman-Harris Window

The Blackman-Harris Window is given by,

$$W[n] = a_0 - a_1 \cos\left(\frac{2\pi n}{N}\right) + a_2 \cos\left(\frac{4\pi n}{N}\right) - a_3 \cos\left(\frac{6\pi n}{N}\right), \tag{C.20}$$

with $0 \leq n < N$, and

$$\begin{aligned} a_0 &= 0.35875 \\ a_1 &= 0.48829 \\ a_2 &= 0.14128 \\ a_3 &= 0.01168 \end{aligned} \tag{C.21}$$

**Usage**: It is used when the highest possible levels sidelobe attenuation are required. However, this often comes at the cost of more noticeably reduced frequency resolution.

### C.3.6 Kaiser-Bessel Window

The Kaiser-Bessel Window is given by,

$$W[n] = \frac{I_0\left(\pi\alpha\sqrt{1 - \left(\frac{2n}{N} - 1\right)^2}\right)}{I_0(\pi\alpha)}, \tag{C.22}$$

with $0 \leq n < N$.

Here, $I_0$ denotes the 0th order Bessel function of the first kind, and $\alpha = 3$ is the typical empirically defined reference value for the tuning parameter.

**Usage**: This is low to moderate complexity window to implement, with reasonable computational efficiency. The trade-off between sidelobe and main lobe width can be adjusted using the tuning parameter, better regulating achieved levels of frequency resolution. This affords much greater versatility than other windows, making it arguably the most general-purpose candidate for the majority of practical applications.

### C.3.7 Nuttall Window

The Nuttall Window is given by,

$$W[n] = a_0 - a_1 \cos\left(\frac{2\pi n}{N}\right) + a_2 \cos\left(\frac{4\pi n}{N}\right) - a_3 \cos\left(\frac{6\pi n}{N}\right), \tag{C.23}$$

with $0 \leq n < N$, and

$$\begin{aligned} a_0 &= 0.355768 \\ a_1 &= 0.487396 \\ a_2 &= 0.144232 \\ a_3 &= 0.012604 \end{aligned} \tag{C.24}$$

**Usage**: This window is used when high levels of side lobe attenuation are required, and maintaining high frequency resolution justifies a wider main lobe. However, it is also often a more computationally expensive window, which can limit efficiency, especially on larger datasets.

### C.3.8 Tapered Cosine (Turkey) Window

The Tapered Cosine (Turkey) Window is given by,

$$W[n] = \begin{cases} \frac{1}{2}\left[1 + \cos\left(\frac{2\pi n}{\alpha N}\right)\right], & 0 \leq n < (\frac{\alpha}{2})N \\ 1, & (\frac{\alpha}{2})N \leq n < \frac{N}{2} \\ W[N-n], & \frac{N}{2} \leq n < N \end{cases} \tag{C.25}$$

with $0 \leq n < N$ and $\alpha \in [0, 1]$.

Here, $\alpha = 0.5$ is a typical reference value for the tuning parameter. At the limit $\alpha = 0$ the Rectangular Window is recovered, and for $\alpha = 1$ the Hanning Window is recovered.

**Usage**: This window is typically used when a lower complexity window is desirable, and less aggressive spectral leakage suppression with tuning functionality (albeit limited) is acceptable.

## C.4 Algorithm – MUSIC

This section deconstructs the numerical implementation of the MUSIC algorithm.

As a spectral estimation technique — widely adopted for signal processing due to its high-resolution capability [358, 368] — the MUSIC (Multiple Signal Classification) algorithm fundamentally exploits signal-noise orthogonality in received wavefronts to return temporal response profiles exhibiting suppressed noise, yielding sharper[3] amplitude peaks than its IFT counterpart.

The process is considered a generalised signal processing technique applicable to arbitrary antenna setup topologies [369], which justifies its direct application to the monostatic, orientable antenna configuration of hybrid-rotational GPR.

Numerical implementation reduces to five key steps:

1. Approximate the signal covariance matrix, $S$.
2. Decompose $S$ to identify eigenvalues, $\lambda_i$, and eigenvectors, $v_i$.
3. Partition $v_i$ by magnitude of $\lambda_i$ to approximate the associated Noise Matrix, $E_w$.
4. Calculate the associated signal steering matrix, $A$.
5. Using $E_w$ and $A$, compute the pseudospectrum to recover the temporal response profile.

This section formalises each step, consolidating relevant mathematics across the relevant literature. Tractability is prioritised, ensured through standardisation of nomenclature. Throughout the process, dimensional analysis was utilised to locate and rectify sources of ambiguity.

[3] In this work, the notion of 'sharpness' can be formally regarded as the Full Width at Half Maximum (FWHM) of an amplitude peak.

Meaningful elaboration on each step requires a formal definition of the problem model. The VNA output signal for each trace can be modelled as

$$X[f] \approx As + w, \tag{C.26}$$

where,

$$\begin{aligned} X[f] &= \begin{bmatrix} x_0 & x_1 & \cdots & x_{N-1} \end{bmatrix}^T, \\ s &= \begin{bmatrix} s_0 & s_1 & \cdots & s_{N-1} \end{bmatrix}^T, \\ w &= \begin{bmatrix} w_0 & w_1 & \cdots & w_{N-1} \end{bmatrix}^T, \\ A &= \begin{bmatrix} a[t_0] & a[t_1] & \cdots & a[t_{N-1}] \end{bmatrix} \end{aligned} \tag{C.27}$$

Here, $s$ is the signal vector, representing the 'true' backscattered signals from $K \in \mathbb{N}$ subsurface anomalies, with the transpose operator denoted $[\dots]^T$. Additive White Gaussian Noise is contributed by the noise vector $w$, to emulate signal clutter and thermal interference. The signal steering matrix, $A$, governs the direction of arrival of received wavefronts. It is comprised from $K$ individual steering vectors which encode the phase delays associated with each wavefront, and by extension, the discrete two-way travel times of the desired temporal response profiles. The steering vector of wavefront $p \in [0, 1, \dots, K-1]$ takes the form:

$$a[t_p] = \left[\exp(-2\pi i f_0 t_p), \exp(-2\pi i f_1 t_p), \dots, \exp(-2\pi i f_{N-1} t_p)\right]^T. \tag{C.28}$$

In Step (1), the ideally required autocorrelation matrix of $X$ is approximated by the $N \times N$ sample covariance matrix,

$$S \approx E[XX^*] = XX^*, \tag{C.29}$$

As each trace recorded corresponds to a standalone VNA signal measurement, computation of the expected value $E[\dots]$ is for a sample size of one, justifying reduction of the expression to a direct conjugate product. This matrix relays the degree of correlation (i.e. standardised covariance) between the antenna elements and the individual backscattered signals which comprised VNA output [370]. It is assumed that each waveform emitted during the VNA frequency sweep is representative of a separate constituent signal 'element' in this approximation.

In Step (2), Eigenvalue Decomposition (EVD) of $S$ satisfies, by definition,

$$Sv_i = S\lambda_i. \tag{C.30}$$

Direct manual numerical implementation of EVD is possible through back-substitution of the roots of the characteristic polynomial,

$$\det(S - \lambda_i I) = 0, \tag{C.31}$$

where $\det(\dots)$ is the determinant operator, and $I$ is the $N \times N$ Identity Matrix.

More sophisticated approaches include use of the Cholesky factorisation algorithm [371], QZ algorithm [372] (i.e. generalised Schur decomposition algorithm) or the Chebyshev-Davison Method [373]. However, to provide maximal computational efficiency and stability, it is pragmatic to utilise a built-in EVD function based on the aforementioned technique(s). For both MATLAB and Python's SciPy Library, EVD can be readily performed by calling `eig()`, `573`, `574`.

Once extracted, it is necessary to sort $v_i$ into monotonic ascending order based on the magnitudes of corresponding $\lambda_i$ (i.e. $0 \leq \lambda_0 \leq \lambda_1 \leq \cdots \leq \lambda_{N-1}$). This order is always well-defined, since $S$ is a Hermitian matrix by formulation. Where not implemented automatically during EVD, a dedicated sorting algorithm such as Heapsort, Bubble Sort, Quick Sort and Radix Sort [374,375] can be utilised.

In Step (3), eigenvectors are partitioned into the constituent Signal Subspace $U_s$ and Noise Subspace $U_w$ of $X$. This is done to exploit the orthogonality of the associated basis vectors (selective $v_i$) to achieve improved noise suppression and scattering centre localisation. Numerical implementation requires horizontal concatenation of $v_i$ (as in construction of $A$ ) associated with low magnitude $\lambda_i$ to approximate the Noise Matrix ($E_w$), which contains the basis vectors of $U_w$. By taking the complement — recovering $v_i$ — with associated high magnitude $\lambda_i$, the approximated Signal Matrix ($E_s$) is recovered. For work presented in Chapter 7, only $E_w$ required explicit computation.

It should be noted that what constitutes a low magnitude is inherently ambiguous. In fact, attempts to establish an optimal partition to form $E_s$and $E_w$ has factored into the development of numerous different approaches, including the Nystrom Method [376], ML Inverse Fitting [377] and more recently, Quantum-Behaved Particle Swarm Optimisation [368]. Practical implementation of these methods can be highly involved, and over-specification for what is often a visually discernible small proportion of dominating $\lambda_i$ (e.g. [0.01,0.05,10,0.2]).

A sufficiently reliable and low complexity alternative is to perform an array search across all $v_i$ for low magnitude $\lambda_i$, which incorporates a manually defined acceptance threshold parameter $\beta$ to facilitate refinement and fine-tuning of subsequent partition attempts. This approach provides a significant reduction in computation complexity and exhibits negligible observable impact on the final temporal profiles recovered.

In accordance with standard practice in statistical confidence tests, this study considered a 10% deviation from the maximal magnitude eigenvalue grounds for inclusion in $E_w$ (other common values include 5% and 1%, subject to context). This was implemented using the acceptance threshold,

$$\lambda_b < \beta := 0.9 \left[ \max_{i \in \{0,1,\ldots,N-1\}} (\lambda_i) \right], \tag{C.32}$$

where $\lambda_b$ for $b \in [0, 1, \ldots, N-1]$ denote an arbitrary eigenvalue under consideration.

Numerical implementation of Step (4) centres on definition of discretised frequency values $f_i$ and temporal values $t_i$ to calculate the Steering Matrix, $a$. This is achieved by recalling the reciprocal relationship presented in Equation C.2 to relate frequency sweep incrementation, $\Delta f$, to the associated frame size, $T$.

Consultation of the literature identifies customary practice in plotting temporal response profiles to durations up to 10-20ns after the final significant amplitude peak. This serves to evidence that the signal has attenuated to the level of background noise, and therein, that the maximal penetrative depth has been reached. In this work $T \approx 80$ns. However, this interval was truncated to $T \approx 40$ns to provide maximal clarity when studying amplitude peaks within the RoI volume.

Finally, in Step (5), the pseudospectrum $P_{MUSIC}[t]$ is evaluated to return the desired temporal response profile, given by,

$$x[t_k] \approx P_{\text{MUISC}}[t_k] = \frac{a[t_k]^* a[t_k]}{a[t_k]^* E_w E_w^* a[t_k]}. \tag{C.33}$$

This relation derives from the aforementioned orthogonality of $U_s$ and $U_w$, which is shared by $E_s$ and $E_w$ by design. Definition of a suitable metric returns zero when the orthogonality condition is met between eigenvectors in $E_w$ and steering vectors $a[t_k]$ (associated with wavefronts returning from backscatter at subsurface anomaly interfaces). This is equivalent to performing a Fourier Transform, thereby transitioning the returned response to the time domain. Taking the reciprocal yields sharp peaks at significant backscatter events and near-zero amplitudes in-between, thereby returning a noise-suppressed temporal response profile with enhanced spatial resolution.

## C.5 Spatial Smoothing

It was highlighted in [138] that GPR systems based on VNA linear sweep measurements are predisposed to the generation of coherent returning wavefronts, which can significantly influence MUSIC processing. Specifically, in Step (1), it was implicitly assumed that all returning wavefronts represented distinct signal waveforms (incoherence) [369]. This has potential to limit the accuracy of recovered temporal responses, including those from hybrid-rotational GPR data, motivating the implementation of Spatial Smoothing Processing (SSP) and Modified-SSP (MSSP) to decorrelate coherent return signals [338].

Numerical implementation first requires subdivision of each trace $X[f]$ (i.e. a single, large snapshot of data) into $M$ overlapping subarrays (i.e. multiple smaller 'snapshots') containing $L < N$ sample points. Subdivision includes a desirable artificial phase variation between snapshots, which is exploited for decorrelation. This can be achieved through spatial averaging of the covariance matrices associated with each subarray. To formally define these matrices, the VNA output signal model (Equation C.26) can be updated to accommodate the additional snapshots.

For snapshot $m \in [0, 1, \ldots, M-1]$,

$$X_m[f] = Bs + w_m, \tag{C.34}$$

where $B$ represents the updated steering matrix, given by

$$B = AD^{K-1}. \tag{C.35}$$

Here, $D$ is a diagonal matrix of phase delays, akin to the artificial phase variation introduced by subdividing the original dataset to combat coherence. It takes the form :

$$D = \text{diag}\left[\exp(-2\pi i \Delta f t_0), \exp(-2\pi i \Delta f t_1), \ldots, \exp(-2\pi i \Delta f t_{K-1})\right], \tag{C.36}$$

where, as prior, $\Delta f > 0$ represents the frequency incrementation of the linear frequency sweep. With this, the reduced $L \times L$ covariance matrix can be approximated:

$$S_m \approx E[X_m X_m^*] = X_m X_m^*. \tag{C.37}$$

The spatially smoothed covariance matrices, for SSP and MSSP respectively, are given by

$$S_{\text{SSP}} = \frac{1}{M} \sum_{m=0}^{M-1} S_m, \tag{C.38}$$

and

$$S_{\text{MSSP}} = \frac{1}{2M} \sum_{m=0}^{M-1} \left( S_m + J S_m^* J \right), \tag{C.39}$$

where $J$ denotes the $L \times L$ 'forward-backward' Exchange Matrix, defined:

$$J = \begin{bmatrix} 0 & 0 & \cdots & 0 & 1 \\ 0 & 0 & \cdots & 1 & 0 \\ \vdots & \vdots & \ddots & \vdots & \vdots \\ 0 & 1 & \cdots & 0 & 0 \\ 1 & 0 & \cdots & 0 & 0 \end{bmatrix}. \tag{C.40}$$

It should be noted that spatial smoothing, like CPM itself, inherently involves a trade-off. By definition of the snapshots and the associated matrix dimensions,

$$N = L + M - 1. \tag{C.41}$$

Therefore, increasing the number of snapshots to improve decorrelation performance will reduce the number of sample points per snapshot. By extension, this decreases the attainable resolution of returned temporal response profiles (and vice versa). A balance is therefore required, and should be contextually justifiable.

For example, in Chapter 7, the value $M = 10$ was selected based on iterative refinement. At this threshold, amplitude peaks with 0.5ns FWHM were returned — a scale comparable to the minimal thickness of expected target geometry in the experimental setup. Moreover, as the more sophisticated technique, MSSP was used for all numerical computations of MUSIC and CPM to leverage its (in principal) greater performance capability.

However, it should be emphasised that as bespoke numerical implementations, added care was required when interpreting temporal profiles, especially in the immediate vicinity of the temporal interval's upper limit in non-truncated domains.

This was highlighted during initial data analysis following the retaining wall test, when multiple symmetric reflections of the main amplitude peaks (for $t < 40$ns) were observed between $70\text{ns} < t \leq 80\text{ns}$. Upon closer inspection and over repeated computations, these were suspected to be false-artifacts, because they were not observed when only SSP was implemented, nor when spatial smoothing was entirely disabled.

The artifacts' manifestation was attributed to the forward-backward averaging pattern of MSSP, owing to the naturally transient nature (i.e. relatively short duration) of the return waveform, which would place main peaks closer to the beginning of the time frame than the middle.

On reflection, such inherent skew would naturally persist through implementation of the averaging pattern, in turn distorting the average temporal response profile at symmetric displacements from the end of the frame — akin to spectral leakage artifacts arising from IFT.